HAL
open science

Surface engineering of stainless steel for dairy fouling management

Manon Saget

To cite this version:

Manon Saget. Surface engineering of stainless steel for dairy fouling management. Chemical engineering. Université de Lille, 2022. English. NNT : 2022ULILR022 . tel-04087170

HAL Id: tel-04087170

https://theses.hal.science/tel-04087170v1

Submitted on 3 May 2023

HAL is a multi-disciplinary open access archive for the deposit and dissemination of scientific research documents, whether they are published or not. The documents may come from teaching and research institutions in France or abroad, or from public or private research centers.

L'archive ouverte pluridisciplinaire **HAL**, est destinée au dépôt et à la diffusion de documents scientifiques de niveau recherche, publiés ou non, émanant des établissements d'enseignement et de recherche français ou étrangers, des laboratoires publics ou privés.

PhD THESIS

SURFACE ENGINEERING OF STAINLESS STEEL FOR DAIRY FOULING MANAGEMENT

Submitted to and defended at

UNIVERSITY OF LILLE
Ecole doctorale de la Matière, du Rayonnement et de l'Environnement
Unité Matériaux et Transformations, CNRS UMR 8207,
Institut d'Electronique, de Microélectronique et de Nanotechnologie, CNRS UMR 8520

For the degree of
Doctor of Philosophy

In Condensed Matter and Molecules
Specialty: Materials Chemistry

By
Manon SAGET

Supervised by
Prof. Maude JIMENEZ and DR Yannick COFFINIER

Defended on the 2nd of May 2022 before the following PhD committee:

DR HDR Guillaume DELAPLACE	INRAe	President
DR Patrick CHOQUET	LIST, Luxemburg	Reviewer
Prof. Stéphane VALETTE	Ecole Centrale de Lyon	Reviewer
Dr. Olivier FURLING	Groupe BEL	Examiner
Dr. HDR Valérie LECHEVALIER	Agrocampus Ouest	Examiner
Mr. Guillaume DAMBLANS	France Energies Marines	Guest
Prof. Vincent THOMY	IEMN	Guest
Prof. Maude JIMENEZ	Université de Lille, UMET	Supervisor
DR Yannick COFFINIER	IEMN	Co-supervisor

Thèse de doctorat

MODIFICATION DE SURFACE DE L'ACIER INOXYDABLE POUR LIMITER L'ENCRASSEMENT LAITIER

Présentée et soutenue publiquement à

UNIVERSITE DE LILLE
Ecole doctorale de la Matière, du Rayonnement et de l'Environnement
Unité Matériaux et Transformations, CNRS UMR 8207,
Institut d'Electronique, de Microélectronique et de Nanotechnologie, CNRS UMR 8520

Pour obtenir le grade de
Docteur

En Molécule et Matière Condensée
Spécialité : Chimie des Matériaux

Par
Manon SAGET

Thèse dirigée par

Prof. Maude JIMENEZ et DR Yannick COFFINIER

Soutenue le 2 mai 2022 devant la commission d'Examen composée de :

DR HDR Guillaume DELAPLACE	INRAe	Président
DR Patrick CHOQUET	LIST, Luxemburg	Rapporteur
Prof. Stéphane VALETTE	Ecole Centrale de Lyon	Rapporteur
Dr. Olivier FURLING	Groupe BEL	Examinateur
Dr. HDR Valérie LECHEVALIER	Agrocampus Ouest	Examinatrice
Mr. Guillaume DAMBLANS	France Energies Marines	Invité
Prof. Vincent THOMY	IEMN	Invité
Prof. Maude JIMENEZ	Université de Lille, UMET	Directrice de thèse
DR Yannick COFFINIER	IEMN	Co-directeur de thèse

A mon père.

Acknowledgments

A l'issu de ces trois ans (et demi) de recherche et de rebondissements et après avoir travaillé à la croisée de trois laboratoires et d'autant d'équipes, nombreuses et nombreux sont celles et ceux à qui je dois aujourd'hui la réussite de ce projet.

Pour commencer, je tiens à remercier le Professeur Patrice Woisel, directeur du laboratoire Unité Matériaux et Transformation, le Docteur Thierry Mélin, directeur de l'IEMN, et le Docteur Guillaume Delaplace, directeur de l'INRAe de Lille, pour m'avoir donné l'opportunité de rejoindre ces trois laboratoires où j'ai effectué mes travaux de recherche.

Naturellement, je tiens à remercier chaleureusement mes directrice et directeur de thèse, la Professeure Maude Jimenez et le Docteur Yannick Coffinier, pour m'avoir recrutée sur le projet ECONOMICS et m'avoir accompagnée tout au long de ce projet de recherche.

A Maude, merci pour ton soutien, ta disponibilité (et les points thèses/goûters), pour les discussions, scientifiques ou non, pour m'avoir donné l'opportunité de participer à des congrès, et pour tes conseils, toujours empreints de bienveillance.

A Yannick, merci pour ta disponibilité pour discuter, ta pédagogie et ta patience (je n'oublierai pas mes « premiers pas » en salle blanche et avec la boîte à gants), tes encouragements et enfin tes conseils sur les manipes.

Un grand Merci pour tout ce que vous m'avez appris et pour votre confiance pendant ces trois années !

Je remercie également le Professeur Vincent Thomy pour son expertise sur la mouillabilité et les mesures de CAH, ses conseils et sa gentillesse. Merci également au Docteur Guillaume Delaplace pour son aide et ses conseils en dynamique des fluides.

Je tiens à exprimer ma gratitude aux Docteur Patrick Choquet, Professeur Stéphane Valette, Docteure Valérie Lechevalier, Docteur Olivier Furling, Docteur Guillaume Delaplace, Professeur Vincent Thomy et M. Guillaume Damblans d'avoir accepté de prendre de leur temps pour évaluer mon travail et faire partie des membres du jury.

Merci l'Agence Nationale de la Recherche pour le financement du projet ECONOMICS (ANR-17-CE08-0032).

Merci également à tous les membres du projet pour les échanges enrichissants lors des réunions plénières. Un merci particulier à Caroline Françolle de Almeida et Alain Celzard de l'Institut Jean Lamour et Romain Jeantet d'Agrocampus Ouest.

Je souhaite aussi remercier Thierry Sindzingre de la société AcXys Technologies pour m'avoir permis de venir faire des manipes en attendant de recevoir la nouvelle enceinte plasma. Merci également à Stéphane Guérin et Eva Jouvet.

Cette aventure n'aurait pas été possible sans l'aide de nombreuses personnes, au sein de toutes les équipes qui y ont pris part.

Au sein de l'UMET, je tiens à remercier :
Séverine Bellayer, pour son expertise en microscopie, les analyses EPMA et ses conseils dans la préparation des échantillons.

Alexandre Fadel, pour m'avoir formée au MEB (et pour m'avoir supportée pendant cette formation où je comparais chaque surface à des gâteaux et cookies…). Je vous remercie, Ahmed Addad et toi, pour vos conseils sur les observations (et promis, je ne ferai plus de manipes avant la soutenance !)

Mathilde Casetta, pour son temps dans la construction du plan d'expérience et son aide dans l'analyse des données.

Philippe Supiot, d'avoir accepté d'installer le plasma au P3 le temps que la salle à l'INRAe soit prête. Je vous remercie Corinne Foissac et toi pour votre temps et votre aide pour les manipes OES. Je tiens également à remercier chaleureusement Christian Malas pour sa disponibilité et son aide technique, et pour avoir pimpé le plasma pour la double injection !

Justine Batisse, ma première stagiaire, pour m'avoir aidée lors des premières manipes plasma avec la double injection. Merci pour ton implication durant ces 5 mois, mais aussi pour tes conseils avisés en bande-dessinées !

David Balloy, qui m'a initiée à la trempe. Merci pour ton temps et ton aide pour les manipes. Je souhaite remercier aussi Charafeddine Jama et Fouad Bentiss pour les tests de corrosions. Merci à Joel Lyskawa de m'avoir formée au profilomètre.

Enfin merci beaucoup à tous les autres membres permanents du C7 pour leur aide, leur bonne humeur et leur gentillesse : Pierre, Johan, Guillaume, Ben, Lotfi, Sophie, Fabienne, Tsilla, Serge, Gaëlle et Fanny.

Au sein de l'IEMN, je souhaite remercier :
Flavie Braud, sans qui les surfaces SLIS n'auraient pas pu voir le jour. Mille mercis pour ta disponibilité, pour ces nombreuses discussions sur le laser (et toutes les autres !) et pour tous les échantillons que tu as structurés (pas loin d'une centaine je pense !).

Santino Jesulín Zapiain Merino pour son aide dans le développement des surfaces à chevrons. Merci tous nos échanges scientifiques ou non (je n'oublierai pas nos discussions pour savoir quel est le meilleur personnage de Friends !).

Je remercie aussi tous les membres qui veillent à la bonne organisation de la salle blanche, le réseau Renatech et l'ANR pour le financement de la plateforme LEAF (ANR-11-EQPX-0025).

Au sein de l'INRAe, je remercie enfin :
Laurent Wauquier, pour son aide précieuse, allant de la découpe d'échantillon, à l'installation de la plateforme plasma à l'INRAe (j'aurais pu écrire un chapitre « déménagement » !). Merci pour tes conseils, ta disponibilité et ta bienveillance lors des tests d'encrassements !

Luisa Azevedo-Scudeller et Simon Gabut pour les nombreux essais d'encrassement (presque 100 à nous trois !), leur bonne humeur et les discussions autour du test qui nous a donné du fil à retordre. Merci à Thierry Six pour les discussions et son aide sur le pilote. Merci à Thomas Danel d'avoir partagé le test certains jours pour tester son capteur.

Anne-Laure Fameau, pour les discussions scientifiques et les conseils pour « l'après-thèse ». Merci pour tes encouragements !

Amandine, merci pour ton aide la mise au point de protocoles ; Christelle et Thomas, merci de m'avoir attendue lorsque je devais terminer tard certains soirs.

Plus globalement, je souhaite remercier tous les autres permanents de l'INRAe pour leur bonne humeur et leur gentillesse, que j'ai pu apprécier au quotidien – je n'oublierai pas les barbecues de l'INRAe !

Un grand merci à Nicolas Nuns et Pardis Simon, de l'UCCS, pour les analyses ToF-SIMS et XPS. Merci pour votre aide précieuse et les discussions pour l'analyse des données.

Merci à Melissa Grunlan et Bryan Khai Ngo de l'université Texas A&M d'avoir accepté de collaborer sur les revêtements amphiphiles auto-stratifiants.

Je tiens également à remercier Corinne, Isabelle, Angélique et Christophe pour leur aide administrative que ce soit pour les commandes ou pour les départs en mission.

Je remercie, enfin, Nadège Schifano et Françoise Delecroix pour m'avoir permis d'encadrer des TPs à l'IUT et m'avoir fait confiance.

Parce que la thèse est loin d'être un long fleuve tranquille et qu'on fut bien nombreux dans le même bateau, il est temps de remercier les doctorants et post-doctorants des différents labos.

A l'UMET, je tiens à remercier :

Les anciens (ceux de l'avant-Covid) : Tatenda pour ta bonne humeur et ton rire communicatif, Ady pour ta gentillesse et tes nombreux secours informatiques, Sophie pour tes lancements départ pour le CROUS qui m'auront manqué après ton départ, Charlotte, que je ne devrais pas trop remercier vu toutes les paires de baskets que tu m'as fait acheter !! Et enfin Roro et Elodie pour vos débats dans le bureau 10.

Ceux qui ont commencé avec moi mais qui ont déjà soutenu (lâcheurs) : Fei pour ta bonne humeur, Alexandre et Angeline pour nos discussions pâtisseries, galères de manipes et de rédaction. Ange merci pour ton soutien et tous les dîners chez toi !

Les actuels : Louis, Melvin, Kévin, Marie-Odile, Jihane, Eric, Matthieu. Merci pour votre bonne humeur quotidienne et les discussions en salle de pause après le déjeuner. Kévin je te lègue le plasma, fais-en bon usage !

Et enfin celles et ceux ont fait un passage par l'UMET : Aurélien, Marie, Solène et Mariette.

A l'IEMN, je souhaite remercier :

Paul, pour les discussions et pour m'avoir laissée squatter ton bureau. N'oublie pas de rédiger ton chapitre biblio !

Anne-Sophie, « partner in crime des SLIS », merci pour ta bonne humeur et nos discussions, pour les journées en salle blanche (imprégnation, pesées et spin-coating). Merci à Thomas et toi pour les soirées jeux et les sorties.

A l'INRAe je remercie :

Audrey, Heni, Angella, Jina, Weiji et Carolina pour votre bonne humeur, vos encouragements et nos discussions. Audrey merci pour les échanges d'infos par rapport à l'ED et pour m'avoir rappelé qu'il fallait aller rédiger !

Parce que certaines personnes deviennent des amies, un remerciement spécial à Laura et Anne-Lise pour leur soutien sans faille, leurs conseils, les rendez-vous du mardi et du jeudi pour le sport, les pauses goûters, les dîners remonte-moral et les discussions boucles d'oreilles (Anne-Lise, Laura nous aura bien corrompues !).

Enfin, mille mercis à celles et ceux qui sont là depuis plus longtemps, et qui m'ont toujours soutenue, du début à la fin de cette thèse :

A Maxime, Alicia, Nicolas, Nelson. Merci pour votre soutien, dans les bons moments comme dans ceux plus difficiles, depuis notre rencontre sur les bancs de la fac.

A Chachou, Banou, Julie, Céline, Léa et Morgane, merci pour vos encouragements et vos petits messages pendant la rédaction. Merci pour les soirées, les repas, les goûters qui m'ont permis de penser à autre chose. Hâte de pouvoir voyager ensemble, bientôt je l'espère ! En un mot, merci d'être là, tout simplement, et ce depuis maintenant toutes ces années.

Aux Royoux, pour votre soutien et vos mots d'encouragements.

A Hélène, pour tes conseils et ton soutien dans la préparation des CV et LM.

A P-A, qui m'a écoutée, remontée le moral tout au long de la thèse et aidée en relisant quelques parties de ce manuscrit. Un énorme merci pour me pousser à dépasser mes limites et pour ton soutien quotidien ! Et vivement le prochain road trip !

A mes grands-parents, mes oncles et tantes, avec qui j'ai pu savourer ces moments de partage et de retrouvailles familiales à Saint-Brévin, entre repas, balades à pied ou à vélo. Hâte de fêter la fin de cette étape, dans quelques mois, autour d'une bonne part de kouign amann ! (N'est-ce pas Brigitte ?)

A ma sœur, pour son soutien, et pour tout ce que nos différences m'apportent. Merci de m'avoir poussée à mieux vulgariser, pour mieux partager mes travaux, mais aussi pour tes conseils littéraires, toujours justes – tu restes à l'origine de la découverte de mon livre préféré, et je suis convaincue que tu feras une formidable libraire ! Merci d'être là, tout simplement.

A mes parents, qui m'ont toujours soutenue,

A ma mère, merci d'être un pilier depuis toujours, et un modèle de résilience.

A mon père, parti trop tôt, merci de m'avoir poussée à donner le meilleur de moi-même.

Table of content

Acknowledgments ..... **I**

List of abbreviations ..... **XIII**

GENERAL INTRODUCTION **1**

CHAPTER 1 – SURFACE MODIFICATIONS MITIGATING DAIRY FOULING **5**

I. Introduction **6**

II. Surface properties **12**

2.1. Mechanical interactions: Roughness and Topography 12

2.2. Molecular interactions: Surface free energy 13

2.2.1. SFE measurement 13

2.2.2. Wettability 14

2.2.3. Contact angle hysteresis (CAH) 16

III. Surface modifications to mitigate dairy fouling deposit **17**

3.1. Impact of surface properties on dairy fouling 18

3.1.1. Batch pasteurization 18

3.1.2. Continuous flow pasteurization 21

3.1.3. Impact of surface free energy (SFE) 25

3.1.4. Impact of roughness (Ra) 27

3.2. Design of surfaces mitigating dairy fouling 29

3.2.1. Top-down techniques 29

3.2.2. Bottom-up techniques 30

3.2.3. Combination of top-down and bottom-up approaches 34

IV. Anti-fouling and fouling-release surfaces **35**

4.1. Anti-fouling or fouling-release surfaces? 35

4.2. Anti-fouling surfaces 36

4.3. Fouling-release surfaces 38

4.4. Anti-fouling and fouling-release surfaces 43

4.4.1. Amphiphilic surfaces 43

4.4.2. Slippery liquid-infused porous surfaces 46

V. Discussion **48**

5.1. Model fluid and process parameters 49

5.2. Surface characterizations 51

5.3. Cleaning conditions 53
VI. Conclusion 54
CHAPTER 2 – PASTEURIZATION PROCESS: METHODOLOGY TO ASSESS ANTI-FOULING OR FOULING-RELEASE PROPERTIES 57
I. Introduction 58
II. Model fluid 58
III. Pasteurization process 59
IV. Repeatability issues and validation of the pasteurization test 62
4.1. Variability of surface density fouling deposit within several Whey Protein Concentrate powder batches: Influence of WPC powder composition 62
4.1.1. Calcium and β-Lactoglobulin contents 63
4.1.2. Phosphate content 64
4.1.3. Casein content 65
4.2. Variability of surface density fouling deposit within one Whey Protein Concentrate powder batch: Influence of $CaCl_2$ hygroscopic state during aging and of pressure drop in PHE 66
4.3. Variability of surface density fouling deposit within one Whey Protein Concentrate powder bag: Influence of surface properties and ways to mitigate errors 68
4.4. Mechanical stress 69
V. Conclusion 71
CHAPTER 3 – NANOSTRUCTURED COATINGS BY ATMOSPHERIC PRESSURE PLASMA 73
I. Introduction 74
II. Deposition of hydrophobic and superhydrophobic thin films by atmospheric pressure plasma 74
2.1. Plasma state 74
2.2. Atmospheric pressure plasma sources 76
2.3. Hydrophobic and superhydrophobic thin coatings created by atmospheric pressure plasma 77
2.3.1. Hydrophobic plasma-polymerized coatings 77
2.3.2. Superhydrophobic plasma-polymerized coatings 79
2.3.3. Hydrophobic and superhydrophobic plasma coatings limiting fouling adhesion 79
III. Atmospheric pressure plasma process 80

3.1. Lab-Scan and set-up for plasma polymer deposition 80
3.2. Manufacturing plasma parameters 81
3.3. Influence of the extraction speed of the fume hood 85
3.3.1. Wettability 85
3.3.2. Morphology 86
3.3.3. Adhesion 87
IV. Optimization of plasma manufacturing parameters for HMDSO 87
4.1. Preparation and pre-treatment of samples 88
4.2. HMDSO deposition using an experimental design 88
4.3. Influence of plasma parameters on surface properties 90
4.3.1. Wettability (WCA) 91
4.3.2. Surface Free Energy (SFE) 91
4.3.3. Roughness (R_a) 92
4.3.4. Correlation between plasma parameters and surface properties 92
4.4. Fouling performances and durability assessment 96
4.4.1. Fouling performances 96
4.4.2. Plasma coatings durability 97
4.4.3. Correlation between plasma parameters and fouling-release performances 99
4.4.4. Surface characterizations 102
V. Bilayers deposition by atmospheric pressure plasma 107
5.1. Plasma coating deposition from the injection of two precursors 107
5.2. Development of superhydrophobic plasma bilayer deposition 108
5.2.1. Atmospheric pressure plasma process 108
5.2.2. Surface characterizations 110
5.2.3. Fouling-release performances 117
5.3. Influence of HMDSO flow rate for bilayer deposition 119
5.3.1. Plasma parameters 119
5.3.2. Surfaces characterizations 119
5.3.3. Fouling-release performances 122
5.4. Influence of power for bilayer deposition 123
5.4.1. Plasma parameters 123
5.4.2. Surfaces characterizations 124
5.4.3. Fouling-release performances 128
VI. Conclusion 130

CHAPTER 4 – SLIPPERY LIQUID-INFUSED SURFACES 133
I. Introduction 134
II. Biomimetic Surfaces 134
2.1. Biomimetic approach 134
2.2. Superhydrophobic and omniphobic surfaces 135
2.3. Slippery Liquid-Infused Porous Surfaces (SLIPS) 136
2.3.1. Nepenthes pitcher plant 136
2.3.2. Design of SLIPS 137
2.3.3. Mitigation of dairy fouling deposit and limitations 141
III. Femtosecond laser process 142
3.1. Femtosecond laser system 143
3.1.1. Laser source 143
3.1.2. Micromachining platform 143
3.1.3. Femtosecond laser vs nanosecond laser 145
3.2. Laser beam characteristics and process parameters 145
3.2.1. Laser beam characteristics 146
3.2.2. Laser process parameters 146
IV. Optimization of laser manufacturing parameters 149
4.1. Influence of laser parameters on surface structuration 149
4.1.1. Influence of laser fluence on surface structuration 149
4.1.2. Influence of velocity and hatch distance on structuration 150
4.2. Impact of beam velocity and hatch distance on depth profile 151
4.2.1. Structuration morphology 152
4.2.2. Depth profile 152
4.3. Comparison of ablation laser process 153
4.3.1. Laser process parameters 153
4.3.2. Laser pattern 154
4.3.3. Characterizations of laser structured surfaces 154
V. Slippery Liquid-Infused Surfaces 156
5.1. Validation of the optimization of laser parameters 156
5.1.1. Chemical modification 156
5.1.2. Assessment of the impregnation method and volume of impregnated oil 157
5.1.3. Fouling performances and assessment of oil retention rate 159
5.2. Development of new SLIS 161

5.2.1. Laser structuration of stainless steel surfaces 161
5.2.2. Fluorine-based SLIS design 161
5.2.3. Coconut-based SLIS design 164
5.2.4. Characterizations 167
5.2.5. Fouling-release performances 169
VI. Conclusion 172
GENERAL CONCLUSION 175
OUTLOOKS 178
Patterned surfaces 178
Self-stratifying amphiphilic coating 181
MATERIALS AND METHODS 185
I. Samples preparation 185
1.1. Substrates 185
1.2. Laser cutting 186
1.3. Surface cleaning 186
II. Surface characterizations 186
2.1. Wettability (static and dynamic) and surface free energy 186
2.1.1. Wettability 186
2.1.2. Contact angle hysteresis 187
2.1.3. Static and dynamic contact angles with model fluid 187
2.1.4. Surface free energy 187
2.2. Profilometer 188
2.3. Digital microscopy 189
2.4. Scanning Electron Microscopy (SEM) 189
2.4.1. Surface morphology 189
2.4.2. X-Ray mappings 189
2.5. Fourier Transform Infrared spectroscopy (FTIR) 189
2.6. Electron Probe Micro-Analysis (EPMA) 189
2.7. Time-of-Flight Secondary Ion Mass Spectrometry (ToF-SIMS) 190
2.8. Cross-Hatch Adhesion Tests 191
References 193
ANNEXES 207
Annex 1 208
Annex 2 210

Annex 3 ..... **215**
Annex 4 ..... **215**
Annex 5 ..... **216**
Annex 6 ..... **217**

List of abbreviations

APP	Atmospheric Pressure Plasma
APTES	(3-Aminopropyl)triethoxysilane
CA	Contact angle
CAH	Contact angle hysteresis
CIP	Cleaning in place
CMR	Carcinogenic Mutagenic Reprotoxic
CNT	Carbon nanotubes
CVD	Chemical vapour deposition
DLC	Diamond like carbon
DOCA	Dodecyl acrylate
EPMA	Electron-probe micro-analysis
FAS-3	(3,3,3-Trifluoropropyl)trimethoxysilane
FAS-5	(Pentafluorophenyl) triethoxysilane
FAS-17	Heptadecafluoro-1,1,2,2-tetrahydrodecyl triethoxysilane
FDA	Food and Drug Administration
FEP	Fluorinated ethylene propylene
FLUSI	Heptadecafluoro-1,1,2,2-tetrahydrodecyl trimethoxysilane
FP	Fluoropolymer
HMDSN	Hexamethyldisilazane
HMDSO	Hexamethyldisiloxane
HSTS	High short high time pasteurization
LCA	Life cycle assessment
LTLT	Low Temperature for a Long Time pasteurization
MF	Model Fluid
ML	Mirror-like stainless steel
MTES	Methyltriethoxysilane
NAT	Native stainless steel
OMCTS	Octamethylcyclotetrasiloxane

OTS	octadecyltrichlorosilane
PACVD	Plasma assisted chemical vapour deposition
PCT	Plasma cycle time
PDMS	Poly(dimethylsiloxane)
PECVD	Plasma enhanced chemical vapour deposition
PEEK	Polyether ether ketone
PEG / PEO	Poly(ethylene glycol) / Poly(ethylene oxide)
PE HD	Polyethylene high density
PEI	Poly(ethylenimine)
PFA	Perfluoroalkoxy alkane
PFDA	1H,1H,2H,2H-perfluorododecyl acrylate
PFH	1-Perfluorohexen
pFOTES	*1H, 1H, 2H, 2H*-Perfluorooctyltriethoxysilane
PFTS	trichloro(*1H,1H,2H,2H*-perfluorodecyl)silane
PHE	Plate heat exchanger
PMMA	Poly(methyl methacrylate)
PP	Polypropylene
PPS	Polyphenylene sulfide
PS	Polystyrene
PTFE	Poly tetra fluoro ethylene
PVD	Physical vapour deposition
REACH	Registration, Evaluation, Authorisation and Restriction of Chemicals
SAMs	Self-assembled monolayers
SEM	Scanning electron microscopy
SFE	Surface free energy
SICAN / SICON	Si-doped DLC / O-doped DLC
SilML / SilNAT / SilTEX	Fluorosilanized mirror-like / native / textured stainless steel
SLIPS / SLIS	Slippery liquid infused porous surface / Slippery liquid infused surface
SMUF	Simulated milk ultra-filtrate
SS	Stainless steel

TEX	Textured stainless steel
TFE	Tetrafluorethylene
Tomcats	Tetramethylcyclotetrasiloxane
TMDSO	Tetramethydisiloxane
TMS	Tetramethylsilane
ToF-SIMS	Time-of-flight secondary ion mass spectroscopy
UHT	Ultra high temperature
WCA	Water contact angle
WPC / WPI	Whey protein concentrate / Whey protein isolate
XPS	X-ray photoelectron spectroscopy
β-Lg	β-Lactoglobulin
R_a	Arithmetic mean roughness (µm, nm)
R_q	Root mean squared roughness (µm, nm)
R_v	Maximum profile valley depth
R_f	Fouling resistance ($K.m^{-2}.W^{-1}$)
γ	Surface energy (mN/m)
θ	Contact angle (°)

GENERAL INTRODUCTION

Fouling is a complex phenomenon which concerns numerous applications, ranging from industrial (food and beverage, petrochemical processes or power generation) and marine equipment to biosensors and biomedical implants and devices.[1], [2]

Fouling is usually described as the accumulation and attachment of unwanted materials at the surface of industrial equipment or devices. In dairy industries, these phenomena occur mainly in plate heat exchangers (PHE). Implanted in most of production lines since the 1930s, these types of equipment are used for the processes of milk pasteurization or sterilization[3], two thermal treatments which are mandatory to prevent food contamination by microorganisms and to increase the food shelf life.[4] During those two thermal processes, heat induces denaturation and/or aggregation of whey proteins and precipitation of calcium phosphates leading to the fouling deposit formation.

This deposit generates many issues. Firstly, it impairs heat transfer mechanisms by creating a thermal resistance, which increases energy consumption and consequently the cost of process. Secondly, it is facilitating the proliferation of bacteria and biofilm which can cause health issues, and their suppression requires regular cleaning of PHEs. Besides of leading to costly waste production and waste management issues, the PHEs cleaning sessions can exceed 5 h per day, inducing a production loss.[5] Consequently, the stakes of fouling mitigation are mainly economical ones, since it has been estimated that 80% of production costs are owed to dairy fouling deposit.[6]

These economic considerations are non-negligible considering that, according to the Food and Agriculture Organization (FAO), world milk production increases constantly. It increased by more than 59 % between 1988 and 2018, varying from 530 million tons to 843 million tons.[4] Milk is an essential raw material as it can be transformed into cheese, butter, cream, yoghourt. More recently, it became very attractive as it was demonstrated that every component could be valorized due to nutritive (baby food to sport supplements) or functional (gelation, foaming, emulsification) properties.[7]

For all these reasons, dairy fouling has been widely studied since the 1960s, notably to understand its growth mechanisms. Despite all these researches, and although recent works have characterized fouling deposit at early and longer stages using macroscopic and microscopic methods, deposit formation still remains under debates. However, these investigations pointed out three factors influencing fouling deposit growth: (i) product characteristics, (ii) process parameters and (iii) surface properties of PHEs. If milk producers cannot control properly the raw milk characteristics[8], several works proposed pathways to mitigate dairy fouling adhesion either by optimizing process parameters or by modifying stainless steel surface.[9]

The optimization of process parameters remains complex to perform at laboratory scale. Therefore, numerous research teams focus on the influence of surface properties by modifying stainless steel surfaces since the 1990s due to the development of new surface modification techniques. Recently, several works revealed very promising results using anti-fouling (*i.e.* prevent fouling adhesion) or fouling-release (*i.e.* ease fouling removal) coatings or materials.[10]–[12]

In this context, the ECONOMICS (ECO-efficient and safe aNtifOuling surfaces for MIlk and egg proCessing industrieS) ANR project aims at either (i) developing coatings onto stainless steel surface or (ii) replacing stainless steel by carbon-based materials. The present thesis work focuses on the development of durable and food-compatible coatings onto stainless steel surfaces (Figure 1) using two main innovative techniques and concepts: nanostructured coatings by atmospheric pressure plasma and bioinspired slippery surfaces by laser ablation and oil infusion. Their surface properties (wettability, surface free energy and roughness) will be assessed to justify their potential anti-fouling and/or fouling-release properties.

To better understand how surfaces modification can induce a fouling mitigation, a state of the art of surface modification techniques for fouling mitigation is presented in the first chapter. The assessment and influence of surface properties on anti-fouling and fouling-release performances is discussed. As no fouling and cleaning procedures are standardized, the comparison of the impact of surface modification on fouling behaviour remains complex.

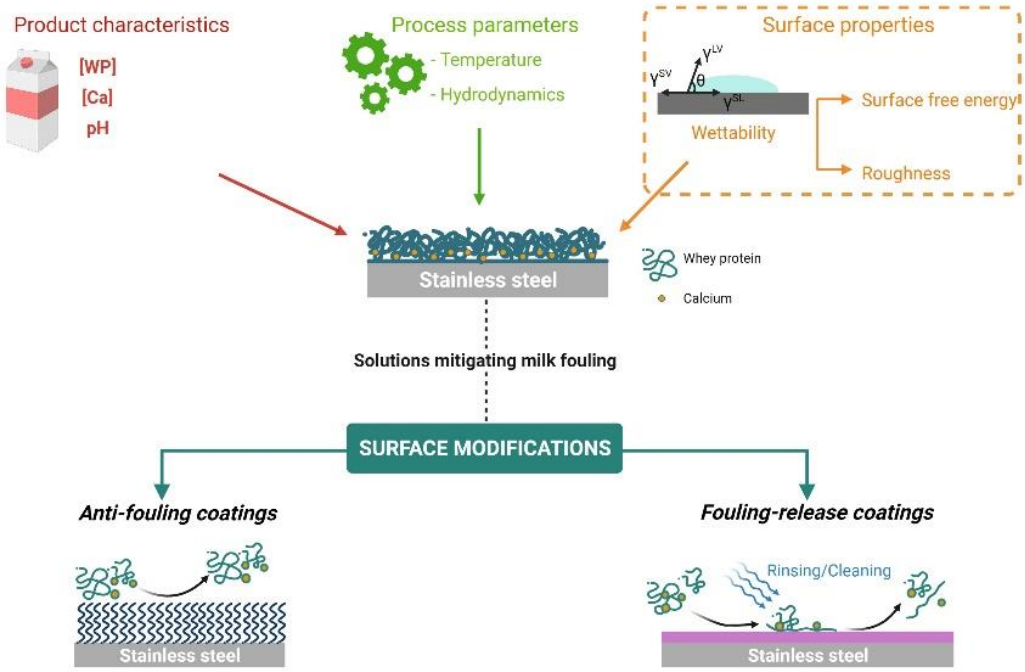

Figure 1. Diagram of the aim of the project: acting on surface properties through surface modification of stainless steel to mitigate dairy fouling.

The methodology used to assess anti-fouling and fouling-release properties of elaborated coatings is based on several former works. The herein used pilot pasteurization system is described in the second chapter along with the steps of a pasteurization run, ranging from fouling solution preparation to the cleaning procedure of the pilot. Besides, as repeatability issues were observed during this study, solutions based on literature have been proposed to improve the fouling protocol.

The third chapter is dedicated to the elaboration of nanostructured coatings. These ones were deposited onto stainless steel surfaces using an atmospheric pressure plasma torch. Two types of coatings were studied. For the first one, based on pure HMDSO (hexamethyldisiloxane) precursor, an experimental design was elaborated to investigate the influence of manufacturing plasma parameters on surface properties. Fouling-release performances of resulting plasma coatings were then correlated to their surface properties. The second type of coating was based on the alternative injection of two precursors: HMDSO and pFOTES (*1H,1H,2H,2H* perfluorooctyltriethoxysilane) to generate a bilayer-like plasma coating, which was never achieved at atmospheric pressure. For this second coating, a parametrical study has been undertaken to evaluate the influence of precursor flow rate and plasma power on bilayer and their fouling-release performances, giving insights on pathways to improve the coating fouling mitigating efficiency.

In the fourth chapter, the elaboration of bioinspired slippery liquid-infused surfaces (SLIS) is reported. This type of surface is elaborated following three steps: (i) surface structuration by femtosecond laser ablation, (ii) chemical modification of the structured surface and (iii) oil impregnation. Based on a former work[13], an optimization of laser parameters is presented. Then, to improve life time and oil retention, the two other steps are investigated as well. Chemical modification usually carried out in glovebox is replaced by the deposition of plasma coating or by the spraying of carnauba wax. Finally, oil impregnation method is also optimized to maximize the volume of infused oil. Promising fouling-release performances were obtained using greener SLIS which were developed by replacing fluorine-based oil by coconut oil.

After summarizing the results of this work, the different coatings designed are discussed in the general conclusion regarding their ability to reduce fouling deposit and their potential industrialization. Other trails for coatings elaboration will be proposed in outlooks, with, for some of them, some preliminary studies and results.

CHAPTER 1 – SURFACE MODIFICATIONS MITIGATING DAIRY FOULING

In this section, an overview of the state of the art concerning surface modification techniques for fouling mitigation is given. It is adapted from the review entitled "A critical review on surface modifications mitigating dairy fouling", published in *Comprehensive Reviews in Food Science and Food Safety* in 2021 (DOI: 10.1111/1541-4337.12794).

I. Introduction

Food processing industries have to respect strict hygiene and safety standards to ensure the shelf life and quality of products while avoiding contamination by microorganisms. Hence, thermal treatments such as pasteurization, sterilization or UHT (Ultra High Temperature) treatment are mandatory for dairy and its by-products. Fluids are treated at temperatures ranging from 62 °C to 150 °C for 30 min to few seconds. [14]–[16] However, thermal processes trigger protein denaturation and salt precipitation, leading to a fouling deposit on heat exchangers' surfaces, that poses many problems for food processing industries. Firstly, if heat exchangers' surfaces are not cleaned regularly, bacteria can accumulate on the surface creating biofilms on it [17]–[19] Secondly, fouling deposits impair heat transfer mechanisms by creating a thermal resistance leading to regular shut down to clean the processes.

304 and 316L stainless steels are mostly used in food processing industries due to their properties, such as high physical durability, chemical neutrality and cleanliness. In food industries, stainless steel surfaces should present $R_a < 0.8$ µm.[20] and several types of finish exist. This can lead to surfaces with various physical and chemical properties.[21], [22] Regardless of the durability and cleanliness of these types of stainless steel, food processing plants have to be cleaned every day to prevent contamination risks. [23] Therefore, harsh cleaning-in-place (CIP) procedures are implemented. CIP involves the use of chemicals and high amount of water, which increases the environmental burden. It is estimated that 80% of production costs are owed to dairy fouling deposit.[6]

In food industries, the fouling step can be defined as the increase of thickness of the fouled layer onto stainless steel surface heat exchanger. Thus, cleaning step corresponds to the decrease of the thickness of this fouled layer. The increase of thickness of fouled layer corresponds to fouling and thus the decrease of this layer corresponds to cleaning. These both steps (fouling and cleaning) are determined by measuring the thermal fouling resistance (R_f) and the pressure drop (Δp). The thermal fouling resistance is related to the overall clean heat transfer coefficient (U_0) and to that after fouling (U_f) through the following equation:

$$R_f = \frac{1}{U_f} - \frac{1}{U_0} \quad (1)$$

The pressure drop can be related to the mass of fouling deposit onto tubular or plate heat exchanger surface. When fouling grows, the cross-sectional area decreases, limiting the product flow and leading to an increase of the pressure drop.[16], [24], [25]

Dairy fouling

Dairy fouling is a complex phenomenon and numerous parameters have to be considered. First of all, the milk's composition itself, which is a biological fluid containing proteins (whey proteins and caseins), lipids, soluble sugars and mineral species. Moreover, the milk's composition can vary as a function of the season and of its source.[8] It is also important to note that, depending on filtration processing, the whey proteins, casein and mineral contents are thus modified, leading to different fouling mechanisms.[26], [27]

Secondly, it has been observed that the composition of milk fouling deposit differs significantly from that of raw milk. Milk fouling deposit is mainly composed of whey proteins and minerals. Caseins, lactose and fat seem to be negligible in milk fouling deposit although they represent 80 % of soluble compounds in milk.[3], [28]–[30]

Furthermore, depending on the temperature to which dairy products are exposed (Table 1), fouling deposits have been classified into two categories. The first one, called Type A, gathers proteinaceous deposits formed at temperatures ranging from 75°C to 100°C. This deposit is white, slightly dense, spongy and mostly composed of proteins (50-60%), more precisely of β-lactoglobulin (β-Lg) [31], [32], minerals such as calcium phosphate (30-35%) and lipids (5%). On the contrary, the second one, called Type B, gathers mineral fouling that builds up at higher temperatures, at 105°C. This type of deposit is grey, denser and rougher and mainly composed of mineral species, calcium phosphate (70%) proteins (20%) and lipids (5%).[33], [34]

Table 1. Table of legal pasteurization standards adapted from [14]–[16]

Process type	Time	Temperature (°C)	Type of fouling (Burton's classification)
Batch pasteurization (LTLT: Low Temperature for a Long Time)	30 min	63	A
High-Temperature Short-Time (HTST) pasteurization	15-20 s	72-75	A
Ultra-pasteurization	2-4 s	125-138	A up to 100 °C B from 110 °C
Ultra-High Temperature (UHT) treatment	Few seconds	134-150	B

At pilot scale (about 300 L/h), the use of fresh raw milk is expensive and its storage can be complicated. Moreover, being a natural fluid, its chemical composition may vary, leading to differences in fouling experiments. For this reason, reconstituted milk solutions from whey protein concentrate (WPC) or whey protein isolate (WPI) have been used to achieve reproducible fouling behaviour. [31], [35] Whey protein concentrate and whey protein isolate are obtained from milk filtration. This process is widely used to separate caseins from whey proteins as both of these proteins have specific properties which can be used for diverse food applications.[36], [37] It has been demonstrated that fouling deposit from WPC solution mimics well fouling deposit type A from milk at pasteurization temperatures (42 – 120 °C). However, at UHT temperatures (120 – 134 °C) fouling deposit from WPC is mainly composed of whey proteins while fouling deposit from milk is mainly composed of mineral salts.[38] Therefore, in most investigations, WPC or WPI solutions with simulated milk ultrafiltrate (SMUF) or calcium and phosphate are used as model fluid mimicking milk.

According to the literature, the proteinaceous fouling deposit (Type A) leads to greater issues for food processing plants than type B fouling deposit. Being less dense, type A fouling deposit increases the pressure drop and thermal resistance and is less easy to remove than type B fouling deposit.[6], [28], [33], [39]. Type A fouling deposit has been therefore more studied. Thus, this chapter will focus on this fouling deposit formed in pasteurization temperature range (< 100 °C) and will not deal with type B fouling deposit.

Dairy fouling mechanisms

Based on the previous section, two major components of milk are responsible of the growth of fouling deposit onto heat exchangers' surfaces. Whey proteins and notably β-lactoglobulin proteins and calcium phosphates are thermosensitive, therefore heat induces denaturation and/or aggregation of whey proteins and precipitation of calcium phosphates in bulk solution and onto heat exchanger's surfaces.

It has been demonstrated that whey proteins are the most thermosensitive proteins in milk. Moreover, Polat [40] showed that β-lactoglobulin proteins denature faster than α-lactalbumin protein in pasteurization temperature range. Therefore, β-lactoglobulin proteins are the main component of type A fouling deposit. When the temperature increases and reaches 65°C, β-lactoglobulin becomes thermally unstable, leading to its denaturation and thus exposing reactive thiol groups. These reactive groups tend to achieve intramolecular polymerisation either with other β-lactoglobulin or other proteins (α-lactalbumin) via disulphide bonds.[41],

[42] Nevertheless, reactive thiol groups are not the only impacting factor, and several investigations reported the role of calcium ions on the interactions between proteins and whey protein denaturation/aggregation.[43]–[45]

In parallel, calcium phosphates are less soluble with the increase of temperature. This decrease of solubility leads to nucleation and crystal growth in the bulk and onto heat exchangers' surfaces. Delsing and Hiddink [46] demonstrated that calcium ions play also a great role in the fouling growth. This has been confirmed by Jimenez *et al.* [47] who pointed out fouling growth mechanisms in the presence or absence of calcium. In the absence of calcium, the substrate and the steel grain boundaries are covered with a very thin layer of whey proteins as displayed in Figure 2 a. In the presence of calcium, high size particles are observed on the protein layer, leading to an arborescent structure (Figure 2 b).

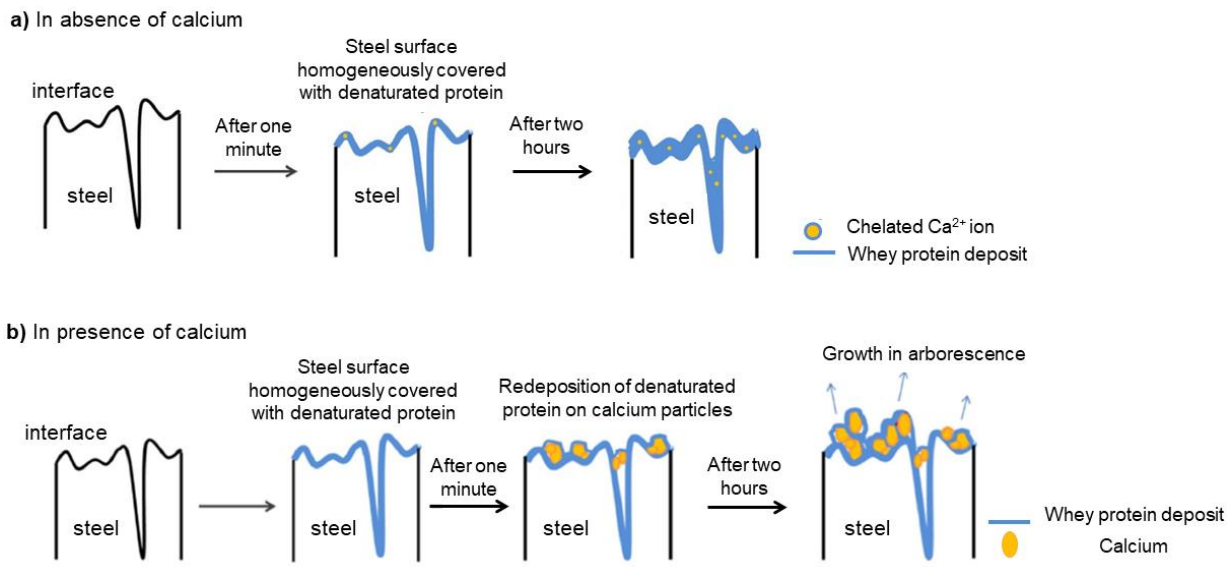

Figure 2. Fouling growth mechanisms: a) in the absence of calcium and b) in the presence of calcium [47] *Reprinted with permission from Elsevier B. V.*

According to the literature, several investigations, reported in different reviews [48]–[50], have studied the mechanisms of milk fouling. Today, it is well accepted that an initial phase, also called induction period takes place, where a thin layer forms onto heat exchangers' surfaces before the fouling deposit is noticeable. During this initial phase, no changes in pressure drop and heat transfer coefficient are observed.[51], [52] The duration of this induction period varies generally from 1 to 60 min in tubular heat exchangers and is often instantaneous in plate heat exchangers. [43], [53]

The composition of the thin first layer has been debated for a long time. Some authors observed a thin layer mainly constituted of calcium phosphate after 1 to 15 min of fouling test at pasteurization temperature.[32], [52], [54] Nevertheless at shorter time (4 s), Belmar-Beiny *et al.* [55] showed thanks to X-ray elemental mapping, X-ray photoelectron spectroscopy (XPS) and Scanning electron microscopy (SEM) that the first layer was mainly composed of whey proteins, allowing the fouling to grow. This has been corroborated by Jimenez *et al.* who performed fouling runs for 1 min. They observed by ToF-SIMS (Time of Flight-Secondary Ion Mass Spectrometry) that the substrate and the steel grain boundaries were covered with a homogeneous layer of whey proteins and the ions Ca^{2+} were concentrated in the upper side of the fouling deposit.[47]

In the meantime, Belmar-Beiny *et al.* [55] carried out investigations for longer time (60 min) and highlighted a higher concentration of calcium phosphate near the heated surface (in the boundary layer). This corroborates the observations made by Jimenez *et al.* [47] after 120 min and by Tissier *et al.* [32]after 240 min.

Fouling deposition relies on simultaneous and/or successive phenomena which have been gathered in different stages described and reviewed by [48], [55]–[57]

- **Bulk activation:** denaturation and/or aggregation of whey proteins in bulk solution
- **Transport/mass transfer:** transport of denatured and/or aggregated whey proteins and calcium and phosphate ions to the heat surface
- **Surface reactions:** Adsorption of denatured/aggregated whey proteins, calcium and phosphate ions initiating the fouling and leading to the fouling growth *via* the incorporation and entrapment of denatured/aggregated whey proteins, calcium and phosphate ions and particulates
- **Ageing of the fouling deposit:** deposit removal and transfer of denatured/aggregated whey proteins and calcium and phosphate particulates back to the bulk solution (re-entrainment)

Factors impacting dairy fouling

According to the literature, numerous factors affect the formation of dairy fouling. These factors are gathered in three main groups: (i) product characteristics, (ii) process parameters and (iii) surface properties displayed in Figure 3. [11] For each group, Boxler [10] reported the trends of the effect of different factors impacting milk fouling.

Förster, Augustin and Bohnet [9] demonstrated that fouling mitigation could be managed by two pathways. The first one consists in modifying the geometry and surface properties of heat exchanger surface to reduce the deposit adhesion. The other one consists in increasing flow rate in order to increase wall shear stress inducing fouling deposit removal. This latter approach to mitigate fouling deposit has been corroborated by Mahdi *et al.*[58]. However, fouling occurs at the interface between the surface and the liquid phase. Thus, the surface properties play also an important role on fouling behaviour.[57], [58]

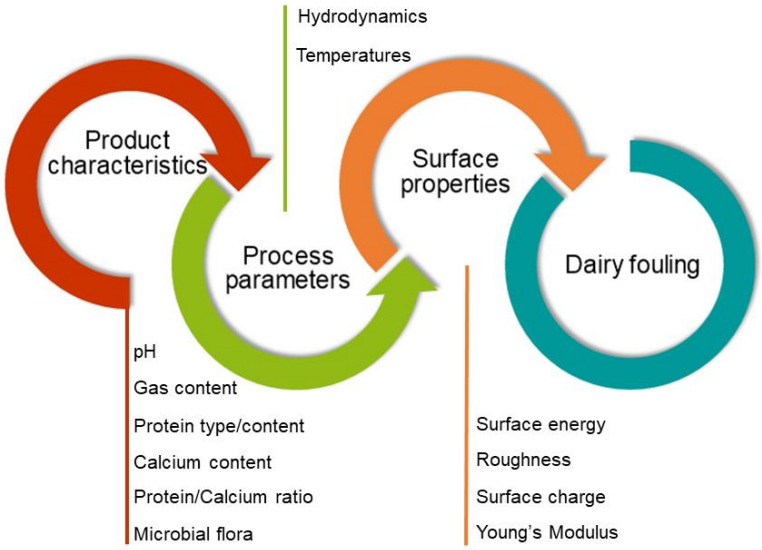

Figure 3. Three categories of factors affecting dairy fouling, adapted from [11]

Therefore, this chapter will only focus on the impact of surface modification on fouling and cleaning behaviour. Surface properties used to characterize coatings and materials will be described in a first section. Numerous investigations have reported the impact of surface properties onto fouling deposit; however, the comparison between these works is difficult. Indeed, fouling tests were performed using various model fluids, process types and conditions. Hence, in a second section, studies are divided as function of the process type, *i.e.*, batch or continuous flow pasteurization. This will lead to establish the influence of surface properties on fouling behaviour and to explain how surface modifications are performed. Some authors also investigated the cleanability of modified surfaces, leading to the distinction between anti-fouling and fouling-release surfaces in a third part. Finally, process parameters of fouling test, surface characterizations and cleaning conditions will be discussed to make the comparison between investigations on surface modifications more relevant. A standardization of surface characterizations and cleaning conditions is then proposed based on different investigations.

II. Surface properties

The induction phase can be seen as the most important step in fouling mechanisms. Indeed, during this short time, the adsorption of whey proteins to heat exchanger surfaces takes place, leading to further adhesion of minerals and whey proteins. Adsorption and adhesion phenomena are governed by physicochemical interactions at the interface. These interactions influencing adsorption and adhesion can be divided into two groups: (i) mechanical interactions and (ii) molecular interactions. Mechanical interactions gather roughness and topography. Molecular interactions include several forces corresponding to the surface energy parameter.[10], [25]

2.1. Mechanical interactions: Roughness and Topography

Surface roughness in an important parameter acting on (i) thermal processing performances and (ii) dairy fouling mechanisms. Rough surfaces lead to an increase of heat transfer and turbulence and thus an increase of mass transfer. [25], [59] On the other hand, rough surfaces are more prone to fouling due to a larger available area (grain boundaries). [10], [47], [60]

Nonetheless, the calculation of the real surface geometry is complex and [61] reported around 60 roughness parameters gathered in three different groups: amplitude parameters, spacing parameters and hybrid parameters. Surface topography is often characterized by amplitude parameters measuring the vertical surface deviations. Especially, the arithmetic average height (R_a) or centre line average (CLA) and the root mean square roughness (R_q or RMS) are the most used roughness parameters. R_a (Eq. (2)) represents the absolute average of vertical surface deviations from the mean centre line over length range Figure 4. R_q (Eq. (3)) describes the standard deviation of the distribution of surface heights.

$$R_a = \frac{1}{n} \sum_{i=1}^{n} |y_i| \quad (2)$$

$$R_q = \sqrt{\frac{1}{n} \sum_{i=1}^{n} Z_i^2} \quad (3)$$

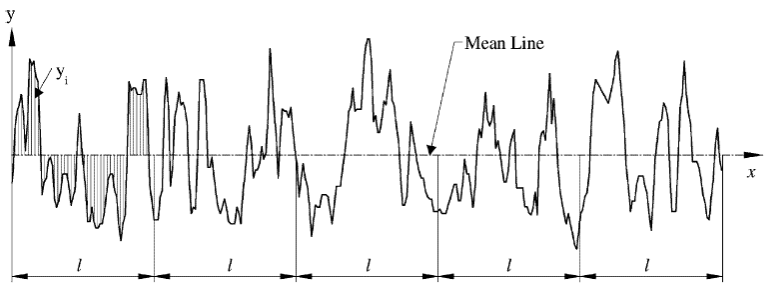

Figure 4. Representation of the arithmetic average height (R_a) (Gadelmawla et al., 2002) Reprinted with permission from Elsevier B. V.

Different techniques exist to measure the surface topography driving to R_a parameter. For instance, profilometer, atomic force microscopy (AFM), coherence scanning interferometry, confocal microscopy.[12]

2.2. Molecular interactions: Surface free energy

The adhesion of whey proteins and calcium phosphates can be explained by the theory developed by Derjauin and Landau [62] and Verwey and Overbeck [63], called DLVO theory from the names of their inventors. According to this DLVO theory, attractive Lifshitz-van der Waals forces and repulsive double layer trigger the attachment phenomenon. However, the DLVO theory has been extended by taking into account the Lewis acid/base forces (hydrophilic repulsion and hydrophobic attraction) and the Brownian motion. [64], [65] Therefore, the total interaction energy between the fouling deposit and the solid substrate (Eq. (4)) is constituted of Lifshitz-van der Waals, electrostatic, and the short-range (Lewis acid/base interactions and Brownian motion) interactions as detailed in following equation (4), where 1, 2, and 3 indicate the fouling deposit, substrate and liquid, respectively

$$\Delta G_{1,2,3}^{TOT} = \Delta G_{1,2,3}^{LW} + \Delta G_{1,2,3}^{EL} + \Delta G_{1,2,3}^{AB} + \Delta G_{1,2,3}^{Br} \quad (4)$$

Nevertheless, the electric double layer repulsion and repulsive forces arising from Brownian motion can be neglected as they are too small to satisfy the balance with attractive Lifshitz-van der Waals and Lewis acid/base forces. [66]–[68] The electric double layer repulsion decays spatially with the characteristic Debye length. In milk, this length is approximately 1 nm, thus the electric double layer interactions decrease of about 37 % within the first nanometer. [12], [69], [70] Consequently, the equation (4) can be simplified as following equation (5):

$$\Delta G_{1,2,3}^{TOT} = \Delta G_{1,2,3}^{LW} + \Delta G_{1,2,3}^{AB} \quad (5)$$

2.2.1. SFE measurement

According to van Oss, the SFE of a solid substrate can be written as the sum of Lifshitz-van der Waals and Lewis acid/base interactions expressed in J/m² or N/m (Eq. (6)).

$$\gamma_i = \gamma_i^{LW} + \gamma_i^{AB} \quad (6)$$

Other empirical models exist, that are reported in Table 2. To calculate the SFE, the Owens, Wendt, Rabel and Kaelble (OWRK) model decomposes it into polar (γ^P) (Lewis acid/base interactions) and dispersive (γ^D) parts (Lifshitz-van der Waals interactions). To go further, the van Oss, Chaudhury and Good's model permits to split the polar part into an acid or electron acceptor component (γ^+) and a basic or electron donor component (γ^-) as follows in equation (7):

$$\gamma_i^{AB} = 2\sqrt{\gamma_i^+ \gamma_i^-} \quad (7)$$

The SFE of a surface can be directly determined using the Young equation (Eq. (8)), where θ is the contact angle between the liquid and the solid phase, γ_{SV} is the solid-vapor interfacial energy, γ_{SL} the solid-liquid interfacial energy and γ_{LV} the liquid-vapor interfacial energy. [71]

$$\gamma_{LV} \times \cos\theta = \gamma_{SV} - \gamma_{SL} \quad (8)$$

The use of at least three liquids with known surface tension allows determining the SFE of a solid substrate.

Table 2. Empirical models for SFE calculation [11]

Name	Component	Model	References
Zisman	One	Measuring several probe liquids' CA and plot the cosine of those angles against the known surface energies, then extrapolate to contact angle equal 0.	[72]
Owens, Wendt, Rabel and Kaelble (OWRK)	Two	$\frac{\gamma_L(\cos\theta + 1)}{2\sqrt{\gamma_L^D}} = \frac{\sqrt{\gamma_S^P}\sqrt{\gamma_L^P}}{\sqrt{\gamma_L^D}} + \sqrt{\gamma_S^D}$	[73] [74]
Wu	Two	$\gamma_{SL} = \gamma_S + \gamma_L - 4\left[\frac{\gamma_S^D \gamma_L^D}{(\gamma_S^D + \gamma_L^D)} + \frac{\gamma_S^P \gamma_L^P}{(\gamma_S^P + \gamma_L^P)}\right]$	[75]
Van Oss, Chaudhury and Good	Three	$\gamma_L(1 + \cos\theta) = 2\left[\sqrt{\gamma_L^{LW}\gamma_S^{LW}} + \sqrt{\gamma_L^+\gamma_S^-} + \sqrt{\gamma_L^-\gamma_S^+}\right]$	[76]

2.2.2. Wettability

The Young equation (Eq. (8)) is the first wetting model allowing to characterize the surface wettability, by measuring the water contact angle (WCA) between the liquid and the surface. The contact angle describes the balance of cohesive (between the molecules of the liquid) and adhesive (between the liquid and the solid) forces precisely located at the triple line (liquid/surface/air interface). Therefore, if the liquid spreads on the surface it means that the

surface has a high affinity for water (cohesive forces < adhesive forces). Contrary to a wetting surface, a surface which has no affinity with the dropped liquid, will repel it (cohesive forces > adhesive forces). [77]

Nevertheless, the Young equation does not take into account the surface topography. It states that SFE of a smooth and homogenous surface depends on molecular interactions only. Surfaces can present irregularities and defects thus, Wenzel rewrote the Young equation, connecting both wettability and surface roughness (Eq. (9))

$$\cos\theta^* = r\cos\theta \quad (9)$$

Where "*r*" has been introduced as the "roughness factor" which represents the ratio of actual surface to geometric surface, θ* as the apparent angle (experimental measurement) and θ the real angle (corresponding to the contact angle of a flat surface). According to Wenzel, owing by the increased surface roughness, both solid-liquid and solid-vapor interfacial surface tensions increase slightly, but liquid-vapor interfacial surface tension does not vary. Consequently, apparent water contact angle is slightly greater than the real water contact angle.[78] If the perfectly flat surface is hydrophobic (hydrophilic), the corresponding roughened surface will be superhydrophobic (superhydrophilic). [79], [80]

Later, in 1944, the Wenzel equation has been further modified. Cassie and Baxter [81] have observed that water does not necessary fill in the porous solid surface, creating liquid-vapor interface: the Cassie-Baxter equation takes into account the solid fraction in contact with water, expressed as φ_S (Eq. (10)) [78], [81]

$$\cos\theta^* = -1 + \phi_S\,(\cos\theta + 1) \quad (10)$$

Hence, Wenzel model refers to homogeneous regime where water droplet fills up the roughness grooves and Cassie-Baxter model refers to heterogeneous regime where water droplet lies on top of the protrusions and air bubbles are trapped between water and the protrusions as displayed in Figure 5. [78], [82]

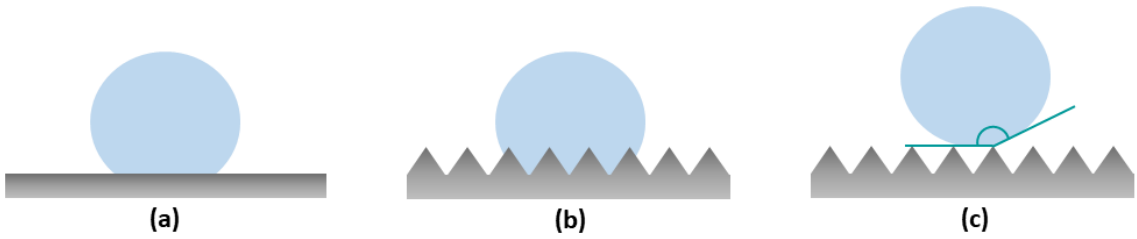

Figure 5. Representation of (a) a smooth hydrophobic solid surface, (b) a rough hydrophobic surface in homogeneous regime (Wenzel) and (c) a rough superhydrophobic surface in heterogeneous regime (Cassie-Baxter)

2.2.3. Contact angle hysteresis (CAH)

However, the parameters r and Φ_s, that distinguish Wenzel model from Cassie-Baxter model, are complex to quantify. Therefore, to discriminate these two superhydrophobic states the measurement of contact angle (CAH) hysteresis is performed. It has been demonstrated that Wenzel state drives to high contact angle hysteresis because the droplet is sticked to the surface. On the contrary, a quasi-null hysteresis is observed in Cassie-Baxter state due to the sliding of the droplet.[82]

The CAH parameter can be measured using two different methods: the volume variation of the droplet or the tilting plate.

The first one consists in slowly pumping the liquid into and out of the droplet giving the advancing and receding angles. The second one consists in tilting the surface where the drop is standing. When the surface is tilted, water droplet undergoes both surface tension and gravity. The drop starts to slide as illustrated in Figure 6 and becomes asymmetric achieving the advancing and receding angles. Advantages and drawbacks of these two methods have been reviewed in [83].

Figure 6. Receding and advancing contact angles determining contact angle hysteresis

Contact angle hysteresis (CAH) can thus be calculated thanks to the equation (11), where θ_h is the contact angle hysteresis, θ_a is the advancing contact angle at the lower side and θ_r is the receding contact angle at the upper side.

$$\theta_h = \theta_a - \theta_r \quad (11)$$

The higher the difference is, the more the droplet will be pinned on the surface. On the contrary, the lower the difference is, the more the droplet will be repelled.[83], [84]

III. Surface modifications to mitigate dairy fouling deposit

Studies on surface modifications to mitigate dairy fouling deposit started in 1968 and extended greatly in the 1990s. Modifying the surface is one of the two pathways mitigating dairy fouling deposit. Heat exchangers' surfaces have been modified in order to make the induction period longer. Indeed, a longer induction phase would enhance heat exchangers' operating efficiency leading to less frequent or less harsh cleaning.[9], [10] In 2015, a study [85] showed that surface modifications could be economically attractive as long as coatings could extend the duration of pasteurization period, reduce cleaning and conserve heat transfer efficiency.

Surface modifications allow to physically or chemically change the surface properties of a material. They are performed via different techniques, which will be presented in another section (section 3.2). The literature gathers about fifty studies on the impact of modified surfaces on dairy fouling. Nevertheless, the comparison remains complex due to several reasons. First of all, milk can be pasteurised under various conditions: (i) Batch pasteurization, (ii) High Temperature Short Time (HTST) pasteurization and (iii) Ultra High Temperature (UHT) pasteurization (Table 1), consequently, some studies have been performed in batch and other in continuous flow mimicking HTST pasteurization.[14]

Secondly, different process parameters (bulk and surface temperatures and hydrodynamic regime) are used for fouling runs, either in batch or in continuous flow. Indeed, the fouling layer growth is not similar in batch and continuous flow conditions. When the liquid to be processed passes through the heated channel once, the composition of the processed fluids (in native,

unfolding and aggregated proteins species…) feeding the fouling layer is fixed. This means that the deposit build-up happens in steady conditions. On the contrary, when the liquid to be processed passes through the heated channel many times, the composition of the foulant fluids fluctuates with time. It means that the formation of the deposit occurs this time in unsteady conditions. Indeed, there is a depletion in native proteins species and a loss of precursor species (unfolded or aggregated species) as the number of passing through the heat exchanger increases.

In some cases, after the fouling run, rinsing and/or cleaning steps are carried out. The latter rinsing step reveals whether the surface helps fouling removal along. This type of surface will be referred to as a fouling-release surface in opposition to an anti-fouling surface that remains un-fouled after a pasteurization cycle. Finally, the surface properties (wettability and/or surface free energy and/or roughness) are not always assessed. Therefore, among the publications on surface modifications, the focus will be on experiments carried out in batch or continuous flow conditions using stainless steel as surface reference and presenting surface characterizations of coated surfaces. In these investigations, fouling is quantified by weighing the deposit, measuring the pressure drop or calculating the thermal fouling resistance through the overall heat transfer coefficients of the soiled and cleaned surfaces.

3.1. Impact of surface properties on dairy fouling

3.1.1. Batch pasteurization

The fouling mechanism under batch conditions differs from that of a continuous flow in a heat exchanger. The flow regime, mass and heat transfer and bulk temperature are indeed not comparable. According to the literature, some studies were realized in laminar regime, with shear stress.[86]–[88] Boxler, Augustin *et al.* [89] performed fouling test in a stirrer tank rotating at 60 rpm, corresponding to a Reynolds number of 12,360, which is in the range of turbulent flow under batch conditions. At this flow regime, fouling deposit removal was observed due to the weak adhesion of the particles onto the surface.[10], [89] In dairy industries, batch pasteurizations are performed at around 63 °C [14], which is slightly lower than the denaturation temperature of β-Lactoglobulin (70-74 °C). Thus, β-Lactoglobulin proteins are not supposed to form aggregates in the bulk; however, when the surface is heated, denaturation can take place near it, in the boundary layer. Consequently, according to Boxler [10], β-Lg can either adsorb on the surface and denature or denature in the boundary layer and then adsorb on the surface. With a high temperature difference between bulk and heated surface, no additional β-Lg aggregates form on the surface. According to Itoh *et al.* [90], aggregation of β-Lg can

occur close to the surface (in the boundary layer) but these aggregates barely adhere to the surface. At high temperature, β-Lactoglobulin first denatures on the surface and then can aggregate to other denatured β-Lg proteins. Therefore, under batch conditions, fouling rate depends on surface reactions and thermal boundary layer.

With these considerations in mind, batch studies are separated from those in continuous flow and are gathered in Annex 1- Table 52 adapted from Boxler [10] and Zouaghi [11]. These studies are divided following their observations and conclusions about the influence of surface properties on dairy fouling. Although divergent points of view are ventured, most of them claim that SFE and especially the polar or electron donor components are the main impacting parameters. Kirtley *et al.* [91] and Mauermann *et al.* [88] both investigated protein fouling (β-Lg protein and whey proteins) behaviour on various surfaces. Kirtley *et al.* [91] pointed out that an optimal SFE value is equal to 45.7 mN/m allowing the reduction of β-Lg protein adsorption. On the other hand, Mauermann *et al.* [88] did not observe any fouling decrease on modified surfaces (fluoropolymer, Diamond-Like Carbon (DLC) and inorganic coatings). However, coatings with SFE lower than 30 mN/m were easily cleaned. Altogether, no clear correlation between the ease of fouling removal and the SFE or the polar component can be highlighted.

Augustin *et al.* [92] also investigated whey proteins fouling on DLC coatings and observed an increase in induction time for higher polar part coatings. However, after 25 hours of pasteurization, the fouling resistance was reduced for coatings having a polar component around 12 mN/m. The latter observation is in agreement with Boxler *et al.* [89] who observed a lower mass deposit for surfaces with electron donor (γ^-) component ranging from 8.3 to 13.4 mN/m (2.4 g/m² for Si and O-doped DLC coating (SICON) compared to 0.6-1.0 g/m² for other coatings) for the same bulk and surface temperatures. As the electron acceptor component of the van Oss model is close to zero, the electron donor component can be compared with the polar part of OWRK model.[89], [92] In fouling tests, with mineral species only, Rosmaninho and Melo [93] observed less fouling deposit onto coated surfaces with a low value of the electron donor part as well as for low and high bulk temperatures. This has been refuted by Boxler *et al.* [89] and Rosmaninho *et al.* [87] who claimed that a lower fouling resistance for surfaces with higher electron donor component leads to a lower final fouling amount. By investigating raw milk fouling, Britten *et al.* [86] demonstrated the impact of a low polar component on the protein and calcium phosphate strength adhesion. Although the fouling amount was comparable on all surfaces, polymeric coatings with a low polar part exhibited lower protein and calcium phosphate adhesion strengths and were easier to clean. Rosmaninho

et al. [93] studied the fouling behaviour of whey proteins in presence of minerals at 50 and 85 °C, respectively below and above the denaturation temperature of β-Lactoglobulin. They observed that at low temperature, the lower the electron donor part, the lower the fouling amount. On the contrary, at high temperature, the higher the electron donor part, the lower the fouling deposit. Consequently, they proposed the mechanisms displayed in Figure 7. At low temperature, the bulk is only composed of native whey proteins and mineral aggregates. These latter are thus able to attach and spread on the surface and preferentially on surfaces of high SFE. On the contrary, at high temperature, denatured whey proteins present in the bulk readily adhere to the surface, hence reducing the adhesion area for minerals attachment.

This high temperature mechanism was confirmed by Boxler *et al.* [89] who studied fouling from whey proteins and mineral solution, by heating the surfaces to 85 and 120 °C. They observed that calcium phosphate attaches preferentially onto low electron donor component surfaces, and that whey proteins are more abundant onto high electron donor component surfaces. To corroborate their observations, they performed an analysis of variance leading to a decrease of the fouling resistance and fouling mass deposit through an optimal value of the electron donor part.

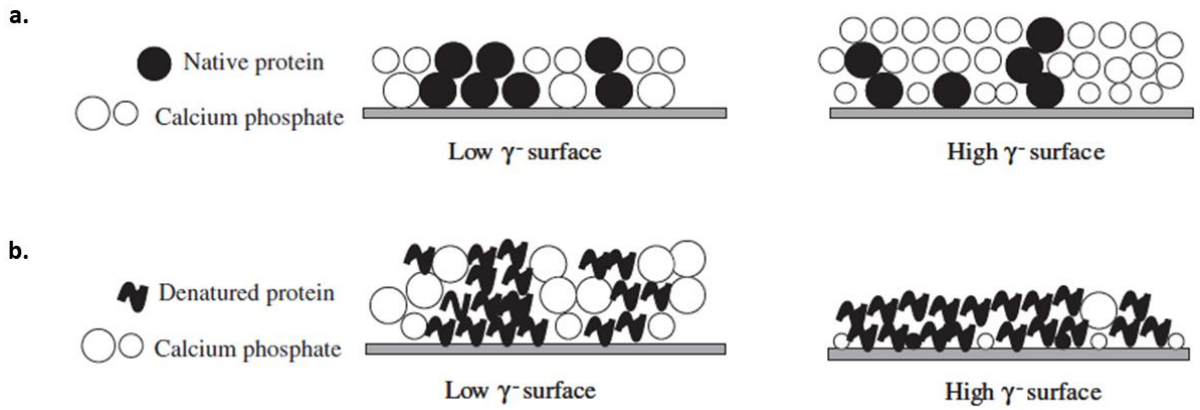

Figure 7. Schematic proposed mechanisms of proteins and minerals fouling onto low and high electron donor component surfaces: a) At low temperature (50 °C), b) At high temperature (85 °C) [93] *Reprinted with permission from Elsevier B. V.*

Piepiórka *et al.* [94] analysed the fouling behaviour of whole milk onto stainless steel with three different roughnesses (R_a: 0.028 µm, 0.174 µm and 0.445 µm). Contrary to previous work, they stated that both the dairy mass deposit and the diameter of deposits were proportional to the surface roughness. They also demonstrated that the smoother the surface the longer the induction phase.

This confirmed the observations of Augustin *et al.* [92], but they pointed out that both the surface roughness and the SFE affect the fouling resistance. Augustin *et al.* [92] compared the whey protein fouling resistance of stainless steel with three modified surfaces: Si-doped diamond-like carbon, electropolished stainless steel and electropolished Si-doped diamond-like carbon surfaces. The results demonstrated that a high polar component combined with low roughness reduced the fouling resistance as shown in Figure 8.

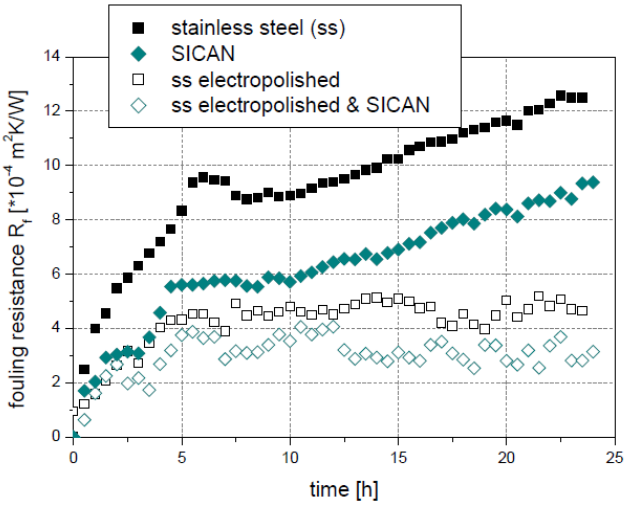

Figure 8. Impact of surface roughness and polar component on fouling resistance [92]

3.1.2. Continuous flow pasteurization

The investigations performed under continuous flow conditions are reported in Annex 2 - Table 53 in the same way as for batch pasteurization. Among these studies, a few, less than ten, were directly performed in plate heat exchangers (PHE), as these heat exchangers are widely used in milk pasteurization. Nevertheless, flow rate or flow velocity for these studies remains lower than those used in the dairy pasteurization industrial sector. It can be noted that most of these works were carried out close to or above the denaturation temperature of β-Lg. Therefore, the fouling mechanism is expected to diverge from batch conditions. Whey protein aggregates may form in the bulk and then adsorb on the surface, or the whey proteins may denature on the surface and aggregate. Furthermore, under continuous flow, the average wall shear stress is commonly higher than the one in batch experiments. Thus, fouling is controlled by mass transfer of foulants from the bulk to the heated surface and by erosion of the dairy deposit from the fouling layer back into the bulk. Nevertheless, some studies were carried out with fluid recirculation, which resulted in a decrease in the native β-Lg concentration and an increase in whey protein aggregates in the bulk as the fouling operating time increased. Consequently, the fouling layer consists mainly of denatured and aggregated whey proteins. Without recirculation,

milk or model fluid is constantly injected; consequently, at a given position, the composition in fouling species is independent of the time leading to the formation of fouling deposit composed of native, unfolded, denatured and aggregated whey proteins.[10]

Annex 2 - Table 53 adapted from Boxler [10] and Zouaghi [11], is split into four main topics. Among the published works investigating the influence of surface properties on the dairy fouling behaviour, only one claims that SFE and roughness do not affect fouling amount or the cleanability.[95] Otherwise, it can be noted that the surface properties (SFE, wettability and roughness) of diamond-like carbon coatings do not differ significantly from the stainless steel surface.

As for batch conditions, SFE and the polar or electron donor component seem to play a greater role than surface roughness on fouling behaviour. Santos *et al.* [96] analysed whey protein fouling and demonstrated that low SFE coatings lead to a decrease in the amount of whey protein adsorbed, but no direct relationship was established. This observation has been confirmed by Rungraeng *et al.* [97], although tests were carried out with pasteurised milk. The nanocomposite CNT-PTFE (carbon nanotubes-polytetrafluoroethylene) coating reduces the SFE by 97 % compared to bare stainless steel and the final mass fouling by 70 %. Liu *et al.* [98] demonstrated promising results using ceramic PTFE-free coating having lower SFE than stainless steel, as the fouling deposit was reduced by 98 %. Among the surfaces tested by McGuire and Swartzel [99], PTFE, which has the lowest SFE, does not exhibit the lowest adsorbed mass. Mcguire *et al.* [99] stated that an optimal SFE value reduces the fouling rate deposition. These observations are at odds with the work of Kananeh *et al.* [100] who found no significant fouling reduction using hydrophobic surfaces (PTFE and polyurethane-based coatings). Nonetheless, these hydrophobic coatings enable to reduce the cleaning time, in particular PTFE coated surfaces, which exhibit a drop by 90 %. Huo *et al.* [101] corroborated the latter observation and demonstrated a 98 % improvement in cleaning by modifying stainless steel with a commercial fluoropolymer.

Although different solutions have been used as model fluid for fouling tests, numerous authors pointed out the positive effect of the polar or electron donor component on fouling. Some of them claimed that coatings with low electron donor component reduce the fouling resistance in the first stage as well as decrease the deposition rate and the final fouling amount.[12], [102]–[104] Boxler *et al.* [105] demonstrated that a minimal fouling resistance as

well as a minimal whey protein adhesion were both obtained for an optimal value of the electron donor component of around 8.5 and 9.5 mN/m. On the other hand, other authors did not observe any reduction in fouling with low polar component surfaces but emphasized the ease of fouling removal after cleaning. Beuf *et al.* [106] revealed the cleaning efficiency of Ni-P-PTFE coating and Zouaghi *et al.* [107] showed that graphite-based composites led to a fouling drop of 95 % after rising with hot water only.

Otherwise, Zouaghi *et al.* [108] contradicted all these previous works highlighting that a fouling reduction with a high polar component is also possible. Pasteurization tests were performed using amphiphilic coatings with a high polar component (30.1 mN/m against 3.7 mN/m for stainless steel). No trace of fouling was present after a fouling test, pointing out that high polar part surfaces can also prevent whey protein adhesion.

Based on Annex 2 - Table 53, few studies have highlighted the role of surface roughness on dairy fouling as it was noticed for batch pasteurization. In 1968, *Gordon et al.* [109] published the first article dealing with the impact of surface modification on dairy fouling. They notably investigated the effect of roughness using stainless steel surfaces with four finishes: pickle finish, which is the roughest, 120 grit finish (R_a: 1.4-2.4 µm), 180 grit finish (R_a: 0.9-1.5 µm) and 320 grit finish (R_a: 0.3-0.5 µm). They concluded that the smoother surface tends to decrease the fouling amount. Yoon *et al.* [110] studied different types of coatings with roughness (R_a) ranging from 0.08 to 0.6 µm. Nevertheless, although this range of surface roughness is lower than that studied by Gordon *et al.* [109], no fouling reduction or enhanced cleaning was achieved.

Other authors claimed that mitigation of dairy fouling can only be achieved by taking SFE and roughness into account simultaneously. They pointed out that low SFE combined to a smooth surface lead to fouling mitigation. Zouaghi *et al.* [60] investigated the influence of stainless steel surface properties to limit dairy fouling in a holding tube using whey protein and calcium solution. 316L stainless steel 2B finish was considered as the reference (NAT), having a SFE of 40.5 mN/m and a R_a of 0.07 µm. Both physical (mirror polishing – ML and laser texturation – TEX) and chemical modifications (fluorosilanization – Sil) were carried out to amplify the roughness or make stainless steel smoother and to reduce the SFE. Surface characterizations as well as fouling densities are gathered in Table 3. It can be noticed that the fouling density of the reference (NAT) is two times greater than the mirror-like stainless steel surface (ML). Furthermore, chemical modification allows to reduce fouling by 83 % in the case

of fluorosilanized mirror-like stainless steel surface (SilML), proving that both SFE and R_a interfere in fouling mitigation.

Table 3. Surface characterizations and fouling density of modified stainless steel surfaces adapted from [60]

Sample	WCA (°)	SFE (mN/m)	Ra (µm)	Density of mass deposit (mg/cm²)
NAT	92.9 ± 4.6	40.5 ± 1.7	0.07 ± 0.01	30.8 ± 4.0
ML	63.9 ± 2.5	42.5 ± 3.8	$3.10^{-}3 \pm 2.10^{-}4$	17.2 ± 0.6
TEX	0 ± 0	Not possible to determine	36.0 ± 2.0	151.2 ± 21.2
SilNAT	111.9 ± 1.1	27.6 ± 3.2	0.98 ± 0.09	8.7 ± 0.6
SilML	105.9 ± 0.8	18.8 ± 4.3	4.10-3 ± $1.10^{-}3$	5.2 ± 0.4
SilTEX	132.9 ± 1.6	Not possible to determine	36.0 ± 2.0	57.4 ± 14.3

NAT: native stainless steel (SS), ML: mirror-like SS, TEX: laser texturized SS, Sil: silanization

Barish and Goddard [111] compared the performance of stainless steel (SFE: 41.4 mN/m and R_a: 0.46 µm) with Ni-P-PTFE coating (SFE: 24.7 mN/m and R_a: 0.17 µm) against raw milk. The density of the fouling mass deposit was significantly lower on the Ni-P-PTFE coating than on the stainless steel surface with 0.45 g/cm² and 12.73 g/cm² respectively, thus leading to a 96 % fouling reduction. Zouaghi *et al.* [13] confirmed this observation by using SLIPS-like surfaces. After a pasteurization test, SLIPS-like surfaces allow to limit dairy fouling by up to 63 %. Jimenez *et al.* [112] corroborate this point of view but emphasize the effect of the electron donor component on fouling mitigation. Comparing samples with equivalent R_a, the lower the electron donor part, the lower the fouling mass. On the contrary, in another work, Zouaghi *et al.* [113] deposited silicone-based films onto stainless steel leading to the formation of uneven particles with a R_a ranging from 0.04 to 0.07 µm and with a higher polar component (ranging from 3.92 to 15.8 mN/m) than that of stainless steel surface (3.7 mN/m). These nanostructured surfaces with a high polar part have proved their effectiveness by mitigating dairy fouling by 90 %. These works do not allow to establish a correlation between R_a and electron donor component, but a competition can be highlighted.

Finally, comparing impacts of surface properties in batch conditions with those in continuous flow gives similar conclusions. Two points of view can be distinguished: the influence of the electron donor component and the combination of the SFE with R_a are discussed in the next sections.

3.1.3. Impact of surface free energy (SFE)

Most studies aimed at reducing the SFE and demonstrating the positive impact of a lower SFE on dairy fouling behaviour, whatever the pasteurization type. Overall, SFE acts on the final fouling amount, structure, composition, fouling resistance, deposition rate or cleanability. Nevertheless, a low SFE value does not necessarily enable to minimize the adhesion of proteins onto surface. An optimal SFE range where biological fouling adhesion is minimal has been well established experimentally by Baier [114], taking place from 20 to 30 mN/m as displayed in Figure 9. This optimal range has been validated for limiting bacteria, mineral and protein adhesion either experimentally or by the Extended Derjaguin-Landau-Verwey-Overbeek (DLVO) theory.[99], [115]–[118] This range corresponds to fouling-release coatings. The difference between fouling-release and anti-fouling surfaces will be discussed later.

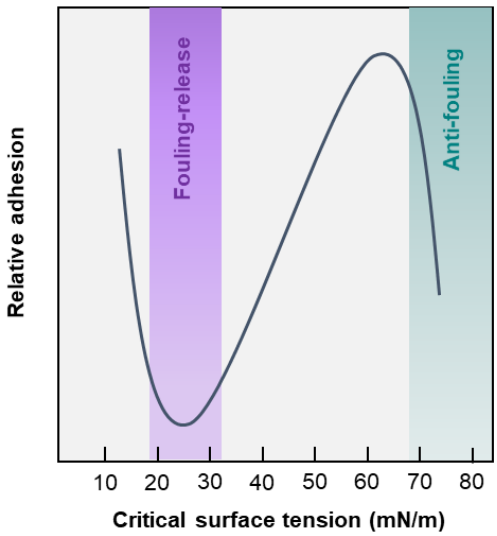

Figure 9. Baier's curve of the fouling degree as a function of critical surface tension adapted from [119]

The SFE of stainless steel currently used in dairy industries is around 40 mN/m. Therefore, based on the Baier's relationship (Figure 9), most research attempted to reduce the SFE of stainless steel and thus the polarity. Materials or coatings with low SFE and low polarity are recognized for their anti-adhesive and fouling-release properties, due to weak substrate-fouling deposit adhesions. Two types of materials or coatings are known to fulfil these criteria: silicone and fluorinated materials.[119] Both of them have been widely tested against milk or whey proteins and/or calcium solutions.

To limit dairy fouling, silica [93], [96], [106], polysiloxane [110] or SiO_x [87], [93], [106], [112], [113] coatings were studied. Albeit, in most cases, SiO_x coatings were deposited by

PECVD. Rosmaninho *et al.* [87], [93] obtained coatings with high electron donor component ranging from 15 to 50.6 mN/m unlike Jimenez *et al.* [112] who reported more hydrophobic coatings with lower electron donor part ranging from 0 to 0.7 mN/m. Consequently, divergent conclusions were drawn about these coatings. Rosmaninho *et al.* [120] did not observe fouling reduction, which was confirmed by Yoon *et al.* [110] with polysiloxane coating although they also explored the cleanability. On the opposite, Jimenez *et al*. [112] and Zouaghi *et al.* [113] reported good results in fouling reduction, and after water rinsing as well. But for these latter cases, surface morphology was shown to have a great impact on fouling.

Fluoropolymer materials such as PTFE (Polytetrafluoroethylene) [12], [97], [109], [110], [121], Ni-P-PTFE [87], [93], [106], [111], [120], [122]–[124], FEP (Fluorinated ethylene propylene) [12], [88], PFA (Perfluoroalkoxy alkane) [12] and commercial coatings [101], [106], [112], [122], [123] have been also investigated. PTFE coating aroused great interest owing to their anti-adhesive properties but its effectiveness is contested. Indeed, Gordon *et al.* [109] and Dupeyrat *et al.* [121] did not observe a decrease of fouling compared to stainless steel. This was asserted by Yoon *et al.* [110], who investigated the cleanability as well. On the contrary, Rungraeng *et al.* [97] demonstrated a 43 % fouling decrease compared to unmodified stainless steel. Magens [12] corroborated this observation, nonetheless, he studied other fluoropolymer coatings and showed that PFA and FEP were more efficient. This could be explained by the combination of their low SFE with their low R_a compared to PTFE coatings. Unlike PTFE coating, Ni-P-PTFE coating presents higher performance to mitigate dairy fouling and is also easier to clean. Most authors pointed out a synergy between a lower electron donor component and a smooth surface masking grain boundaries of stainless steel.[106], [111]

Divergent conclusions for PTFE or SiO_x coating can be explained by the fact that the adhesion of hydrophilic molecules such as proteins is favourable on low energy surfaces, but larger conformational changes of β-Lg were observed on hydrophobic than on hydrophilic surfaces.[125] Moreover, the presence of Ca^{2+} reinforces protein adhesion acting as electron acceptor, neutralizing electron donor sites on surface, thus the surface becomes more hydrophobic.[77] Some authors have therefore tried to correlate the electron donor part to fouling behaviour. Britten *et al.* [86] found that the polar component is the main parameter affecting the strength adhesion of proteins. The bacteria adhesion was correlated with the ratio of the Lifshitz-van der Waals (γ^{LW}) part over the electron donor (γ^-) part. This was confirmed by Boxler *et al.* [105] who found an optimal electron donor component around 8.5-9.5 mN/m

(Figure 10). Rosmaninho *et al.* [93] and Liu *et al.* [126] also found optimal electron donor values affecting fouling, but much larger, ranging from 10 to 55 mN/m.

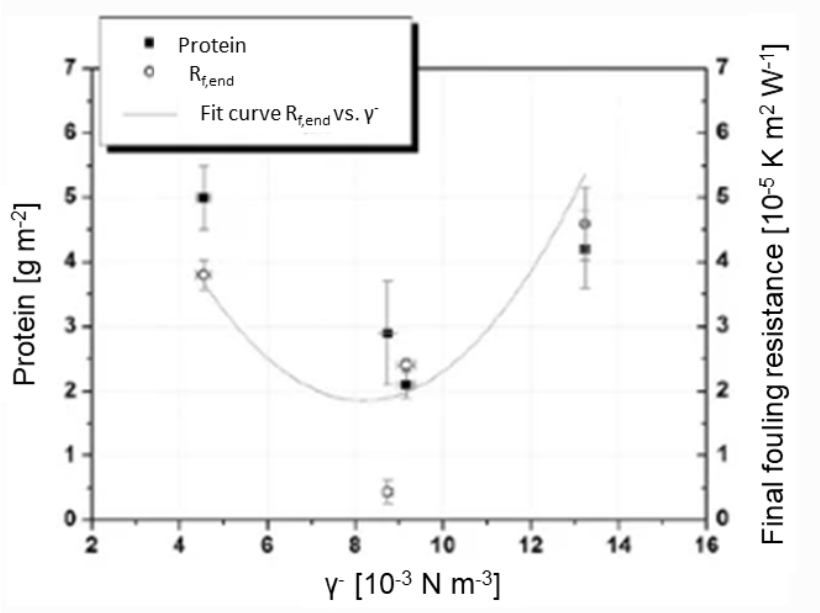

Figure 10. Analysis of the influence of the electron donor component on deposit protein content and final fouling resistance [105]

3.1.4. Impact of roughness (Ra)

As mentioned in section 2, R_a is related to SFE through wettability. Therefore, very few works have analysed the effect of R_a on dairy fouling alone because it is complex to isolate. Gordon *et al.* [109] investigated stainless steel surfaces with different R_a and concluded that the lower the R_a, the lower the dairy deposit. This observation was further validated by Piepiórka *et al.* [94] and Zouaghi *et al.* [60] who have also explored roughness of stainless steel surfaces. Piepiórka *et al.* [94] emphasized that R_a affects the fouling structure as well. They found larger clusters on surfaces with higher R_a. By comparing stainless steel to electropolished stainless steel, Boxler [10] observed a lower fouling resistance on the electropolished one. Moreover, the structure of electropolished stainless steel differs from that of stainless steel. Boxler [10] assumes that smoother surfaces are more prone to the adhesion of aggregated whey proteins and mineral agglomerates than rough surfaces hinge on the large diameter of whey proteins and mineral aggregates, ranging from 5 to 100 µm [127]–[129] and 0.1 to 80 µm [130], [131] respectively. Hence, aggregated whey proteins and mineral agglomerates must diffuse into the boundary grains before being adsorbed. On the contrary, rough surfaces favour prevail the attachment of native (1-10 nm [10]) and denatured whey proteins (50-60 nm [47]) as well as

calcium and phosphate clusters (1 nm [10]), as depicted in Figure 11. Jimenez *et al.* [112] confirmed the latter hypothesis by observing calcium deposit at the grain boundary, leading to an increase in dairy fouling.

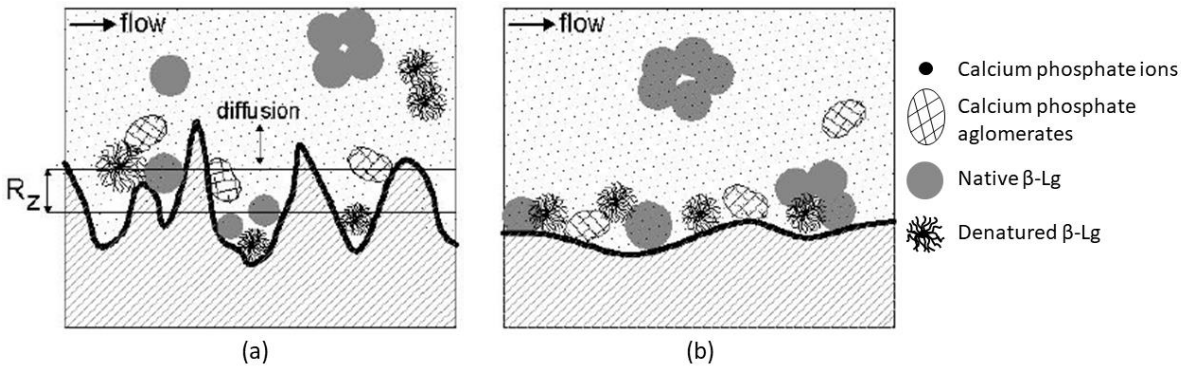

Figure 11. Impact of roughness depth (Rz) on the formation of the first fouling layer from a solution of whey proteins and calcium phosphates. (a) Onto unpolished stainless steel surface and (b) Onto electropolished stainless steel surface [10]

Surface morphology affects the structure and fouling deposit amount but also the cleanability. According to Detry *et al.* [132], fouling can remain into surface defects even after cleaning. Reducing R_a could thus facilitate fouling removal. However, Yoon *et al.* [110] studied several substrates with roughness ranging from 0.08 to 0.6 µm and claimed that R_a difference had no impact on fouling amount or on cleanability. Given the size of proteins and minerals depending on their state, R_a was however too high to prevent fouling adhesion. This has been proved by Zouaghi *et al.* [113] who reported that nano-rough surfaces (< 0.05 µm) enable the reduction of fouling after water rinsing.

Although, according to these investigations, a low R_a leads to milk fouling reduction and easier cleaning, to date no correlation has been established. Nevertheless, several authors stated that both low SFE and R_a at the nanoscale lead to a decrease of fouling deposit and improve the cleaning step. Zouaghi *et al.* [60] demonstrated that, by lowering both SFE and R_a, fouling was reduced by 83 %. Barish *et al.* [111], Zouaghi *et al* [13] and Jimenez *et al.* [112] validated this conclusion, suggesting a competition between both surface parameters for fouling control.

3.2. *Design of surfaces mitigating dairy fouling*

The design of materials or coatings mitigating dairy fouling developed in the 1990s with the outbreak of new high-performance technologies for producing nanomaterials. The latter are elaborated following two different approaches gathering several manufacturing processes. The first one is the top-down method, where matter is removed from the material to give a structured surface, while the bottom-up method consists in matter deposition to build-up the wanted surface. As for nanomaterials, processes used to design surfaces for reducing dairy fouling have been divided into two groups.

3.2.1. Top-down techniques

The top-down approach consists in sculpting a raw material (from the top) in order to obtain new micro or nanostructures (down) with new properties (physical or chemical). Micro-nanofabrication processes by etching/ablating based methods (dry or wet etching) allow creating micro or nano-roughness on smooth surfaces to structure a material. When combined to a lithography process or other masking methods, a periodic or quasi-periodic network can be obtained.

The top-down techniques used to design surfaces limiting dairy deposit are gathered in Table 4. Electropolishing process was used either alone to decrease intrinsic roughness of stainless steel or combined with a bottom-up technique (see next section). Most of top-down processes displayed, such as chemical or laser etching, providing specific roughness to stainless steel, have been combined with a bottom-up procedure leading to Ni-P-PTFE or SLIPS-like coatings for example. Procedures of fabrication of both of these coatings will be described later. Globally, techniques gathered in Table 4 are used either to decrease or increase intrinsic roughness of stainless steel. Recently, Ahn *et al.* [133] have used electrochemical etching to make porous stainless steel plate heat exchangers with holes at the micro and nano scale. However, these modified surfaces were tested against an inorganic fouling, $CaCO_3$, closer to type B fouling (mineral fouling).

Table 4. Top-down techniques

Fabrication method	Type of coating	Industrialisable method	References
Electropolishing	Electropolished stainless steel	✓	[110], [92], [100], [10]
Chemical etching	Pickling process for Ni-P-PTFE coating	✓	[106], [87], [111]
Laser etching	Surface structuration for Slippery liquid-infused surface	×	[13]

3.2.2. Bottom-up techniques

The bottom-up approach refers to an assembly of small building blocks (molecules/atoms) (bottom) to form larger and more complex object (up) with new properties. The fabrication methods mainly require physical and chemical based processes. Bottom-up processes have been much more investigated than top-down techniques in the dairy industry. Indeed, as shown previously, surface modifications have been performed in order to reduce the SFE of stainless steel. This has been achieved, in most cases, by depositing coatings directly on stainless steel surfaces and thus using only bottom-up techniques. These latter are reported in Table 5.

These techniques of fabrication can be also divided in two categories: (i) the wet route and (ii) the dry route. Wet routes gather sol-gel, self-assembly and electroless deposition methods, whereas dry routes gather ion implantation, PVD (Physical Vapour Deposition), sputtering, CVD (Chemical Vapour Deposition), PACVD (Plasma-Assisted Chemical Vapour Deposition), PECVD (Plasma-Enhanced Chemical Vapour Deposition) and APP (Atmospheric Pressure Plasma). As displayed in Table 5, most of coatings are produced by dry routes. These procedures are more environmentally friendly than wet routes as they do not require the use of solvents or catalyst, but require specific equipment. Diamond-like carbon, silicon-based and implanted ion coatings have been amply elaborated by these dry routes.

Diamond-like carbon (DLC) coatings have been extensively produced through various dry methods due to their numerous attractive properties.[88], [89], [92], [96], [104]–[106] DLC coatings demonstrate good thermal conductivity, similar to that of metals, and are extremely smooth, wear-resistant and hard.[134], [135] In addition, the amorphous nature of DLC coatings allows their mechanical properties and surface free energies to be adjusted by introducing specific elements. The incorporation of Si or F in the DLC matrix results in the decrease of SFE. The opposite tendency is observed by adding O or N in the matrix.[136], [137] As reported in Table 5, DLC and doped DLC have been produced by various vacuum deposition methods, and PECVD is the most used (Figure 12 a). As CVD process, plasma-enhanced CVD method enables to growth thin films onto a substrate through gaseous phase. Here, plasma is usually generated through radio frequency radiations or microwaves, allowing chemical reactions of gaseous precursors injected in the vacuum chamber. Properties and growth of thin films can be controlled *via* several parameters such as gas pressure, gas nature, power and substrate temperature. Various gases are used to grow diamond-like carbon films. C_xH_x gases such as methane or acetylene are typically chosen as carbon sources to obtain DLC coatings while

tetramethylsilane (TMS), hexamethyldisiloxane (HMDSO) or tetrafluorethylene (TFE) are Si and F sources, respectively, allowing the formation of doped DLC coatings.

Table 5. Bottom-up techniques

Fabrication method	Type of coating	Industrialisable method	References
Sol-gel	Inorganic and hybrid nanocomposites	✓	[88]
	Silica		[106], [96]
	Thermolon		[98]
Self-assembly	Silanization step for Slippery liquid-infused surface	✓	[13]
Casting solution	PMMA, PS, Cellulose, Agarose and Nylon	✓	[86]
	Amphiphilic Si-PEO		[108]
Electroless deposition	Ni-P-PTFE	✓	[106], [87], [111]
Ionic implantation	SiF_3^+	×	[87], [96]
	SiF^+		[106]
	MoS_2		[106], [87], [96]
	TiC		[96]
PVD	Ti-DLC	×	[88]
	TiN		[102], [103]
	DLC		[96]
CVD	DLC	×	[96]
	Si-O-DLC		[96]
	Multiwalled carbon nanotubes (MWCNT) for CNT-PTFE coating		[97]
PACVD	Si-DLC	×	[88]
	Doped DLC		[95]
PECVD	DLC	×	[106], [92], [104], [89], [105]
	Si-DLC		[104]
	Si-O-DLC		[104]
	SICAN		[92], [89], [105]
	SICON		[92], [89], [105]
	SiO_x		[106], [87], [93]
	TMDSO		[112]
APP	HMDSO	✓	[113]

As explained above, silicon-based coatings were widely investigated due to their numerous properties (chemically stable and inert, environmentally-friendly, smooth surface, drag reduction) [138] and have demonstrated interesting results either to reduce dairy deposit or facilitate fouling removal. Silica and SiO_x coatings were prepared from organosilicon precursors such as methyltriethoxysilane (MTES), tetramethydisiloxane (TMDSO) and HMDSO. These molecules have been widely used to deposit hydrophilic SiO_x coatings as adhesive or gas barrier film. Santos *et al.* [139] and Rosmaninho *et al.* [87], [93] obtained hydrophilic silicon-based coatings elaborated either by sol-gel or PECVD processes. However, other authors have proven that hydrophobic coatings could be obtained using PECVD or APP processes.[106], [112], [113] By optimizing manufacturing parameters of these dry methods, silicon-like coatings can be obtained. Under plasma discharge, such organosilicon monomers form a strong -Si-O-Si- backbone with terminal CH_x functions conferring hydrophobic properties. Although repeatable and reliable, PEVCD processes are time-consuming and expensive due to the use of vacuum pumps and chambers. To scale up plasma treatments for industrial applications, atmospheric pressure plasma sources have been developed. Zouaghi *et al.* [113] deposited silicon-based coatings using an atmospheric pressure plasma torch (Figure 12 b), commercialised by AcXys Technologies, and they obtained hydrophobic coatings by injecting HMDSO as precursor in the plasma post-discharge. According to Dimitrakellis *et al.* [140], HMDSO is largely chosen to form hydrophobic coating by APP hinge on its chemical inertness, high vapour pressure and low toxicity.

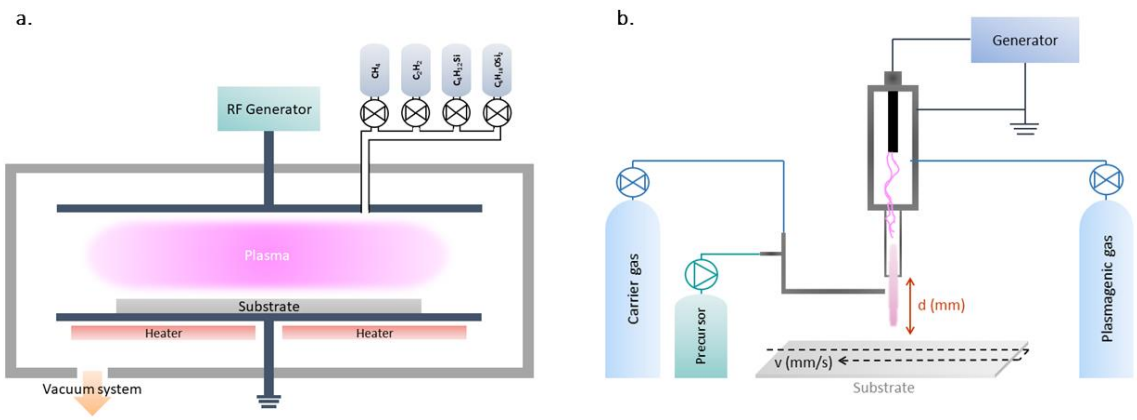

Figure 12. a) Plasma-Enhanced Chemical Vapour Deposition (PECVD) technique, b) Atmospheric pressure plasma (APP) torch

Some authors have also used ionic implantation to modify stainless steel surface. This process consists in implanting atoms on the surface of a solid substrate. Ions are accelerated in the keV to MeV energy range and then hit the surface to slot into the uppermost layers of the surface.[141] Depending on the accelerating energy of ions, their mass, and the mass of the atoms of the targeted material, ions can penetrate to a depth from 10 to 1000 nm. Therefore, ion implantation can change SFE and R_a without changing the bulk properties. Based on the Electric Double Layer theory, Zhao and Burnside [142] stated that both the free electrons on the metal surface and the SFE can be reduced by implanting elements having less free electron than pure metal (F, Si, C, …).[142]–[144] This technique allows doping the surface, thus no adhesion issues such as in CVD are observed. Two types of ion implantation have been used to reduce the SFE of stainless steel: (i) direct ion implantation, which is described above, and (ii) turbulent ion implantation (Figure 13). The latter technique is comparable to sputtering where the substrate is directly in contact with a plasma, but in this case, the substrate is placed at the cathode. Due to collisions in the plasma, atoms can penetrate the surface deeper, up to 100 µm. MoS_2 particles were injected in the vacuum chamber in order to be implanted into the stainless steel surface, as it is used as anti-adhesive in the mechanical engineering field.[106], [139] Nevertheless, XPS (X-Ray Photoelectron Spectroscopy) analyses exhibited a very low content of implanted molybdenum compared to bare stainless steel due to the low concentration of MoS_2 particles used in the process.

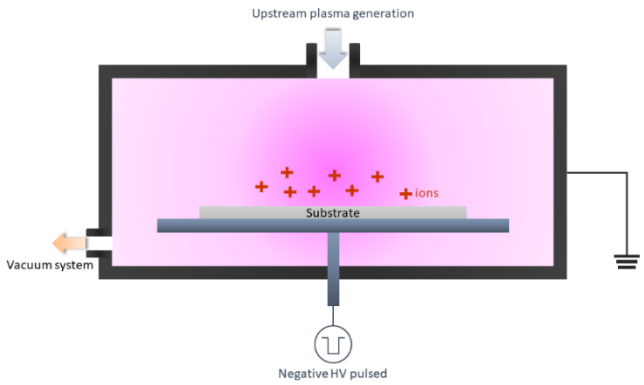

Figure 13. Schematic diagram of turbulent ion implantation process

3.2.3. Combination of top-down and bottom-up approaches

Some of the studies cited above report combination of top-down and bottom-up approaches: Ni-P-PTFE coatings and SLIPS-like surfaces. These were elaborated following different steps. The fabrication of Ni-P-PTFE coatings was reported by Santos *et al.* [139] and Barish *et al.* [111] and SLIPS-likes surfaces were detailed by Zouaghi *et al.* [13].

The process of fabrication of Ni-P-PTFE coatings is illustrated in Figure 14. First, the stainless steel substrate is submitted to a pickling process consisting of preparing the surface by removing impurities and/or oxide layer. Then, the activated substrate undergoes a galvanic deposition of Ni followed by an autocatalytic reaction depositing a Ni-P plating. Finally, nanoparticles of PTFE are incorporated in the Ni-P matrix.

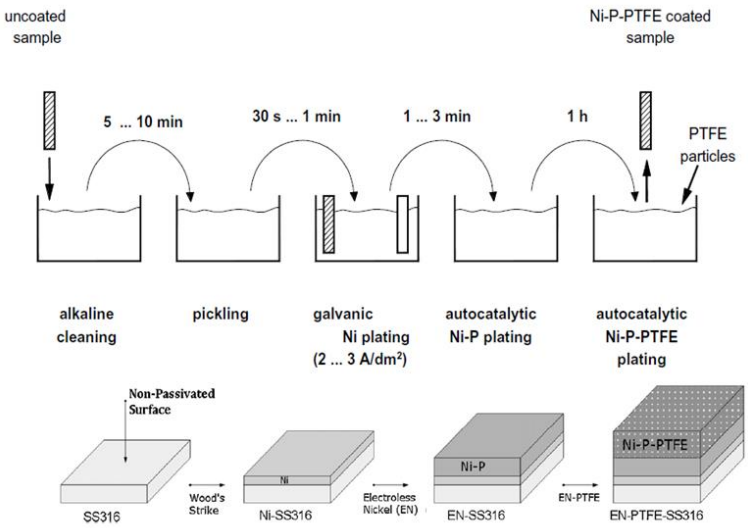

Figure 14. Process of fabrication of Ni-P-PTFE coating [111], [139] *Reprinted with permission from Elsevier B. V.*

Numerous ways exist to design SLIPS, which have been reviewed by Howell *et al.* [145] recently. Zouaghi *et al.* [13] developed their own SLIPS-like surfaces in order to mitigate dairy fouling. The first step was to roughen the stainless steel using femtosecond laser ablation. Cauliflower-like surfaces were obtained and the roughness raised from 68 to 1243 nm, as shown in Figure 15. After that, these surfaces were activated using a UV/ozone cleaner generating hydroxyl groups. These surfaces were then silanized with a perfluorosilane, prior to being impregnated by a perfluorinated oil (DuPont Krytox GPL 103).

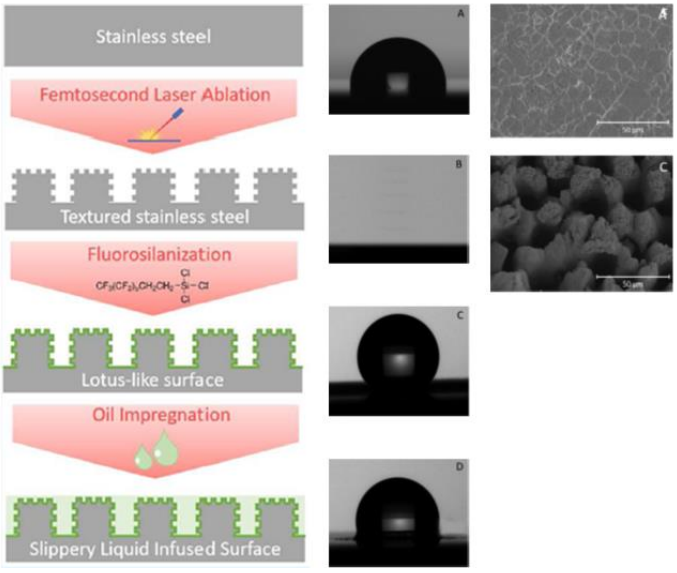

Figure 15. Elaboration of SLIPS-like surface with the wettability corresponding to each step of fabrication and the surface morphology of stainless steel before and after the laser ablation. [13] *Reprinted with permission from American Chemical*

IV. Anti-fouling and fouling-release surfaces

4.1. Anti-fouling or fouling-release surfaces?

In dairy fouling field, the distinction between anti-fouling and fouling-release surfaces is not always evident. According to Leonardi *et al.* [119] and Hu *et al.* [138], anti-fouling surfaces prevent the attachment of proteins, bacteria and microorganisms as displayed in Figure 16 a.[119], [138] Contrary to anti-fouling surfaces, fouling-release surfaces allow the ease removal of bacteria, proteins or microorganisms through hydrodynamic shear stress coming from mechanical cleaning or the ships' navigation in marine field (Figure 16 b). Based on these definitions, this section will distinguish anti-fouling surfaces from fouling-release surfaces conceived for dairy fouling mitigation.

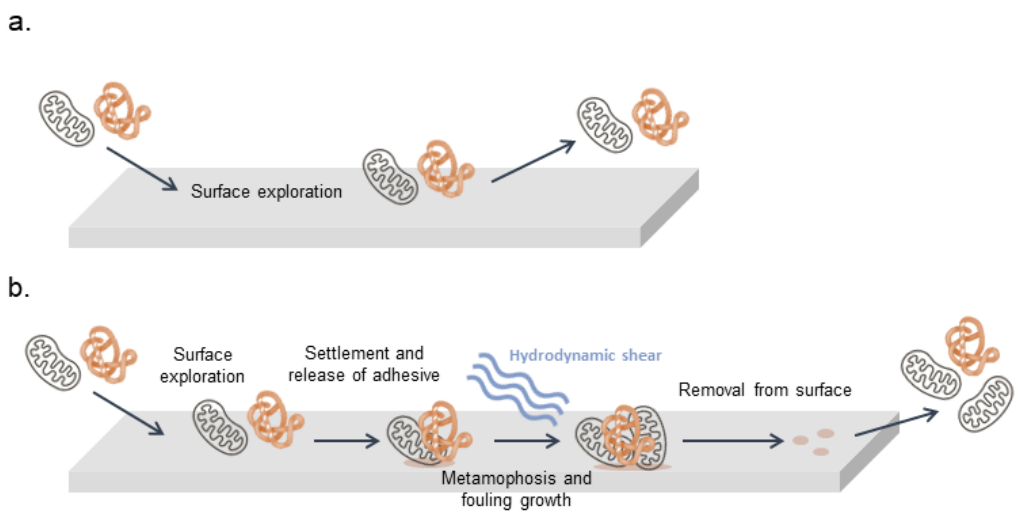

Figure 16. Schematic mechanisms of a. anti-fouling surfaces and b. fouling-release surfaces adapted from [119]

4.2. Anti-fouling surfaces

Banerjee *et al.* have reviewed the different ways for designing anti-fouling coatings preventing adsorption of proteins, bacteria and marine organisms. Various solutions are reported as displayed in Figure 17. Most of them have been extensively explored in biomedical and marine fields. Banerjee *et al.* [2] subdivided coatings preventing proteins adhesion in two categories: (i) resistant coating and (ii) degrading coating. Coatings resisting to protein adhesion gather tethered PEG (poly(ethylene glycol)), SAMs (Self-assembled monolayers) and zwitterions, while coatings degrading protein correspond to enzymes and self-cleaning surfaces.

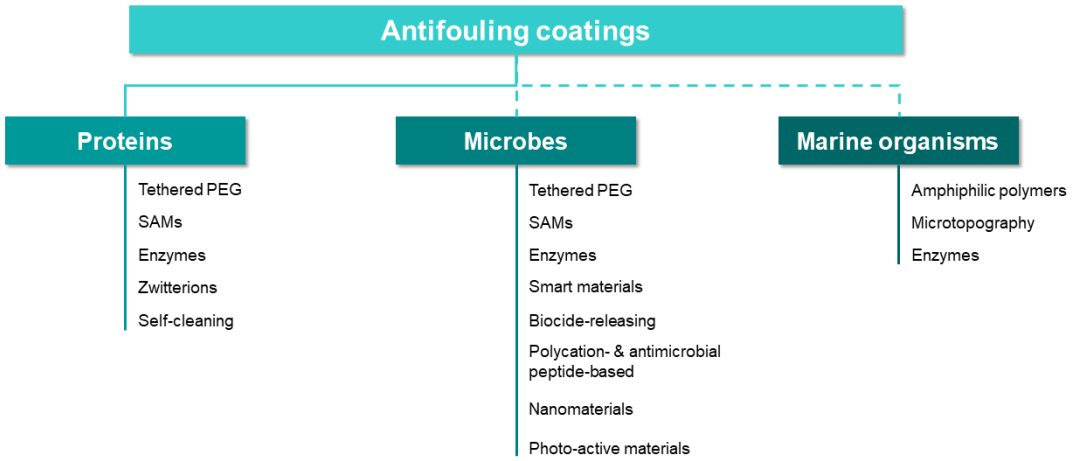

Figure 17. Ways of designing anti-fouling surfaces adapted from [2]

According to the literature, only one of these techniques has been used against β-Lg. Wei *et al.*[146] investigated stainless steel modified by a PEG layer aiming at hindering protein adsorption. Due to the poor adhesion of PEG onto stainless steel, the surface was first functionalized with amine groups. PEI (poly(ethylenimine)) was physisorbed onto stainless steel surface, allowing PEG grafting through amine groups. These PEG surfaces were then immersed in a β-Lg solution at room temperature for one hour. Wei *et al.* (2003) pointed out that the higher the concentration of PEI, the higher the grafted PEG amount. Surfaces were analysed before and after immersion by ToF-SIMS. As shown in Figure 18, no difference of intensity was observed for SS-PEI(30)-PEG before and after immersion. Hence β-Lg protein adsorption was prevented for the highest PEI concentration.

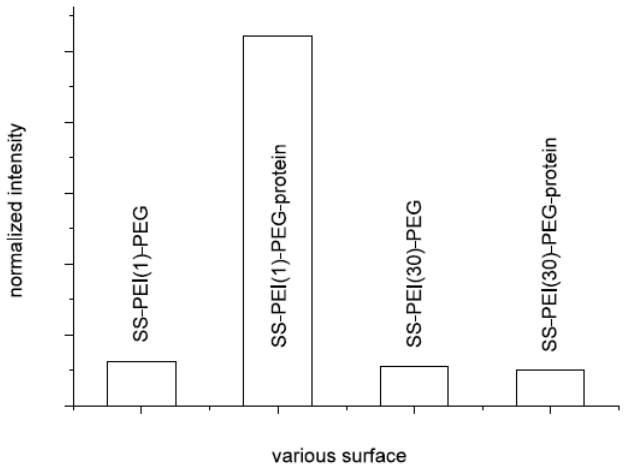

Figure 18. Anti-fouling performances of SS-PEI-PEG surfaces as a function of grafted PEG amount [146] *Reprinted with permission from Elsevier B. V.*

Albeit these results exhibit promising anti-fouling performance to reduce β-lactoglobulin protein adsorption, the adhesion tests were performed at room temperature, well below the denaturation temperature and under static mode. These conditions are not representative of a pasteurization cycle. Thus, it is intricate to conclude on the effectiveness of these PEG coatings for mitigating dairy fouling as well as on their advantages and drawbacks.

To date, other types of anti-fouling coatings were not assessed in the mitigation of dairy fouling. Although they proved their effectiveness in biomedical or marine field, they present drawbacks that could limit their action for preventing dairy deposits. Protein-resistant coatings based on SAMs with oligo(ethylene glycol) terminations display higher anti-fouling

performance than tethered PEG surfaces and are easy to fabricate but they are less robust due to the presence of defects.[147], [148] It could lead to a loss of anti-fouling performance at high flow rate. According to Leonardi *et al.*, [119] zwitterions are a promising alternative to PEG coatings in the marine sector; however, the elaboration of zwitterionic surfaces is troublesome. Monomers are often expensive, their dissolution in organic solvent remains complex and they are unstable during polymerisation reactions.[119], [149] Among coatings degrading proteins, enzyme-based surfaces seem unfavourable to mitigate dairy fouling. Enzymes are proteins with a catalytic activity. Thus, as whey proteins, enzymes are mostly thermosensitive. Indeed, when they are submitted to high temperature, they denature, leading to a loss of activity. Protein adhesion tests performed on enzyme-based surfaces are usually carried out between 30 and 40 °C.[150], [151] The last type of surface reported by Banerjee *et al.* [2] is photoactivated self-cleaning coating, where foulants are decomposed by ultraviolet or visible radiation.[2] TiO_2 particles are commonly used as photocatalyst for that purpose. Nonetheless, once again, transfer of photoactivated coating to dairy field is objectionable, knowing that TiO_2 is recognized for being potentially carcinogenic to humans. Hence the use of TiO_2 particles could cause health issues if they get entrapped in dairy products.[152]

4.3. Fouling-release surfaces

As previously noticed, based on Baier's relationship between the SFE and foulants' adhesion, research was widely focused on surface modification of stainless steel in order to reduce its SFE. Moreover, due to the weaker adhesion of foulants combined with hydrodynamic shear stress, fouling-release surfaces are easier to clean. Thus, in the literature, some works have investigated the cleanability of different materials and coatings. However, it is intricate to compare the cleaning effectiveness of coatings with each other. Indeed, as displayed in Annex 1 - Table 52 and in Annex 2 - Table 53, numerous cleaning conditions were used in both batch and continuous flow conditions. Some of them have chosen harsh conditions, close to those used in CIP procedures, and other have assessed fouling-release performances with water only.

A recent study has investigated the influence on the wetting behaviour of different concentrated cleaning solutions (NaOH) and water on the surface foulant as the function of the surface temperature. In food industries, CIP are now standard automated techniques, avoiding the dismantlement of processing equipment. The circulation of cleaning solutions aims at re-establishing the initial pressure and heat transfer performances and at countering microbial risks

contamination through surface disinfection. CIP procedures can be detailed in five steps: (i) pre-rinsing, (ii) detergent cycle, (iii), intermediate rinsing, (iv) sanitization and (v) final rinsing.[51] The second cleaning step "detergent cycle" can be completed in a single-stage process (with the use of acidic or alkaline solutions or detergents) or in a two-stages process.[153]

An example of a two-stages process has been detailed by Bylund as following [15]. First, processing equipment is pre-rinsed with hot water for about 10 minutes to remove excess, weakly adhering, fouling deposits from the surface. Then, heat exchanger surfaces undergo a chemical cleaning to release the fouling deposit with: (i) an alkaline solution (0.5-1.5 %) at 75 °C for 30 minutes removing organic foulants such as proteins, (ii) warm water for 5 minutes for rinsing out alkaline solution (NaOH), (iii) an acidic solution (HNO_3, H_3PO_4) (0.5-1 %) at 70 °C for 20 minutes to eliminate inorganic components such as mineral species. This is followed by a post-rinsing with cold water to remove all traces of fouling deposits and chemical cleaning (chlorinated agents) from the system, subsequent surface disinfection and a final water rinse.

Fouling-release surfaces can present real advantages concerning environmental and economic costs of cleaning in dairy thermal processing. Most of chemical solutions are not biodegradable, dairy wastewaters have to undergo several post-treatments and dairy thermal treatments processes are regularly shut down to be cleaned.

An investigation [154] pointed out that an optimal cleaning time could increase the cost-effectiveness of modified surfaces. Using modified stainless steel surfaces would allow the cleaning to be spaced from 24 to 100 days. This would reduce cleaning cost up to 35 %. To go further, in an LCA study, Zouaghi *et al.* [155] demonstrated that repeated CIP burdens the environmental footprint of the pasteurization process. They pointed out that surface modification leading to clean surfaces with water only (no need of detergents) reduces the environmental impact of the pasteurization process by more than 70%.

Zouaghi *et al.* [107], [113] presented works with drastic reduction of fouling after water rinsing only. Works having investigated the cleaning behaviour are gathered in Table 6 and are classified as a function of the cleaning conditions in three categories: (i) green cleaning, (ii) soft cleaning and (iii) harsh cleaning.

Table 6. Classification of cleaning conditions

Cleaning conditions		References
Green cleaning	Water	[86], [103], [111], [107], [113]
Soft cleaning	≤ 0.5 % NaOH solution and ≤ 0.5 % HNO_3 solution	[106], [156], [157], [120], [104], [10], [101]
Harsh cleaning	≥ 1 % NaOH solution and ≥ 0.5 % HNO_3 solution	[110], [88], [100], [111]

Overall, most of the studies having investigated the cleanability agreed that surfaces with low SFE and more precisely low polar component are easier to clean. Consequently, surfaces with low a polar component demonstrate good fouling-release properties. Nevertheless, it is clear that materials or coatings cleaned only with water are extremely promising. Therefore, we will focus on these surfaces.

Britten *et al.* [86] did not directly investigate the cleanability but they analysed the strength of adhesion of dairy deposit onto surfaces. They stated that the strength of adhesion is the key parameter determining the work of adhesion between the surface and the deposits such as proteins or minerals. The work of adhesion (W_A) is defined as the required energy to separate the liquid phase from the solid one and is related to the SFE of the solid (γ_{SV}) and liquid (γ_{LV}) and the interfacial tension between the liquid and the solid (γ_{SL}) as follows:[121]

$$W_A = \gamma_{SV} + \gamma_{LV} - \gamma_{SL} \quad (12)$$

Consequently, the lower the SFE, the weaker the adhesion between the surface and proteins and minerals, hence increasing the ease of removal. Here, the strength of adhesion was analysed using an ultrasonic bath in distilled water at room temperature for 300 seconds inducing shear stress. After that, bare stainless steel surface was still fouled whereas all coated surfaces were almost cleaned.[86] In that case, no conclusion can be drawn on the efficiency of water rinsing under shear stress. Indeed, the proportion of fouling deposit removal is not evaluated for stainless steel surface or coated surfaces. This could have been carried out by weighing surfaces before and after water rinsing. Hence, it is hard to conclude what is the most promising fouling-release coating among the polymer coatings tested.

In order to remove both loose and harder adsorbed fouling deposit, Rosmaninho *et al.* [103] analysed cleaning performances of 2R stainless steel and TiN surfaces in two stages. The first cleaning step was performed at the same flow velocity than the fouling experiment and the second one at higher flow velocity, both in water at 48 °C for 24 hours. The second cleaning stage was more effective. Nevertheless, despite that TiN surfaces were less fouled than 2R stainless steel surface, important fouling amount still remained on both surfaces.[103] Barish *et al.* [111] compared the cleanability of unmodified stainless steel surface and Ni-P-PTFE coated one through three cleaning conditions: (i) deionised water at same flow rate of fouling experiment, (ii) deionised water at higher flow rate and (iii) NaOH solution (1M) at higher flow rate. Although the increase of water flow rate led to a reduced fouling amount for both surfaces (13 % for stainless steel and 36 % for Ni-P-PTFE), alkaline cleaning led to a drastic drop of dairy deposit, reaching 78 % and 93 % for stainless steel and Ni-P-PTFE coating, respectively. As concluded by Rosmaninho *et al*. [103], water rinsing does not provide satisfying results; however, cleaning time and temperature were not indicated in this study.

Zouaghi *et al.* [107] have investigated commercial graphite-based composites revealing promising fouling-release performances. Two types of composites were tested to mitigate dairy fouling: XC samples corresponding to a combination of artificial graphite with pitch binder submitted to carbonisation and XTH samples corresponding to a combination of artificial graphite with PTFE binder. Both XC and XTH samples presented higher SFE than native stainless steel; however, both types exhibited much lower polar component, *i.e.*, 0.6 mN/m and 0 mN/m for XC and XTH, respectively. These surfaces underwent 1.5 hours of pasteurization followed by 20 minutes of water rising at 85 °C. Fouling amounts were assessed before and after water rinsing and the obtained results are depicted in Figure 19. On one hand, before water rinsing, both XC and XTH surfaces presented a fouling increase compared to native stainless steel. On the other hand, the water rinsing led to a fouling drop for both types of composite (less than 10 mg/cm² against 75 mg/cm² for native stainless steel). These results are very encouraging and, furthermore, their high thermal conductivity and lightness make graphite-based materials interesting candidates for replacing stainless steel. Nevertheless, this investigation did not indicate the durability of fouling-release properties of the graphite-based composite after several pasteurization runs.

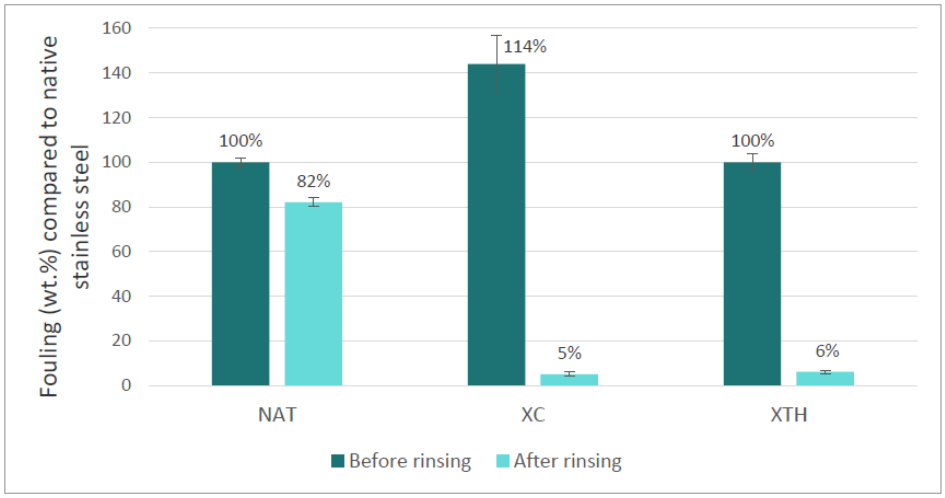

Figure 19. Fouling performances after fouling test and after rinsing [107]

Silicon-based coatings, developed by Zouaghi *et al.* [113], exihibited good fouling-release properties with water rinsing only. These coatings were deposited onto stainless steel using an atmospheric pressure plasma torch as described in section 3.2.2. Several coatings were obtained by varying the manufacturing parameters. After 1.5 hours of pasteurization, the coated surfaces were submitted to water rinsing at 85 °C for 20 minutes and demonstrated oustanding results with a fouling reduction ranging from 90 to 99 %. Nonetheless, after a second fouling run followed by water rinsing, some of the modified surfaces were more fouled than stainless steel surface and other displayed loss of their fouling-release character. On the other hand, a coating, corresponding to certain manufacturing parameters, presented good fouling-release properties, decreasing fouling up to 92 %. However, Zouaghi *et al.* [113] have demonstrated that the fouling-release properties of silicon-based surfaces are not due to the SFE, which is close to that of stainless steel, or to the polar component, which is higher than that of stainless steel, but can be explained by the formation of uneven nanoparticles providing nanorough surfaces as showed in Figure 20. Despite their low durability, which could be increased by optimizing plasma manufacturing parameters, these silicon-based coatings present interesting fouling-release properties, while their deposition process is quick compared to PECVD processes. The deposition of a coating on a stainless steel plate heat exchanger (530 mm × 180 mm) could take around 60 seconds at maximal scanning speed (300 mm/s).

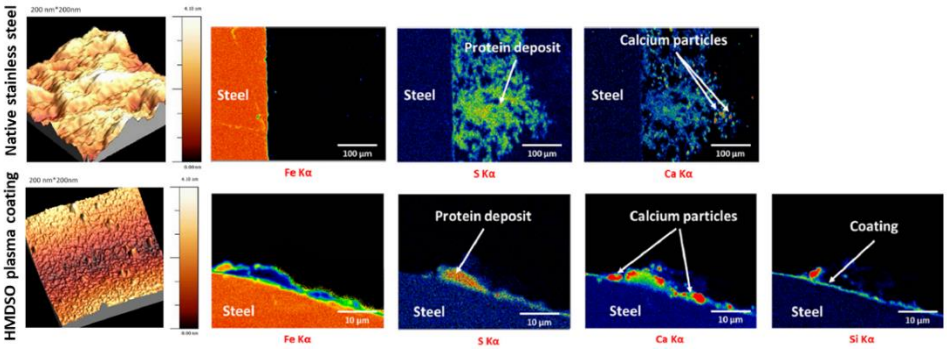

Figure 20. AFM pictures of native stainless steel surface and HMDSO plasma coating (left) and cross-section EPMA X-ray (Electron Probe Microanalysis) mappings demonstrating good fouling-release performances of HMDSO plasma coating (right). [113]

4.4. Anti-fouling and fouling-release surfaces

4.4.1. Amphiphilic surfaces

Amphiphilic surfaces were developed to obtain new materials being both anti-fouling and fouling-release. Hence, this type of surface includes hydrophobic and hydrophilic areas. By designing micro or nano- hydrophilic and hydrophobic regions, the surface becomes ambiguous, making biomolecules adhesion unfavourable.[158], [159] These amphiphilic surfaces have been mainly investigated against biofouling and proven efficient. Galli and Martinelli [160] reviewed different pathways to realize amphiphilic coatings. Furthermore, some studies reported by Mérian and Goddard [161] have demonstrated the ability of amphiphilic coatings to prevent the adsorption of a range of proteins. According to Mérian *et al.* (2012), the amphiphilic aspect is given either by hydrophobic and hydrophilic monomer parts in the copolymer or by amphiphilic end chains on the polymer backbone. Nonetheless, in most of these amphiphilic coatings, the hydrophobic part is composed of fluorinated groups such as perfluoroalkyl chains. These ones can degrade and form perfluroalkyl acids which have toxicological effects. Few examples of fluorine-free hydrophobic part in amphiphilic coatings have been published, replacing fluorine groups either by alkyl groups or polysiloxane networks like PDMS (Polydimethylsiloxane).[162]–[165] Anti-fouling and fouling-release properties in amphiphilic coatings were optimized following specific ratios of hydrophilic and hydrophobic moieties. Hawkins *et al.* [166], [167], Rufin *et al.* (2015; 2016) and Faÿ *et al.* [170] synthesized an amphiphilic molecule that is a PEG-siloxane with crosslinkable triethoxy end groups (Figure 21 a.), which was incorporated in an elastomeric matrix enhancing PEG resistance and stability (Figure 21 c.). Studies of PEG and siloxane chain length were carried out. Increasing siloxane tether length reduces the formation of biofilms by improving the mobility of PEG chains. This

is not the case for PEG chain length: shorter PEG units do not confer hydrophilic properties and longer PEG units present limited mobility in the matrix.

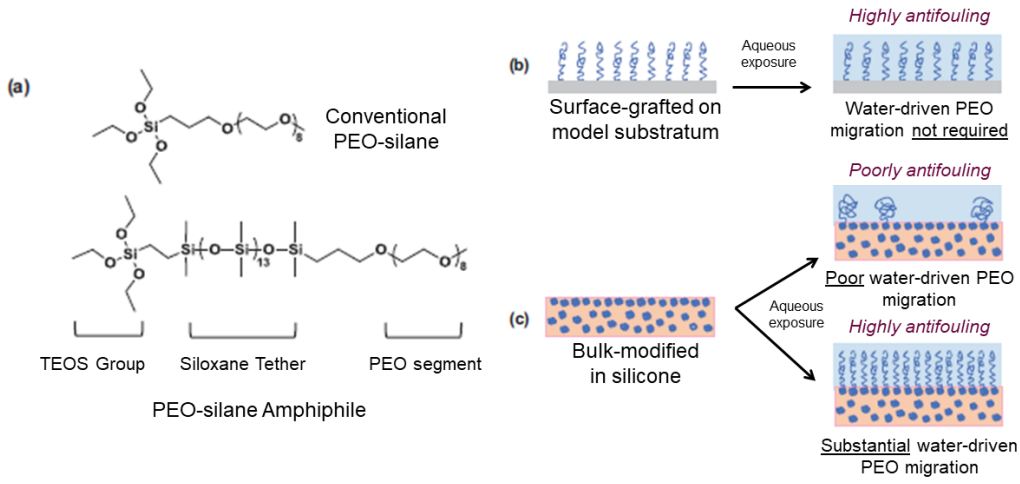

Figure 21. a) Conventional PEO-sliane and PEO-silane amphiphile developed by Hawkins et al., b) Behaviour of conventional PEO-silane when it is exposed to aqueous medium c) Behaviour of conventional PEO-silane in silicone matrix vs. PEO-silane Amphiphile in silicone matrix when it is exposed to aqueous medium[108] *Reprinted with permission from Taylor & Francis*

To date, only one group used an amphiphilic coating to reduce dairy deposits. Based on the development of amphiphilic coatings of Grunlan's team, Zouaghi *et al.* [108] used amphiphilic coating onto stainless steel samples and plate heat exchanger to perform isothermal and *in situ* fouling tests, respectively. They also assessed the adhesion of the amphiphilic coating using various techniques such as plasma activation, polydopamine coating and commercial primer (NuSil SP 120). The variation of WCA over time was assessed: as displayed in Figure 22, at t_0, the WCA for all surfaces stand between 105 and 115 °, demonstrating hydrophobic character. After 150 s, non-pre-treated surfaces and polydopamine and primer pre-treated surfaces exhibited a lower WCA value, around 30 °, indicating the migration of PEO (poly(ethylene oxide) segments at the interface.

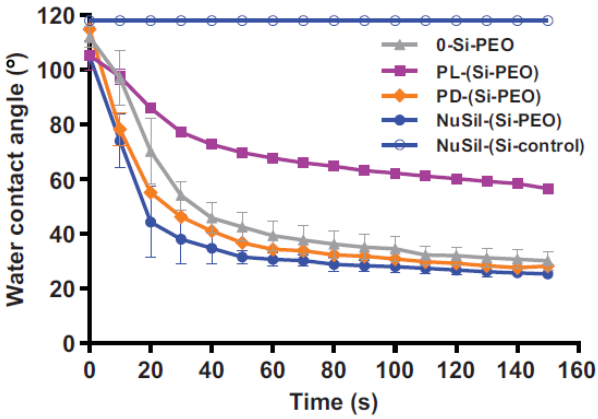

Figure 22. Variation of WCA over time of the different pre-treated Si-PEO surfaces: PL and PD corresponding to plasma and polydopamine, NuSil is a commercial primer.[108] *Reprinted with permission from Taylor & Francis*

These surfaces were tested against a whey protein and calcium solution under continuous flow conditions for 1.5 hours in the pilot plate heat exchanger. After a single pasteurization cycle, non-pre-treated surfaces were removed from sample holders without dairy deposits, contrary to native stainless steel surfaces, as shown in Figure 23 a. Promising results were obtained for primed Si-PEO surfaces. This type of surface remained unfouled even after five pasteurization cycles. Therefore, a stainless steel heat exchanger plate (plate number 8) was pre-treated with the commercial primer, coated with the Si-PEO amphiphile and tested *in situ* for 1.5 hours. No trace of dairy deposit was observed on the eighth plate, thus indicating that this amphiphilic coating has great anti-fouling properties and that PEO chains migrate at the interfaces even when the surface undergoes temperature changes (Figure 23 c).

Zouaghi *et al.* [108] have proven the efficiency of amphiphilic Si-PEO coating in the mitigation of dairy deposits. This type of coating seems to be promising for food industries and presents numerous advantages: PEO is food-compatible, and excellent anti-fouling properties are preserved after 7.5 hours of pasteurization and under temperature changes. Nonetheless, after five pasteurization cycles, the thickness of the Si-PEO surfaces decreased, showing erosion during the process. Moreover, the primer used, NuSil SP 120, is classified as Carcinogenic Mutagenic Reprotoxic (CMR), which could cause health issues. The effectiveness of the amphiphilic coating after CIP procedures was assessed after 7.5 hours of pasteurization (5 fouling runs). It can be observed in Figure 23 b that anti-fouling performance was negatively affected. Thus, further researches have to be carried out to improve resistance to shear stress.

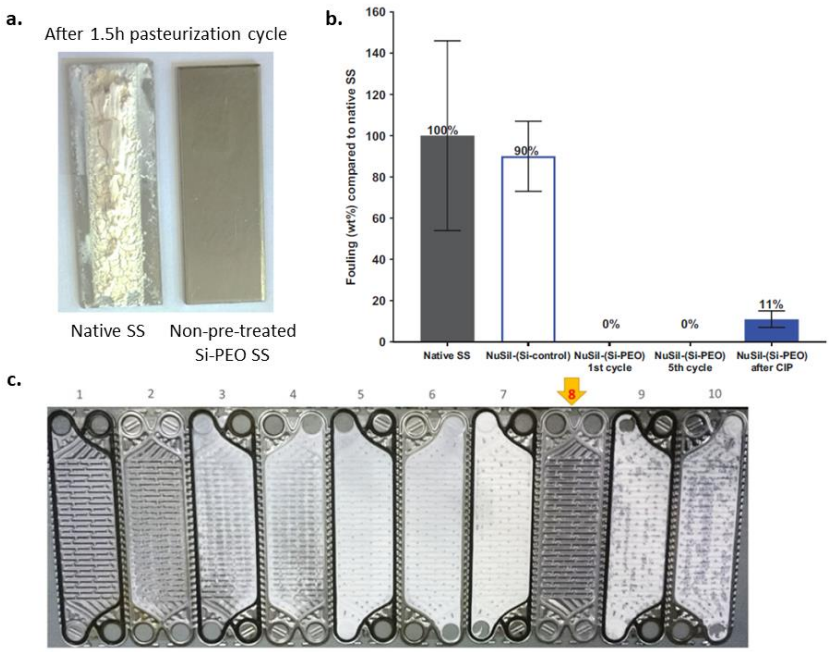

Figure 23. a) Fouling deposit onto native stainless steel and amphiphilic coating under isothermal conditions, b) anti-fouling of amphiphilic coating and c) Fouling deposit onto V7 plate heat exchanger under in situ conditions [108] *Reprinted with permission from Taylor & Francis*

4.4.2. Slippery liquid-infused porous surfaces

Few years ago, slippery liquid-infused porous surfaces (SLIPS) were developed by Aizenberg's group.[171], [172] These surfaces are bio-inspired by *Nepenthes* pitcher plants which have a slippery area allowing catching and trapping their food. Observations of insects placed on *Nepenthes* plants showed that the inner waxy pitcher wall is the most important zone to capture insects. This waxy area has anisotropic structures trapping insects from adhesive secretion.[173] This feature has attracted attention to design anti-fouling coatings. SLIPS consist in porous or nanostructured surfaces impregnated by low surface energy lubricants. The obtained surface is extremely smooth, homogeneous and slippery (Figure 24). Usually, SLIPS have low contact angle hysteresis (< 2 °) and low sliding angle. Thus, fluids and biological fouling cannot hold on the surface and slide off.

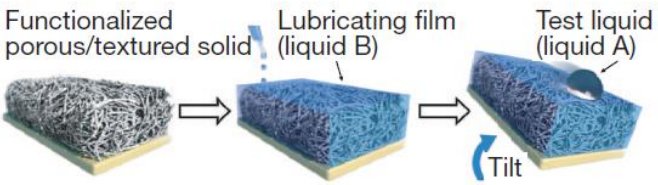

Figure 24. Fabrication of Slippery Liquid-Infused Porous Surface [171] *Reprinted with permission from Springer*

Nonetheless, designing such materials can be complex and several ways are reported in the literature to design such surfaces. The elaboration of SLIPS is based on three principles in order to obtain a smooth and stable liquid surface: (i) the lubricant must have a higher chemical affinity for the underlying support than for the surrounding medium, (ii) nano- or micro-structured substrate improves the lubricant immobilization and retention through Van der Waals and capillarity forces and (iii) the lubricant should be immiscible with the surrounding medium.[145]

In the literature, most papers deal with the design of SLIPS for antifouling applications against microorganisms and microalgae in the marine sector or against blood and bacteria in the medical sector. For instance, Epstein *et al.* [172] have proven that such slippery surfaces were more efficient than PEGylated surfaces by preventing biofilm adhesion up to 99 % under low flow conditions.

As for the amphiphilic coating, only one work has been done on the development of SLIPS against dairy fouling deposits. Recently, Zouaghi *et al.* [13] have fabricated SLIPS-like surfaces with good anti-fouling and encouraging fouling-release properties. SLIPS-like surfaces were elaborated in several steps that have been detailed in section 3.2.3. As in most studies, a perfluorinated oil was chosen as lubricant (DuPont Krytox GPL 103). CAH measurements confirmed the slippery feature of these SLIPS-like surfaces, giving a contact angle hysteresis of 0.6 ° and a sliding angle of 2 °. After 1.5 hours of pasteurization test at 85°C, SLIPS-like surfaces exhibited a fouling decrease up to 63 % and, as depicted in Figure 25 b, dairy deposit seems to be less adherent onto slippery surfaces than onto native stainless steel. Thus, these surfaces underwent another fouling run followed by a water rinsing, corresponding to “SLIPS-r” in Figure 25 a. The rinsed slippery surfaces were totally clean, demonstrating exceptional fouling-release properties.

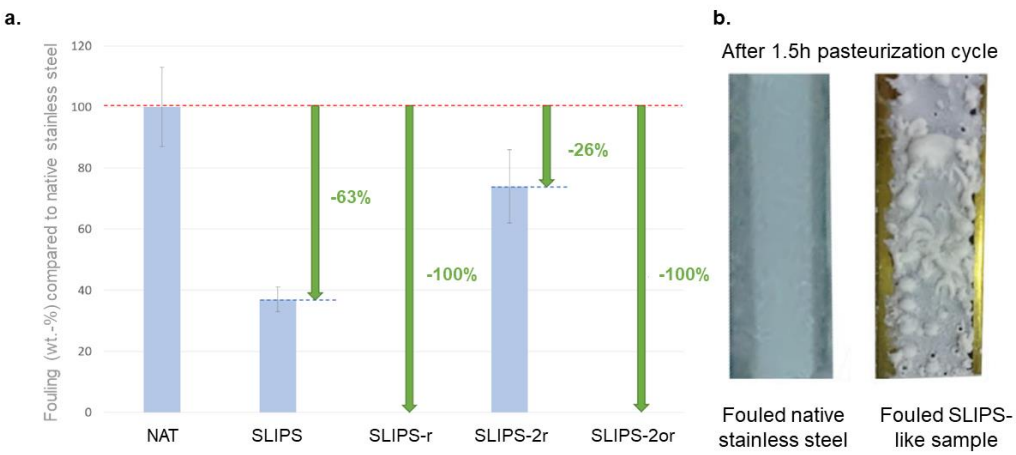

Figure 25. a) Anti-fouling and fouling-release performances of SLIPS-like surface, b) Physical aspect of dairy fouling onto SLIPS-like sample compared to that onto native stainless steel after 1.5h pasteurization [13] *Reprinted with permission from American Chemical Society*

These results are very promising and manifest a real potential to reduce dairy fooling due to both anti-fouling and fouling-release properties. Furthermore, SLIPS-like surfaces present environmental and economic advantages owing to a "greener" cleaning step, *i.e.*, requiring water only. However, as observed by other groups, Zouaghi *et al.* [13] noticed a lubricant loss during the run, leading to a loss of fouling-release performance. In order to improve lubricant retention, some authors recently proposed a solution using the PDMS layer, either as a vascularized substrate by creating channels in PDMS matrix, or grafted to the substrate. PDMS has also been used in brush or as a matrix to graft the lubricant. But these solutions were not assessed under high flow conditions.[174]–[177] Another drawback is the non-food grade of the fluorinated lubricant which should be replaced by pharmaceutical-grade oils, silicone oil or vegetable oils. Several works have been published on this latter type of oils, but not applied in the dairy fouling field.[178]–[181]

V. Discussion

Dairy fouling depends on several factors such as product characteristics, process parameters and surface properties. For this reason, in this chapter, studies in batch conditions have been separated from those in continuous flow to investigate the impact of surface properties. However, it appears that the comparison of the impact of surface properties remains intricate due to numerous process parameters, model fluids and cleaning conditions used in fouling tests whatever the process equipment used to evaluate the surface. Based on the knowledge of industrial habits and former studies, a standardization of model fluid for fouling tests, process

parameters, surface characterizations and cleaning conditions could make comparisons more meaningful. For instance, different techniques are proposed to systematically characterize coatings and/or materials. A classification of cleaning conditions is also proposed to evaluate the fouling-release behaviour of the tested coatings and/or materials in order to mitigate fouling deposition.

5.1. Model fluid and process parameters

As shown in Annex 1 - Table 52 and Annex 2 - Table 53, various types of fluid have been used: β-lactoglobulin in phosphate buffer solution, whey protein concentrate with or without calcium ($CaCl_2$), whey protein isolate with or without calcium (SMUF) and whole, raw, skim or pasteurised milk. For these fluids, not only the composition in proteins (whey only or mixture of casein/whey) and in mineral (mainly the type of calcium complex -Ca^{2+}, $CaHPO_4$, $Ca_3(PO_3)_2$, $CaCO_3$…- depending both on the presence of chelating agents such as phosphate ions and citrate and physico-chemical conditions such as pH and temperature in the dairy derivative) but also the content in carbohydrate (lactose) and lipids, are very different.

Consequently, depending on the fluid composition, the concentration balance of species (protein and /or mineral) in the bulk can be seriously affected and may significantly alter the fouling layer build-up.[26], [27], [182]

Ignoring the effect of carbohydrate and lipids on fouling which has been less investigated, currently, it is widely admitted that protein denaturation and salts precipitation of calcium element are the two major underlying mechanisms responsible for fouling, but the exact pathways by which proteins and calcium salts interact and feed the layer of deposit onto stainless steel surface are far from being wholly understood.

For whey protein isolate (WPI) solutions, when phosphate ions content is low, it seems that free ionic calcium content actively participates in the formation of the fouling layer but calcium carbonate [47] and calcium phosphate [26], [121], [182], [183] have also been mentioned when phosphate ions content increases.

For dairy derivatives which are mixtures of whey protein (WP) and casein (as the case of milk containing 80% casein and 20% WP), fouling mechanisms are less demystified. As explained by Liu *et al.* [27] the presence of casein micelles in milk makes more complex the possibilities of protein aggregation and salts precipitation as they constitute both a source of proteins (alpha, beta, kappa caseins) and of mineral elements through their calcium phosphate

nanoclusters which can also modify the calcium balance between colloidal and soluble phases. The understanding of mineral/protein interaction is better in whey, which could be considered as a simpler protein solution than milk due to the absence of casein micelles.

Consequently, depending on the fluid composition, interactions with surfaces could also differ for a given temperature as shown by Rosmaninho *et al.* (2008) and later by Blanpain-Avet *et al.* (2020) and Scudeller *et al.* (2021).

This tricky situation regarding the scientific understanding of fouling mechanism at the molecular level, and the fact that continuous flow equipment are not so usual for academic laboratories, explain why fouling and cleaning abilities of surface are often tested on a first approach. Then, if coating exhibits good anti-fouling or fouling-release performances, it could be tested against whole or skim milk.

To date, two studies have investigated the fouling deposit onto modified stainless steel or coatings using both whey protein solutions and milk. Patel *et al.* [95] performed tests in batch conditions using skim milk and WPI solution to foul 2B 316L stainless steel and DLC surfaces at pasteurization temperature. A lower fouling mass was observed with WPI solution DLC surfaces. Therefore, at pasteurization temperature, whey protein solution and milk can lead to fouling deposit with close composition, however, it seems that interactions between surfaces and fluids (milk or whey protein solutions) differ. This has been corroborated by Magens' work [12]. Raw milk and whey protein solution were used in continuous flow at pasteurization temperature, fouling 2R 304 stainless steel surface and FEP (Fluorinated ethylene propylene) coating. With WP solution, the calcium fraction is the same in fouling deposit onto SS surface (5.1 mg/g) and FEP coating (6.6 mg/g), but differs using milk. A higher calcium fraction is found into fouling onto SS surface, 92.3 mg/g, against 74.1 mg/g onto FEP coating. Thus, this demonstrates that more investigations should be carried out on both model fluids and milk to confirm the effectiveness of new coatings at mitigating fouling deposit.

Fouling behaviour was assessed through a large variety of apparatuses such as heating rod, rotating disk apparatus, flow cell, benchtop PHE or PHE. Hence, different process parameters such as: (i) bulk and surface temperatures in batch, (ii) inlet and outlet temperatures in continuous flow, (iii) hydrodynamic conditions have been used even in similar configurations.

Hydrodynamic conditions are characterized by flow regime or flow rate and the hydrodynamic regime is seldom reported. In dairy industries, the flow is turbulent to ensure a homogeneous thermal treatment, moreover, in turbulent regime, wall shear stresses increase,

inducing fouling removal.[43] Some authors have also proven that Reynolds number influences aggregate size and fouling deposit structure. de Guibert *et al.* [184] found larger aggregate in transient regimes than in laminar or turbulent regimes, corroborating works of Simmons *et al.* [185] and Wolz *et al.* [186]. Moreover, Guérin *et al.* [44] observed that the structure of fouling deposit appears denser from Re = 3200 in connection with smaller aggregates size. Nevertheless, it has been also demonstrated that heating temperature has a stronger impact on protein aggregation. Finally, although aggregate size depends on flow regime, this dependency decreases with raising temperature.[127], [184], [185] Since a large variety of apparatuses is used and as the equipment geometry affects flow regime, standardization of process parameters remains complex. Therefore, these parameters, and especially the flow regime, should be systematically notified.

5.2. Surface characterizations

By modifying stainless steel surface with a coating or using other types of materials, studies have demonstrated fouling reduction and/or fouling removal improvement. The investigations of the influence of SFE and R_a on dairy fouling behaviour in both batch and continuous flow conditions led to similar conclusions. Three trends can be identified from the analysis of the literature: i) initially, some authors agreed that SFE only impacts fouling deposit, ii) based on Baier's relationship,[114] an optimal SFE value may tend to mitigate whey protein adhesion, otherwise, Boxler *et al.* [105] suggested the existence of an optimal electron donor value, iii) finally, another group of authors stated that both SFE and R_a act on dairy fouling. However, for these three trends, no clear correlations have been established.

The lack of information regarding SFE, R_a or wettability makes the comparison difficult between coatings tested against dairy fouling behaviour. Globally, coatings and materials have been characterized by SFE and R_a but, in some works, one of these surface characterizations is missing. In addition, although SFE and R_a are related by wettability, few works have evaluated this latter parameter and none of them reported the potential impact of wettability on fouling or cleaning behaviours. In order to obtain as much information as possible about surface properties, systematic surface analyses should be carried out by providing at least SFE, R_a and wettability.

To go further, different models exists for SFE calculation, and there is no consensus on which one should be used when studying a certain matter, which makes the comparison between

results complicated. Among those presented in section 2.2, the OWRK model is the most used. But results can be slightly different between two models. Boxler [10] worked on SFE evaluation *via* two models, OWRK and van Oss, and pointed out very different results: lower polar part (γ^{AB}), higher dispersive component (γ^{LW}) as well as higher total energy (γ^{TOT}) in van Oss approach than in OWRK (γ^{P}, γ^{D} and γ^{TOT}).[10] Moreover, according to Hejda, Solař and Kousal [187], the selection of liquids used for contact angle measurements is more important in van Oss model than in OWRK. In order to corroborate or contradict Boxler's conclusions, SFE should be assessed by both van Oss and OWRK models.

Topography data are mostly measured by profilometer or atomic force microscopy (AFM), and are usually given through one value, which is the arithmetic mean R_a. In food industries, surfaces should present $R_a < 0.8$ µm.[20] Nevertheless, works exhibit the effectiveness of smoother coatings for mitigating dairy fouling and cleaning, ranging from 0.02 to 0.5 µm.[94], [109], [112], [113] But AFM probes relatively small areas. Besides AFM, R_a should be assessed by dynamic contact angle measurements given by CAH, which depends on R_a and surface heterogeneity. Barish *et al.* [111] confirmed AFM analyses with CAH measurements, exhibiting that low R_a leads to a low CAH due to a more homogeneous surface. This has been corroborated by Zouaghi *et al.* [13]. It seems that the lower the CAH, the higher the fouling reduction; however, no correlation has been established yet. Hence, it could be interesting to systematically assess the dynamic contact angle as well.

To date, only one study has considered another surface property: surface charges. Nevertheless, the results on surface charges impact on fouling behaviour remain unclear. Indeed, when electrostatic interactions are not neglected,[12] the impact of measured surface charges of stainless steel and DLC coatings on fouling behaviour are not established.[10].

The adhesion of coatings onto stainless steel is a great issue, which is barely reported. Zouaghi *et al.* [108] have assessed the adhesion of amphiphilic coating onto 316L stainless steel surfaces using several techniques: (i) plasma activation, (ii) polydopamine coating and (iii) commercial primer (NuSil SP 120). The durability of the coating as a function of the adhesion technique was consistent with adhesion cross hatch test. Coating adhesion to stainless steel surfaces should be characterized in order to assess the potential durability of the coating.

5.3. Cleaning conditions

As previously defined, fouling-release surfaces facilitate fouling removal through shear stress from cleaning. Consequently, fouling-release properties of materials or coatings are assessed through the cleaning step. Nevertheless, as mentioned in section 4.3, numerous cleaning conditions have been used, thus making the comparison between surfaces complex. Indeed, some studies have only used a mechanical cleaning with water and others have combined both mechanical and chemical cleaning. Zouaghi *et al.* [13], [107], [113] demonstrated that water rinsing was sufficient in certain cases to drastically remove fouling deposit. Barish *et al.* [111] also observed a fouling reduction after water rinsing and pointed out a greater mass of fouling removed with a flow rate increase. On the other hand, they emphasized better fouling-release performance using alkaline cleaning. Moreover, and as for fouling tests, it is important to note that in most of studies, cleaning or rinsing conditions are not always detailed. For instance, in Barish's work, temperature of water and duration of cleaning are not specified, although these are two important factors. Investigations have demonstrated that the cleaning rate increases with temperature.[51], [188], [189] Timperley *et al.* [189] showed a decrease in cleaning time up to 60 % when the cleaning solution temperature rised from 60 to 90 °C and up to 40 % when the temperature cleaning was comprised between 60 and 75 °C.

Standardization of cleaning step with specific conditions could allow classifying surfaces as a function of their cleanability, revealing their fouling-release performance. In the same way that anti-fouling performances are probed, the cleanability could be evaluated by weighing the fouling deposit remaining onto surfaces. Other methods (heat transfer measurements, pressure drop, conductivity, pH) allowing to follow the cleaning step have been reviewed by [190]

Surfaces could be divided into four groups as displayed in Figure 26. The first group corresponds to anti-fouling surfaces, thus no or less frequent cleaning should be needed. The second category is called fouling-release Type 1, and only mechanical cleaning using water as cleaning solution is required. Temperature and time ranges are based on works of Hankinson and Carver [188] and Zouaghi *et al.*[13], [107], [113], [188]. Fouling-release Type 2 corresponds to mechanical and chemical cleaning with alkaline and acid solutions less concentrated than in CIP procedures. On the contrary, fouling-release Type 3 corresponds to harder cleaning conditions. For both Type 2 and Type 3, temperature and time are based on CIP procedures detailed by Bylund [15].

Among these different types of cleaning, it is more difficult to select the flow rate range as various types of fouling test exist. Consequently, a low flow rate corresponds to the same flow rate used for fouling test. High flow rate is two times higher than low flow rate, a distinction based on Barish *et al.* [111], Rosmaninho *et al.* [103] and Beuf *et al.* [106]' works. This proposed classification is build-up from works having investigated the cleanability of coatings and materials and CIP procedures. Hence, conditions can be modified with further tests. It could be also interesting to assess surface properties after a significant number of fouling and cleaning cycles to evaluate coating ageing, it is known that alkaline solution can degrade silica-based coatings.

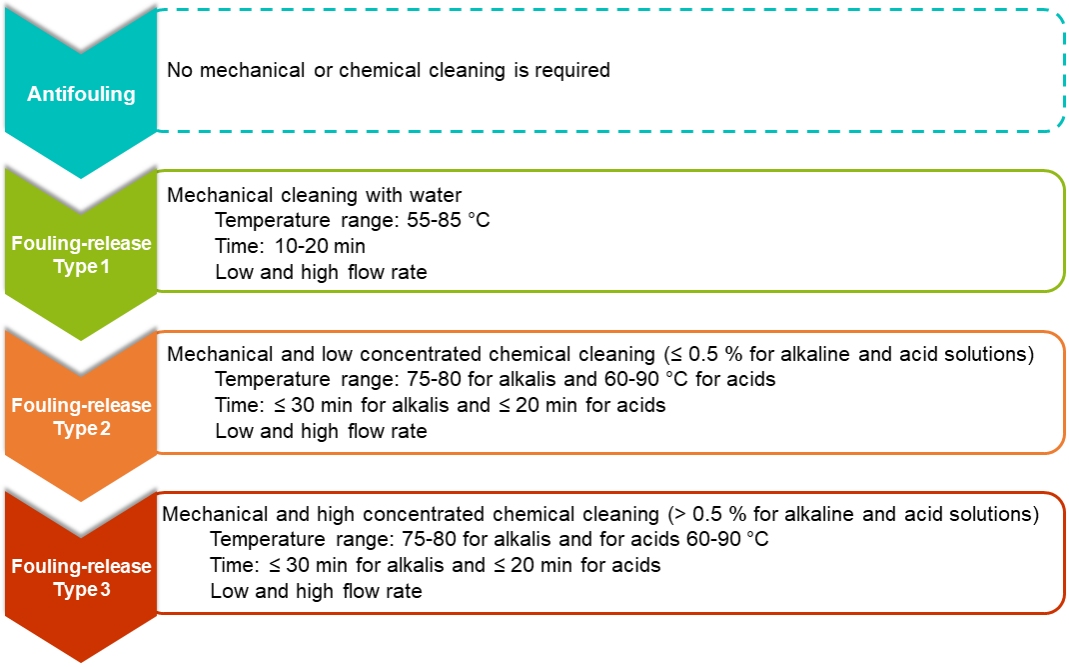

Figure 26. Cleaning conditions assessing fouling-release performances

VI. Conclusion

The aim of this chapter was to investigate the impact of surface modifications on fouling and cleaning behaviours.

Generally, the comparison of the impact of surface modification on fouling behaviour remains complex due to several points. To begin with, fouling tests are led either in batch or in continuous flow conditions. For both conditions, different model fluids and process parameters are used but not always reported, leading to an intricate interpretation of the real effect of the studied coating. Moreover, surface analyses such as surface free energy, roughness or

wettability are not systematically carried out, leading to the non-complete understanding of the coating effects.

It seems in both batch and continuous flow, a similar conclusion stands out: either surface free energy or the combination of surface free energy and roughness reduce final fouling amount or facilitate fouling removal. However, no clear correlation has been yet established. Other molecular interactions as the repulsive electric double layer could be taken into account.

Some fouling-release coatings seem promising as they can be cleaned using water rinsing only. Therefore, several surface modifications will be used to design efficient fouling-release surfaces as they could offer real advantages regarding the environmental and economic cleaning costs in dairy thermal processing.

CHAPTER 2 – PASTEURIZATION PROCESS: METHODOLOGY TO ASSESS ANTI-FOULING OR FOULING-RELEASE PROPERTIES

I. Introduction

The Chapter 1 demonstrated that assessing anti-fouling and/or fouling-release properties of modified stainless steel surfaces is not normalized, and highly dependent of application sector. Numerous fouling tests exist at laboratory, semi-industrial or industrial scale, thus the comparison between investigations remains complex.

In this chapter, the procedure of model fluid preparation, the pilot pasteurization system and process parameters are described. Repeatability issues met in this study are also discussed in the last part. These issues allowed to propose solutions in order that the results repeatability could be increased, facilitating the identification anti-fouling or fouling properties of modified stainless steel surfaces.

Before being tested, stainless steel surfaces are cleaned, modified and characterized as illustrated in Figure 27. Surface preparation characterizations are detailed in Materials and Methods section. Surface modifications are presented in Chapter 3 and Chapter 4.

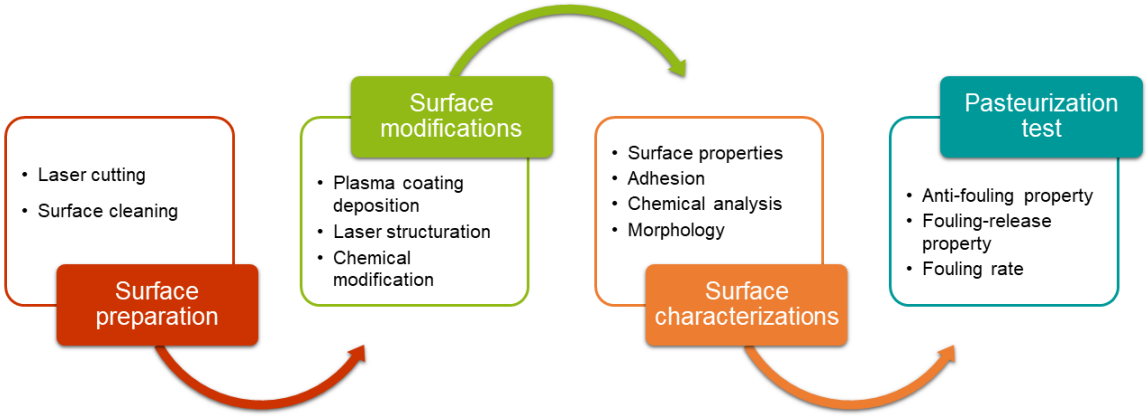

Figure 27. Schematic procedure of the study: from surface elaboration to the application in the pilot pasteurization rig.

II. Model fluid

Milk being a complex biological fluid, its composition can vary as a function of seasons and of its source. This is why its use for fouling tests could lead to high deviations for experimental results. Moreover, the standardization of milk and storage of high quantity of fresh milk remains complex and require considerable amount of analysis and control loop which are not possible to acquire at academic scale. Therefore, as reported in Chapter 1, most of studies use model fluid instead of milk to investigate anti-fouling or fouling-release properties of modified stainless steel surfaces.

As β-Lg and calcium are the main components of dairy fouling deposits, whey protein concentrate (WPC) powder (Promilk 852 FB1, 80% protein in dry state, Ingredia, France) and $CaCl_2$ (Sigma Aldrich) were used for the preparation of the model fluid.

The model fluid is a 1 % of WPC solution and calcium concentration is adjusted to 100 ppm by adding $CaCl_2$. The calcium concentration has been chosen to avoid overpressure or blockage in the PHEs while extending the runs duration as far as possible.[191] 325 L of model fluid were prepared for each fouling run, WPC and $CaCl_2$ were first rehydrated and dissolved under stirring separately in reverse osmosis water for 1 hour and half and then mixed together for 30 min. Model fluid preparation was done at room temperature.

III. Pasteurization process

Fouling tests were performed using a pilot pasteurization system (Figure 28), resulting from the downscaling of an industrial process (~1/10). It is composed of a stirred tank, a volumetric pump (PCM, France) and two plate heat-exchangers (V7 models from Alfa-Laval-Vicarb, France) in a counter-current configuration. PHE 1 is composed of 10 passes, one channel by pass, and pre-heats the treated fluid from room temperature to 60°C. PHE 2 is composed of 5 passes, one channel by pass and heats the model fluid to 85°C, which is a commonly used temperature in classical pasteurization schedule. For both PHEs, the equivalent space between two consecutive plates is 3.93 mm.

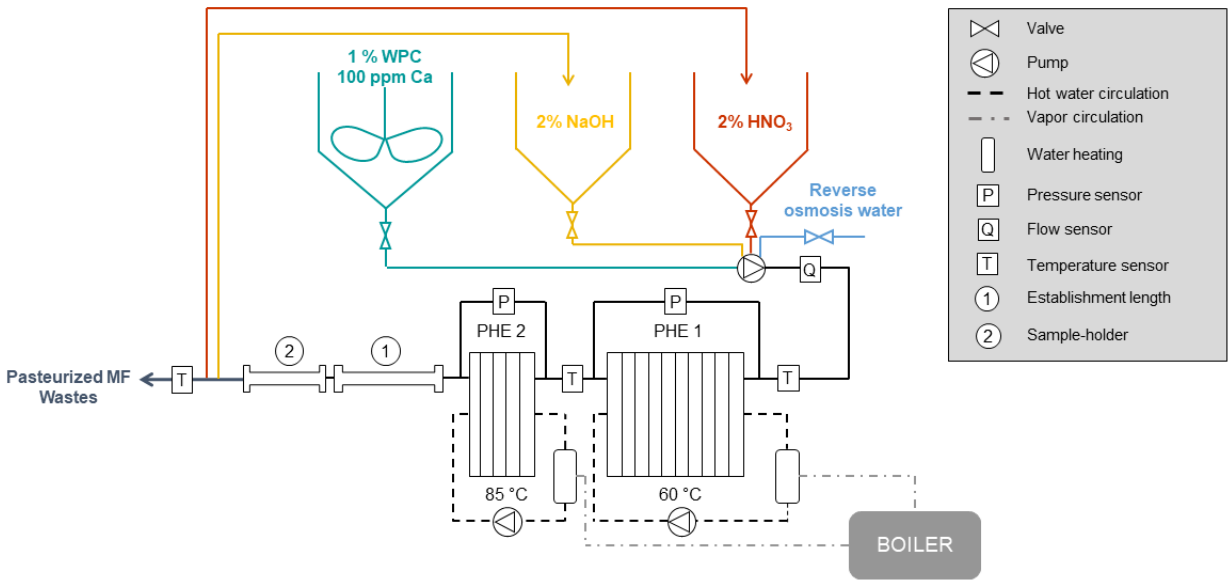

Figure 28. Synoptic of the pasteurization pilot plant

Reference and modified stainless steel coupons were placed in a sample-holder, *i.e.* square pipe of 150 mm² section. In order to stabilize the product flow in the sample-holder, an establishment length (500 mm length) is connected between the heating section and the sample-holders. Consequently, samples were not heated and thus the studied deposits resulted from isothermal fouling. The temperature probe placed at the outlet of the sample-holder showed a variation of 1°C from its target value of 85°C. The samples were thus submitted to fouling conditions comparable to the holding section of a classic pasteurizer. Similar pasteurization loop has been used in other studies.[7], [11], [26], [182]

For all experiments, hot water and model fluid flow rates were set at 900 and 300 L/h respectively. As the sample-holder presents a square section as displayed in Figure 29, the Reynolds number was calculated following the equation:

$$Re = \frac{v \,.\, Dh \,.\, \rho}{\mu} \quad (13)$$

with v (m/s), Dh (m), ρ (kg/m^3) and μ (Pa/s) corresponding to the fluid velocity, hydraulic diameter, density and dynamic viscosity of the fouling solutions respectively. Density and dynamic viscosity of the fouling solutions were approximated at water properties. Dh (m) is equal to 4.S/Pm where S is the cross section area of the duct and Pm the wet perimeter of the duct. Thus, inside the sample-holder the Reynolds number was 19350, corresponding to a turbulent regime. In the PHE, the Reynolds number was lower, 3230, but corresponded to a turbulent regime as well. Indeed, Leuliet established for the corrugated V7 plates used in this work that the turbulence regime occurs over Re = 260.

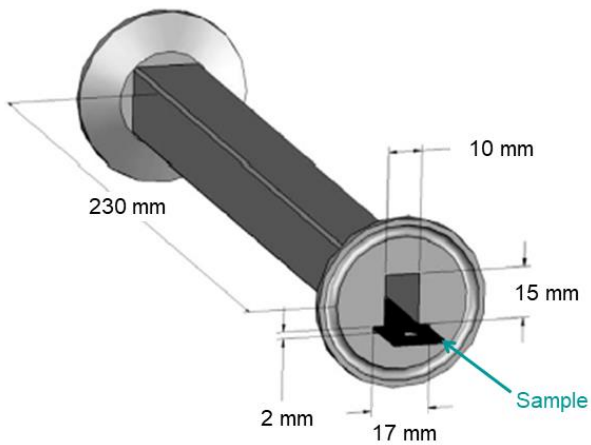

Figure 29. Characteristics of a sample-holder[192]

The pilot plant was started and brought to steady-state conditions with circulation of reverse osmosis water to reach 85 ± 1°C in the sample-holders. Once steady-state was reached, the circulation of reverse osmosis water was switched to allow the model fluid to foul the samples. Depending on the WPC batch, fouling experiment was run for 60 to 90 min. Samples were then either taken out of the samples-holders to assess anti-fouling property or left in the samples-holders to undergo a 20 min-water rinsing at 85°C assessing fouling-release property. Anti-fouling and fouling-release properties were quantified by weighing samples and comparing modified stainless steel surfaces to bare stainless steel surfaces following equation 14 leading to the fouling rate (F%):

$$F\% = \frac{m_{Fouling\ Sample} - m_{Fouling\ Ref}}{m_{Fouling\ Ref}} \times 100 \quad (14)$$

with, $m_{Fouling\ Sample}$, fouling mass on modified stainless steel and $m_{Fouling\ Ref}$, fouling mass on bare stainless steel, both in mg.

Fouling deposit was dried in a cold room at 4°C before weighing. The drying time of fouling deposit was estimated using two batches of 8 bare stainless steel samples. As shown in Figure 30, fouling mass dropped after the first day in cold room and remained stable after the fifth day. Thus, fouling rate was calculated five days after a pasteurization run.

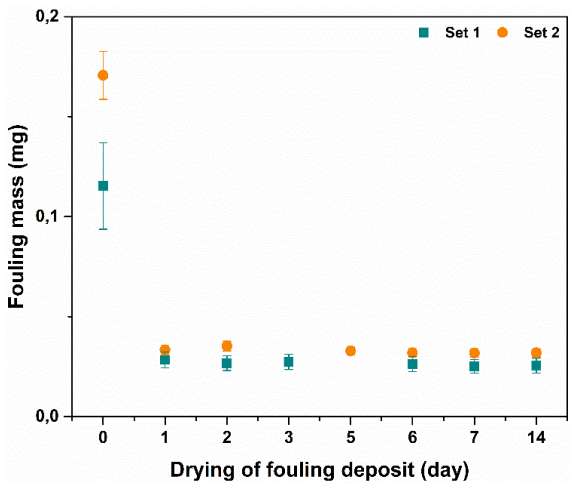

Figure 30. Assessment of the drying time of fouling deposit in the cold room

The pasteurization plant was finally cleaned following cleaning-in-place (CIP) procedures. First a 20 min-water pre-rinsing at 85°C was performed to remove excess, weakly adhering fouling deposits from the surface. Then a chemical cleaning was circulated: (i) a 2 % (w./v.) NaOH solution at 80°C for 20 min to remove organic species and mainly proteins, (ii) warm water (80°C) for 5 minutes for rinsing out NaOH solution, (iii) a 2 % (v./v.) HNO_3 at 75°C for

20 min to eliminate mineral species. Finally, a post-rinsing with water at room temperature was performed for 5 min to remove all traces of chemical cleaning.

The cleaning solutions were circulated at the same flow rate than the model fluid (300 L/h) and NaOH and HNO_3 solutions were recirculated. Fresh alkaline and acidic solutions were prepared every third CIP cycles.

IV. Repeatability issues and validation of the pasteurization test

Repeatability issues were observed using the pilot pasteurization system during this PhD thesis. The potential causes of these issues which are (i) Whey Protein Concentrate powder batch and lack of knowledge of the full history (from collect till spray drying), (ii) calcium chloride addition and (iii) the tricky assessment of anti-fouling and fouling-release properties, are detailed in this part and solutions are proposed to maximize results repeatability.

4.1. Variability of surface density fouling deposit within several Whey Protein Concentrate powder batches: Influence of WPC powder composition

Several whey protein concentrate powder batches have been used for fouling experiments. Preliminary tests were performed with bare stainless steel surfaces only in order to assess the fouling behaviour and validate the WPC powder batch. Fouling behaviour was evaluated through wet and dry surface density of fouling deposit (in mg/cm²) by weighing the samples. Four batches were tested: (i) 150847, (ii) 201401, (iii) 191092 and (iv) U20454 and the results shown in Figure 31 were obtained from two pasteurization tests performed on different days. Tests carried out with batches 191092 and U20454 were run for 60 min due to the pressure drop increase in the PHEs. For the batches 150847, 191092 and U20454 wet surface densities are between 40.5 and 95.6 mg/cm² which is consistent with previous investigations performed on the same pilot plant (between 30.8 and 92.0 mg/cm²). However, wet surface density for batch 201410 is much lower, 17.1 mg/cm². Although this batch was not retained for pasteurization tests, powders were analyzed to understand why bare stainless steel surfaces were not fouled enough with this batch.

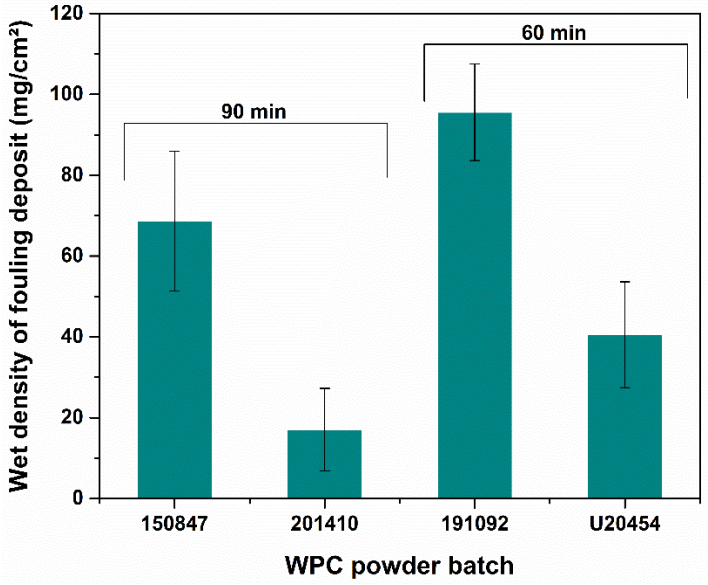

Figure 31. Comparison of WPC powder batches as the function of the density of fouling deposit

4.1.1. Calcium and β-Lactoglobulin contents

Calcium and β-Lactoglobulin contents of each WPC powder were thus analyzed through atomic absorption spectrometry and HPLC respectively (Table 7). According to the literature, free calcium (Ca^{2+}) promotes denaturation, aggregation and fouling mass deposit. Petit *et al.* pointed out that the kinetic rate of β-Lg denaturation increases with Ca concentration is more important in the aggregation-limited range (above 80°C), meaning that effect of Ca is more important in β-Lg bridging than in unfolding step.[45] From 80°C, β-Lg molecules are quickly unfolded and as solution pH is higher than the isoelectric point of β-Lg, the molecules are negatively charged. Therefore, Ca^{2+} can be complexed interact with carboxylic groups of β-Lg, stabilizing protein aggregates and leading to the growth of fouling deposit. Moreover, Khaldi *et al.* highlighted that the mass of fouling deposit is governed by the Ca/β-Lg molar ratio up to a ratio close to about 11.[183]

Taking into account experiences carried out for 90 min, wet surface density of fouling deposit increased indeed with Ca/β-Lg molar ratio. Same trend was observed for fouling tests performed for 60 min. However, lower surface density was obtained for batch 201410 than for batch U20454, although Ca/β-Lg molar ratio was higher, thus this result is not completely consistent with that of Khaldi *et al.*[183], made on a unique batch.

These analyses reveal that Ca/β-Lg molar are known fully satisfactory to guarantee identical properties of model fluid from powder reconstitution. It is likely that other factors coming from collect and process routes may affect fouling abilities.

Table 7. β-Lactoglobulin and calcium contents of the different WPC powder batches

Batch	β-Lg solution (g/L)	WPC powder calcium concentration (ppm)	Total calcium content in solution (ppm)	Calcium/ β-Lg molar ratio	Surface density of fouling (mg/cm²)
150847[a]	5.45	38.6	100	8.38	68.62 ± 17.29
201410[a]	6.01	47.2	100	7.6	17.05 ± 10.20
191092[b]	6	39.9	100	7.61	95.59 ± 11.98
U20454[b]	6.39	38.2	100	7.15	40.52 ± 13.09

a: pasteurization test running for 90 min, b: for 60 min

4.1.2. Phosphate content

In milk, minerals composition can be divided into two: (i) diffusible fraction and (ii) non diffusible fraction which represents ions bound to casein micelles. Potassium, sodium and chloride ions belong to the diffusible fraction although calcium, magnesium and inorganic phosphate belong to both diffusible and non-diffusible fractions.[193]

Ions contained in the diffusible fraction are not completely "free": based on affinity or solubility of salts, associations between cations and anions occur. Holt *et al.* proposed a calculation for ions association in the diffusible fraction.[194], [195] Regarding calcium, it exists as "free" ion, Ca^{2+} (2.00 mM) and as stable complex with Cit^{3-} (Citrate) (6.96 mM), with inorganic phosphate $H_2PO_4^-$ (0.07 mM) and HPO_4^{2-} (0.59 mM) and with Cl^- (0.26 mM).
According to Table 7, although, the total calcium content in solution was adjusted to 100 ppm, the initial calcium concentration was indeed higher for batch 201410. Therefore, a lower amount of $CaCl_2$ was thus added to the solution, leading to potentially less free ion Ca^{2+} available to act on β-Lg aggregation. Indeed, recently Blanpain-Avet *et al.* and Scudeller *et al.* highlighted the effect of phosphate ions on fouling deposit and mechanisms of whey protein solutions.[26], [182] Blanpain-Avet et al. demonstrated that the fouling deposit mass decreases with the addition of phosphate ions to whey protein solution. This was corroborated by Scudeller *et al.* but for a phosphate concentration higher than 20 mg/L. At pH closed to 7, phosphate ions exist under two forms ($H_2PO_4^-$ and HPO_4^{2-}) and according to Blanpain-Avet *et al.*[26], these ions act as a calcium chelating agent by binding one calcium ion per phosphate ion following these reactions[196]:

$$Ca^{2+} + HPO_4^{2-} \leftrightarrow CaHPO_4 \downarrow \quad (15)$$

$$Ca^{2+} + H_2PO_4^{2-} \leftrightarrow CaHPO_4 \downarrow + H^+ \quad (16)$$

Content of phosphate ions of the different WPC batches were not analyzed. However, a higher phosphate ions concentration in batch 201410 could explain the low surface density of fouling obtained for some batch, by chelating free calcium ions.

4.1.3. Casein content

Another way to explain the difference in density of fouling deposit of batch 201410 with other batches is the casein content. Liu *et al.* have demonstrated that Casein/WPI ratio impacts the fouling deposit mass.[27] The fouling mass drops until a minimum value as Casein/WPI increases to 0.2 and above this critical value, fouling mass increases with Casein/WPI ratio, as illustrated in Figure 32.

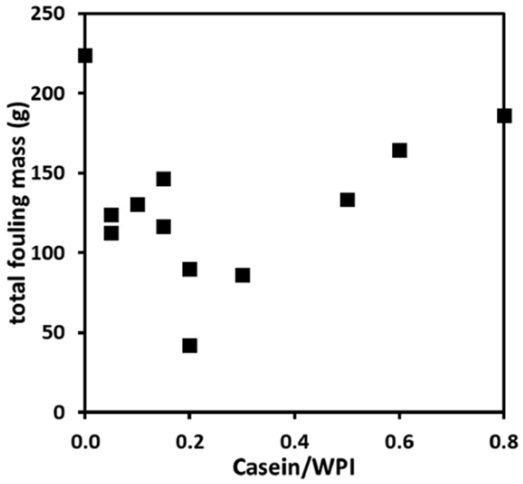

Figure 32. Relationship between Casein/WPI ratio and total fouling mass in PHE[27]

Therefore, WPI and Casein contents were analyzed by Ingredia (Kjeldahl method) and the results are gathered in Table 8. As batch 191092 was completely used before this analysis was set up, casein content has not been measured. Therefore, whatever pasteurization time, the surface density of fouling deposit drops from 40.5 to 17.1 mg/cm² for a Casein/WPI ratio of 0.16, thus close to 0.2 and then increases with Casein/WPI ratio. It seems consistent with Liu's study albeit surface density of fouling deposit was analyzed from samples placed in sample-holders and not directly in PHE.

Table 8. WPI and Casein contents in WPC powder batches

Batch	WPI (% wt)	Casein (% wt)	Casein/WPI ratio	Surface density of fouling (mg/cm²)
150847[a]	79.81	20.19	0.25	68.62 ± 17.29
201410[a]	86.25	13.75	0.16	17.05 ± 10.20
191092[b]	N/D	N/D	N/D	95.59 ± 11.98
U20454[b]	96.4	3.6	0.037	40.52 ± 13.09

a: pasteurization test running for 90 min, b: for 60 min

In this study which happens in a long period of time (more than 3 years), four WPC powder batches were used to prepare the model fluid in order to foul samples. Nevertheless, resulting surface densities of fouling highly differed between the four WPC batches and analyses of β-Lg, calcium contents did not allow to completely explain these differences. We propose that analysis of casein and phosphate contents could be performed in a more systematic way, as well as β-Lg, and calcium contents, to secure the foulant ability of WPC powder batch.

4.2. Variability of surface density fouling deposit within one Whey Protein Concentrate powder batch: Influence of $CaCl_2$ hygroscopic state during aging and of pressure drop in PHE

As observed in the previous section, bare stainless steel surfaces can be more or less fouled depending on the WPC powder batch used. Moreover, it can be noticed that standard deviations are not negligible regarding one WPC powder batch. As mentioned earlier, calcium chloride was added to the model fluid to adjust the total calcium concentration. Several investigations emphasized the increase of fouling mass with calcium content. Khaldi *et al.* observed a three-time higher fouling mass with a calcium content difference of 16.5 mg/L only.[191]

Calcium chloride is highly hygroscopic thus, it could be possible that weighed $CaCl_2$ contained in fact water and that water content increased with time. Consequently, the model fluid could be potentially less concentrated in Ca^{2+}. This could explain the results obtained in Figure 33, where wet surface density of fouling deposit decreased with time using the same $CaCl_2$ batch. Therefore, a new $CaCl_2$ batch was used and placed in oven at 105°C in order to store it at a controlled temperature. Although, at 105°C $CaCl_2$ is not totally dried, the storage in oven leaded to repeatable results compared to those obtained with the use of $CaCl_2$ batch 2 stored at room temperature. Nevertheless, higher standard deviations were noticed with the new calcium chloride batch, which was maybe more sensitive to the relative humidity.

Increasing the storage temperature could allow to confirm that water content in $CaCl_2$ actually decreases Ca^{2+} concentration in the model fluid and impacts fouling mass. On the other hand, according to Karunadasa, the dehydration of $CaCl_2$ leads to structural rearrangements[197], which could act on fouling mechanism or amount.

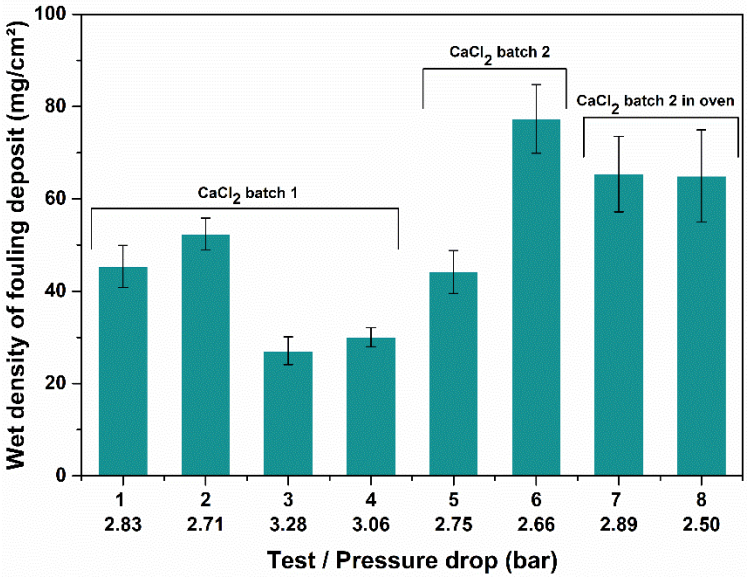

Figure 33. Influence of $CaCl_2$ added to the model fluid and pressure drop in PHE

Another parameter could influence the variability of surface density of fouling deposit: pressure drop. It corresponds to the difference of pressure between the inlet and outlet of PHE. When fouling grows, the cross-sectional area decreases, limiting the product flow and leading to an increase of the pressure drop.[24], [25], [34] This pressure increase reduces residence time of the foulant solution in PHE and consequently limit the denaturation of β-Lg, leading to lower fouling deposit mass, as observed in Figure 33, test number 3.

Nonetheless, according to Delplace *et al.*[35], although pasteurization tests are performed in same conditions (temperature and flow rate), pressure drop can vary while resulting fouling deposit masses are equivalent. This could be explained by variation of the deposit nature: a spongy-like fouling deposit would expand in the foulant and restrain even more the product flow and increase the pressure drop, while a denser fouling deposit will do the opposite.

In Figure 33, the pasteurization test number 3 carried out corresponds to a new bag opening and it is hard to negate that the foulant composition could have changed. It remains consequently hard to tell if the variation of wet density of fouling is whether the result of the variation of the pressure drop, of the foulant composition, or of a combination of both.

To sum up, the precise origin of the variability of surface density of fouling deposit remains uncertain, but probably lies in a combination of both foulant composition alteration and pressure drop variations.

4.3. Variability of surface density fouling deposit within one Whey Protein Concentrate powder bag: Influence of surface properties and ways to mitigate errors

As highlighted in the previous section, non-negligible variability of the surface density of the fouling deposit was observed within one WPC powder batch, with a standard deviation value up to 15 % (Figure 33). Each pasteurization run is performed in the same conditions (temperature, flow rate), thus it seems unlikely that process parameters are the origin of this high dispersion of results. The variation of surface density lies rather probably in the samples characteristics themselves.

To confirm that, three pasteurization runs were performed using bare stainless steel surfaces only, with a solution prepared using the same WPC powder batch (U20454) from one unique. All parameters were fixed identically, and only a slight pressure drop variation was recorded. However, the results, displayed in Table 9, confirm that the standard deviation of surface density can be tolerable in the two first runs (less than 10 % of standard deviation) whereas the third test showed a very high dispersion (up to 21 %). With theoretically similar runs, only samples differences can be responsible for this dispersion of results. However, by averaging the surface density of all studied samples, the global standard deviation of surface density of fouling decreases to 14 %, increasing the accuracy.

Table 9. Surface density of dry fouling deposit and its standard deviation within one WPW bag

Test number	Surface density of dry fouling (mg/cm²)	Standard deviation of surface density of fouling (%)	Pressure drop (bar)
1	7.89	9	2.69
2	7.84	10	2.88
3	7.53	21	2.53
Average on all samples	**7.75**	**14**	

Several characteristics of the samples could impact the dispersion of results in the case of stainless steel, like a local variation of surface free energy, or the density of grain boundaries. Most probably, surface roughness can be responsible for this dispersion of results. Indeed, it is

well known in fluid mechanic community that surface roughness may significantly influence the flow in turbulent regime and underlying fouling deposit attachment/detachment.[198] Given the standard deviation of roughness of this stainless steel samples (41 ± 7 nm), so a standard deviation of 17%), this parameter could definitively be expected to impact the surface density of fouling deposit.

Besides, the location of the sample in the sample-holder could also have an influence, notably because some works underline the potential impact of bubbles in the fouling process, a parameter that we were not able to study nor control.[33], [199]

As a conclusion, the fouling process is very sensitive to little alteration of the surface characteristics, which can lead to high standard deviation values, despite all the efforts to make the runs perfectly identical.

Since these experiments proved that repeating the runs could limit this dispersion of result, it was decided to systematically realize three runs for each studied samples, each of these runs containing three similar samples, in order to improve repeatability and parry this high sensitivity of fouling with samples particularities.

The standard deviation of surface density of fouling between theoretically similar samples will be measured all along this manuscript. A higher standard deviation of surface density of fouling will be considered as a hint of a non-perfectly repeatable process of surface preparation or fabrication, or of non-homogeneous surfaces.

4.4. Mechanical stress

To assess anti-fouling property of modified stainless steel surfaces, samples were taken out of sample-holders after the circulation of model fluid for 60 or 90 min depending on WPC powder batch. Regarding fouling-release property, hot water (85°C) was circulated for 20 min and samples were then taken out.

However, some coatings or surface modifications can present both properties. Therefore, in order to evaluate both anti-fouling and fouling-release properties, samples were first taken out of samples-holders, weighed, put back inside samples-holders and subjected to hot water-rinsing for 20 min.

Nonetheless, as displayed in Figure 34, assess both anti-fouling and fouling-release properties led to the delamination of fouling deposit during water-rinsing. This effect was probably owed by the mechanical stress applied when samples were taken out of samples-

holders. For instance, after the fouling step, fouling layer on bare samples 7 and 9 had split and after the rinsing, there was no fouling layer anymore on sample 9. When fouling-release property was targeted only, fouling layer was not delaminated during the rinsing step, as no mechanical stress was applied (Figure 34). Consequently, to avoid the delamination of fouling layer, anti-fouling and fouling-release properties were assessed separately.

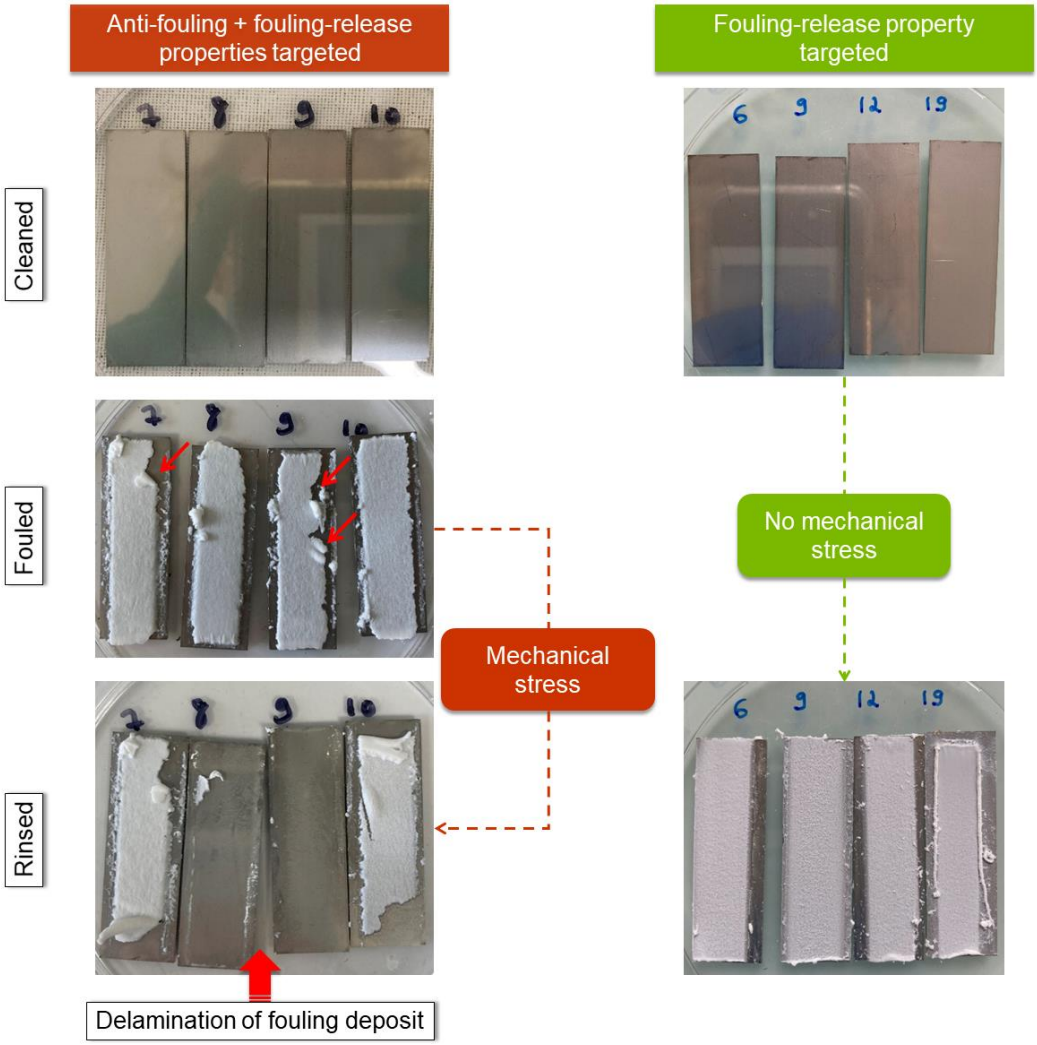

Figure 34. Comparison of the assessment of both anti-fouling and fouling properties and fouling-release property only

To sum up, repeatability issues can be due to several causes: (i) WPC powder manufacture history, (ii) water content in $CaCl_2$ added to the model fluid, (iii) pressure drop, (iv) surface roughness, and (v) mechanical stress on fouling layer. To minimize these issues, a protocol could be done systematically. In order to better ensure repeatability of fouling test of WPC solutions elaborated from powder batch, WPI, casein, calcium and phosphate contents should

be analyzed and at least three fouling tests using bare stainless steel surfaces have to be performed.

As $CaCl_2$ is a hygroscopic compound, it should be stored in a temperature and relative humidity-controlled environment.

To avoid delamination of fouling layer owed by a mechanical stress when both anti-fouling and fouling-release phenomena are investigated, assessing both of these properties should be carried out separately.

V. Conclusion

The aim of this chapter was to introduce the pasteurization process used to assess anti-fouling or fouling-release properties of modified stainless steel surfaces.

Milk being a complex fluid, a model fluid was prepared in order to avoid high deviations for experimental results. Whey protein concentrate powder and $CaCl_2$ were mixed together to obtain the model fluid, then injected in a specific pilot pasteurization system used for fouling tests, described here along with relevant process parameters. Anti-fouling properties were assessed by performing a pasteurization run, whereas targeting fouling-release properties consists in a pasteurization run followed by a water-rinsing.

Repeatability issues were observed using the pilot pasteurization system between runs using different WPC powder, runs using the same WPC powder, and finally between the samples of a lone run. Potential causes were identified for each situation: (i) WPC powder manufacture route, (ii) water content in $CaCl_2$ added to the model fluid (iii) pressure drop, (iv) surface roughness and others surface characteristics, and (v) mechanical stress on fouling layer while targeting both anti-fouling and fouling-release properties.

Considering these new data, an improved method was proposed to maximize the pasteurization reliability:

- $CaCl_2$ was stored in oven at 105°C
- At least three pasteurization runs were performed to assess fouling properties
- Anti-fouling or fouling-release properties were evaluated separately

Nonetheless, since these issues were identified during this PhD thesis, all tests were not realized following these rules. Consequently, for each test WPC powder batch, the storage

condition of $CaCl_2$ and the number of tests will be specified in the following parts, as well as if a mechanical stress was applied.

As outlook, a lot of studies and improvements could still be proposed for a better accuracy of these fouling tests, which relies on very complex, and not perfectly understand biological mechanism, as seen in chapter 1. As an example, the foulant ability of new WPC powder batches could be secured by defining a standard composition in β-Lg, casein, calcium and phosphate, and establish a routine analysis of each bag before its use.

CHAPTER 3 – NANOSTRUCTURED COATINGS BY ATMOSPHERIC PRESSURE PLASMA

I. Introduction

Plasma processes were widely used to create nanostructured surfaces. Nonetheless most of these processes are expensive and time-consuming as they need to work under vacuum. With the development of atmospheric pressure plasma, new design of sources appeared, allowing to use them in continuous and to set them up in production lines. Previous investigations demonstrated that thin films deposited by atmospheric pressure plasma allowed to reduce fouling deposit up to 90% or to increase induction time. In this study, HMDSO coatings were deposited using an atmospheric pressure plasma system developed by AcXys Technologies. The influence of plasma parameters on surface properties and fouling deposit were first investigated using an experimental design. The second part is dedicated to the development of superhydrophobic plasma bilayer deposition. The impact of precursor flow rate and power were studied on both surface properties and fouling deposit.

II. Deposition of hydrophobic and superhydrophobic thin films by atmospheric pressure plasma

2.1. Plasma state

Plasma is the fourth state of matter and is defined as electrically neutral gas or fluid composed of ions, electrons, radicals, atoms and molecules. Irving Langmuir named the fourth state of matter “plasma” as a reference to blood plasma. Plasmas can be described by different characteristics such as electronic temperature (T_e), ionization degree (α) and density (n).

The density, n, corresponding to the particle number (ions, electrons, molecules) per volume (cm^{-3}) enables to assess the ionization degree through the equation 17:

$$\alpha = \frac{n_e}{n_n + n_e} \quad (17)$$

with n_e and n_n corresponding to the density of electrons and neutral species respectively.
The electronic temperature is proportional to the electronic kinetic energy $k_B Te$ (eV). Therefore, plasmas are gathered into three groups following their electronic temperature and ionization degree: (i) equilibrium state plasma, (ii) thermal plasma and (iii) non-equilibrium plasma.

For plasmas at equilibrium state, all species have the same temperature ($T_e = T_{ions} = T_{gas}$). T_e is very high and can reach 10^7 K and the ionization degree is generally close to 1. These plasmas are also referred to as "hot plasma".

In case of thermal plasmas, equilibrium state is locally reached, thus, the equation $T_e = T_{gas} = T_n$ is partially correct. T_e reaches 10^4 K and $\alpha > 10^{-4}$.

Finally, non-equilibrium plasmas are characterized by a $T_e >> T_{ions} \approx T_{gas}$, with T_{ions} and T_{gas} closed to room temperature and by $\alpha < 10^{-4}$. These plasmas are referred to as "cold plasma".

Cold plasmas have been widely considered for surface modification for different domains. Plasma process enables to modify surface properties without degrading bulk properties of the material. Surface activation, surface etching, surface functionalisation, polymer thin film deposition and surface grafting can be performed (Figure 35).[200]

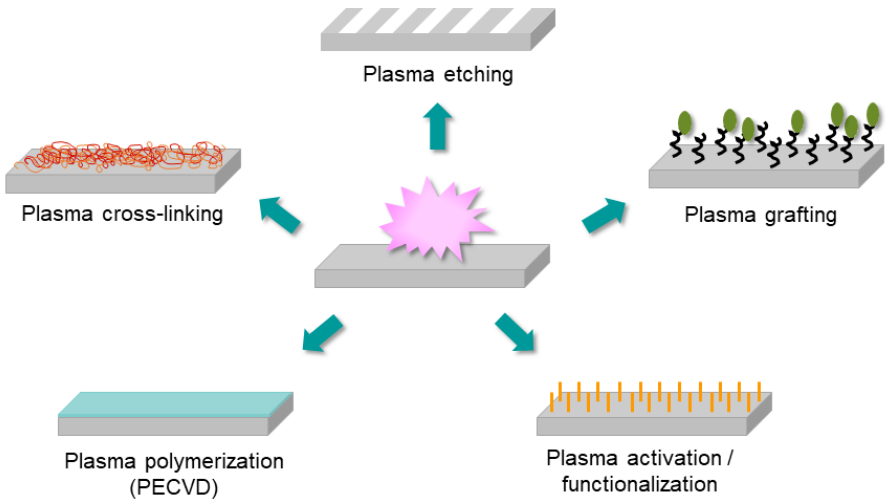

Figure 35. Plasma processes allowing surface modification adapted from [200]

Many papers report the use of these different surface modifications by low-pressure plasma. Nevertheless, although repeatable and reliable, these low-pressure systems are time-consuming and expensive due to the vacuum pumps and chambers. To scale up plasma treatments for industrial applications, atmospheric pressure plasma sources have been developed. As well as low-pressure plasma, atmospheric pressure plasma (APP) does not require solvent or catalyst, it is quick, controllable and reproducible and it is applicable to a large range of materials (metals, polymers, ceramics, …) with different shapes.

2.2. *Atmospheric pressure plasma sources*

According to Massines *et al.* atmospheric pressure plasma processes are divided into two main categories. In the first configuration the substrate is placed between the two electrodes or the substrate plays the role of electrode. Plasma and thus active species are generated directly on the surface. This configuration is named "direct plasma". On the contrary, in the "indirect plasma" configuration, the active species are created close to plasma source and then are blown on the substrate. It also called "post-discharge" deposition.

Direct plasma is largely used in material sterilization and in dermatological field. However, indirect atmospheric pressure plasma remains more investigated and more used for industrial applications. Thin film deposition by direct atmospheric pressure plasma process is complex due to the substrate influence on both the plasma and the gas injection.[201]

At atmospheric pressure, plasma can be generated from different types of excitation modes: (i) DC (direct current) and low frequency discharges, (ii) radio-frequency (RF) discharges and (iii) microwave discharges. Tendero *et al.* classified APP sources following their excitation modes.[202] Among the numerous APP sources presented, some configurations were widely developed such as (i) corona discharge, (ii) dielectric barrier discharge (DBD), (iii) plasma jet and (iv) pencil-like torch (Figure 36).

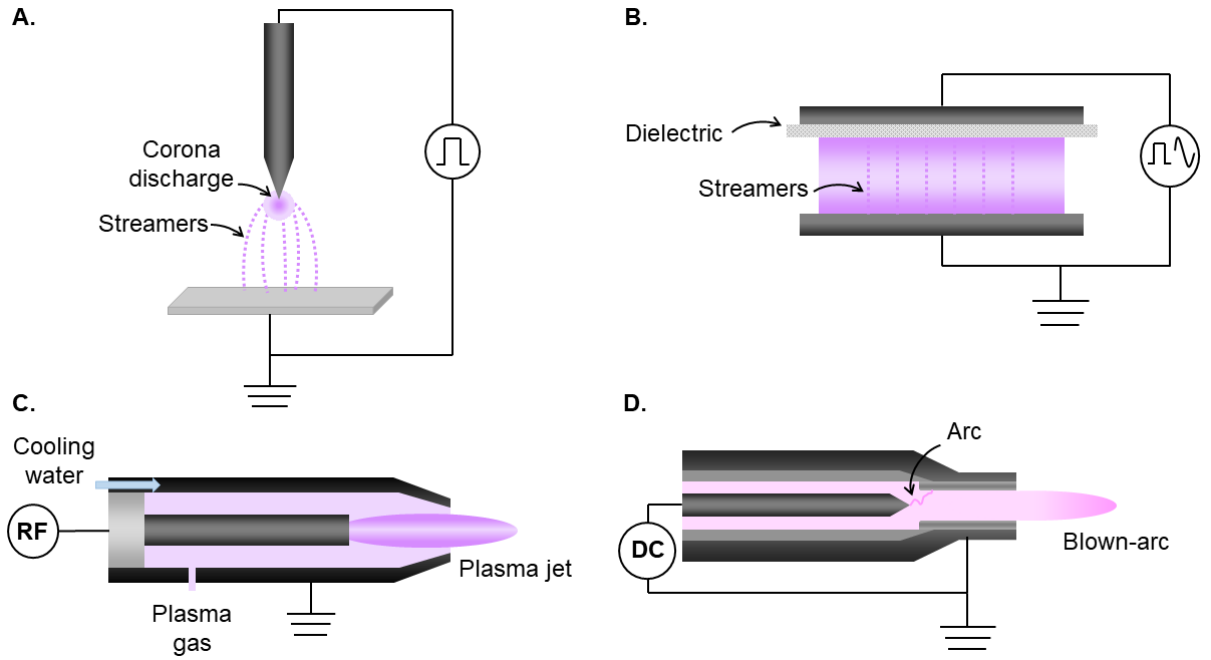

Figure 36. Atmospheric pressure plasma sources. (a) Corona discharge. (b) Dielectric barrier discharge (DBD). (c) Plasma jet. (d) Pencil-like torch. Adapted from [202], [203]

APP sources were described in several reviews [202], [204]–[206] thus the way they work will not be detailed in this manuscript. Both Corona discharge and DBD are broadly implanted for 2D materials treatment in the industry. Although these sources demonstrated limitations in materials processing, they were adapted for the treatment of various shaped-materials.[202], [204], [207]

Plasma jet and pencil-like torch were developed in the 1990s. In the literature it is common to find plasma jet or pencil-like torch for the same source. Indeed, their configurations are really close (Figure 36 c and d) however, their excitation mode differs. Plasma jet is usually generated by applying RF power between the two concentric electrodes.[202], [204], [208] In the case of pencil-like torch, plasma is generated at low power by a current-carrying arc.[202], [204], [206]

These sources were extensively used in oxide, polymer or carbon thin film deposition as they presented the ability to treat materials of three-dimensional shapes. Generally, APP are used in open-air but, interactions between plasma and surrounding environment affect the surface modifications and create undesirable species. Therefore, optimisation of plasma parameters is required to control the process and obtain reproducible results.[140], [209]

2.3. Hydrophobic and superhydrophobic thin coatings created by atmospheric pressure plasma

Atmospheric pressure plasma process enables to deposit thin coatings, change the degree of hydrophobicity/hydrophilicity *via* plasma parameters or create surface roughness. The deposition of thin films is performed using mainly plasma jet or pencil-like torch, either made in laboratories or developed by companies such as PlasmaTreat, AcXys Technologies or Dow Corning …[140], [207]

In 2018, Dimitrakellis *et al.* reviewed different approaches performed by plasma treatment to produce hydrophobic and superhydrophobic surfaces. They reported four ways to design hydrophobic surfaces and two approaches for superhydrophobic surfaces: a single-step processing and a multi-step processing. [140]

2.3.1. Hydrophobic plasma-polymerized coatings

Deposition of plasma-polymerized coating takes place in a single step and consists in polymerizing a monomer creating thin films on the substrate. These coatings are also called plasma polymers. However, they cannot be compared to conventional polymers since they are mainly amorphous and highly cross-linked. In that case, monomers or precursor molecules are

injected either in gas phase directly in the discharge area or in liquid form in the discharge or in the post-discharge thanks to a nebulizer and a gas carrier forming droplets. Dimitrakellis *et al.* reported four categories of precursors: (i) carbohalogen compounds, (ii) hydrocarbon compounds, (iii) fluorosilane compounds and (iv) organosilicon compounds.[140]

Since polymerization from carbohalogen compounds has been essentially done at low pressure and as hydrocarbon compounds are flammable thus, the focus is put on fluorosilane and organosilicon compounds. Fluorosilane precursors are especially interesting because they are easily dissociated in plasma discharge. Moreover, plasma-polymerized thin films are composed of a stable and highly resistant -Si-O-Si- backbone and CF_x side groups improving hydrophobic properties. The longer the fluorocarbon chain, the better the surface water repellence. Organosilicon molecules have been widely used to deposit hydrophilic SiO_x coatings as adhesive or gas barrier film. Nevertheless, by optimizing manufacturing plasma parameters, silicone-like coatings can be obtained. Such compounds, under plasma discharge, form a strong -Si-O-Si- backbone with CH_x end functions conferring hydrophobic properties. Both fluorosilane and organosilicon precursors are summarized in Table 10.[140]

Table 10. Precursors used for hydrophobic thin coatings

Precursor name	Substrate	WCA (°)	References
(3,3,3-Trifluoropropyl)trimethoxysilane (FAS-3)	Silicon wafer	91	[210]
(Pentafluorophenyl) triethoxysilane (FAS-5)	Silicon wafer	94	[210]
Heptadecafluoro-1,1,2,2-tetrahydrodecyl triethoxysilane (FAS-17)	Silicon wafer	116	[210]
Heptadecafluoro-1,1,2,2-tetrahydrodecyl trimethoxysilane (FLUSI)	Glass	115	[211]
1H, 1H, 2H, 2H-Perfluorooctyltriethoxysilane (pFOTES) or (FS)	Silicon wafer; 316L stainless steel	124; 120	[212], [213]
Hexamethyldisiloxane (HMDSO)	316L stainless steel	102	[113]
Tetramethyldisiloxane (TMDSO)	316L stainless steel	90	[214]
Tetramethylsilane (TMS)	Polyester synthetic leather; Epoxy resin surface	138; 95	[215], [216]

2.3.2. Superhydrophobic plasma-polymerized coatings

As mentioned in the previous sections, micro- and nano- roughness and low-surface energy are required to reach superhydrophobic properties. Plasma-polymerized deposition can lead to superhydrophobic surfaces and particles have been observed onto the coating and probably create surface nano-roughness. Those particles form with monomer condensation in the gas phase. The precursors or precursor mixtures found in the literature are gathered in Table 11.

Table 11. Precursors and precursor mixtures used for superhydrophobic thin coatings

Precursor name	Substrate	WCA (°)	References
Hexamethyldisiloxane (HMDSO)	Silicon wafer; Cotton fabrics	156; 162	[217],[218]
Hexamethyldisilazane (HMDSN)	Nano-films	161	[219]
Toluene:HMDSO mixture	Glass	150	[220]
Tetramethylsilane (TMS)	Silicon wafer and glass	162	[221]
Tetramethylcyclotetrasiloxane (Tomcats)	Silicon wafer	155	[217]
(pFOTES):Tomcats mixture (called TCFS)	Silicon wafer	158	[217]
Octamethylcyclotetrasiloxane (OMCTS)	Electro chromium coated steel	150	[222]

2.3.3. Hydrophobic and superhydrophobic plasma coatings limiting fouling adhesion

Only few works have highlighted the potential of thin coatings deposited by atmospheric pressure plasma for fouling mitigation. In fact, Dowling *et al.* [212] observed the influence of precursor and precursor mixtures and pointed out that the Tomcats (TC), FS/TEOS and TCFS exhibited superhydrophobic properties with water contact angle greater than 150°. Fouling tests consisted in a static immersion of the sample in $CaCO_3$ slurry solution for 15 days. After water rinsing, no fouling was observed on TC and TCFS coated samples. Later, in 2018, Zouaghi *et al.*[113] deposited thin films from HMDSO which exhibited hydrophobic properties (WCA ranging from 79° to 102°). Fouling-release properties of the HMDSO coatings has been evaluated in a pilot scale milk pasteurizer and good results have been obtained with a decrease of 90% of dairy fouling deposit after two consecutive fouling runs.

In the following parts both hydrophobic and superhydrophobic plasma thin coatings were investigated to mitigate dairy fouling. A new atmospheric pressure plasma system was received; therefore, plasma manufacturing parameters were optimized for HMDSO deposition. In a second part HMDSO was combined to a fluorine precursor leading to superhydrophobic bilayers.

III. Atmospheric pressure plasma process

3.1. Lab-Scan and set-up for plasma polymer deposition

The deposition of nano-structured coatings was performed using a pencil-like torch at atmospheric pressure. This APP torch was developed by AcXys Technologies (Saint Martin le Vinoux, France) and integrated in a cell (Figure 37) gathering two modules: (i) ULS (Ultra-Light System) and (ii) QuickSet. The ULS module allows to control the plasma generation by setting the frequency and plasmagenic gas flow rate. The second one is a 3-axis Cartesian robot, allowing to move the APP torch over the samples by programming the trajectory. Both ULS and QuickSet modules are placed under the Cartesian robot and are commanded thanks to a digital interface.

Figure 37. Lab-Scan, AcXys Technologies, plasma treatment cell

The deposition of thin films was carried out by fragmenting a liquid monomer in the post-discharge. Liquid monomer is driven to a nebulizer (Mira-Mist, Burgener Reasearch, Canada) by pumping (M12 mini CORI-FLOW, Bronkhorst, France) which is fixed to the robot. By introducing gas in the nebulizer, it generates an aerosol which is sprayed into the post-discharge as illustrated in Figure 38.

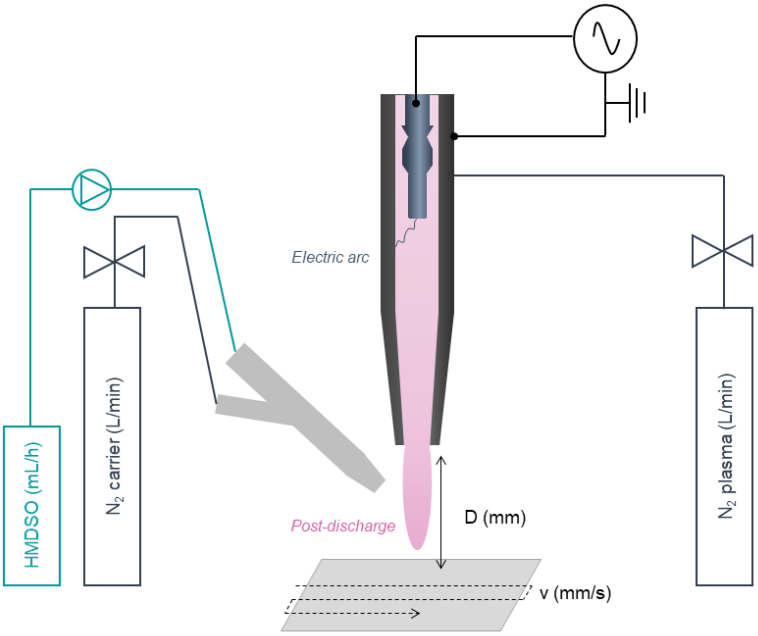

Figure 38. Schematic diagram of APP torch with the coating deposition system

3.2. Manufacturing plasma parameters

Numerous manufacturing parameters can be set in order to deposit coatings with specific surface properties: plasmagenic gas nature and flow rate, frequency, voltage, scanning speed, nozzle-to-substrate distance, pitch, carrier gas nature and flow rate, precursor type and flow rate, number of cycles and deposition time.

Several studies have investigated the influence of plasma parameters on physico-chemical characteristics of HMDSO (Figure 39) thin films such as chemical composition, wettability or morphology.

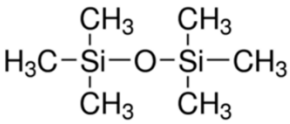

Figure 39. Chemical structure of Hexamethyldisiloxane (HMDSO).

HMDSO thin coating was deposited using industrial APP torch and the resulting observations are displayed in Table 12. Pulpytel *et al.* have studied the impact of numerous parameters thanks to an experimental design on the chemical composition. They highlighted that both nozzle-to substrate distance and scanning speed were the most important parameters. Increasing both the distance and speed leads to a higher organic thin film.[223] Asadollahi *et*

al. observed an increase of organic character at a high precursor flow rate and a low power.[224] Therefore, from these studies, it seems that several plasma parameters act on the organic character of HMDSO coating and thus on the precursor fragmentation. On the one hand, regarding the wettability, two works agreed that the higher the precursor flow rate, the higher the water contact angle.[218], [224] HMDSO fragmentation in the post-discharge leads to nanoparticles formation. Nonetheless, when the size of deposited particles increases, the formation of silica powder is promoted, making the coating mechanically unstable.[224]

In this work, HMDSO plasma coatings were deposited in three different environments (laboratories, temperature, relative humidity and air extractor). Temperature and relative humidity likely influence oxygen content in thin film as well as the morphology. Indeed, Asadollahi *et al.* added a quartz tube around the atmospheric pressure post-discharge in order to locally control the environment. They demonstrated that the quartz tube enables to limit oxygen diffusion from ambient air to the post-discharge, increasing the cross-linking of the plasma polymer and leading to dendrite-like structures.[224] The extraction speed of the fume hood can also affect the treatment and deposition dynamics. This will be detailed in the next section.

Table 12. Influence of plasma parameters on physico-chemical characteristics of HMDSO thin film deposited with industrial APP torch

Type of plasma source and producer	Investigated parameters	Target	Observations	References
APP torch from Plasmatreat	Treatment time Treatment distance Precursor flow rate	Film thickness	Thickness increases with both the increase of treatment time and precursor flow rate while decreases with the distance.	[225]
	Position of precursor injection in the post-discharge	Film composition	Films with different structures are obtained indicating that the fragmentation differ as the function of the injection position.	
APP torch AS400, Plasmatreat	Voltage Frequency Plasma cycle time (PCT) Gas flow rate Precursor flow rate Carrier gas flow rate Distance Scanning speed Pitch Scan Time between scans	Film composition	Screening of factors using an experimental design (Hadamard matrix of 12 experiments). Scanning speed and distance influence chemical composition of thin films. Increasing both scanning speed and distance rises organic character of thin film.	[223]
APP torch AS400, Plasmatreat	Precursor flow rate Plasma cycle time	Wettability and morphology	Both nanoparticles and water contact angle increase with PCT and precursor flow rate.	[218]
	Gas flow rate		Hydrophobic thin film is observed for an optimum flow rate before and after washing	
	Nature of gas	Wettability and durability (at a standard washing procedure)	O_2 plasma slightly rises thin films durability compared to N_2 plasma	
APP torch, UL-Scan, AcXys Technologies	Precursor flow rate Distance Scanning speed	Wettability and fouling-release performances	Wettability increases with precursor flow rate. No influence observed on wettability for both distance and scanning speed. No correlation between plasma parameters and fouling-release performances.	[113]

APP torch, AS400, Plasmatreat	Precursor flow rate Power	Film composition and wettability	Diminution of wettability with the increase of both precursor flow rate and power. Composition and structure of film are influenced by both precursor flow rate and power. Monomer fragmentation increases with power but decreases with precursor flow rate	[224]

3.3. Influence of the extraction speed of the fume hood

During this PhD thesis, the Lab-Scan was moved into three different laboratories, leading to reproducibility issues. In fact, at atmospheric pressure, external parameters such as temperature and relative humidity likely influence the final chemistry and morphology of thin films. By moving the Lab-Scan, another external parameter seems to impact the reproducibility of plasma coatings: air extraction speed. Indeed, for a given plasma condition, resulting coatings were apparent and adhesive at a high air extraction speed (13 m/s) but became opaque and powdery at a lower air extraction speed (3 m/s). Therefore, the extraction system of laboratory 3 was modified to obtain an air speed of 13 m/s. Air extraction speed was measured using an anemometer in each laboratory (Table 13).

Table 13. Air extraction speed measured in each laboratory

Laboratory	Air extraction speed (m/s)
1	13
2	0
3	3
	13

HMDSO was deposited onto stainless steel surfaces at different air speeds and resulting coatings were analyzed to demonstrate the influence of the extraction. All the experiments were performed in laboratory 3 and compared to an experiment carried out in laboratory 1.

3.3.1. Wettability

Wettability of HMDSO coatings deposited as a function of the air extraction speed was investigated. Resulting WCAs are presented in Figure 40. One can observe that air extraction speed acts on wettability. Indeed, wettability decreases with the decrease of air speed. At low air extraction speed (0 and 3 m/s), resulting HMDSO coatings were powdery and non-adhesive. It could be possible that a low air extraction affects deposition dynamics by locally increasing post-discharge temperature, leading to the higher fragmentation of precursor which increases the oxygen content and the formation of silica powder.[201], [224], [226]

The comparison of WCA of HMDSO deposited in the same plasma conditions and with the same air extraction speed shows a strong difference of 20°, which can be due to external temperature and relative humidity.

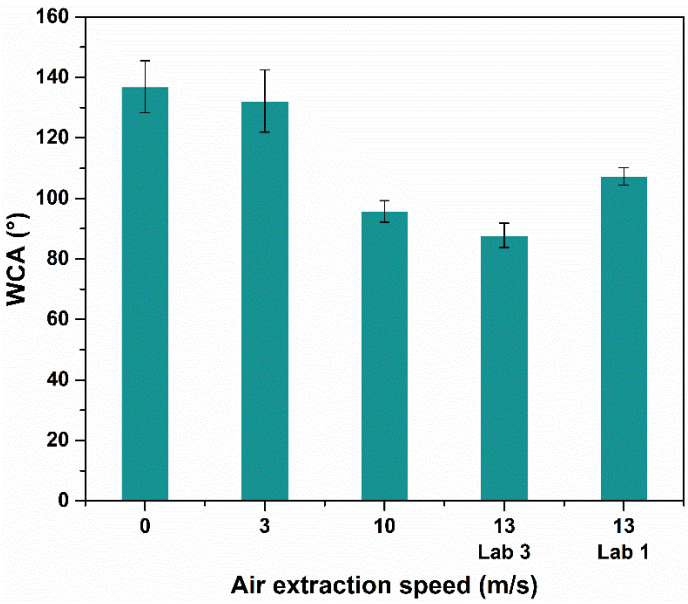

Figure 40. Wettability of HMDSO coating as the function of air extraction speed.

3.3.2. Morphology

SEM images (Figure 41) represent HMDSO coatings deposited without air extraction (a) and with an air extraction of 13 m/s (b). Without air extraction stainless steel surface is fully covered by nanoparticles and large aggregates. Same result was obtained with an air extraction of 3 m/s. With a higher air extraction (10 and 13 m/s), HMDSO coating is formed of nanoparticles however, grain boundaries are still visible.

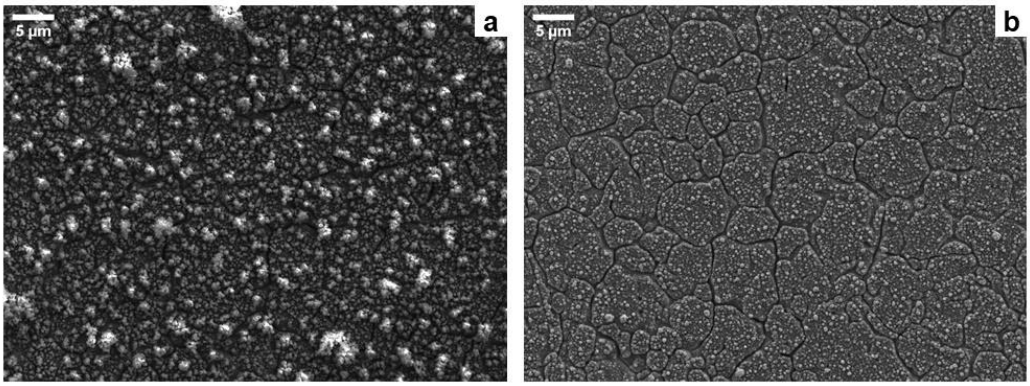

Figure 41. SEM images of HMDSO coatings deposited (a) without air extraction and (b) with an air extraction of 13 m/s (Laboratory 3).

3.3.3. Adhesion

Although HMDSO coatings reach high WCA values (without and with an air extraction of 3 m/s), they have to be adhesive to stainless steel substrate as they will be submitted to high shear stress during pateurization run. Figure 42 shows that HMDSO coatings demonstrating high WCA values are opaque and not adhesive (white arrows) due to the resulting silica powder. At 10 m/s, HMDSO coating is transparent but partially adhesive thus, all experiments presented in the manuscript were performed with an air extraction speed was fixed at 13 m/s.

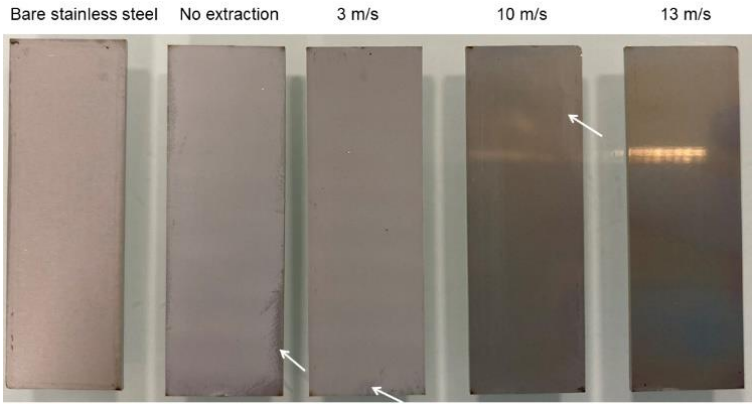

Figure 42. Assessment of HMDSO coating adhesion as the function of air extraction speed.

In this part, the importance of air extraction speed was pointed out regarding the reproducibility of plasma coatings but also regarding coating adhesion to substrate. As plasma depositions were performed in several environments, air extraction speed and laboratory will be specified in each section.

IV. Optimization of plasma manufacturing parameters for HMDSO

As previously mentioned, depending on plasma parameters, air extractor and ambient air, coatings with different properties can be obtained for the same precursor. Therefore, in order to obtain optimal parameters reducing dairy fouling deposit and evaluate their influence on surface properties, an experimental design was carried out.

4.1. Preparation and pre-treatment of samples

316L-2B stainless steel samples (45 x 15 mm² and 10 x 15 mm²) were first cleaned using the protocol detailed in Materials and Methods part. Before HMDSO plasma deposition, they were submitted to a N_2 plasma pre-treatment using the Lab-Scan (Figure 37) to improve thin film-substrate adhesion.[11] Pre-treatment parameters are gathered in Table 14.

Table 14. Pre-treatment parameters

Plasmagenic gas Flow rate (L/min)	Frequency (kHz)	Scanning speed (mm/s)	Distance (mm)	Cycles	Speed of the extraction (m/s)
N_2 60	80	100	20	4	13 (Lab 1)

WCA measurements were performed to validate the pre-treatment effectiveness. Resulting WCA was of 26.4 ±1.6°, which is consistent with the literature. In fact, this activation step leads to change the surface chemistry through the oxidation of the contamination layer.[227]–[229] Between the pre-treatment and HMDSO deposition, samples were left for 15 min to cool down. Plasma parameters for HMDSO deposition were investigated using an experimental design presented in the following section.

4.2. HMDSO deposition using an experimental design

Among the plasma parameters previously cited, nature of plasmagenic and carrier gas, carrier gas flow rate and type of precursor were fixed for the experimental design elaboration. Speed of the extraction was of 13 m/s and all the plasma coatings were deposited in the same laboratory. Nitrogen was used as both plasmagenic and carrier gas, carrier gas flow rate was set to 1.1 L/min. HMDSO was the precursor selected for hydrophobic thin films deposition. Therefore, the influence of nitrogen flow rate (plasmagenic gas), frequency, distance, scanning speed, precursor flow rate and cycles were studied using a Plackett and Burmann design. It consists in an Hadamard matrix including 12 experimental runs.

Experiments were carried out randomly to provide protection against the extraneous factors, which could affect the measured response. For statistical calculations, the variables U_i were coded as X_i according to the following transformation (Eq. 18):

$$X_i = \frac{U_i - U_0}{\Delta U} \quad (18)$$

where X_i is the dimensionless coded value of the variable U_i, U_0 represents the value of U_i at the center point and ΔU is the step change. The experimental values associated to the coded levels of the different variables are given in Table 15.

The mathematical model for predicting the optimal conditions does not take into account potential interaction between plasma parameters and is expressed according to equation 19:

$$Y_{pred} = \beta_0 + \sum \beta_i X_i \quad (19)$$

where y is the predicted response, b_0 is the value of the fitted response at the center point and b_i correspond to the linear terms.

Table 15. Coded and real values of experimental parameters used for the Plackett-Burman design

Coded variable	Parameter	Level	
		-1	+1
X_1	U_1, N_2 flow rate (L/min)	40	60
X_2	U_2, HMDSO flow rate (mL/h)	10	50
X_3	U_3, Distance (mm)	15	50
X_4	U_4, Scanning speed (mm/s)	50	300
X_5	U_5, Frequency (kHz)	80	190
X_6	U_6, Cycles	1	5

Modde7.0 software developed by Umetrics was used to generate the experimental design reported in Table 16. A run order was randomly assigned to each experiment to compensate the potential effects of external and uncontrollable parameters (such as relative humidity or ambient temperature). It can be noticed for experiment 12 that all plasma parameters are assigned to the level -1.

HMDSO plasma coatings were deposited using the Lab-Scan with the set-up displayed in Figure 38.

Table 16. Plackett-Burman design in coded and real values

Experiments	Run order	X_1	X_2	X_3	X_4	X_5	X_6	U_1	U_2	U_3	U_4	U_5	U_6	Process trouble
1	6	+1	-1	+1	-1	-1	-1	60	10	50	50	80	1	
2	1	+1	+1	-1	+1	-1	-1	60	50	15	300	80	1	
3	2	-1	+1	+1	-1	+1	-1	40	50	50	50	190	1	
4	5	+1	-1	+1	+1	-1	+1	60	10	50	300	80	5	
5	10	+1	+1	-1	+1	+1	-1	60	50	15	300	190	1	
6	12	+1	+1	+1	-1	+1	+1	60	50	50	50	190	5	
7	7	-1	+1	+1	+1	-1	+1	40	50	50	300	80	5	
8	9	-1	-1	+1	+1	+1	-1	40	10	50	300	190	1	
9	3	-1	-1	-1	+1	+1	+1	40	10	15	300	190	5	
10	4	+1	-1	-1	-1	1	+1	60	10	15	50	190	**5**	**U_6: 1**
11	8	-1	+1	-1	-1	-1	+1	40	50	15	50	80	**5**	**U_6: 1**
12	11	-1	-1	-1	-1	-1	-1	40	10	15	50	80	1	

Two experiments were not performed as planned by the experimental design: 10 and 11. The plasma torch scanned samples too close and too slow, damaging the sample holder thus, only 1 cycle over 5 was performed.

As reported in Chapter 1, anti-fouling and/or fouling-release properties have been explained through wettability, surface free energy and roughness. All plasma coatings were first characterized in order to study the potential influence of manufacturing plasma parameters on surfaces properties.

4.3. Influence of plasma parameters on surface properties

The following surface properties of HMDSO plasma coatings were analyzed: (i) wettability, (ii) surface free energy and (iii) roughness. Adhesion of coatings onto stainless steel was assessed as well. The analysing methods are detailed in the Materials and Methods section. Surface properties of bare and HMDSO-modified stainless steel samples are gathered in Table 17.

Table 17. Surface properties of bare stainless steel and HMDSO plasma thin films

Sample	WCA (°)	Surface free energy (mNm)			R_a (nm)	Adhesion grade
		γ^{TOT}	γ^{D}	γ^{P}		
REF	81.9 ± 0.8	34.4 ± 11.8	31.1 ± 8.5	3.3 ± 3.3	41 ± 7	-
1	98.6 ± 0.9	22.8 ± 3.9	21.3 ± 3.0	1.4 ± 0.9	39 ± 8	5B
2	93.8 ± 1.7	25.2 ± 5.0	23.3 ± 3.7	1.9 ± 1.4	41 ± 11	5B
3	96.4 ± 1.3	25.0 ± 4.2	24.4 ± 3.3	0.6 ± 0.9	46 ± 8	5B
4	92.3 ± 1.4	27.7 ± 0.9	25.4 ± 0.5	2.3 ± 0.4	44 ± 6	5B
5	84.6 ± 0.6	25.7 ± 13.3	19.6 ± 8.5	5.7 ± 4.7	43 ± 7	5B
6	102.4 ± 2.0	22.4 ± 2.8	22.1 ± 2.3	0.3 ± 0.5	62 ± 7	5B
7	89.3 ± 1.8	24.4 ± 6.2	21.9 ± 4.1	2.5 ± 2.1	50 ± 6	5B
8	90.1 ± 1.1	23.0 ± 9.9	20.7 ± 6.8	2.3 ± 3.1	41 ± 4	5B
9	90.7 ± 2.1	27.7 ± 2.9	25.4 ± 2.0	2.3 ± 0.9	43 ± 10	5B
10	90.5 ± 2.9	29.3 ± 0.9	26.8 ± 0.5	2.5 ± 0.4	39 ± 5	5B
11	130.3 ± 1.9	7.3 ± 1.9	7.2 ± 1.6	0.1 ± 0.3	76 ± 12	4B
12	107.3 ± 2.9	18.1 ± 0.8	17.2 ± 0.6	0.9 ± 0.2	39 ± 5	5B

4.3.1. Wettability (WCA)

For all plasma conditions, HMDSO deposition enables to decrease wettability of stainless steel. WCA increases from 81.9 ± 0.8° to 130.3 ± 1.9° corresponding to bare and modified (condition 11) stainless steel. HMDSO coatings reveal slight (84.6 ± 0.6°) to high (130.3 ± 1.9°) hydrophobicity, which is consistent with other studies on the deposition of HMDSO at atmospheric pressure.[113], [230], [231]

4.3.2. Surface Free Energy (SFE)

The resulting value of surface free energy of bare stainless steel (34.4 ± 11.8 mN/m) is consistent with the literature.[10], [11] The deposition of HMDSO by plasma decreases surface free energy of bare SS down to 7.3 ± 1.9 mN/m for condition 11. Except conditions 11 and 12, all other plasma conditions exhibit a SFE between 20 and 30 mN/m, which, according to Baier, corresponds to the fouling-release zone.[114] Nonetheless, some studies have demonstrated a stronger relationship between the polar component and dairy fouling mitigation than SFE and dairy fouling mitigation. Among those, three points of view can be distinguished: (i) a low polar component reduces fouling amount and proteins and minerals adhesion, (ii) an optimal polar component leads to a decrease in fouling resistance and amount and (iii) a high polar component lowers fouling amount. Polar parts of HMDSO coatings are lower (γ^{P}: 0.08 ± 0.25 – 5.63 ± 4.73 mN/m) than those (γ^{P}: 2.6 ± 0.9 – 15.8 ± 2.0 mN/m) reported by Zouaghi *et al.*[113]. Although

plasma processes are very similar, this demonstrates that plasma parameters can lead to different surface properties.

4.3.3. Roughness (R_a)

Arithmetic mean roughness (R_a) of bare and HMDSO-modified SS are reported in Table 17. Taking into account standard deviations, R_a of HMDSO coatings do not differ from that of bare stainless steel except condition 11 exhibiting a R_a of 76 ± 12 nm. Good fouling-release performances were previously obtained for HMDSO coatings exhibiting a lower R_a, around 49 ± 3 nm.[113] However, according to several investigations, the mitigation of dairy fouling relies on both physical (R_a) and chemical surfaces properties (SFE or the polar part γ^p).[60], [111], [112]

4.3.4. Correlation between plasma parameters and surface properties

Influence of plasma parameters on surfaces properties was investigated by analyzing the responses of water contact angle (Y_1), surface free energy (Y_2), polar part (γ^p) of the SFE (Y_3) and roughness (R_a) (Y_4) reported in Table 18. Modde7.0 software was used for regression and analysis of the obtained experimental data. The statistical significance of the main, quadratic and interaction effects of the variables was determined by analysis of variance (ANOVA), and a multiple regression analysis was performed to fit the experimental data to the polynomial equation (Eq. 2). The determination coefficient (R^2) describes the fraction of variation of the response explained by the model and the prediction coefficient (Q^2) describes the fraction of variation of the response that can be predicted by the model.

Table 18. Experimental design in coded values with corresponding responses

Experiments	X_1	X_2	X_3	X_4	X_5	X_6	Y_1 (°)	Y_2 (mN/m)	Y_3 (mN/m)	Y_4 (nm)
1	+1	-1	+1	-1	-1	-1	98.6	22.8	1.4	39
2	+1	+1	-1	+1	-1	-1	93.8	25.2	1.9	41
3	-1	+1	+1	-1	+1	-1	96.4	25.0	0.6	46
4	+1	-1	+1	+1	-1	+1	92.3	27.7	2.3	44
5	+1	+1	-1	+1	+1	-1	84.6	25.7	5.7	43
6	+1	+1	+1	-1	+1	+1	102.4	22.4	0.3	62
7	-1	+1	+1	+1	-1	+1	89.3	24.4	2.5	50
8	-1	-1	+1	+1	+1	-1	90.1	23.0	2.3	41
9	-1	-1	-1	+1	+1	+1	90.7	27.7	2.3	43
10	+1	-1	-1	-1	+1	+1	90.5	29.3	2.5	39
11	-1	+1	-1	-1	-1	+1	130.3	7.3	0.1	76
12	-1	-1	-1	-1	-1	-1	107.3	18.1	0.9	39

Experiments 10 and 11 were not performed as planned by the experimental design (*i.e.* only one cycle over five was carried out). After analyzing the responses obtained, WCA and SFE do not vary significantly. Indeed, the initial determination coefficient was too low because R^2 was around 86 % and 60 % for WCA and SFE, respectively. Moreover, the coefficient of prediction Q^2 was less than 50 % for both of these responses, meaning that WCA and SFE are not well predicted by the chosen experimental design. Consequently, only two surface responses: Y_3: Polar part and Y_4: R_a will be taken into account for the optimization step with the experience plan.

First, the determination coefficient obtained for the polar part (γ^P) response (Y_3) was very low. Indeed, R^2 was around 60 % indicating that 40 % of the total variation was not explained by the model. Therefore, condition 2 was removed from the experimental design to improve the statistical significance of the model. Afterwards, R^2 value was equal to 99.5 %, indicating that less than 1% of the total variation was not explained by the model. Polar part was well predicted by the model as the coefficient of prediction Q^2 was equal to 90.7 %.

Secondly, for the roughness (R_a) response (Y_4), the determination coefficient showed that the regression model correlates with the experimental data. Indeed, R^2 was equal to 91 %, indicating that 9 % of the total variation was not explained by the model. Nonetheless, the coefficient of prediction Q^2 was less than 50 % meaning that roughness was not well predicted by the model. Consequently, condition 8 was removed from the experimental design to improve the statistical significance of the model. R^2 and Q^2 values increased to 99.6 % and 92.7 % respectively. After checking the reliability of the models, the significance of the different model terms can be discussed. Their values are listed in Table 19.

Table 19. Coefficients of the model estimated with Modde7.0 for polar part and roughness responses

Variable	Coefficient	Y_3: γ^P	Y_4: R_a
Constant	β_0	2.120	45.917
N_2 flow rate	β_1	**0.550**	1.417
HMDSO flow rate	β_2	**0.540**	**4.500**
Distance	β_3	**-0.595**	-1.000
Scanning speed	β_4	**1.405**	**-4.333**
Frequency	β_5	-0.175	0.333
Cycles	β_6	**-0.655**	**6.500**

In bold: significant terms and in red: non influent terms.

Each response will be considered separately and importance of the model coefficients is always considered in absolute terms.

Regarding the response Y_3, it can be noticed that β_4 coefficient is the highest in absolute value, thus the scanning speed (X_4) is an important parameter to minimize the polar part. Nonetheless, β_1, β_2, β_3 and β_6 are close in absolute value, therefore, their corresponding variables (N_2 flow rate, HMDSO flow rate, distance and number of cycles) cannot be neglected. β_3 and β_6 coefficients being negative, it indicates that an increase in the distance and the number of cycles leads to a decrease of the polar part. β_1, β_2 and β_4 coefficients being positive, it means that a decrease of N_2 and HMDSO flow rates and the scanning speed leads to a decrease of the polar part. This is partly logical and the coherence between the predicted variables and the literature is reported in Table 20.

Table 20. Coherence of predicted variables to minimize the polar part and literature

Variable	Prediction to minimize the polar part (Y_3)	Coherence	Explanations	Reference
N_2 flow rate	↘	✗	Increase of gas flow rate decreases gas temperature leading to a reduction of monomer decomposition.	[223]
HMDSO	↘	✗	At fixed power, the increase of HMDSO flow rate decreases precursor fragmentation, leading to a higher hydrophobic thin film.	[224]
Distance	↗	✓	The increase of the distance decreases the temperature gradient along the plasma jet, which reduces the monomer fragmentation.	[223]
Scanning speed	↘	✗	The increase of torch speed reduces substrate temperature generating a higher organic HMDSO thin coating.	[223]
Cycles	↗	✓ / ✗	At low torch speed (5 m/min corresponding to 83 mm/s), substrate temperature increases with the number of cycles leading to a lower organic character of HMDSO thin layer. Above a torch speed of 250 mm/s, substrate temperature is stable after two cycles.	[223]

According to Table 20, the only predicted parameter in agreement with the literature is the distance, whose importance was less clear than scanning speed, as its coefficient was very close in absolute value from N_2 and HMDSO flow rates and the number of cycles. Consequently, no correlation between plasma parameters and the polar part can be ventured.

Coefficients related to the response Y_4 are listed in Table 19. The most important plasma parameters regarding the roughness are the HMDSO flow rate (X_2), the scanning speed (X_4) and the number of cycles (X_6). It can be noted that β_2 and β_6 coefficients are positive, meaning that a decrease of HMDSO flow rate and the number of cycles lead to a decrease of R_a. The negative sign of β_4 indicates that an increase in scanning speed leads to a decrease of R_a.

This confirms the observations of Yang *et al.*[218] who emphasized that the higher HMDSO flow rate, the higher the roughness. Increasing the scanning speed leads to decrease the residence time of the monomer and thus its fragmentation. As several studies pointed out that HMDSO deposition forms nanoparticles, [113], [218], [223], [224] increasing the scanning speed and decreasing the number of cycles could limit nanoparticles aggregates and thus lower the roughness.

Plasma condition corresponding to the combination (X_2 = -1, X_4 = +1, X_6 = -1) is the condition 8 showing a R_a of 41 nm which is close to the minimal value (39 nm). Nonetheless, this condition was removed from the experimental design, therefore no correlation can be emitted between plasma parameters and roughness. In that case, it could be due to an experimental trouble or to the chosen limits of the variables.

Although the determination (R^2) and prediction (Q^2) coefficients were higher than 90 % and 50 % respectively for the polar part (Y_3) and roughness (Y_4), the experimental design did not allow to correlate plasma manufacturing parameters and these two responses.

The influence of plasma parameters on the fouling deposit will be investigated in the next section.

4.4. Fouling performances and durability assessment

4.4.1. Fouling performances

Anti-fouling and fouling-release performances of HMDSO plasma coatings were assessed. The fouling test was running for one hour, using WPC powder batch U20454. Samples were then removed from sample holder to be weighed and put back inside sample holder to be rinsed

with hot water for 20 min. In Figure 43 both anti-fouling and fouling-release results are represented. Only two plasma conditions demonstrate good anti-fouling properties: conditions 3 and 11 with a fouling deposit reduction of 89 ± 11 % and 82 ± 18 % respectively. After the rinsing step, 7 plasma conditions (3, 5, 6, 7, 8 10 and 11) show a fouling deposit reduction higher than 85 %, corroborating previous results observed by Zouaghi *et al.*[113]

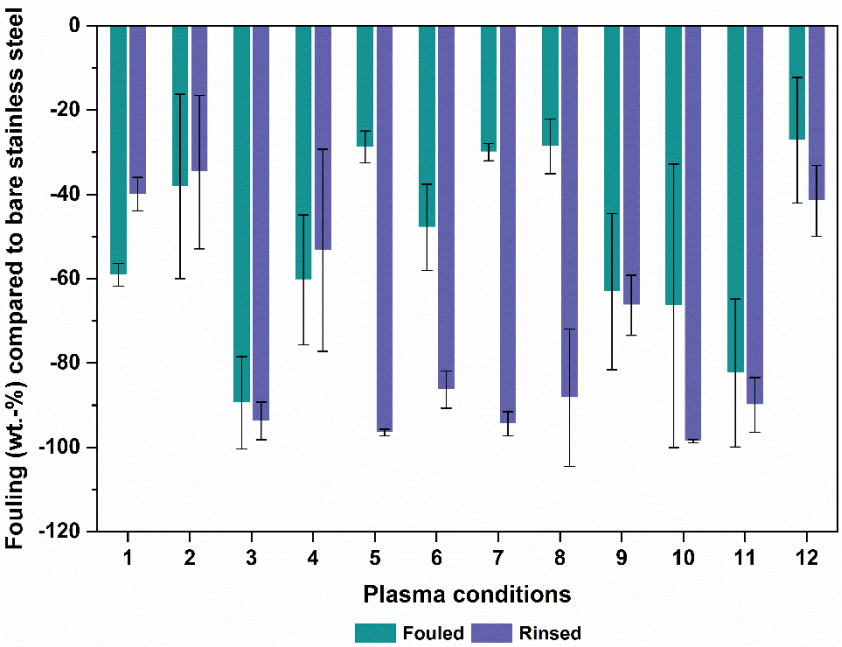

Figure 43. Anti-fouling and fouling-release (rinsed) performances of HMDSO plasma coatings normalized compared to bare stainless steel

4.4.2. Plasma coatings durability

Plasma conditions 3, 5, 6, 7, 8, 10 and 11 were submitted to a second pasteurization run to assess their durability. Nonetheless, after the rinsing step, a very thin layer was noticed onto plasma coatings, thus samples were rinsed for 5 min in hot water (85°C) using an ultrasonic bath. The second fouling run was performed as the first one, described above, using WPC powder batch U20454. Fouling-release performances are displayed in Figure 44. It can be noted that only condition 3 still shows good fouling-release performances, with a fouling deposit reduction of 86 ± 9 %. Consequently, a third run was carried out and resulting fouling-release performances presented in Figure 44 demonstrate a fouling deposit reduction of 12 ± 2 %.

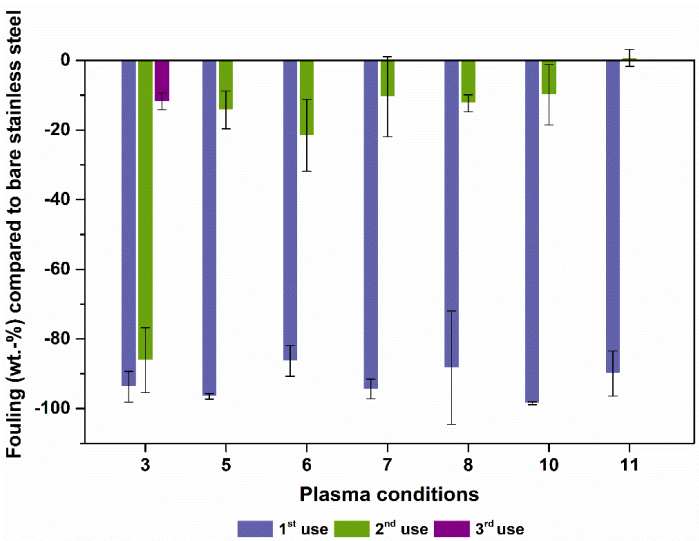

Figure 44. Assessment of HMDSO plasma coatings durability

WCA were measured after the supplementary rinsing in ultrasonic bath. As illustrated in Figure 45, for all plasma conditions WCA decreases after a pasteurization cycle. For condition 11, the WCA reduction is higher than 50 %. Several factors could have explained the poor durability of this coating. In fact, as showed in Table 17, this coating was less adhesive than the others and roughness was higher. Therefore, it is likely that high flow rate damaged partly plasma thin film and that fouling remained trapped. It could also be possible that ultrasonic bath damaged plasma thin film. Regarding condition 3, which demonstrated good-fouling-release properties for two pasteurization runs, a slight WCA decrease is noticed after the first fouling run but not after the second run, thus it seems likely that ultrasonic damaged this plasma thin film.

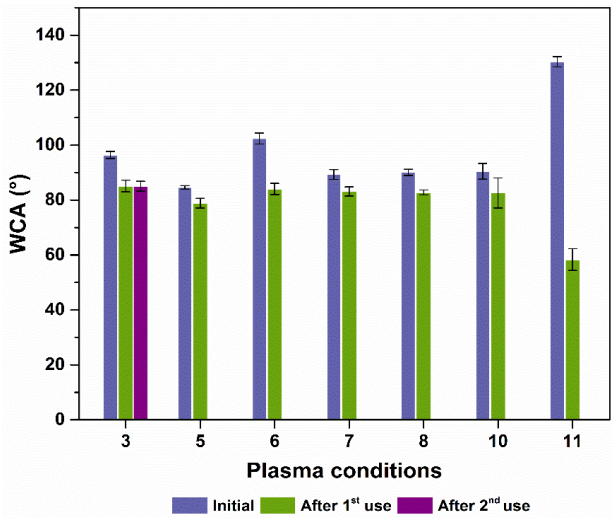

Figure 45. WCA measurements before each fouling run.

The loss of fouling-release properties can be due to persistent fouling deposit which was not removed by ultrasonic rising and promoting the fouling growth during the third test.

X-ray mappings of condition 3 after plasma deposition and after the third pasteurization run were carried out to evaluate the potential degradation of plasma thin film. Resulting analyses of silicon and iron elements show a higher detection of Si and a lower detection of Fe after plasma deposition (Figure 46 A) than after three pasteurization runs (Figure 46 B). Nonetheless, it is not possible to affirm that the lower Si detection (Figure 46 B) comes from a potential degradation owed by ultrasonic rinsing or from the three pasteurization runs.

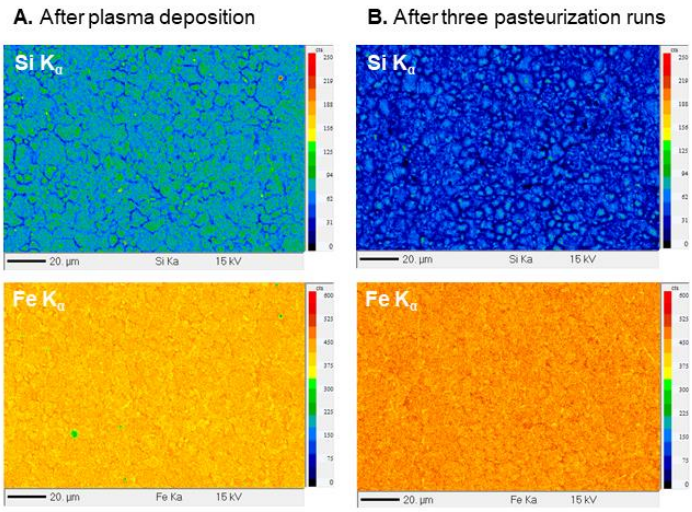

Figure 46. X-ray mappings of Si and Fe elements by EPMA (A). After plasma deposition and (B). After three pasteurization runs.

4.4.3. Correlation between plasma parameters and fouling-release performances

The influence of plasma parameters on fouling-release performances was also investigated by analyzing the responses of the fouling deposit (Y_5) reported in Table 21. As previously, experiments 10 and 11 (in red) were not performed as planned by the experimental design (*i.e.* only one cycle over five was carried out).

Table 21. Experimental design in coded values with corresponding response (Y_5)

Experiments	X_1	X_2	X_3	X_4	X_5	X_6	Y_5 (%)
1	+1	-1	+1	-1	-1	-1	60
2	+1	+1	-1	+1	-1	-1	65
3	-1	+1	+1	-1	+1	-1	6
4	+1	-1	+1	+1	-1	+1	47
5	+1	+1	-1	+1	+1	-1	4
6	+1	+1	+1	-1	+1	+1	14
7	-1	+1	+1	+1	-1	+1	6
8	-1	-1	+1	+1	+1	-1	12
9	-1	-1	-1	+1	+1	+1	34
10	+1	-1	-1	-1	+1	+1	2
11	-1	+1	-1	-1	-1	+1	10
12	-1	-1	-1	-1	-1	-1	59

The determination coefficient obtained for the fouling deposit response (Y_5) was low. Indeed, R^2 was around 85 % indicating that 15 % of the total variation was not explained by the model. Therefore, condition 5 was removed from the experimental design to improve the statistical significance of the model. Afterwards, R^2 value was equal to 99 %, indicating that 1% of the total variation was not explained by the model. Polar part contact angle was well predicted by the model because the coefficient of prediction Q^2 was equal to 80 %. After checking the reliability of the model, the significance of the different model terms can be discussed. Their values are listed in Table 22.

Table 22. Coefficients of the model estimated with Modde7.0 for fouling deposit response

Variable	Coefficient	Y_5: Fouling deposit
Constant	β_0	37.039
N_2 flow rate	β_1	**11.781**
HMDSO flow rate	β_2	-7.811
Distance	β_3	**-13.016**
Scanning speed	β_4	-1.733
Frequency	β_5	-8.286
Cycles	β_6	-4.722

In bold: most significant terms and in red: non influent terms.

According to Table 22, it can be noticed that the most important process parameters to minimize the fouling deposition are N_2 flow rate (X_1) and the nozzle-to-substrate distance (X_3). β_1 coefficient being positive, it indicates a decrease of N_2 flow rate leading to a decrease of the fouling deposit. β_3 coefficient being negative, it means that an increase of the distance leads to a decrease of the fouling deposit.

Plasma conditions corresponding to the combination (X_1 = -1, X_3 = +1) are the 3, 7 and 8 showing a fouling deposit reduction of 94 %, 94 % and 88 % respectively. Taking into account the sign and influence of coefficients, Modde7.0 software allows to obtain a first prediction to minimize fouling deposition. It is represented in Figure 47 A as the function of N_2 flow rate and distance. Less important factors such as HMDSO flow rate and frequency were set at +1 level. Non influent terms such as scanning speed and the number of cycles were set at the center level. To refine the correlation between plasma parameters and fouling deposit the optimizer function of Modde7.0 was used targeting the minimization of fouling deposit. The optimization is finally very close to the prediction (Figure 47 B), as only the scanning speed factor was modified to +1 level. Consequently, it seems that scanning speed has not a strong impact on fouling deposition, thus the plasma parameters combination resulting from the optimization corresponds closely to condition 3.

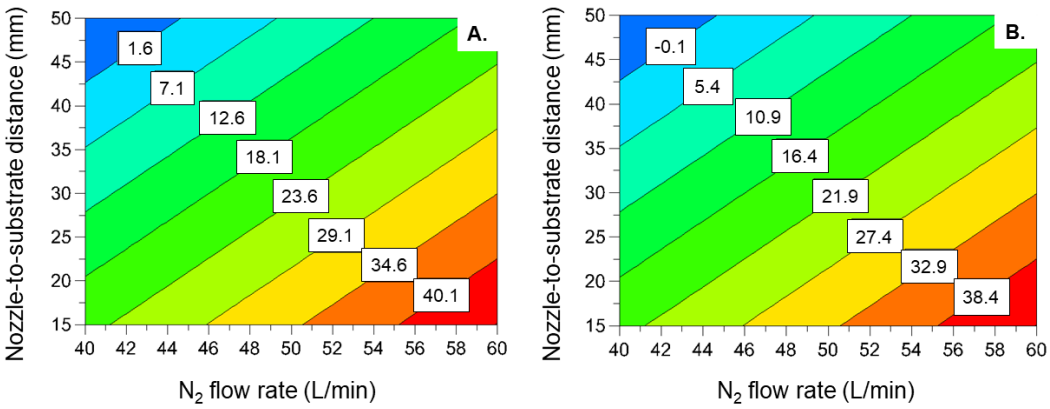

Figure 47. Contour plot showing the evolution of the fouling deposition (%) as a function of N_2 flow rate and distance. A. For a high HMDSO low rate, frequency, a scanning speed = 175 mm/s and a number of cycles = 3. B. For a high HMDSO low rate, frequency, a scanning speed = 300 mm/s and a number of cycles = 3

To understand the higher efficiency of condition 3, its surface properties were compared to those of conditions 7 and 8. Moreover, further surface characterizations were performed: (i) morphology of these three coatings were observed by SEM and (ii) surface chemistry was analyzed using FTIR spectroscopy.

4.4.4. Surface characterizations

4.4.4.1. Surface properties

Wettability, surface free energy and its polar part as well as roughness (R_a) of conditions 3, 7 and 8 are displayed in Figure 48. WCA of coating 3 is slightly higher than that of coatings 7 and 8. This difference cannot be justified by the SFE as it is equivalent for the three plasma coatings. Higher differences can be noticed for the polar part and roughness. Indeed, the polar part of coating 3 is lower than that of the two other coatings. Regarding the roughness, coatings 3 and 7 seem slightly rougher than coating 8. Therefore, a low polar part and a roughness lower than 60 nm allow to reduce dairy fouling deposit. This corroborates the work of Jimenez *et al.* [112] who pointed out a competition between the polar part and roughness for the mitigation of fouling deposition.

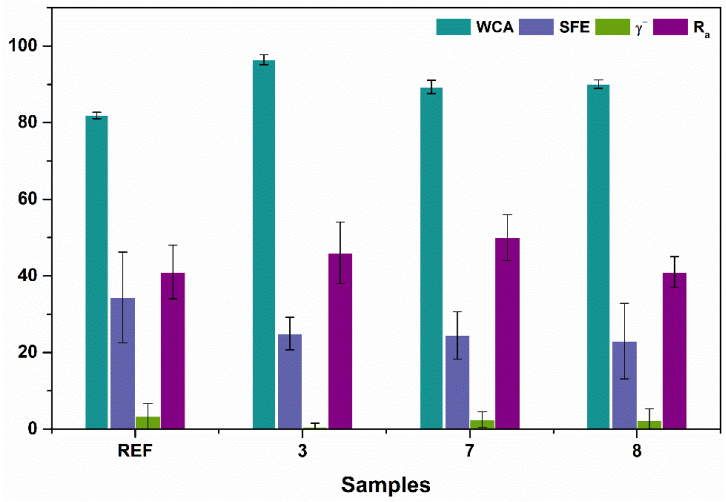

Figure 48. Surface properties comparison of plasma condition 3, 7, 8 and bare stainless steel (REF).

4.4.4.2. Morphology

Conditions 3, 7 and 8 were observed by SEM to analyze coatings morphology (Figure 49). The morphology of coating 8 differs from that of coating 3, indeed nanoparticles can be observed in this latter while coating 8 looks like bare stainless steel, which is consistent with R_a measurements. This difference can be explained through plasma parameters. In fact, the comparison of condition 8 with condition 3 demonstrates that HMDSO flow rate was lower (10 mL/h against 50 mL/h) and scanning speed was faster (300 mm/s against 50 mm/s). Therefore, the amount of HMDSO and time residence in the post-discharge are lower in case of condition 8, reducing nanoparticles formation.

Coating 7 shows more nanoparticles than coating 3 but it seems thicker as some grain boundaries are less visible (white arrows). Taking into account the plasma parameters, this difference could be due to the frequency. In fact, coating 3 was deposited at low scanning speed (50 mm/s), high frequency (190 kHz, i.e. low power ~ 1115 W) with 1 cycle whereas coating 7 was deposited at high scanning speed (300 mm/s), low frequency (80 kHz, *i.e.* high power ~ 1515 W) with 5 cycles. By comparing treatment time for one sample, 1.5 s is needed with condition 7 to coat the entire surface against 1.8 s with condition 3. Therefore, treatment times are equivalent. Regarding the frequency (or power), Asadollahi *et al.*[224] highlighted that the higher the power, the higher the monomer fragmentation and the nanoparticles formation. Therefore, the increase of monomer fragmentation owed by the low frequency (high power) increases the formation of nanoparticles as observed for condition 7.

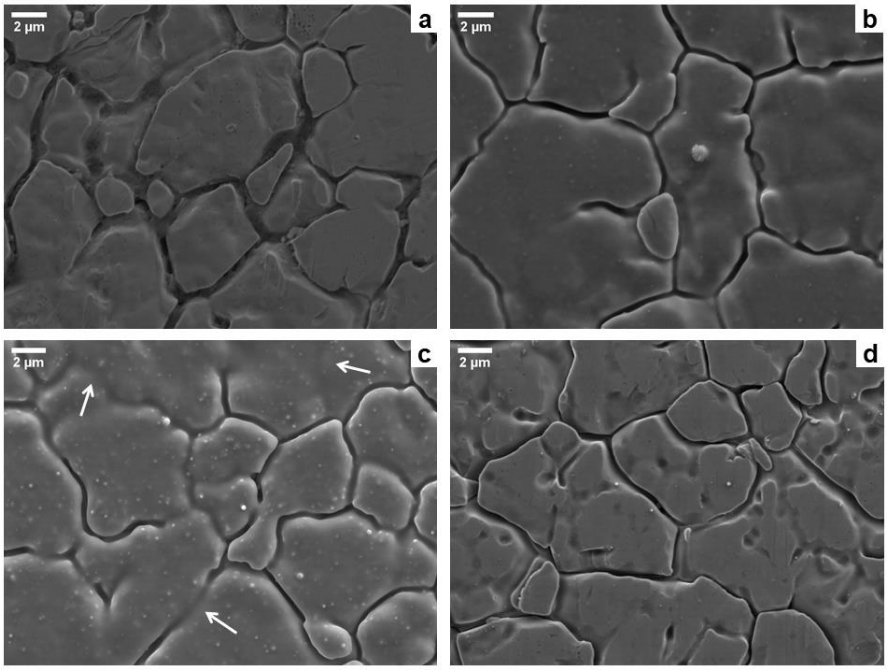

Figure 49. SEM images of (a) bare stainless steel, (b) HMDSO coating 3, (c) HMDSO coating 7 and (d) HMDSO coating 8.

4.4.4.3. Surface chemistry

To study the chemical composition of conditions 3, 7 and 8, FTIR spectroscopy in ATR mode was used. Figure 50 displays the full range spectra of these three coatings and peaks attribution are gathered in Table 23. All plasma conditions show characteristic peaks of siloxane-based thin films around 1100-1000 cm^{-1}, 800 cm^{-1} and 450 cm^{-1}. Several bands at

2965 cm^{-1}, around 1275 cm^{-1} and 800 cm^{-1} also reveal the presence of carbon in all coatings. As the peak around 1275 cm^{-1}, characteristic of Si-$(CH_3)_x$ bonding is not shifted for the three conditions, it allows to confirm that the coating for condition 7 is thicker than coatings 3 and 8 as the strongest Si-O-Si band (1100-1000 cm^{-1}) is more intense. This correlates SEM observations.

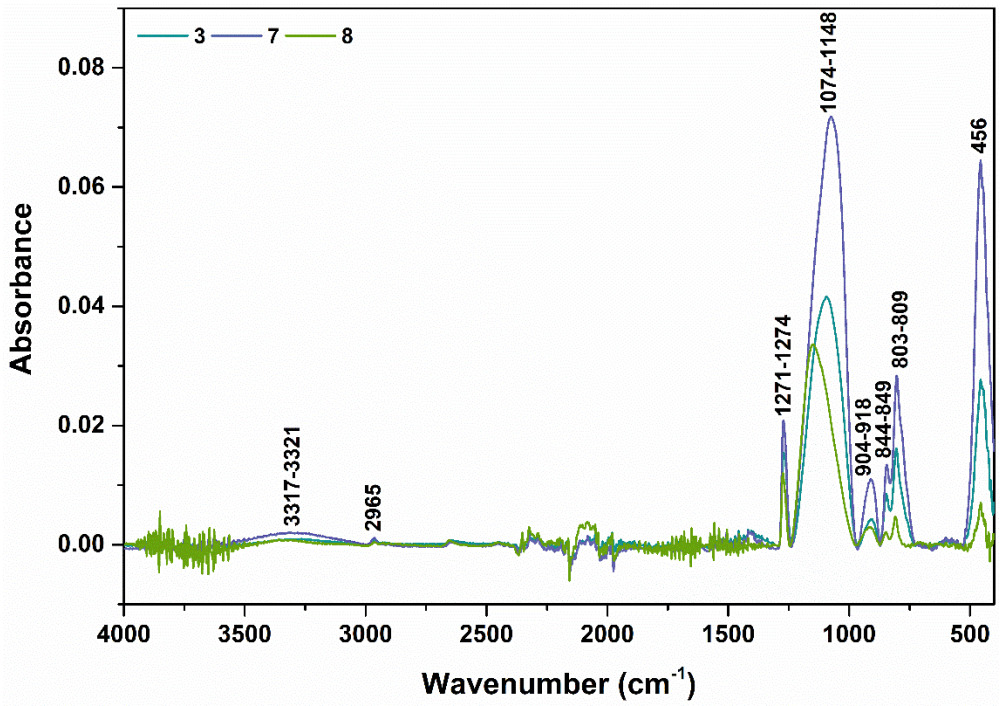

Figure 50. FTIR spectra of HMDSO plasma coatings (in blue: condition 3, in purple: condition 7 and in green: condition 8).

Table 23. Peaks assignment for each plasma coating.

Wavenumber (cm^{-1})			Peaks attribution	References
3	7	8		
3317	3319	3321	ν O-H	[232]
2965	2965	2965	ν^a (CH_3)	[225], [233]
1271	1272	1274	δ^s Si-$(CH_3)_x$	[225], [233]
		1148	ν^a Si-O-Si (LO_4), Si-O-C	[232]
1093	1074		ν^a Si-O-Si (TO_3)	[232]
904	911	918	ν Si-OH	[225], [233]
846	844	849	ρ Si-O	[233]
804	803	809	ν^s Si-O-Si (TO_2), ρ Si-C in Si-$(CH_3)_x$	[225], [232]
456	456	456	ρ Si-O-Si (TO_1)	[232], [234]

Abbreviations: ν: stretching, δ: bending, ρ: rocking, a: asymmetric, s: symmetric.

Based on two studies [223], [224], it is possible to estimate qualitatively the content of carbon in thin films by calculating the ratio between the surface area of the Si-$(CH_3)_x$ peak and the surface area of the Si-O-Si (TO_3) peak. As the Si-O-Si band is broad, a deconvolution of IR spectra was performed, which is displayed in Figure 51. Peaks assignment is reported in Table 24. It can be noticed from spectra deconvolution that the large Si-O-Si band leads to three peaks corresponding to different angles of the Si-O bonding.[233] According to Asadollahi *et al.*[224] the ratio between the surface area of the Si-O-Si (LO_4) peak and the surface area of the Si-O-Si (TO_3) peak can bring structural information on Si-O-Si network.

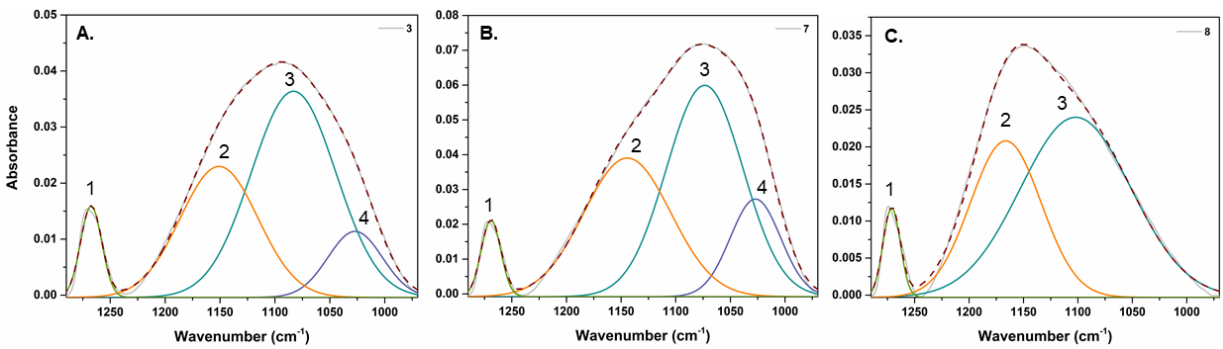

Figure 51. Deconvoluted FTIR spectra in the 1290-970 cm^{-1} range. (A) Condition 3. (B) Condition 7. (C) Condition 8.

Table 24. Assignment of deconvoluted bands of each plasma coatings.

Peak number	Wavenumber (cm^{-1})			Peaks attribution	References
	3	7	8		
1	1267	1269	1271	δ^s Si-(CH3)x	[225], [233]
2	1151	1144	1166	ν^a Si-O-Si (LO_4) (angle ~ 150°), Si-O-C	[232], [233]
3	1083	1073	1102	ν^a Si-O-Si (TO_3) (angle ~ 144°)	[232], [233]
4	1027	1027		ν^a Si-O-Si (angle < 144°)	[232], [233]

Abbreviations: ν: stretching, δ: bending, a: asymmetric, s: symmetric.

The calculation of both Si-$(CH_3)_x$/Si-O-Si(TO_3) and LO_4/TO_3 ratios were done using surface areas under peaks 1, 2 and 3 called A_1, A_2 and A_3 respectively. Surface areas were obtained from spectra deconvolution. Resulting ratios are presented in Table 25.

For the condition 8, a lower amount of HMDSO was injected in the post-discharge than in condition 3, leading to a higher amount of energy available per molecule, thus increasing the fragmentation. Therefore a lower Si-$(CH_3)_x$/Si-O-Si ratio is obtained for condition 8 compare to condition 3 and thus a lower carbon content. Regarding the Si-O-Si network, LO_4/TO_3 ratio

is very close between conditions 3 and 8. The slight difference could be justified by the residence time, which is higher in condition 3, increasing fragmentation of Si-O-Si network, generating shorter siloxane chains.

As pointed out by Asadollahi *et al.* [224] at a fixed precursor flow rate, when the power increases, a higher amount of energy is available per precursor molecule, leading to a higher fragmentation. As power was higher for condition 7, lower Si-$(CH_3)_x$/Si-O-Si and higher LO_4/TO_3 ratios are expected compare to condition 3 which is observed in Table 25. This means that condition 3 leads to a higher carbon content than condition 7 and longer siloxane chains in its Si-O-Si network. This could explain the lower polar part obtained for condition 3.

Table 25. Ratios between surface areas of specific bands calculated using spectra deconvolution

Plasma condition	A_1/A_3 (Si-$(CH_3)_x$/TO_3)	A_2/A_3 (LO_4/TO_3)
3	0.11	0.58
7	0.09	0.74
8	0.08	0.55

Finally, surface chemistry and morphology enable to understand that the higher efficiency of the condition 3 is due to both a low polar part, likely owed by a certain carbon content in the thin film and a roughness lower than 60 nm.

To sum up, in this section the influence of plasma parameters on surface properties and fouling deposit was studied through an experimental design. A Plackett-Burman design including 12 experiments was generated to investigate the potential influence of plasmagenic gas (N_2) flow rate, HMDSO flow rate, nozzle-to-substrate distance, scanning speed, frequency and number of cycles.

The influence of plasma parameters was first investigated on surface properties: (i) wettability, (ii) surface free energy, (iii) polar part and (iv) roughness. As the initial determination (R^2) and prediction (Q^2) coefficients were too low for WCA and SFE, these responses were not studied.

Regarding the polar part, no correlation with plasma parameters was ventured as the predicted parameters for its minimization were not coherent. The experimental design did not allow either to correlate roughness to manufacturing plasma parameters. In fact, the optimization corresponded to an experiment which was from the experimental design to

increase the statistical significance of the model. Consequently, it seems that the type of design or limits of variables were not adapted.

Secondly, the influence of plasma parameters on fouling deposit was studied. The optimization of plasma parameters was coherent with experimental results as it led to the condition 3 which demonstrated excellent fouling-release performances for at least two additional fouling cycles. Surface properties, chemistry and morphology show that a low polar part, likely owed by a certain carbon content in the thin film and a roughness lower than 60 nm leads to a fouling deposit reduction of 86% after two uses.

Another type of plasma coating was investigated to improve fouling-release performances: superhydrophobic plasma bilayer. The next section will present the development of this plasma bilayer deposited from two precursors. Two plasma parameters will be studied: HMDSO flow rate and frequency (power).

V. Bilayers deposition by atmospheric pressure plasma

As mentioned in part 1.3.3. Dowling *et al.*[212] demonstrated the effectiveness of superhydrophobic thin film deposited by an APP torch to mitigate $CaCO_3$ fouling. This superhydrophobic coating was obtained by mixing two precursors. This section will be focused on the development of superhydrophobic thin films from two precursors as well, but injected alternatively in the post-discharge leading to the formation of plasma bilayer coating.

5.1. Plasma coating deposition from the injection of two precursors

To date, no study has demonstrated the deposition of bilayers by atmospheric pressure. In most of investigations dealing with two precursors, these are mixed before the injection or introduced separately but through the same channel, either directly in the plasma or in the post-discharge. These studies are gathered in Table 26.

Table 26. Investigations reporting atmospheric pressure plasma deposition of two precursors

Precursors	Mixing before injection	Type of injection	Injection site	Plasma type	References
HMDSO/Toluene	✓	Vaporization	Discharge	DBD	[220]
TEOS/FP TEOS/FS TC/FP TC/FS	✓	Nebulization	Discharge	Plasma jet (PlasmaSream®, Dow Corning)	[212]
APTES/FLUSI	✓	Atomization	Post-discharge	APP torch (PlasmaSpot®, Vito)	[211]
APTES/PFH	✓	Atomization	Post-discharge	APP torch (PlasmaSpot®, Vito)	[235]
PFDA/DOCA		Atomization	Discharge	DBD	[236]
HMDSO/APTES	✓ (separate vaporization)	Vaporization	Post-discharge	APP torch	[237]
TMS/APTES	✓(separate vaporization)	Vaporization	Post-discharge	APP torch	[238]
HMDSO/Limonene	✓ (separate vaporization)	Vaporization	Post-discharge	APP torch (Plasmatreat)	[239]

In this thesis, the design of a setup allowing to alternate the deposition of different precursors will be presented, and the obtained superhydrophobic plasma bilayer will be characterized.

5.2. Development of superhydrophobic plasma bilayer deposition

5.2.1. Atmospheric pressure plasma process

5.2.1.1. Samples preparation

316L-2B stainless steel samples (45 x 15 mm² and 10 x 15 mm²) were first cleaned using the protocol detailed in Materials and Methods part. Before plasma deposition, they were submitted to a N_2 plasma pre-treatment using the Lab-Scan (Figure 37) to improve thin film-substrate adhesion.[11] Pre-treatment parameters are gathered in Table 14. Between the pre-treatment and deposition, samples were left for 15 min to cool down.

Although the speed of the air extractor was of 13 m/s as well, it is important to note that these plasma depositions were performed in a different laboratory (laboratory 3). Therefore, previous results on HMDSO deposition cannot be taken into account for this section.

5.2.1.2. *Bilayer deposition process*

To deposit several layers a second nebulizer (Mira-Mist, Burgener Reasearch, Canada) was fixed to the 3-axis robot. As previously described, HMDSO (Figure 52 A) was driven to the nebulizer by pumping (M12 mini CORI-FLOW, Bronkhorst, France) and the second precursor; *1H,1H,2H,2H* perfluorooctyltriethoxysilane (pFOTES) (Figure 52 B) was driven to the second nebulizer through a syringe pump (NE-300, New Era Pump System, United States).

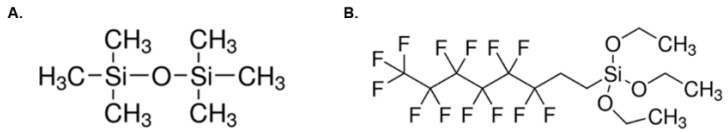

Figure 52. Chemical structure of (A) HMDSO and (B) pFOTES precursors

In both nebulizers nitrogen gas was introduced, producing an aerosol which was sprayed into the post-discharge as illustrated in Figure 53.

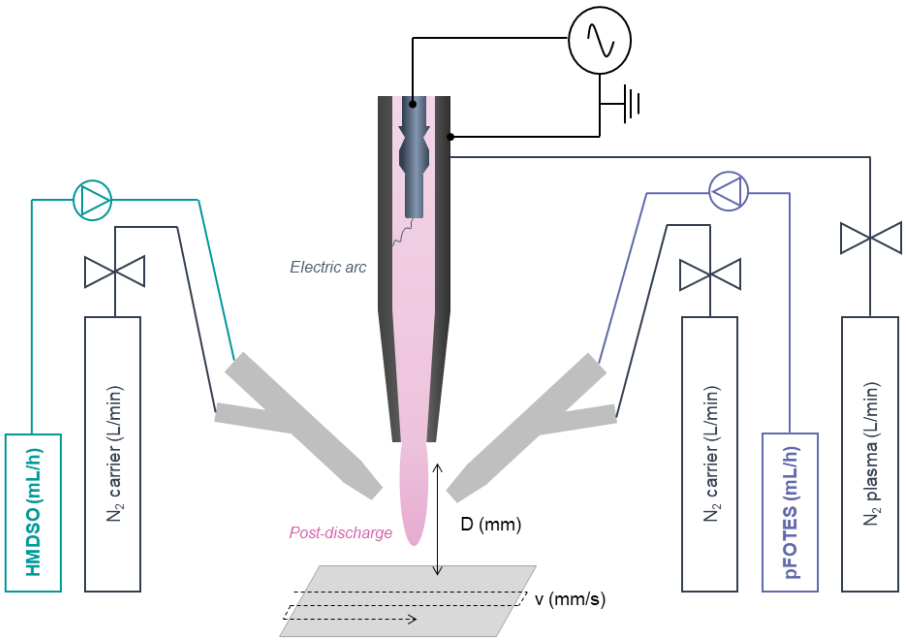

Figure 53. Schematic diagram of APP torch with the double injection system.

Mono and bilayers were deposited onto activated stainless steel surfaces. Plasmagenic gas (N_2), frequency, nozzle-to-substrate and scanning speed were set to 60 L/min, 80 kHz, 20 mm and 100 mm/s respectively. The deposition of monolayers was performed by one cycle. Two cycles (one cycle of each precursor) were performed for the bilayer. Carrier gas and precursors flow rates are reported in Table 27. For the bilayer deposition, samples were left for 15 min to cool down between HMDSO and pFOTES deposition. This time (15 min) was chosen randomly and will deserve optimization in further work.

Table 27. Carrier gas and precursors flow rates for mono and bilayers deposition

Sample	Step	HMDSO (mL/h)	N_2 Carrier (L/min)	pFOTES (mL/h)	N_2 Carrier (L/min)
H20		20	1.1	0	0
F20		0	0	20	1.1
H20F20	1	20	1.1	0	0
	2	0	0	20	1.1

5.2.2. Surface characterizations

Monolayers deposited either from HMDSO or pFOTES and bilayer deposited from both precursors were characterized to assess surface properties (wettability, surface free energy and roughness), surface chemistry and morphology. Ageing of the different thin layers in air was evaluated by WCA measurements.

5.2.2.1. Surface properties

Surface properties of both plasma monolayers and bilayer were analyzed: (i) wettability, (ii) surface free energy and (iii) roughness. The analysing methods are detailed in the Materials and Methods section. Surface properties of bare and modified stainless steel samples are gathered in Table 28. Contact angle measurements were performed using water at room temperature to assess wettability and using the model fluid (fouling solution) beforehand heated to 85°C to evaluated its spreading behaviour onto both bare stainless steel and plasma coatings.

Table 28. Surface properties of HMDSO and pFOTES monolayers and HMDSO/pFOTES bilayer

Sample	WCA (°)	CA with MF* (°)	Surface free energy (mNm)			R_a (nm)
			γ^{TOT}	γ^{D}	γ^{P}	
REF	81.9 ± 0.8	72.8 ± 1.1	34.7 ± 11.8	31.1 ± 8.5	3.3 ± 3.3	41 ± 7
H20	107.7 ± 3.1	105.3 ± 2.7	19.2 ± 0.3	18.8 ± 0.3	0.4 ± 0.1	42 ± 2
F20	138.1 ± 3.4	131.8 ± 2.6	4.0 ± 0.0	4.0 ± 0.0	0.0 ± 0.0	48 ± 2
H20F20	Superhydrophobic	149.7 ± 2.8	N/D	N/D	N/D	42 ± 3

*MF: model fluid (fouling solution)

Both HMDSO and pFOTES monolayers are hydrophobic showing WCA of 107.7° and 138.1° respectively. WCA of pFOTES coating is higher than those obtained by Dowling *et al.*[212] (120°) and Ma *et al.*[213] (126°) which is likely due to the different plasma sources and parameters used. The deposition of water droplets onto HMDSO/pFOTES bilayer was impossible, thus the combination of both precursors generated a superhydrophobic thin film.

A decrease of around 10° was observed onto bare SS using model fluid, leading to a CA of 72° which is consistent with the work of Ozden [240] who measured a CA of 72° onto stainless steel with whole milk. For both monolayers and bilayer, the same trend is observed, CA decreases using the model fluid. This can be explained by the lower surface tension of the model fluid (53.2 ± 1.1 mN/m), which was measured by the pendant drop method. This value can be explained by the temperature (the model fluid was beforehand heated before) and by the presence of proteins. [241], [242]

Regarding surface free energy, as expected the higher the WCA, the lower the SFE. Nonetheless, the SFE of HMDSO and pFOTES thin films do not fit in the fouling-release range, which finds between 20 and 30 mN/m. For the bilayer, the SFE was not calculated as the coating is superhydrophobic.

Taking into account standard deviations, arithmetic mean roughness of monolayers and bilayer does not differ from that of bare stainless steel. R_a values of plasma coatings are lower than 50 nm, which should be favourable to mitigate dairy fouling deposit.

5.2.2.2. Plasma coatings adhesion and ageing

The adhesion of both monolayers and bilayer was assessed using cross-hatch test, described in Materials and Methods section. All types of thin films showed a 5B grade, corresponding to a very good adhesion to stainless steel substrate.

It is known that plasma polymers can rearrange themselves after few days.[243], [244] Therefore, the stability of both monolayers and bilayer were evaluated by WCA measurements. Samples were stored in Petri dishes for 28 days. Plasma thin films ageing is displayed in Figure 54. WCA increases of 7° for HMDSO coating whereas it decreases of 4° for pFOTES. This WCA could be due to a rearrangement of polymer chains as stated by former works [243], [244] or to the adsorption of carbon. This phenomenon was observed for laser-ablated stainless steel surfaces.[245] Likely owed by fluorine groups, pFOTES monolayer is slightly more stable than HMDSO monolayer. Regarding the plasma bilayer, the deposition of water droplets was impossible for 28 days, highlighting an excellent stability.

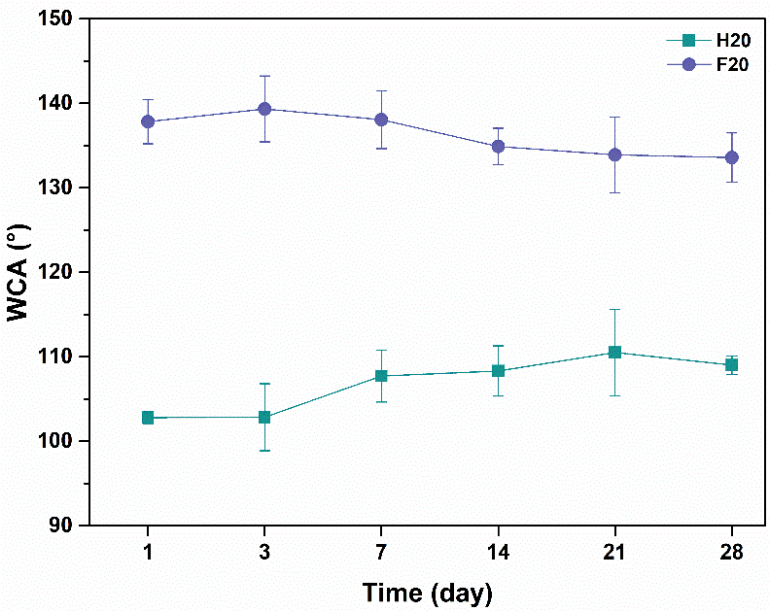

Figure 54. Assessment of plasma coatings ageing in air for 28 days.

5.2.2.3. Morphology

The morphology of monolayers and bilayer were observed by SEM (Figure 55). Although nanoparticles were observed for both HMDSO and pFOTES coatings, HMDSO thin film shows a higher number of nanoparticles with larger aggregates. O'Neill *et al.*[246] pointed out the influence of precursor volatility on vaporization which impacts the roughness. As the volatility of HMDSO is higher (20 hPa at 20 °C) than that of pFOTES (0 hPa at 25 °C), the vaporization of HMDSO is higher leading to a rougher coating. The HMDSO/pFOTES bilayer looks as rough as HMDSO monolayer, as HMDSO was deposited before pFOTES. This is consistent with the study of Carpentier *et al.*[247] who deposited a bilayer of hexamethyldisilane (HMDS) and heptadecafluoro-1-decen (HDFD) by a microwave plasma at low pressure.

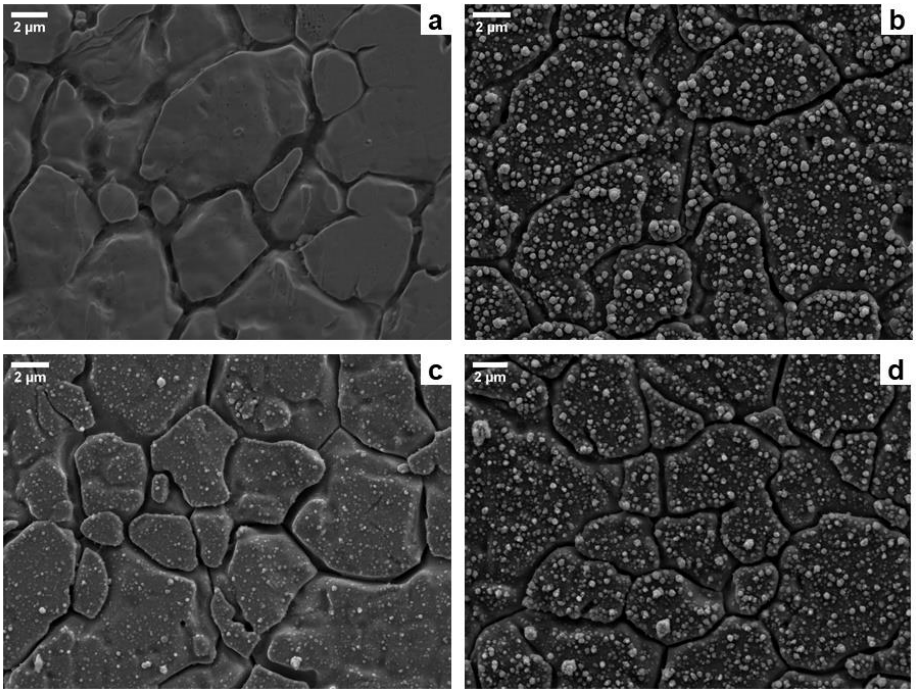

Figure 55. SEM images of (a) bare stainless steel, (b) HMDSO monolayer, (c) pFOTES monolayer and (d) HMDSO/pFOTES bilayer

5.2.2.4. Surface chemistry

To study the chemical composition of both monolayers and bilayer FTIR spectroscopy in ATR mode was used (Figure 56). FTIR spectra were recorded in 4000-400 cm^{-1} range and peaks attribution for each plasma coating is reported in Table 29. All plasma conditions show characteristic peaks of siloxane-based thin films around 1200-1000 cm^{-1}, 800 cm^{-1} and 450 cm^{-1}. As previously observed, several peaks around 1275 cm^{-1} and 800 cm^{-1} confirm the presence of carbon content in all thin films. Characteristic bands of CF_x groups find between 1250 cm^{-1} and 1000 cm^{-1}, overlapping Si-O-Si network. Therefore, this broad peak was deconvoluted.

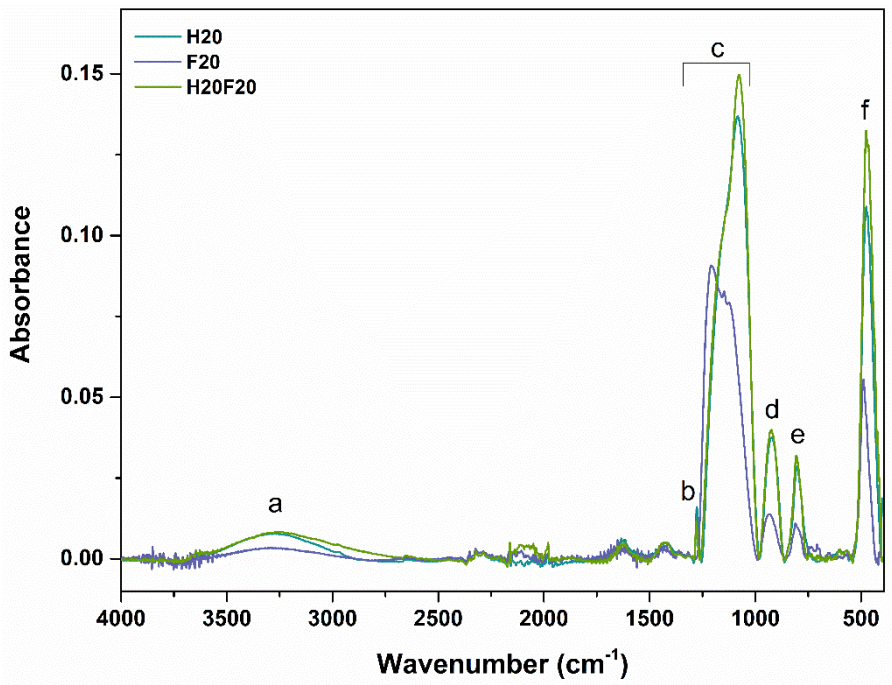

Figure 56. FTIR spectra of plasma coatings (in blue: HMDSO coating, in purple: pFOTES coating and in green: HMDSO/pFOTES coating).

Table 29. Peaks assignment for each plasma coating.

Peak ID	Wavenumber (cm^{-1})	Peaks attribution	References
a	3300-3250	ν O-H	[232]
b	1280	δ^s Si-$(CH_3)_x$	[225], [233]
c	1200-1080	ν^a Si-O-Si (TO_3), CF_X	[232], [211]
d	930-900	ν Si-OH	[225], [233]
e	800	ν^s Si-O-Si (TO_2), ρ Si-C in Si-$(CH_3)_x$	[225], [232]
f	480	ρ Si-O-Si (TO_1)	[232], [234]

The deconvolution of mono and bilayers is displayed in Figure 57 and peaks assignment is reported in Table 30. HMDSO monolayer presents characteristic bands of the Si-O-Si network, previously observed. Regarding pFOTES monolayer, Si-O-Si network is observed as well. Moreover, characteristics bands of CF_x groups can be noticed at 1241 cm^{-1} and 1147 cm^{-1}. Resulting bands in HMDSO/pFOTES bilayer confirm the presence of fluorine (at 1228 cm^{-1} and 1149 cm^{-1}). In order to evaluate its repartition along the depth of the coating and validate the deposition of two layers, ToF-SIMS analyses were performed.

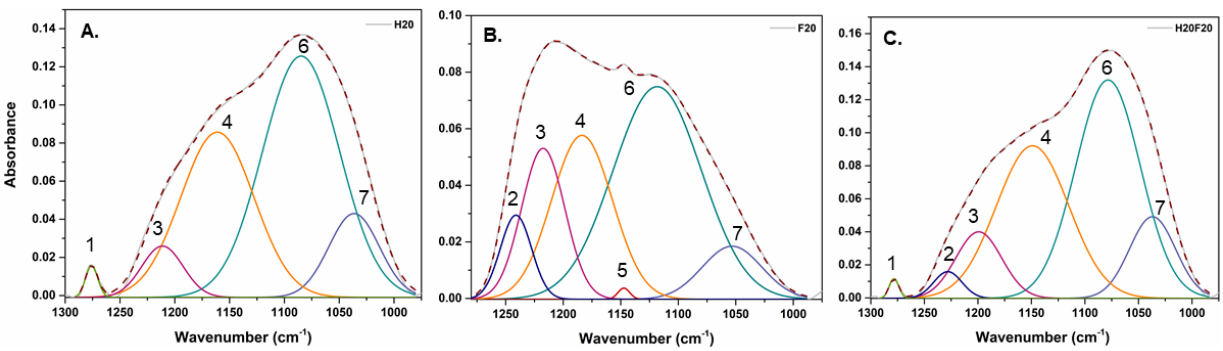

Figure 57. Deconvoluted FTIR spectra in the 1300-970 cm^{-1} range. (A)HMDSO monolayer. (B) pFOTES monolayer. (C) HMDSO/pFOTES bilayer.

Table 30. Assignment of deconvoluted bands of mono and bilayers.

Peak number	Wavenumber (cm^{-1})			Peaks attribution	References
	H20	F20	H20F20		
1	1276		1278	δ^s Si-$(CH_3)_x$	[225], [233]
2		1241	1228	ν^a CF_2	[210], [211], [213], [247]
3	1211	1217	1199	OCH_2CH_3	[211], [235]
4	1161	1184	1149	ν^a Si-O-Si (LO_4) (angle ~ 150°), Si-O-C	[232], [233]
5		1147		ν^a CF_3	[210], [211], [247]
6	1085	1118	1078	ν^a Si-O-Si (TO_3) (angle ~ 144°)	[232], [233]
7	1036	1053	1037	ν^a Si-O-Si (angle < 144°)	[232], [233]

5.2.2.5. Depth profile analysis of the plasma bilayer

ToF-SIMS depth profiles of bare silicon wafer, plasma mono- and bilayers onto silicon wafer were performed to validate the deposition of two layers. The mono- and bilayers were deposited with plasma parameters reported in Table 27. Resulting depth profiles are displayed Figure 58.

For bare silicon wafer, a strong signal corresponding to Si^- is obtained, while for HMDSO monolayer, intense O^-, SiO_2^- and SiO_3^- signals can be observed.

An intense F^- signal is firstly observed in the depth profile of the pFOTES monolayer corresponding to fluorine groups, combined with a SiO_2^- signal corresponding to the siloxane backbone. Although depth profile analysis does not allow to precisely measure the coating thickness, pFOTES monolayer may be thinner than HMDSO layer since the sputter time to reach the substrate (Si^- signal) is shorter.

Finally, for HMDSO/pFOTES bilayer, two layers can be successfuly identified. The first one is characterized by fluorine-based signals F^- and SiO_2F^-, resulting from the decomposition of pFOTES monomer. The second one shows an intense signal corresponding to SiO_2^- fragment

and, by comparing the HDMSO and pFOTES monolayers signatures with the one of the bilayer, it is likely that this intense SiO_2^- signal comes from a HMDSO monolayer.

Hence, this analysis successfully confirmed that we managed to build a plasma bilayer from successive HMDSO and pFOTES plasma torch polymerization.

Some other useful information can be obtained with this analysis. Firstly, by taking into account sputter times HMDSO/pFOTES bilyer seems as thick as HMDSO monolayer. Besides, it is important to note fluorine-based signals are also observed more deeply, which could testify for a potential rearrangement of polymer chains or could be due to a competition between etching and deposition processes.

Figure 58 E presents post-processing of depth profiles data allowing to 2D reconstructions in x-z directions. These results highlight the presence of a fluorine-based layer, located at the outer surface (F^- and SiO_2F^- fragments) and the presence of a second siloxane-based layer (SiO_2^- fragment). This confirms the deposition of a bilayer by APP torch.

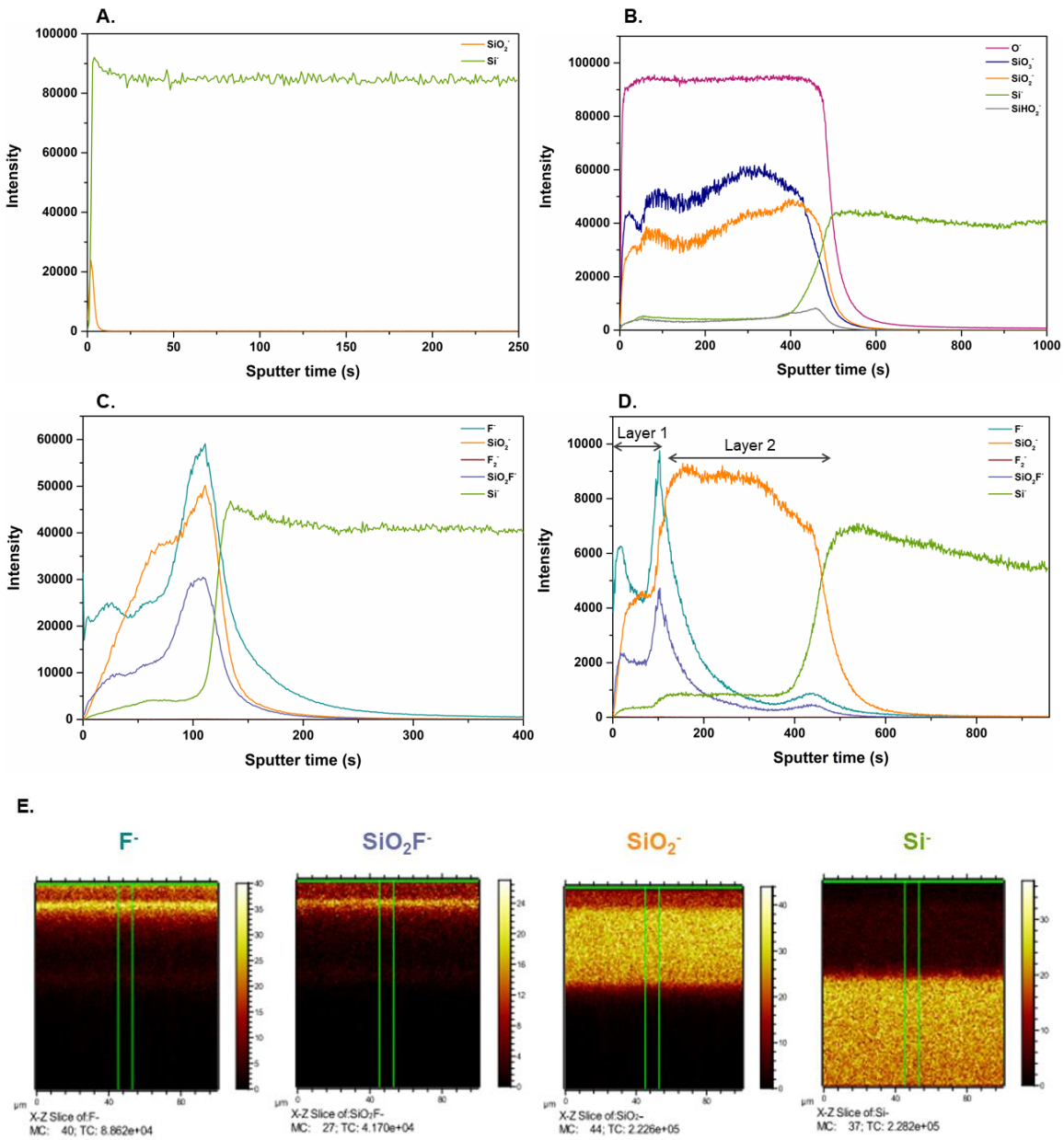

Figure 58. ToF-SIMS depth profiles of (A) bare silicon wafer, (B) HMDSO plasma monolayer, (C) pFOTES plasma monolayer, (D) HMDSO/pFOTES plasma bilayer onto silicon wafer and (E) 2D reconstruction (x-z direction) of the bilayer.

5.2.3. Fouling-release performances

As demonstrated in the part 3, HMDSO plasma coatings showed good fouling-release performances. Consequently, only fouling-release properties were assessed in this section. The fouling test was run for one hour, using WPC powder batch U20454 followed by a hot water-rinsing for 20 min.

Fouling-release performances of HMDSO and pFOTES monolayers as well as HMDSO/pFOTES bilayer are displayed in Figure 59. HMDSO monolayer does not reach fouling-release performances as good as previously obtained as it shows a fouling deposit reduction of 14 ± 19%. Although HMDSO/pFOTES was superhydrophobic, it was slightly less efficient than pFOTES monolayer to reduce fouling deposit: 54 ± 24% against 65 ± 17% respectively. This can be explained by the presence of large nanoparticles in both HMDSO monolayer and HMDSO/pFOTES bilayer making the surface rougher, which could favour the attachment of native whey proteins and calcium clusters.[10] The comparison of fouling deposits displayed in Annex 5, shows that fouling is less homogenous onto coatings containing fluorine, likely due to its anti-adhesive property. The fact that the fouling layer was not completely removed after the rinsing could be due to a heterogeneous fluorine distribution in plasma coatings.

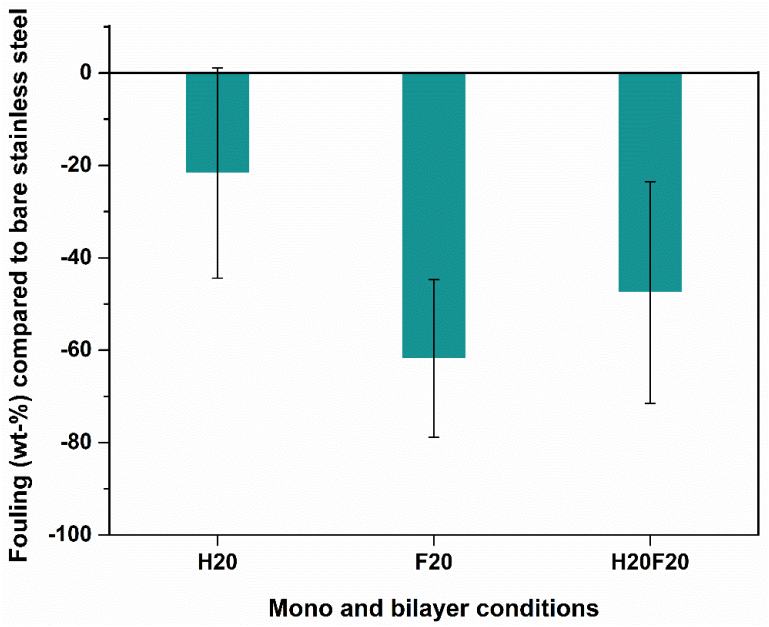

Figure 59. Fouling-release performances as the function of plasma mono and bilayers.

Although pFOTES monolayer exhibits better fouling-release performances, HMDSO/pFOTES bilayer is more stable, which could lead to a better durability. Therefore, two plasma parameters were investigated to improve fouling-release properties of the bilayer. In order to reduce the formation of large nanoparticles, which seems to favour fouling growth, the influence of (i) HMDSO flow rate and (ii) plasma power on the bilayer deposition was studied. Indeed, O'Neill *et al.*[246] pointed out the influence of precursor volatility on

vaporization which impacts the roughness. Thus, the decrease of HMDSO flow rate could decrease the formation of large nanoparticles leading to a lower roughness. On the other hand, Massines *et al.*[201] highlighted that the power decrease can limit the precursor fragmentation and thus the formation of large nanoparticles.

5.3. Influence of HMDSO flow rate for bilayer deposition

5.3.1. Plasma parameters

HMDSO/pFOTES bilayers were deposited onto stainless steel samples. Prior to plasma treatment, they were cleaned and pre-treated as described above (part 4.2.1.1.). As previously, plasmagenic gas (N_2), frequency, nozzle-to-substrate and scanning speed were set to 60 L/min, 80 kHz, 20 mm and 100 mm/s respectively. One cycle of each precursor was performed. Carrier gas and precursors flow rates are reported in Table 31 (Figure 53). Between HMDSO and pFOTES deposition, samples were left for 15 min to cool down.

Table 31. Carrier gas and precursors flow rates of bilayers deposition

Sample	Step	**HMDSO (mL/h)**	N_2 Carrier (L/min)	pFOTES (mL/h)	N_2 Carrier (L/min)
H20F20	1	**20**	1.1	0	0
	2	0	0	20	1.1
H10F20	1	**10**	1.1	0	0
	2	0	0	20	1.1
H5F20	1	**5**	1.1	0	0
	2	0	0	20	1.1

In bold: investigated parameter

5.3.2. Surfaces characterizations

Surface properties (wettability, surface free energy and roughness), morphology and surface chemistry of bilayers were analyzed to assess the potential influence of HMDSO flow rate. Adhesion to stainless steel substrate was evaluated as well as the ageing.

5.3.2.1. Surface properties and adhesion

To assess the adhesion of bilayer as the function HMDSO flow rate, cross-hatch test was used. All types of bilayer showed a 5B grade (Table 32), corresponding to a very good adhesion to stainless steel substrate.

Table 32 reports wettability, surface free energy and roughness results of plasma bilayers. Moreover, as previously, contact angle measurements were carried out using the model fluid (fouling solution), which was heated at 85°C then deposited onto samples.

The decrease of HMDSO flow rate demonstrates no influence on wettability. In fact, as observed previously for the bilayer, the deposition of water droplets was impossible whatever the HMDSO flow rate. Consequently, SFE cannot be determined as all HMDSO/pFOTES bilayers are superhydrophobic.

Regarding CA measurements with the model fluid, and taking into account standard deviations, the three bilayers exhibit very high values close to 150°. Thus, contact angle hysteresis was calculated to identify if the thin films show a Wenzel or Cassie-Baxter state.

Whatever the HMDSO flow rate, model fluid droplets did not roll on the surface and remained stick as illustrated in Figure 60 b, corresponding to the Wenzel state. As a result, it is likely that the decrease of HMDSO flow rate will not improve fouling-release performances due to the high CAH.

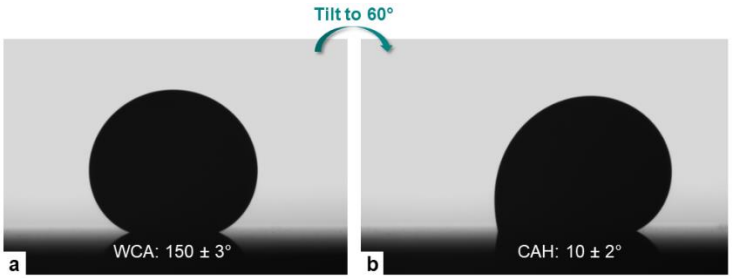

Figure 60. CAH measurement (a) Before surface tilting and (b) After surface tilting

Furthermore, variations of HMDSO flow rate induced no significant difference for arithmetic mean roughness (Table 32) Therefore, samples were observed by SEM to analyze their morphology.

Table 32. Surface properties and adhesion of HMDSO/pFOTES bilayers

Sample	WCA (°)	CA (°) with MF*	Surface free energy γ^{TOT} (mN/m)	R_a (nm)	Adhesion grade
REF	81.9 ± 0.8	72.8 ± 1.1	34.4 ± 11.8	41 ± 7	-
H20F20	Superhydrophobic	149.7 ± 2.8	N/D	42 ± 3	5B
H10F20	Superhydrophobic	147.4 ± 3.6	N/D	40 ± 5	5B
H5F20	Superhydrophobic	146.4 ± 3.1	N/D	48 ± 3	5B

*MF: model fluid (fouling solution)

5.3.2.2. Morphology

SEM images of bilayers are displayed in Figure 61. Nanoparticles can be observed in all bilayers coatings, whatever HMDSO flow rate. Nevertheless, Figure 61 c which corresponds to the lower HMDSO flow rate, demonstrates a decrease of large aggregates. This is consistent

with the works of Asadollahi *et al.* and Roth *et al.* who claimed that at a given power, the amount of energy available per molecule increases with the decrease of monomer flow rate. Thus leading to an increase of in particle charge which inhibits aggregation and prevents the formation of larger particles.[224], [248]

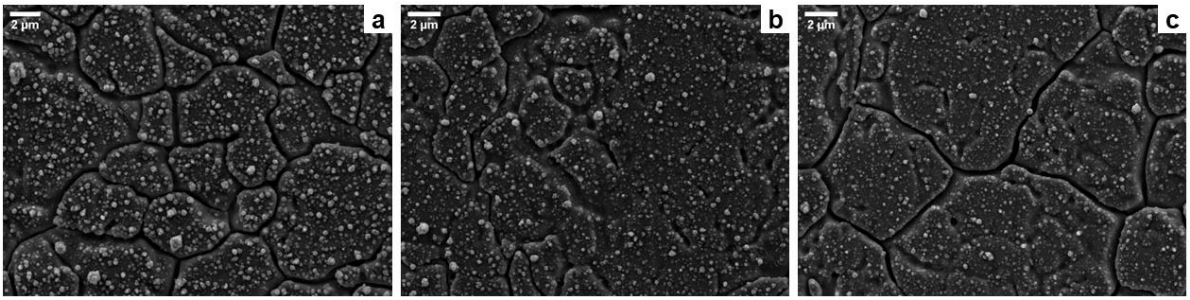

Figure 61. SEM images of HMDSO/pFOTES bilayers (a) HMDSO flow rate: 20 mL/h, (b) HMDSO flow rate: 10 mL/h, (c) HMDSO flow rate: 5 mL/h

5.3.2.3. Surface chemistry

The chemical composition of plasma bilayers as the function of HMDSO flow rate was analyzed by FTIR spectroscopy in ATR mode. Resulting spectra in 4000-400 cm^{-1} range are displayed in Figure 62 and peaks assignment is reported in Table 29. According to the Figure 62, the reduction of HMDSO flow rate does not influence the surface chemistry of the plasma bilayers. This is consistent with the study of Zouaghi *et al.* who revealed that the chemical composition of HMDSO did not differ as the function of the flow rate.[113] Nonetheless, it can noted that the intensity of the peak at 1200-1080 cm^{-1} decreases with HMDSO flow rate. Thus, as the Si-$(CH_3)_x$ band is present in the three spectra at the same position (1280 cm^{-1}), it can be concluded that the higher the HMDSO flow rate, the thicker the plasma bilayer.

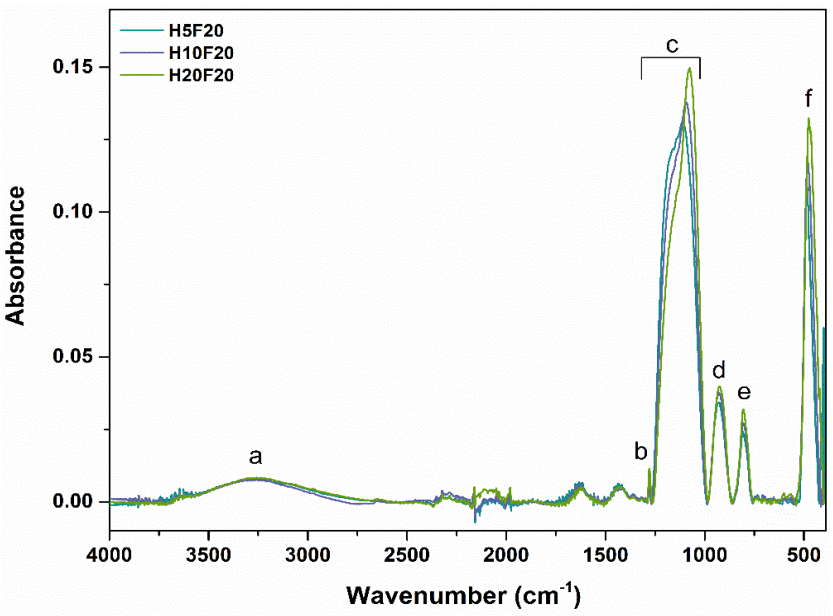

Figure 62. FTIR spectra of plasma bilayers (in blue: HMDSO flow rate: 5 mL/h, in purple: HMDSO flow rate: 10 mL/h and in green: HMDSO flow rate: 20 mL/h).

5.3.3. Fouling-release performances

Fouling-release performances of the three types of plasma bilayers were evaluated to point out the potential effect of HMDSO flow rate. The fouling test was run for one hour, using WPC powder batch U20454 followed by a hot water-rinsing for 20 min.

Figure 63 presents resulting fouling-release performances. HMDSO flow rate reduction has no influence as all bilayers exhibit a fouling deposit reduction around 50 %. Although, the reduction of HMDSO flow rate reduces the formation of larger particles, H5F20 condition (*i.e.* lowest HMDSO flow rate) did not display better fouling-release performances than H20F20 (*i.e.* highest HMDSO flow rate).

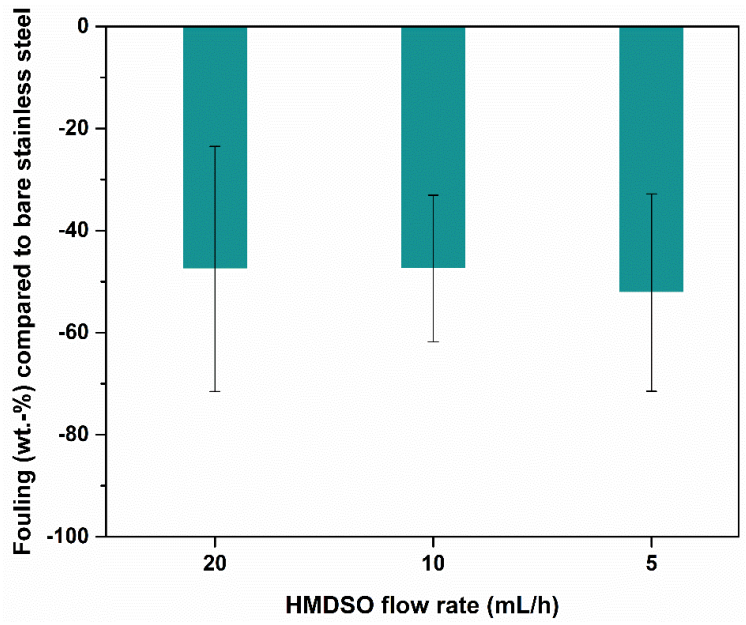

Figure 63. Fouling-release performances of plasma bilayers as the function of HMDSO flow rate.

The decrease of HMDSO flow rate did not allow any improvement of fouling-release properties, as all plasma bilayers showed a similar reduction around 50%. Consequently, at this point, the plasma bilayer remains less performant than pFOTES monolayer.

5.4. Influence of power for bilayer deposition

As emphasized by several authors, the decrease of plasma power decreases the available energy per molecule leading to a lower fragmentation of monomer. This can prevent the formation of large nanoparticles.[224], [226], [248] Therefore, the influence of power is studied in this part.

5.4.1. Plasma parameters

Plasma bilayers were deposited using the process detailed in Figure 53. Prior to thin coating deposition, samples were cleaned and pre-treated as described above (part 4.2.1.1.). As previously, plasmagenic gas (N_2), nozzle-to-substrate and scanning speed were set to 60 L/min, 20 mm and 100 mm/s respectively. One cycle of each precursor was performed. Frequency, carrier gas and precursors flow rates are reported in Table 33. Between HMDSO and pFOTES deposition samples were left for 15 min to cool down.

Table 33. Plasma parameters of bilayers deposition as the function of the frequency

Sample	Step	**Frequency (kHz)**	HMDSO (mL/h)	N_2 Carrier (L/min)	pFOTES (mL/h)	N_2 Carrier (L/min)
H20F20 80	1	**80**	20	1.1	0	0
	2		0	0	20	1.1
H20F20 135	1	**135**	20	1.1	0	0
	2		0	0	20	1.1
H20F20 190	1	**190**	20	1.1	0	0
	2		0	0	20	1.1

In bold: investigated parameter

Bres demonstrated that the plasma generator developed by AcXys technologies showed a negative correlation between the power and frequency. This phenomenon can be explained by the characteristics of the power supply used.[207] Consequently, increasing the frequency leads to power decrease (Annex 3 Figure 109).

As power varied during plasma treatments, a mean power is reported in Table 34 for each set frequency.

Table 34. Correlation between set frequency and power

Set frequency (kHz)	Mean power during the plasma treatment (W)
80	1515
135	1315
190	1115

5.4.2. Surfaces characterizations

Plasma treated samples were analysed to observed the impact of power. Surface properties (wettability, surface free energy and roughness), morphology and surface chemistry, as well as adhesion and ageing were studied.

5.4.2.1. Surface properties

Surface properties of HMDSO/pFOTES bilayers are gathered in Table 35. In this part, CA measurements using the model fluid (fouling solution) were performed as well. As mentioned above, before its deposition onto samples, the model was heated at 85 °C.

A CA decrease can be noticed with both water and model fluid as the function of plasma power. This could be due to a reduction of nanoparticles leading to smoother thin film or a poorer retention of CF_X groups reducing the anti-adhesive effect.

Regarding surface free energy, as expected the higher the WCA, the lower the SFE. Nonetheless, it can be noted that, although the SFE increases with the decrease of power, the polar part is in the same order of magnitude. At high power (*i.e.* low frequency), the SFE was not calculated as the coating is superhydrophobic.

According to R_a measurements, roughness increases with the decrease of power. Morphology of plasma bilayers was analyzed to confirm this trend.

Table 35. Surface properties of HMDSO/pFOTES bilayers

Sample	WCA (°)	CA (°) with MF*	Surface free energy (mNm)			R_a (nm)
			γ^{TOT}	γ^{D}	γ^{P}	
REF	81.9 ± 0.8	72.8 ± 1.1	34.4 ± 11.8	31.1 ± 8.5	3.3 ± 3.3	41 ± 7
80	Superhydrophobic	149.7 ± 2.8	N/D	N/D	N/D	42 ± 3
135	128.3 ± 2.0	123.5 ± 2.0	5.0 ± 0.3	4.8 ± 0.2	0.2 ± 0.1	44 ± 3
190	113.8 ± 1.1	110.6 ±1.1	10.9 ± 3.0	10.6 ± 2.4	0.2 ± 0.5	51 ± 2

*MF: model fluid (fouling solution)

5.4.2.2. Plasma bilayers adhesion and ageing

The adhesion of bilayers was assessed using cross-hatch test. All types of thin films showed a 5B grade, corresponding to a very good adhesion to stainless steel substrate.

As previously mentioned, plasma polymer can be unstable after few days. Consequently, WCA measurements were carried out to evaluate the stability of bilayers over 28 days. Between each measurement, samples were stored in Petri dishes. Ageing of plasma bilayers is presented in Figure 64. At high power (*i.e.* low frequency: 80 kHz) the deposition of water droplets was impossible for 28 days, pointing out an excellent stability. At lower power (*i.e.* higher frequency: 135 and 190 kHz) wettability slightly decreased. This very low variation of WCA allows to confirm the good stability whatever the plasma power.

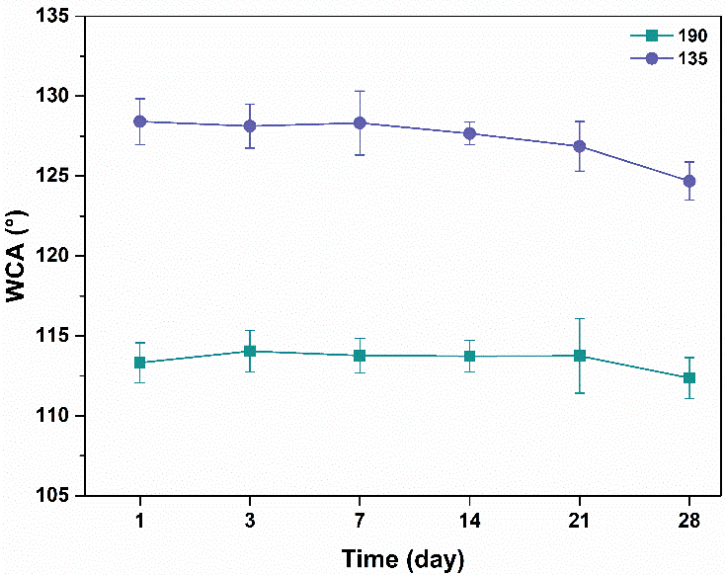

Figure 64. Assessment of plasma bilayers ageing as the function of power in air for 28 days.

5.4.2.3. Morphology

Figure 65 displays SEM images of plasma bilayers as the function of power. It can be noticed that the higher the power, the higher the number of nanoparticles and the larger the nanoparticles. This observation corroborates the study of Ussenov *et al.* highlighting an increase of nanoparticles size with the power.[226]

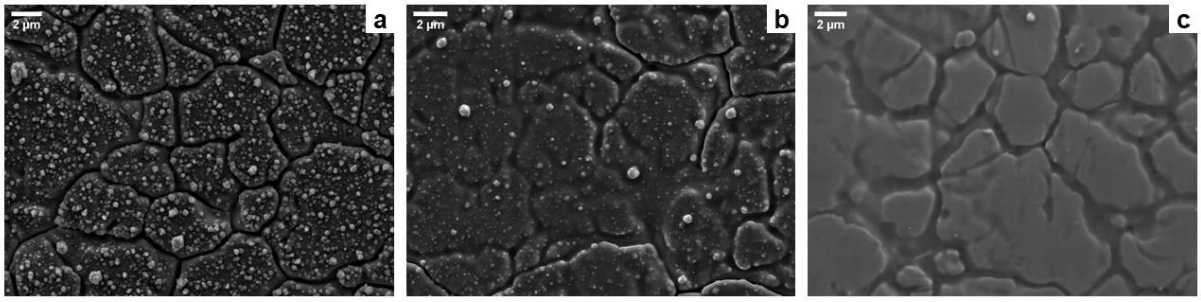

Figure 65. SEM images of HMDSO/pFOTES bilayers (a) Frequency: 80 kHz, Power: 1515 W, (b) Frequency: 135 kHz, Power: 1315 W, (c) Frequency: 190 kHz, Power: 1115 W.

5.4.2.4. Surface chemistry

In order to assess the power influence on the chemical composition of the bilayers FTIR spectroscopy in ATR mode is used. Figure 66 displays full range (4000-400 cm^{-1}) spectra. Except “g” peak, all identified peaks are reported in Table 29. This “g” peak observed at low power corresponds to a C-H bonding which could be due to a lower fragmentation. Moreover, at the lowest power (*i.e.* frequency: 190 kHz) the shape of the broad band at 1200-1080 cm^{-1} strongly differs from the two other spectra.

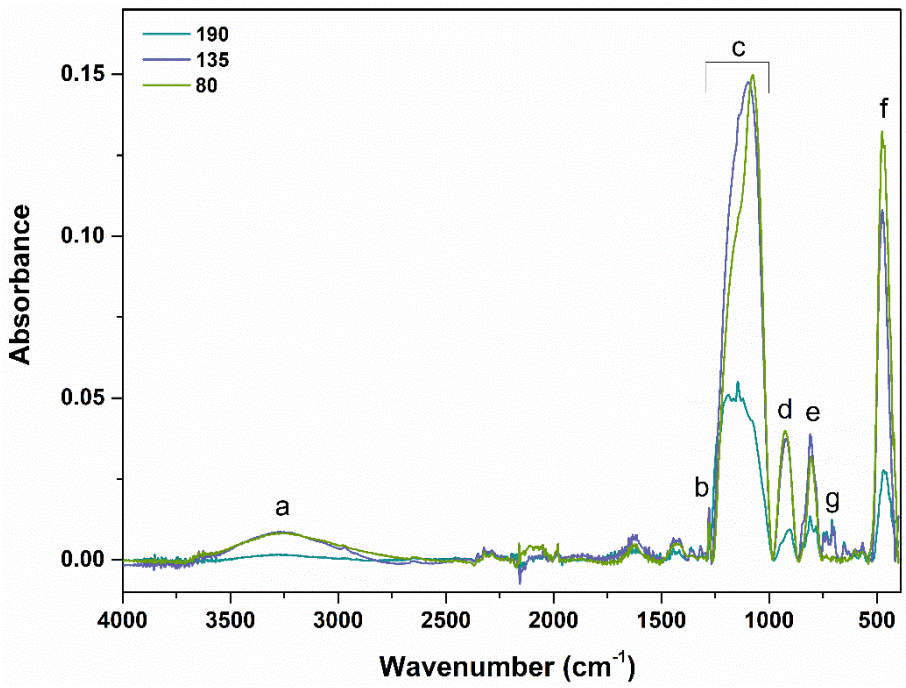

Figure 66. FTIR spectra of plasma bilayers (in blue: Frequency: 190 kHz, Power: 1115 W, in purple: Frequency: 135 kHz, Power: 1315 W and in green: Frequency: 80 kHz, Power: 1515 W).

To validate the power influence on the precursor fragmentation, FTIR spectra were deconvoluted in the 1290-970 cm^{-1} range to calculate the ratio between the surface area of the Si-$(CH_3)_x$ peak and the surface area of the Si-O-Si (TO_3) peak. As mentioned in section 4.4.4.3., this Si-$(CH_3)_x$/Si-O-Si(TO_3) ratio allows to estimate the carbon content in the coatings, bringing information on precursor fragmentation. [224] The calculation of both was done using surface areas under peaks 1 and 5 (Table 36) called A_1 and A_5 respectively.

Nonetheless, at the lowest power (*i.e.* highest frequency 190 kHz), the Si-$(CH_3)_x$ peak was located at the lower boundary of this range (1278 cm^{-1}), and its shape and intensity were possibly affected by the other peaks. As a result, the Si-$(CH_3)_x$/Si-O-Si ratio was not calculated. The deconvolution of bilayers as a function of power is displayed in Figure 67, and peaks assignment is reported in Table 36.

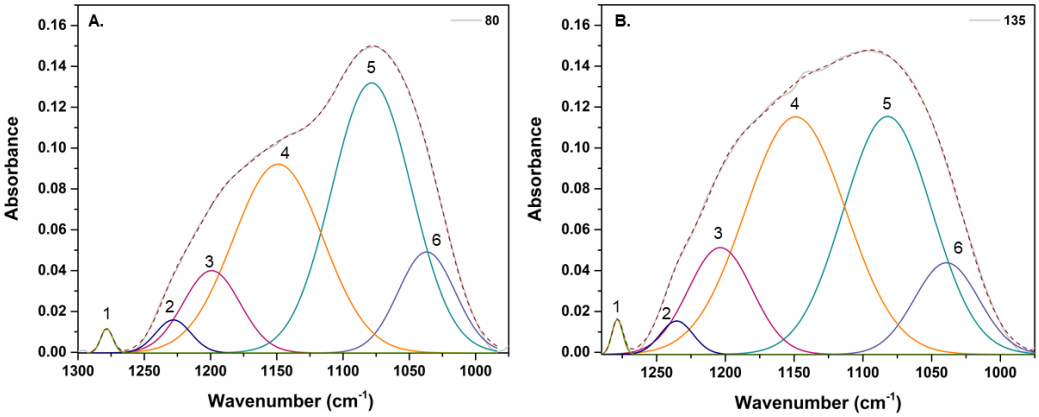

Figure 67. Deconvoluted FTIR spectra in the 1290-970 cm^{-1} range. (A) Frequency: 80 kHz (Power: 1515 W) and (B) Frequency: 135 kHz (Power: 1315 W)

Table 36. Assignment of deconvoluted bands as a function of frequence (and power).

Peak number	Wavenumber (cm^{-1}) 80	135	Peaks attribution	References
1	1278	1278	δ^s Si-$(CH_3)_x$	[225], [233]
2	1228	1235	ν^a CF_2	[210], [211], [213], [247]
3	1199	1203	OCH_2CH_3	[211], [235]
4	1148	1149	ν^a Si-O-Si (LO_4) (angle ~ 150°), Si-O-C, ν^a CF_3	[232], [233], [210], [211], [247]
5	1078	1082	ν^a Si-O-Si (TO_3) (angle ~ 144°)	[232], [233]
6	1036	1039	ν^a Si-O-Si (angle < 144°)	[232], [233]

The bilayer deposited at 80 kHz (1515 W) exhibits a Si-$(CH_3)_x$/Si-O-Si ratio of 0.013, while the bilayer at 135 kHz (1315 W) shows a ratio of 0.018. These results mean that a lower power leads to a higher carbon content, which is consistent with the work of Asadollahi *et al.* [224], who emphasized that the lower the power, the higher the carbon content and the lower the precursor fragmentation.

Therefore, at 190 kHz (1115 W) the fragmentation should theoretically be lower, increasing potentially the retention CF_x groups.

This corroborates also MEB analyses (Figure 65) showing large nanoparticles at high power likely owed by the high precursor fragmentation and no particles at low power.

5.4.3. Fouling-release performances

HMDSO/pFOTES bilayers were submitted to a pasteurization run to evaluate their fouling-release properties as the function of plasma power. WPC powder batch U20454 was used to prepare the model fluid, which was circulated for one hour. Samples were then rinsed with hot water for 20 min.

Fouling-release performances of plasma bilayers are showed in Figure 68. Although standard deviations are important, it seems that the fouling deposit slightly decreases with the power. The bilayer deposited at low power (*i.e.* high frequency) shows a fouling deposit reduction of 72 ± 20 % while a reduction of 48 ± 24 % is obtained for the bilayer deposited at high power. The absence of nanoparticles seems not favourable either to fully reduce fouling adhesion. An equilibrium has to be found between the deposition of very small particles as observed in section 3 (Figure 49 b) and the deposition of thin film with a good retention of CF_x groups allowing an anti-adhesive effect.

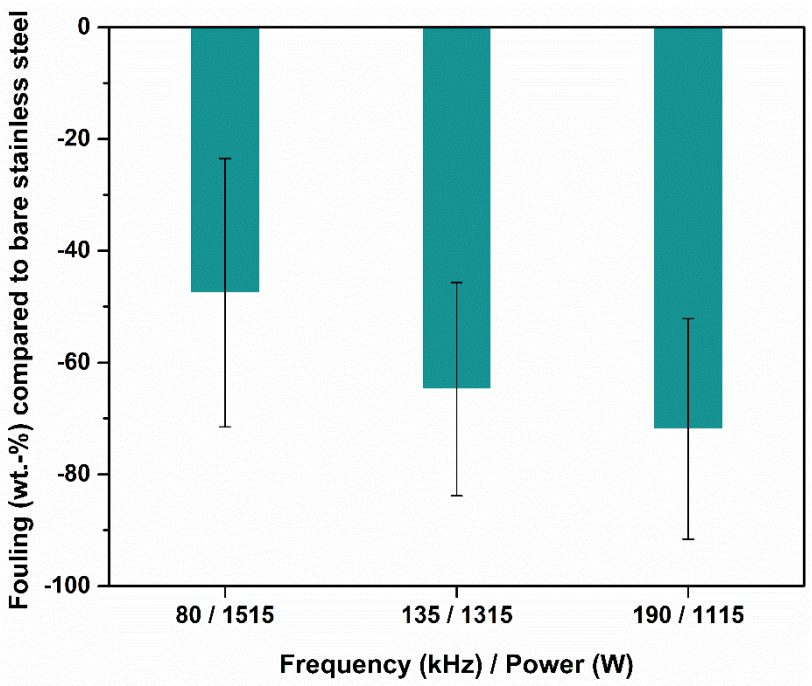

Figure 68. Fouling-release performances of plasma bilayers as the function of power.

Although, the plasma bilayer deposited at low power was not completely cleaned after the rinsing step, the power decrease improved fouling-release performances, even overtaking the one of pFOTES monolayer (at 1515 W).

To sum up, this section presented the development of the deposition of bilayers at atmospheric pressure plasma using two precursors: HMDSO and pFOTES. Several methods were used to characterize this new thin film. WCA measurements reveal that this coating is superhydrophobic and very stable (ageing evaluated for 28 days). Depth profile by ToF-SIMS confirmed the deposition of two layers with the presence of fluorine at the extreme surface.

HMDSO and pFOTES monolayers and HMDSO/pFOTES bilayer were submitted to a pasteurization cycle. The bilayer was less efficient than pFOTES monolayer, likely due to its morphology. In fact, as HMDSO monolayer, the bilayer showed large nanoparticles, which could favour the adhesion of native or calcium clusters.

Consequently, to reduce the formation or large nanoparticles, the influence of HMDSO flow rate and power were investigated. By decreasing HMDSO flow rate, the formation of large nanoparticles is indeed reduced, but not enough to improve fouling-release performances of the bilayer. On the other hand, the power reduction, decreases the monomer fragmentation, making the bilayer smoother. The power decrease allowed to improve fouling-release performances from 48 ± 24 % to 72 ± 20 %. To enhance the effectiveness, an equilibrium could be found between the deposition of very small particles as observed in section 3 (Figure 49 b) and the deposition of thin film with a good retention of CF_x groups, allowing an anti-adhesive effect.

VI. Conclusion

Atmospheric pressure plasma torch allows the quick deposition of monomers generating thin film without solvent or catalyst. Moreover, being a versatile process, for a given monomer it is possible to obtain coatings with different surface properties. Nonetheless, external parameters such as temperature or relative humidity likely influence final physico-chemical properties. As the plasma process was moved in three different laboratories, this study revealed the influence of air extraction speed on coatings adhesion. Consequently, all plasma depositions were performed at an air extraction speed of 13m/s to ensure a good adhesion.

Manufacturing plasma parameters were optimized in order to minimize fouling deposit using a Plackett-Burman design including 12 experiments. The potential influence of plasmagenic gas (N_2) flow rate, HMDSO flow rate, nozzle-to-substrate distance, scanning speed, frequency and number of cycles were considered. The most important parameters to reduce fouling deposit were gas flow rate and the nozzle-to-substrate distance. The optimization of plasma parameters was coherent with experimental results as it led to the condition 3 which demonstrated excellent fouling-release performances for at least two uses. Surface properties, chemistry and morphology show that a low polar part, likely owed by a certain carbon content in the thin film and a roughness lower than 60 nm lead to a fouling deposit reduction of 86% after two uses.

The second part presented the development of the deposition of bilayer at atmospheric pressure plasma using two precursors. Superhydrophobic and very stable bilayer was deposited from HMDSO and pFOTES. The deposition of two distinct layers were confirmed by ToF-SIMS depth profile analyses. The study of HDMSO flow rate and power on physico-chemical properties of bilayers highlighted that the power decrease allowed to improve fouling-release performances from 48 ± 24 % to 72 ± 20 %. To enhance the effectiveness, an equilibrium could be found between the deposition of very small particles and the deposition of thin film with a good retention of CF_x groups allowing an anti-adhesive effect. However, to improve food-compatibility of the bilayer, pFOTES should be replaced by another silane-based precursor with a long alkyl chain.

CHAPTER 4 – SLIPPERY LIQUID-INFUSED SURFACES

I. Introduction

According to literature, Slippery Liquid-Infused Surfaces (SLIS) have both anti-fouling and fouling-release properties. Nevertheless, their durability is limited due to a poor oil retention induced by a high shear stress. It was highlighted that nano or micro structuration could increase oil trapping. In this study, stainless steel surfaces were structured by a femtosecond laser source. Therefore, in order to improve oil retention, an optimization of laser manufacturing parameters was carried out. This allowed to select laser parameters to develop greener and food compatible SLIS based on coconut oil showing promising fouling-release performances.

II. Biomimetic Surfaces

2.1. Biomimetic approach

The term "biomimetics" was coined by Otto Schmitt in 1957 and appeared in *Webster's dictionary in* 1974 with this definition: *"The study of the formation, structure, or function of biologically produced substances and materials (as enzymes or silk) and biological mechanisms and processes (as protein synthesis or photosynthesis) especially for the purpose of synthesizing similar products by artificial mechanisms which mimic natural ones."*

However, in the literature, the term "biomimetics" is not clearly defined and other words (bioinspiration, biological design or bio-inspired design) are employed to convey the same idea.[249]

According to CEEBIOS (Centre Européen d'Excellence en Biomimétisme de Senlis), biomimetics can be defined as the possibility to innovate by taking biological systems as model to link industrial activities and environment protection.[250]

In the past few years, biomimetics has been widely used by scientists to develop surfaces with specific function as fouling mitigation for example. Among biological materials studied, lotus leaf is the most studied and the most mimicked to perform superhydrophobic surfaces. Other biological systems as butterfly wing, gecko foot, spider silk or Salvinia leaf present interesting properties, including superhydrophobic characteristic.[82], [251], [252] The main characteristic of these biological surfaces is the dual-scale structure ranging from nanoscale to microscale or to nanoscale to microscale to macroscale as displayed in Figure 69.

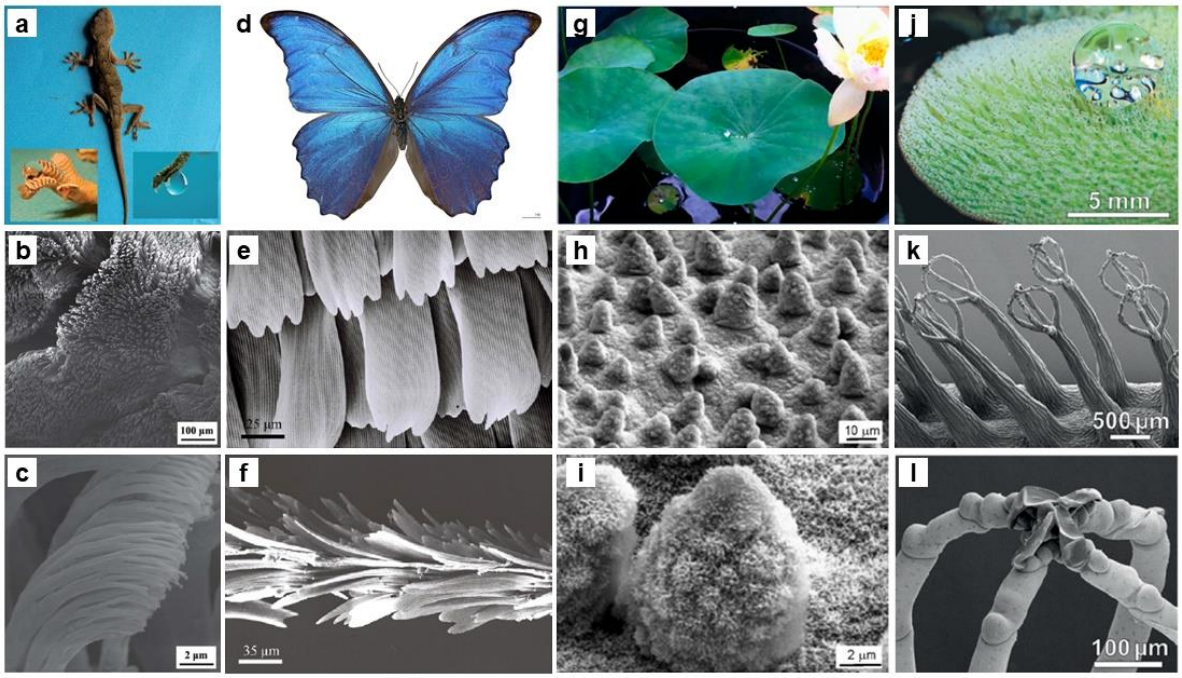

Figure 69. Hierarchical structures of different biological systems. (a) Picture of a gecko under anaesthesia (b) and (c) SEM images at different magnifications (100 µm and 2 µm)[251]. *(d) Picture of a butterfly (e) SEM images showing transection of the wing surface and (f) the flat arranging*[253]. *(g) Picture of Euphorbia myrsinites leaves (h) and (i) represent SEM images of Euphorbia leaf micro (scale bar = 10 µm) and nanostructure (scale bar = 2 µm)*[82]. *(j) Salvinia surface (k) SEM image of the hairs connected at the terminal end (i) Terminal end forming a patch of four cells.*[252]

2.2. Superhydrophobic and omniphobic surfaces

Superhydrophobic surfaces have been extensively investigated for their ability to reduce water adhesion. This property is of great interest for industrial applications such as anti-icing, anti-fogging, anti-corrosion or anti-biofouling.[140] Nonetheless, they demonstrated under certain conditions such as vibration, evaporation, pressing, droplet bouncing, a transition state from Cassie-Baxter to Wenzel, generating a loss of anti-fouling properties.[254] Therefore, depending on their applications, superhydrophobic surfaces can have a limited lifetime.[255]

Moreover, milk has a lower surface tension than water, (49 mN/m against 72.8 mN/m respectively) due to proteins and fat [256], thus omniphobic surfaces seem more suitable to limit dairy fouling adhesion. Tuteja *et al.* [257] designed omniphobic surfaces repelling liquids with low surface tension such as methanol (22.7 mN/m), octane (21.6 mN/m), and pentane (15.1 mN/m). However, under harsh conditions, like external abrasion, these omniphobic surfaces demonstrate a poor mechanical durability comparable to that of superhydrophobic surfaces.[258], [259]

Consequently, as surfaces mitigating milk fouling will be submitted to a milk-like fluid possessing a surface tension lower than water (53.2 ± 1.1 mN/m at 85°C) and to a high shear stress, another type of bioinspired surfaces was investigated: Slippery Liquid-Infused Surfaces (SLIPS), described below.

2.3. Slippery Liquid-Infused Porous Surfaces (SLIPS)

Slippery liquid-infused porous surfaces, also called SLIPS, were invented a few years ago by Aizenberg's group.[171], [172] These surfaces are bio-inspired by *Nepenthes* pitcher plants which have a slippery area allowing to catch their food. Based on this feature, SLIPS consist in porous or nanostructured surface impregnated by low surface energy lubricants. The obtained surface is extremely smooth and slippery. Thus, fluids and biological fouling cannot hold on the surface and slide off. This innovative material has demonstrated good results against biofouling for biomaterials.[145], [260]

2.3.1. Nepenthes pitcher plant

Nepenthes pitcher plants have inspired Aizenberg's group to design SLIPS. *Nepenthes* pitchers are carnivorous plants catching insects by different strategies: extrafloral nectar, flower fragrance or UV light absorption patterns near the pitcher opening. These plants have distinct zones for specific functions, which are operculum, peristome, slippery zone, and digestive zone. Observations of insects placed on Nepenthes plants show that the inner waxy pitcher wall is the most important zone to capture insects. This waxy area has anisotropic structures (Figure 70 c) trapping insects from adhesive secretion.[173]

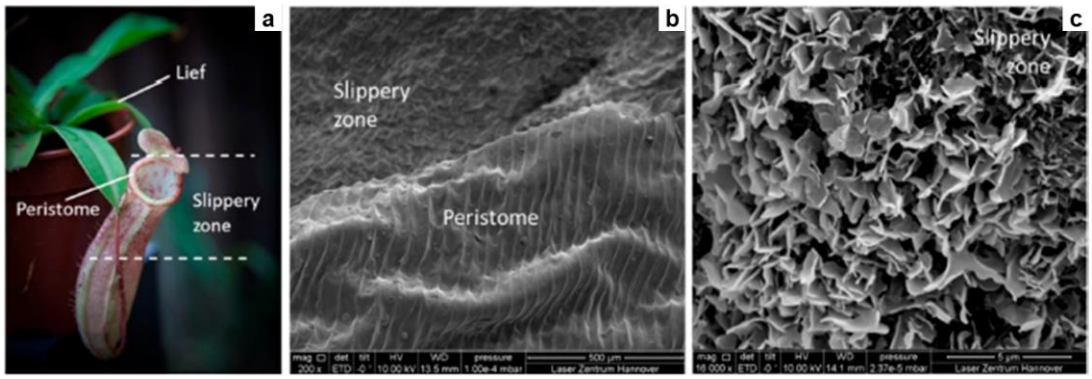

Figure 70. (a) Nepenthes pitcher. (b) SEM image of peristome and slippery zone. (c) SEM image of the slippery zone morphology.[255]

2.3.2. Design of SLIPS

Inspired by living-world, scientists started to develop fluid-impregnated materials such as metals, ceramics, polymer networks and gels. However, designing such materials can be complex. In 2018, Howell *et al.* reported different methods to design SLIPS.[145]

SLIPS are composed of two essential constituents, the textured material and the infused liquid. In order to obtain a smooth and stable liquid surface, the underlying support must have a surface chemistry fitting with the chemical nature of the liquid. The underlying surface can be flat, nano- or micro-structured. When the substrate is flat, infused-liquid is held by weak bonding like Van der Waals forces. If the substrate presents surface roughness, impregnated-liquid is held thanks to Van der Waals and capillarity forces.[145]

2.3.2.1. Underlying substrates

Various types of materials were used to fabricate stable liquid overlayer, such as poly(ethylene terephthalate), polycarbonate, polyethylene, polypropylene, polyimide, polystyrene, titanium, aluminium, steel and glass.[145], [261] Depending on the type of material, two strategies exist to match the chemistry of the lubricant. The first one consists in modifying the pre-existing roughened surface and the second one consists to roughen the surface. However, in most of studies both of these strategies were applied. Although some surfaces already present chemical affinity with the lubricant, it has been demonstrated that the lubricant retention increases by texturizing the surface. To increase surface roughness, different techniques (top-down and bottom-up approaches) can be used to either remove matter (substractive process) to create topography or to add texturized layer (additive process) to the substrate.

Lian *et al.* reported several techniques used to engineer metallic substrates, gathered in Table 37.[262] Among these investigations, five of them aimed at creating SLIPS onto stainless steel surfaces.[13], [261], [263]–[265]

Sunny *et al.* textured stainless steel substrate though Layer-by-Layer method, where positively charged polyelectrolytes and negatively charged silica nanoparticles were alternatively deposited (Figure 71). The assembled film was then oxygen plasma-treated in order to remove the polymer, leading to a porous structure made of activated silica nanoparticles. Before infusing the porous structure, silica nanoparticles were silanized to obtain a fluorinated surface.[261] Another bottom-up technique has been used to create structures onto stainless steel surface. Tesler *et al.* used electrodeposition to deposit hierarchical structures:

microscale islands covered with nanoscale flakes (Figure 71), which were functionalized as well before oil impregnation.[265]

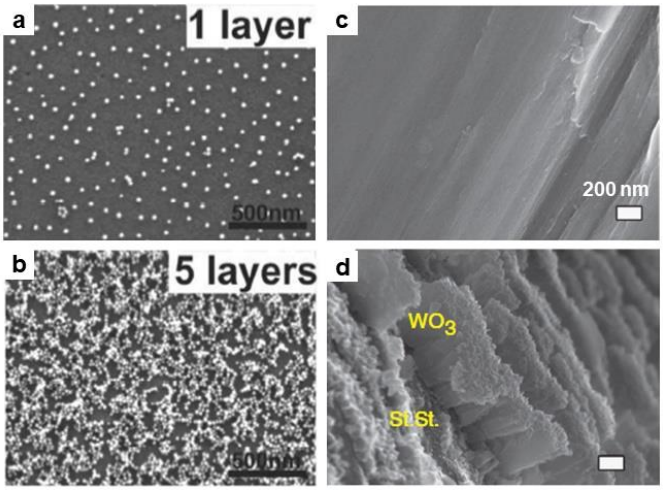

Figure 71. SEM images of textured stainless steel using bottom-up approaches. (a, b) LbL-deposited silica nanoparticles after different deposition cycles. (c, d) bare 304 stainless steel and WO_3 films deposited onto stainless steel.

Top-down approaches were used to structure stainless steel as well (Figure 72). Sandblasting was used to texture stainless steel, leading to micro-scale roughness.[263] Lee *et al.* reported an electrochemical etching method to modify the surface stainless steel samples. It led to porous stainless steel with different sizes of pores (nano and micro scale pores) depending on the tension applied.[264] More recently, Zouaghi *et al.* performed stainless steel structuration using a femtosecond laser leading to Cauliflower-like structures.[13] Sandblasted and laser ablated stainless steel surfaces were chemically modified before lubricant impregnation.

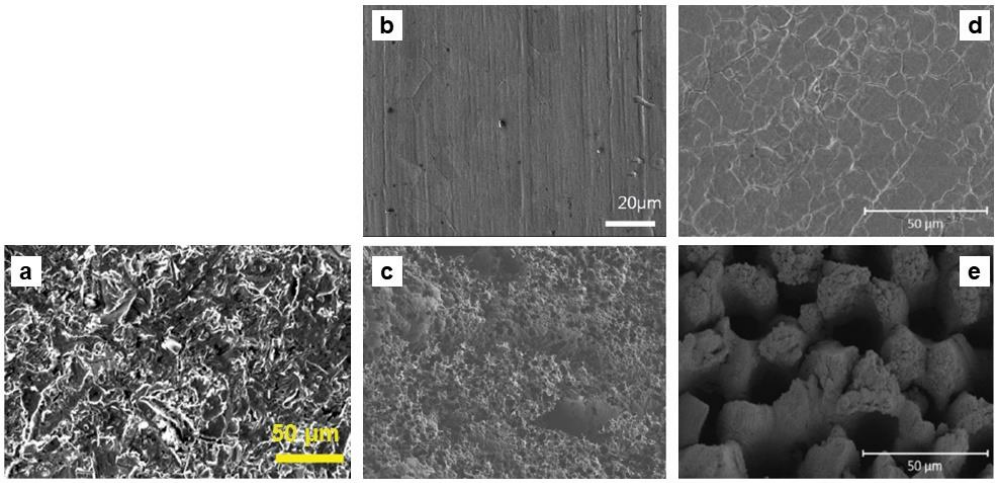

Figure 72. SEM images of textured stainless steel using top-down approaches. (a) Sandblasted stainless steel. (b, c) bare and electrochemically etched 304 stainless steel. (d, e) bare and laser ablated 316L stainless steel.

Table 37. Methods to structure metallic substrate for SLIPS elaboration

Technique	Advantage/disadvantage	Material	Morphology	SA (°)[a]	Reference
Femtosecond laser processing	High processing precision, stable microstructure and good surface quality, but high cost, low processing efficiency, high environment requirements, and difficult to apply to large scale production	Titanium	Spike structures	-	[266]
		Stainless steel	Cauliflower-like structure	2	[13]
		Ni/Ti alloy	Porous microstructures	15	[267]
Nanosecond laser processing	Low cost, high processing speed, low environment requirements, suitable to apply to large-scale production, but low quality surface, relatively poor controllability	Carbon Steel	Stacked micro/nano structures	2.5	[268]
Electrochemical deposition	Fast, large-scale, low-cost and easily controlled, but weak binding force with substrate and energy consumption	Tungsten oxide onto Stainless steel	Porous WO_3 nano-textured films	3	[265]
		Polypyrrole (PPy) onto Aluminum alloy	Large globule with nanoscale bumps	2	[269]
		Ag onto Titanium	Dendritic structure	8	
		Cu onto Cu or Cu/Al alloy	Dendritic structure	-	[270]
Electrochemical etching	Controlled, less hazardous, and more environmentally safe, but energy consumption	Stainless steel	Nanoscale and microscale pores and microscale bumps	-	[264]
		Steel	Flower-like microstructures	2.3	[271]
		Zn	Needle-like and flake nanostructures	10	[272]
Electrochemical deposition + oxidation	Fast, large-scale, low-cost and easily controlled, but energy consumption and multiple steps	Cu/Zn alloy	Needle-like structure with the porous feature	11.3	[273]

Electrochemical etching/deposition	Fast, large-scale, low-cost and easily controlled, but energy consumption and multiple steps	Iron tetradecanoate onto Low alloy steel	Volcano configuration with discrete granules	-	[274]
Electrochemical etching + anodization	Fast, large-scale, low-cost and easily controlled, but energy consumption and multiple steps	Aluminum	Micron-sized stepped structures and nano-sized holes	2.0-5.0	[275]
Electropolishing + anodization	Fast, large-scale, low-cost and easily controlled, but energy consumption and multiple steps	Aluminum	Self-aggregated wire structure	5.2	[276]
		Aluminum	Thin nano-wire-like layer on thick nano-pore-like layer	< 10	[277]
Galvanic replacement	Fast, low-cost, suitable to apply to large-scale production, but poor controllability and deposition of insoluble byproducts	Cu onto Al/Mg alloy or Low alloy steel	Dendritic structures	-	[270]
		Cu/Zn alloy	Pyramid structures	8.5	[278]
Sandblasting	Simple texturing technique but low quality surface, relatively poor controllability	Stainless steel	Uneven relief	-	[263]
Layer-by-Layer	Simple, low-cost and easily controlled but multiple steps	Silica nanoparticles onto stainless steel	Nanoscale structures	1.4	[261]
WDEM[b]	Large-scale, high-efficiency precision construction of porous microstructure but energy consumption, multiple steps	Aluminum alloy	Craters and porous microstructures	5	[279]

[a] SA: sliding angle, [b] Wire Electrical Discharge Machining

2.3.2.2. Lubricants

The lubricant is essential in SLIPS as it allows the surface to be smooth and repellent. Therefore, the lubricant's choice depends on its application. Peppou-Chapman *et al.* reported the lubricants the most used.[280] Two categories are mainly selected for impregnation: (i) Polyfluoroethers (PFPEs) and (ii) linear polydimethylsiloxane (PDMS or silicone oil). Both PFPEs and silicone oils are chemically inert and have a low surface tension and low vapour pressure. However, silicone oils are more attractive than PFPE, as they are relatively low cost.

Other oils have been used such as perfluorodecalin, which is approved by the Food and Drug Administration (FDA) to limit biofouling and bacterial adhesion for biomedical applications.[281]–[283] Vegetal oils such as canola oil[178], [181], olive oil[178], [181], sesame oil[180], [181], grape oil[181], linseed oil[181], coconut oil[178], [284], almond oil[179], oleic acid oil[181] were also adopted as lubricants in areas of food handling and processing. Another class of lubricant has been recently used: ionic liquids. These liquids are tuneable and have demonstrated promising results [285]–[287] to repel hot water for instance [288]. Moreover, as the use of fluorine compounds might be restricted by REACH (Registration, Evaluation, Authorisation and Restriction of Chemicals)[289], thus vegetal oils and ionic liquids could be a good alternative.

2.3.2.3. Stability and durability

Stability and durability of SLIPS are limited under high flow rates. Indeed, SLIPS lose their slippery properties due to lubricant depletion induced by shear stress. Zouaghi *et al.* highlighted a lubricant loss during a pasteurization run under a turbulent regime.[13] An investigation pointed out that the viscosity ratio of lubricant and medium could impact the interface stability and thus oil retention. Moreover, regarding lubricant viscosity, Doll *et al.* showed that, for specific ranges of lubricant viscosity and structure dimensions of the substrate, SLIPS are stable.[266] Lubricants with high viscosity are not completely trapped by structures, whereas lubricants with low viscosity are easily removed by physical forces (dynamic flow or centrifugal forces). To improve SLIPS durability, other authors recently proposed to use a PDMS layer as an oil tank, a microfluidic network or in brush to graft the lubricant to the substrate and to ease the replenishment.[175]–[177], [261]

2.3.3. Mitigation of dairy fouling deposit and limitations

As mentioned in Chapter 1, section 4.4.2, only one investigation has demonstrated the potential of SLIPS for dairy fouling mitigation. These SLIPS-like surfaces were developed in

collaboration with the University of British Columbia (Canada), the *Institut d'Electronique, de Microélectronique et de Nanotechnologie* (IEMN UMR 8520, France) and the *Unité Matériaux et Transformations* (UMET UMR 8207, France).[13]

The SLIPS-like surfaces were designed in three steps as illustrated in Figure 73: (i) stainless steel texturation, (ii) chemical modification and (iii) oil impregnation. The texturation (Figure 72) was performed with a femtosecond laser source. The laser process will be detailed in the next part. Then structured stainless steel surfaces were chemically modified with a perfluorosilane, prior to be impregnated by a perfluorinated oil (DuPont Krytox GPL 103).

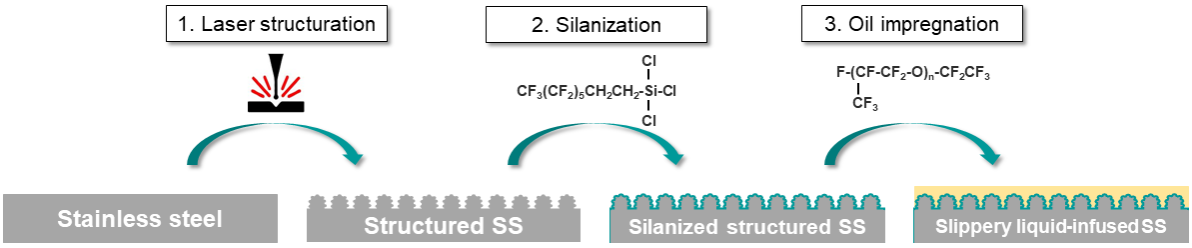

Figure 73. SLIPS-like surfaces process fabrication workflow.

These surfaces were submitted to the pasteurization test presented in Chapter 2. They demonstrated good anti-fouling performances with a fouling reduction up to 63 %. Moreover, promising fouling-release properties were obtained, as surfaces were completely cleaned after a water-rinsing.

Nevertheless, some limitations were noticed with these SLIPS-like surfaces. First, the fouling-release effect was efficient for one pasteurization run only, owed by a loss of lubricant. Fouling-release properties were recovered by re-infusing the surfaces. Secondly, the perfluorinated oil is not a food-grade oil, thus to avoid milk contamination, pharmaceutical grade or vegetable oils could be a good alternative.

Therefore, the following parts are dedicated to the optimization of laser manufacturing parameters to improve oil retention and the elaboration of slippery liquid-infused surfaces (SLIS) through different processes.

III. Femtosecond laser process

This part presents the laser ablation process used to structure stainless steel substrates. The femtosecond laser source as well as the micromachining platform will be detailed. Finally, laser process parameters will be described.

3.1. Femtosecond laser system

The femtosecond laser system is composed of a laser source which is incorporated into an integrator. This femtosecond laser is part of the LEAF platform, which gathers a nanosecond laser system and a laser 3D lithography machine.[290]

3.1.1. Laser source

The laser source is the Tangerine model (Figure 74) developed by Amplitude Systèmes (Bordeaux, France). It is an Ytterbium-doped fiber laser, delivering ultrafast impulsions ranging from 300 fs to 10 ps at a wavelength of 1030 nm (in near infrared). It combines both high energy per pulse (150 µJ) and high repetition rate (2 MHz), with an average power of 20 W.

Figure 74. Femtosecond laser source, Tangerine model

3.1.2. Micromachining platform

The femtosecond laser source is integrated into a micromachining platform (Figure 75) developed by Oxford Lasers (United-Kingdoms). This platform gathers also a Second and Third Harmonic Generation (SHG/THG) module as well as different optical elements controlling and focalizing the beam.

Figure 75. Micromachining platform, J series

The optical path is detailed in Figure 76. Right after the femtosecond laser, a Second and Third Harmonic Generation (SHG/THG) module, developed by Amplitude Systèmes (Bordeaux, France) is placed, allowing to work with two other wavelengths, in visible (515 nm) range and ultra-violet (343 nm) range. This module is composed of a half-wave plate allowing the IR beam to pass or to be deviated. If the IR beam is deviated, it passes through nonlinear crystals and dichroic mirrors to generate the second and third harmonic at 515 nm and 343 nm respectively.

The beam then passes through a Beam Expander Telescope (BET) composed of two lenses which extend the beam diameter to 6 mm. A mirror guides the beam to an attenuator. It is composed of a polarizer and half-wave plate. Following that, a quarter-wave plate is placed to obtain a circular polarization. Right after, the beam is directed toward the trepanning head which consists in moving the beam by circular motions. This process enables to obtain extremely precise holes. Then, galvanometric mirrors allow the laser beam to scan samples up to 100 mm/s. Finally, the beam is focused with a 100 mm focal length F-theta lens onto stainless steel samples placed on the X-Y translation stage.

To structure stainless steel surfaces, the laser beam was set at the 1030 nm wavelength.

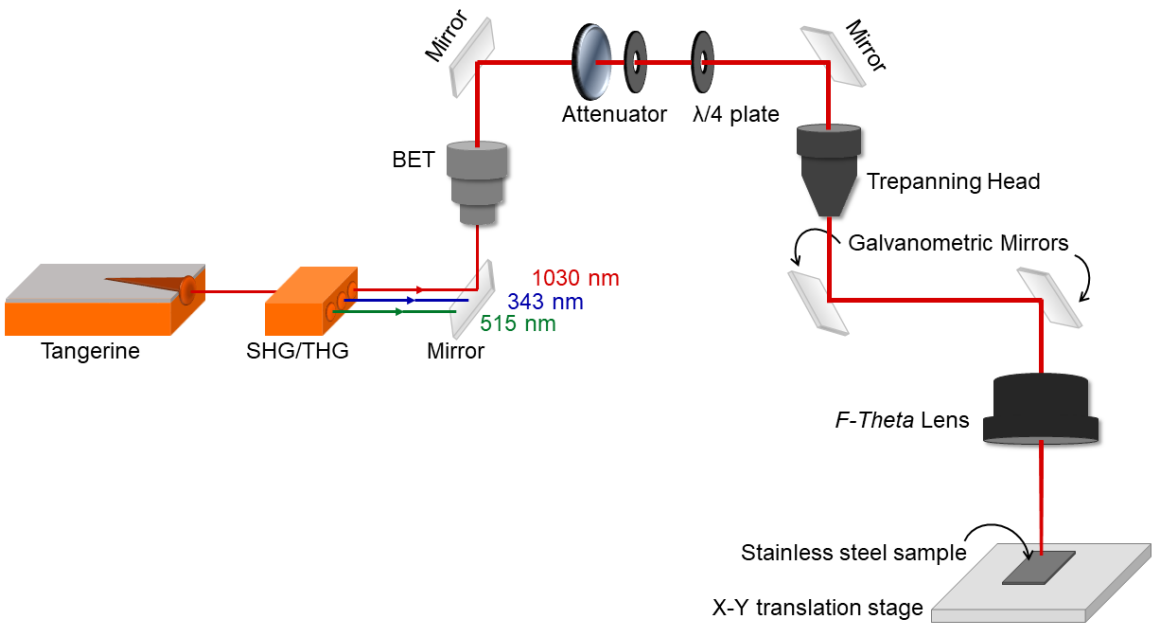

Figure 76. Synoptic of the micromachining platform gathering the femtosecond laser source (Tangerine), SHG/THG module, mirrors, a Beam Expander Telescope (BET), an attenuator, a quarter wave plate, a trepanning head, galvanometric mirrors, the F-Theta lens and the translation stage, adapted from [291]

3.1.3. Femtosecond laser vs nanosecond laser

Both nanosecond and femtosecond lasers were used to structure metallic surfaces.[262] However, femtosecond lasers lead to more precise machining processes than nanosecond lasers.[292] Indeed, several phenomena take place right after the laser-matter interaction. First, laser beam energy is absorbed by free electrons of the material, which are then ionized. Finally resulting energy is transferred and dissipated trough the lattice, driving to structural modification with physical and chemical changes. It has been demonstrated that the laser-matter interaction and pulse duration were strongly bound. Indeed, depending on pulse duration, energy absorbed by the lattice is more or less dissipated, leading to thermal effects during machining processes (hole drilling or cutting) near the laser-impacted area. This area is referred to as heat affected zone (HAZ). Heat dissipation (energy relaxation) appears after around 10 ps (this time can vary depending on the material). Thus, for laser pulse longer (nanosecond laser) than the relaxation time, HAZ becomes large and edge effects are observed resulting from melting of matter (Figure 77 a). On the contrary, with laser pulse lower (femtosecond laser) than the relaxation time, heat is quickly dissipated and remains localized in the HAZ (Figure 77 b).[291]–[293]

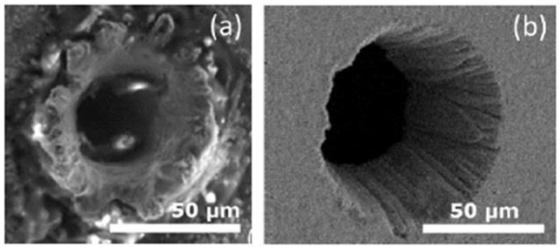

Figure 77. Laser ablation of stainless steel at different pulse duration highlighting thermal effects. (a) nanosecond duration: 8 ns. (b) femtosecond duration: 180 fs.[294]

3.2. Laser beam characteristics and process parameters

Surface treatments by laser increased thanks to solid-state Ti:Sapphire laser sources development. Nevertheless, industrial uses are limited due to their low structuration velocity. Fiber laser sources outbreak allow to reach higher repetition rate which could make laser process faster for industrial applications.[291], [295] Zouaghi *et al.* used an amplified solid-state Ti-Sapphire laser for stainless steel structuration at a velocity of 0.37 mm/s [13], which is hundred times slower than the Ytterbium-doped fiber laser used in this work. Therefore, laser beam characteristics will be first introduced. Secondly, laser process parameters will be detailed.

3.2.1. Laser beam characteristics

Surface structuration is an intricate process depending on the nature of the material and on laser beam characteristics. Several laser process parameters (laser fluence, hatch distance, velocity and number of repetitions) can be varied to control laser-matter interactions. These parameters will be introduced in the next section.

Table 38 reports laser beam characteristics of solid-state Ti:Sapphire laser, which highly differ from those of Yb laser. Indeed, pulse duration of Ti:Sapphire laser is twice shorter than that of Yb laser and pulse energy is hundred times higher.

Table 38. Laser beam characteristics of a solid-state Ti:Sapphire laser and an Ytterbium-doped fiber laser

Beam characteristics	Solid-state Ti:Sapphire laser[13]	Ytterbium-doped fiber laser
Wavelength	800 nm	1030 nm
Pulse duration	120 fs	300 fs
Polarization	Linear	Circular
Beam Quality facor M^2	< 1.1	< 1.3
Pulse energy	1700 µJ	60 µJ

3.2.2. Laser process parameters

To control the shape and scale of structures created by laser ablation, several laser process parameters can be varied: (i) spot diameter, (ii) laser fluence, (iii) beam velocity and (iv) hatch distance. According to Vorobyev *et al.*, structuration will be dominated by nanostructures when both number of laser pulse and laser fluence are lower, while macrostructures will be observed with a higher number of pulse and fluence.[296] It is also possible to obtain different types of structures with both nano and microstructures acting on beam focus.[297]–[299]

3.2.2.1. Spot diameter

As illustrated in Figure 76, after going through the BET, the laser beam diameter (D_{beam}) is extended to 6 mm, then it is focused with a F-theta lens onto samples. According to the literature, surface structuration can be obtained either by focusing (d_{foc}) or defocusing ($d_{\Delta z}$) the beam.[297] In this study, stainless steel surfaces were irradiated by focusing the laser beam. The spot diameter (d_{foc}) at the focal point was calculated using the following equation:

$$d_{foc} = \frac{M^2 4 f \lambda}{\pi D_{beam}} \quad (20)$$

with M^2 the beam quality factor, f the focal length of the lens (in mm), λ the wavelength (in nm) and D_{beam} the beam diameter before the lens (in mm). Thus, at the focal point the spot diameter was of 37 µm.

3.2.2.2. Laser fluence

Modifying topography or removing matter require energy corresponding to the ablation threshold. Required energy is quantified using the laser fluence, defined as the optical energy per area per pulse. In case of femtosecond laser sources, it is assumed that laser intensity across the focal spot has a Gaussian distribution.[300] Moreover, as femtosecond laser sources are pulsed sources, the mean laser fluence is used and expressed following equation 21:

$$F_{Gaussian} = \frac{2\,E_{pulse}}{S_{spot}} = \frac{8\,P_{mean}}{\pi\,\nu_{rep}\,{d_{foc}}^2} \quad (21)$$

where E_{pulse} is the pulse energy (in µJ or mJ), S_{impact} the spot surface at the focal point (in cm^2), P_{mean} the mean output power (in W), ν_{rep} the repetition rate (in kHz) and d_{foc} the spot diameter at the focal point (µm). The mean power P_{mean} is obtained for a given repetition rate ν_{rep}.

Although solid-state Ti:Sapphire lasers are more commonly used for surface modification, Hairaye demonstrated that an Ytterbium-doped fiber laser could reach a larger laser fluence range than solid-state Ti:Sapphire lasers.[291]

3.2.2.3. Beam velocity and hatch distance

To increase the surface roughness, two other parameters have to be taken into account: (i) the beam velocity (v_{scan}) and (ii) the hatch distance (h).[291] First, the laser beam can scan stainless steel samples thanks to galvanometric mirrors up to 100 mm/s. At a given repetition rate with a focused beam, a longitudinal overlapping rate (LO) can be defined as the function of the velocity (Eq. 22):

$$LO\ (\%) = \left(1 - \frac{v_{scan}}{d_{foc}\nu_{rep}}\right) \times 100 \quad (22)$$

with v_{scan} corresponding to the beam velocity (in mm/s), d_{foc} the spot diameter at the focal point (in µm) and ν_{rep} the repetition rate (in kHz). As showed in Figure 78, the lower the beam velocity, the higher the longitudinal overlapping rate.

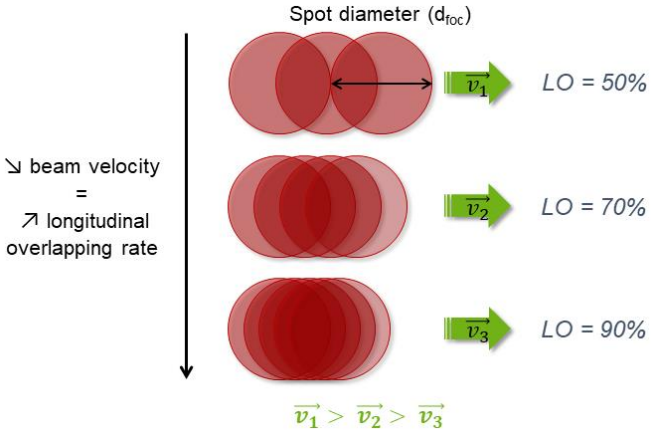

Figure 78. Illustration of the impact of the beam velocity v_{scan} at a fixed repetition rate v_{rep} on the longitudinal overlapping rate LO adapted from [291]

The second parameter corresponds to the distance between two parallel laser passes (Figure 79). This distance referred to h enables to determine the transverse overlapping rate (TO) following equation 23:

$$TO\ (\%) = \left(1 - \frac{h}{d_{foc}}\right) \times 100 \quad (23)$$

where h is the hatch distance (in µm) and d_{foc} the spot diameter at the focal point (in µm).

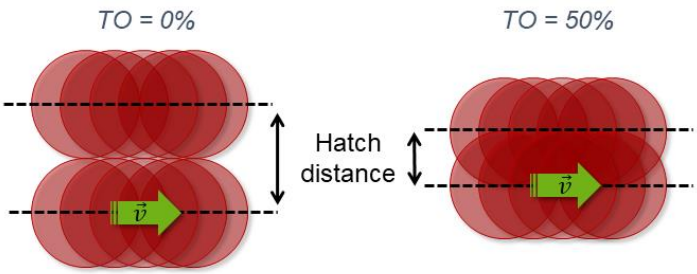

Figure 79. Illustration of the impact of the hatch distance h on the transverse overlapping rate TO adapted from [291]

The Ytterbium-doped fiber laser used to structure stainless steel surfaces was introduced, as well as the advantages of using ultra-short pulse laser. Laser characteristics were presented and compared to those of the solid-state Ti:Sapphire laser previously used. Finally, laser process parameters were described and among them: (i) laser fluence, (ii) beam velocity and (iii) hatch distance will be optimized in the next part.

IV. Optimization of laser manufacturing parameters

Zouaghi *et al.* [13] obtained excellent fouling-release properties for SLIPS-like surfaces. However structuration of stainless steel was performed using a Ti:Sapphire laser at a very low velocity. Therefore, as a different laser source was used in this study (Ytterbium-doped fiber laser), laser process parameters were optimized to obtain similar structures. First influence of laser parameters: (i) laser fluence, (ii) velocity and (iii) hatch distance on structuration (pattern and depth profile) was investigated. In a second part, optimized parameters and resulting structuration were compared to those of Zouaghi's work.

4.1. Influence of laser parameters on surface structuration

Influence of laser fluence, velocity and hatch distance were first investigated by structuring surfaces of 0.5 x 0.5 mm² with a repetition rate fixed at 50 kHz and a focused beam (spot diameter = 37 µm). Samples were structured following a grid-like pattern (see Figure 84, 154). Resulting structuration was observed by SEM.

4.1.1. Influence of laser fluence on surface structuration

Based on the work of Hairaye, repetition rate, velocity and hatch distance were set at 50 kHz, 75 mm/s and 30µm respectively.[291] At 50 kHz, the output mean power was 3 W. The influence of laser fluence on structuration was investigated for 10% and 100% of the mean power corresponding to a fluence of 1.1 and 11 J/cm² respectively. The grid-like pattern was repeated 10 times. Figure 80 displays structured stainless steel surfaces at 1.1 and 11 J/cm². At low laser fluence (1.1 J/cm²) structuration is composed of smooth periodic hills (microstructures) overlaid of ripples (nanostructures). At high fluence (11 J/cm²), structuration differs significantly. Deeper chaotic structures are obtained which seem comparable to those obtained by Zouaghi *et al.*[13]

To maximize oil retention, deep structures seem more suitable. Therefore, laser fluence was fixed at the highest value, *i.e.* 11 J/cm².

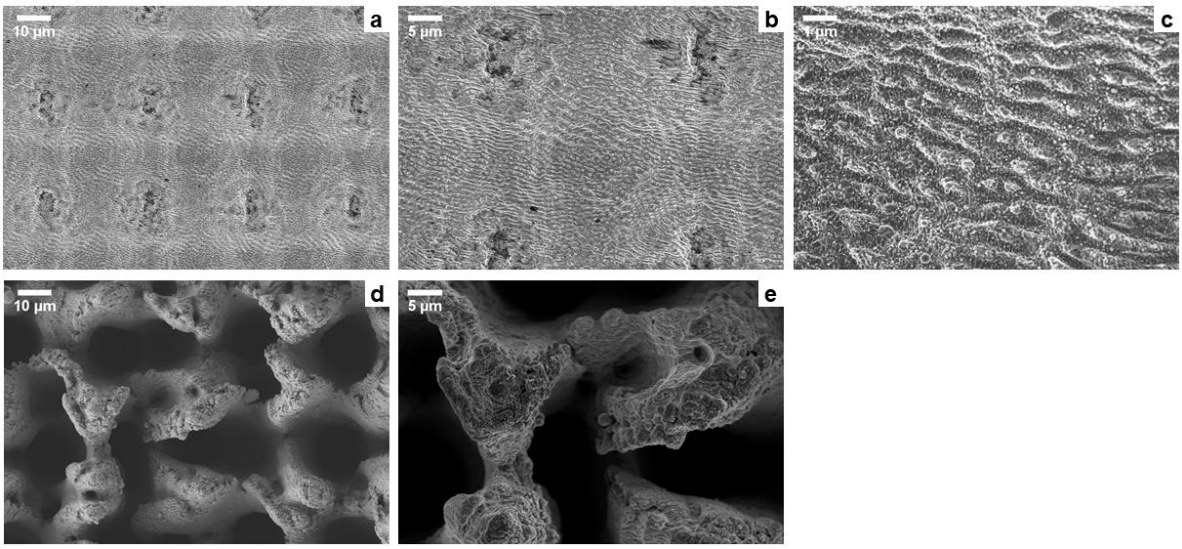

Figure 80. SEM images of structured stainless steel surfaces at low and high laser fluence. (a, b, c) At 1.1 J/cm². (d, e) At 11 J/cm².

4.1.2. Influence of velocity and hatch distance on structuration

The study of velocity and hatch distance was carried out with a repetition rate of 50 kHz and a fluence of 11 J/cm². The velocity and hatch distance were varied from 10 to 100 mm/s and hatch from 19 to 38 µm, respectively.

First, as explained in section 2.2.2.3, for a given repetition rate and spot diameter, the velocity is related to the longitudinal overlapping rate (LO). Thus, according to equation 3, 10 mm/s corresponds to a LO of 99% and 100 mm/s to 95%. Structurations performed at 10 mm/s and at 100 mm/s are shown in Figure 81 (a and c) and in Figure 81 (b and d), respectively. Resulting structures are well-defined at 100 mm/s compared to those obtained at 10 mm/s, where stainless steel seems melted with few available voids for oil impregnation. Therefore, a high velocity enables to obtain a quick process with a well-defined structure.

Secondly, as observed in Figure 81, for a given velocity, the hatch distance (or transverse overlapping rate (TO)), acts on structuration as well. For instance, at a velocity of 100 mm/s and a hatch distance of 38 µm (TO = 0%) a periodic structure (Figure 81 b) is obtained and the grid-like laser pattern is clearly observed. By decreasing the hatch distance to 19 µm (TO = 50%), the structure becomes chaotic, like a labyrinth (Figure 81 d).

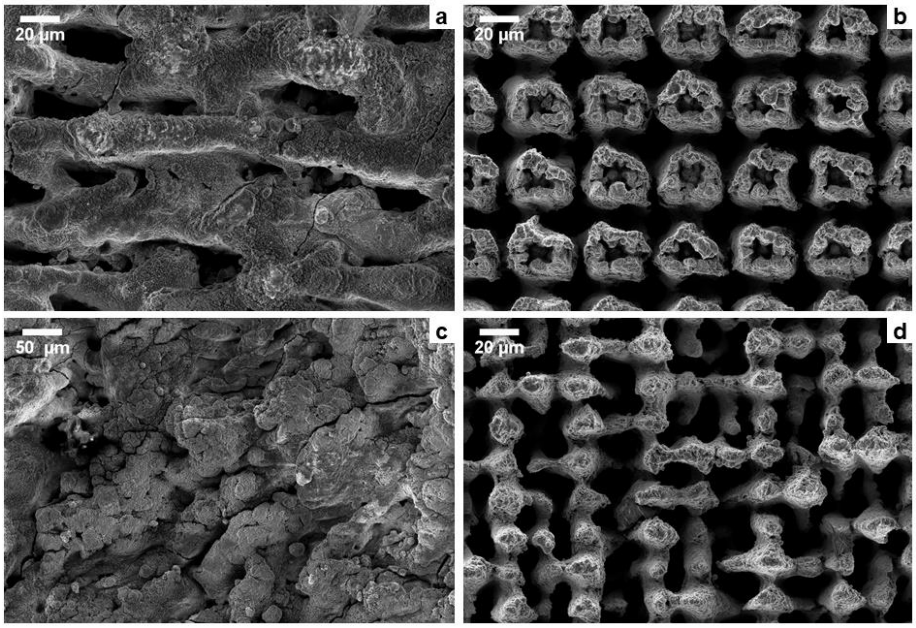

Figure 81. SEM images of the influence of the velocity and hatch distance. (a) velocity: 10 mm/s and h: 38 µm. (b) velocity: 100 mm/s and h: 38 µm. (c) velocity: 10 mm/s and h: 19 µm. (d) velocity: 100 mm/s and h: 19 µm.

To conclude, laser fluence, velocity and hatch distance influence structuration of stainless steel. The laser fluence acts on scale structuration, a low fluence drives to nanostructures while a high fluence allows to create deeper structures, suitable for oil impregnation. The velocity influences the structure formation. A low velocity drives to stainless steel melting, while a high velocity enables the formation of well-defined structures. Finally, the hatch distance impacts the structures pattern. For a large hatch distance, a grid-like structure is obtained, while for a short hatch distance a labyrinth-like pattern is observed.

In order to determine what type of structure could be the most suitable to increase oil retention rate, depth profile, mass of impregnated oil and method of impregnation will be assessed in the next part.

4.2. Impact of beam velocity and hatch distance on depth profile

In order to determine the depth structuration, both velocity and hatch distance were studied. Surfaces of 15 x 10 mm² were structured at a repetition rate of 50 kHz, a fluence laser of 11 J/cm² and a focused beam (spot diameter = 37 µm). Samples were structured following a grid-like pattern repeated 10 times. Velocity was varied from 75 to 100 mm/s and hatch distance from 38 to 19 µm. Resulting structuration was observed by SEM and depth profile was analyzed using a mechanical profilometer.

4.2.1. Structuration morphology

Structured surfaces were first observed by SEM and the results are displayed in Figure 82. Surfaces structured at 75 mm/s correspond to images a, b and c and at 100 mm/s to d, e and f. It seems that the velocity has no influence on the morphology, contrary to hatch distance. Indeed, it can be observed that the larger the hatch distance, the more periodic the structuration.

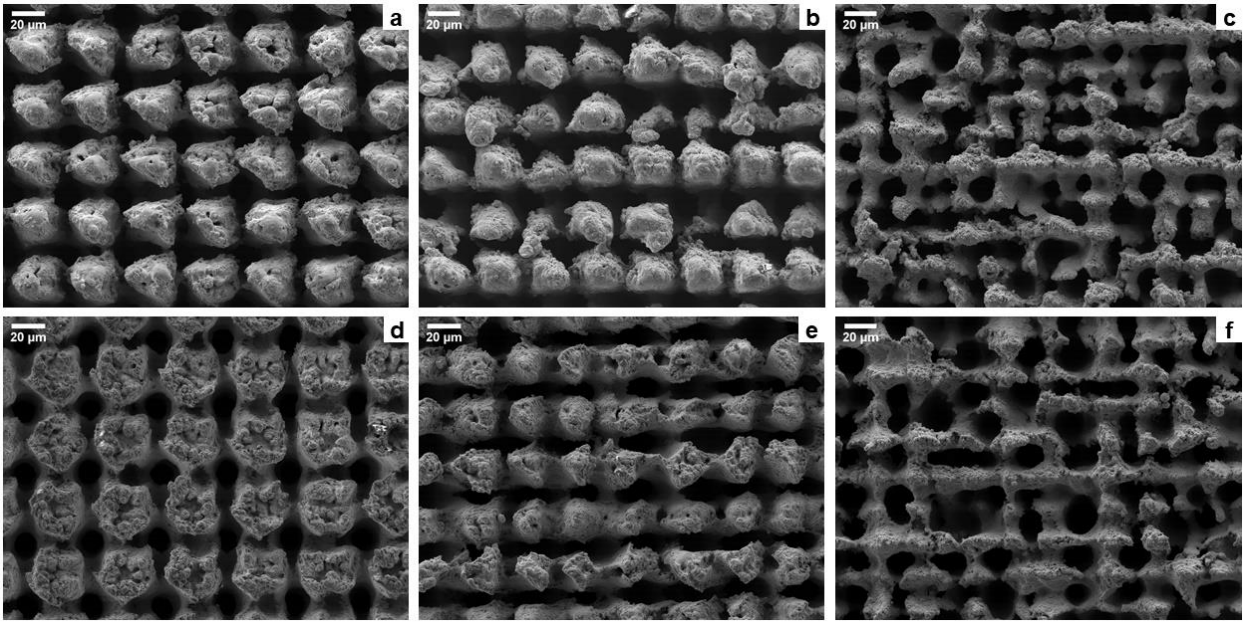

Figure 82. SEM images of the evolution of the structuration as the function of the velocity and hatch distance. (a) velocity: 75 mm/s and h: 38 µm. (b) velocity: 75 mm/s and h: 30 µm. (c) velocity: 75 mm/s and h: 19 µm. (d) velocity: 100 mm/s and h: 38 µm. (e) velocity: 100 mm/s and h: 30 µm. (f) velocity: 100 mm/s and h: 19 µm.

4.2.2. Depth profile

The structuration depth was measured by a mechanical profilometer and given by the R_v parameter corresponding to the maximum profile valley depth, thus three measurements were performed on each surface. Figure 83 exhibits that velocity, by taking into account the standard deviation, does not act on the structuration depth, whereas hatch distance does. In fact, the shorter the hatch distance, the deeper the structuration. This is consistent with the work of Moradi *et al.* who demonstrated that the energy absorption decreases with the decrease in the percentage of overlap (*i.e.* the increase of hatch distance), leading to the decrease of crater height.[301]

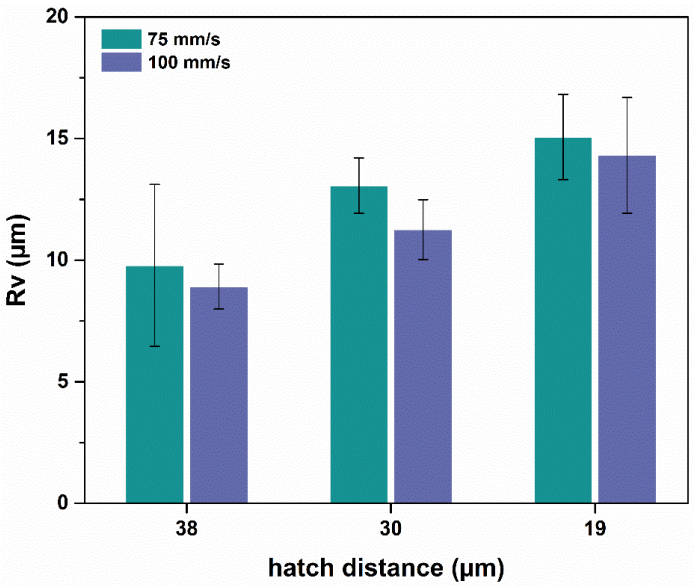

Figure 83. Maximum profile valley depth as the function of the velocity and hatch distance

To sum up, the type of structure and depth profile were studied as the function of the velocity and hatch distance. Surface morphology of samples structured at 75 mm/s does not differ from those structured at 100 mm/s. Moreover, the same trend was observed for the depth profile. However, it was shown that hatch distance influences both morphology and depth profile. A large hatch distance (38 µm) drives to a periodic structuration with a R_v of about 9 µm while a short hatch distance (19 µm) drives to a labyrinth-like structuration with a R_v of about 15 µm. Consequently, labyrinth-like samples seem more suitable to increase oil retention due to their morphology and depth.

4.3. Comparison of ablation laser process

A brief comparison of Ti:Sapphire and Yb-doped fiber lasers will be presented in this section. Laser process parameters used by Zouaghi *et al.* [13] and in this study will be compared. Obtained surfaces were characterized by SEM and profilometry.

4.3.1. Laser process parameters

Table 39 gathers process parameters of Ti:Sapphire and Yb lasers used by Zouaghi *et al.*[13] and in this study respectively. Laser parameters of this study were selected based on the optimization presented above. It can be noted that spot diameter and hatch distance are in the same order of magnitude whereas laser fluence and beam velocity strongly differ. Laser fluence of Ti:Sapphire laser is ten times higher than the one of Yb laser due to its high pulse energy and low repetition rate.

Table 39. Laser process parameters

Process parameters	Solid-state Ti:Sapphire laser [13]	Ytterbium-doped fiber laser
Laser fluence	480 J/cm²	11 J/cm²
Repetition rate	1 kHz	50 kHz
Mean power	1.7 W	3 W
Spot diameter at focal point	30 µm	37 µm
Velocity	0.37 mm/s	75 mm/s
Hatch distance	15 µm	19 µm

4.3.2. Laser pattern

Zouaghi *et al.* [13] used a line-like pattern, which was performed one time, while in this study, a grid-like pattern was chosen and repeated ten times (Figure 84). The laser process duration was calculated by taking into account a surface of 15 mm x 10 mm, velocity and hatch distance. About 4h are needed to structure a surface of 150 mm² using the laser process described by Zouaghi *et al.* against around 1h30 with the laser process used in this work.

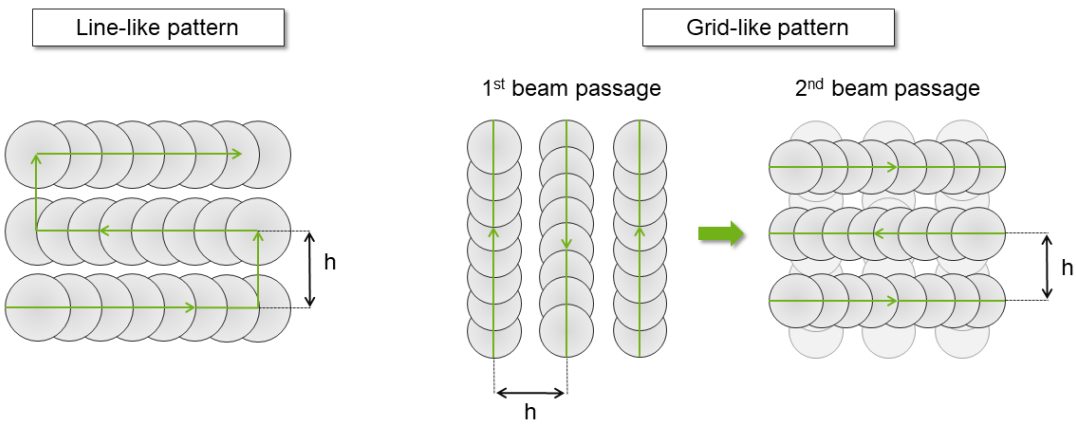

Figure 84. Diagram of laser pattern.

4.3.3. Characterizations of laser structured surfaces

Structured surfaces by both Ti:Sapphire and Yb lasers were analyzed and compared. Morphology of structured samples were observed by SEM and digital microscopy. Roughness parameters were assessed through mechanical profilometer (R_a and R_v) and digital microscopy (S_a and S_v).

SEM images (Figure 85) represent stainless steel surface before the laser structuration (a,b) and after (c, d). The resulting structure looks like a labyrinth with a dual-scale roughness, as previously observed with these parameters. This allows to validate the reproducibility of this laser process.

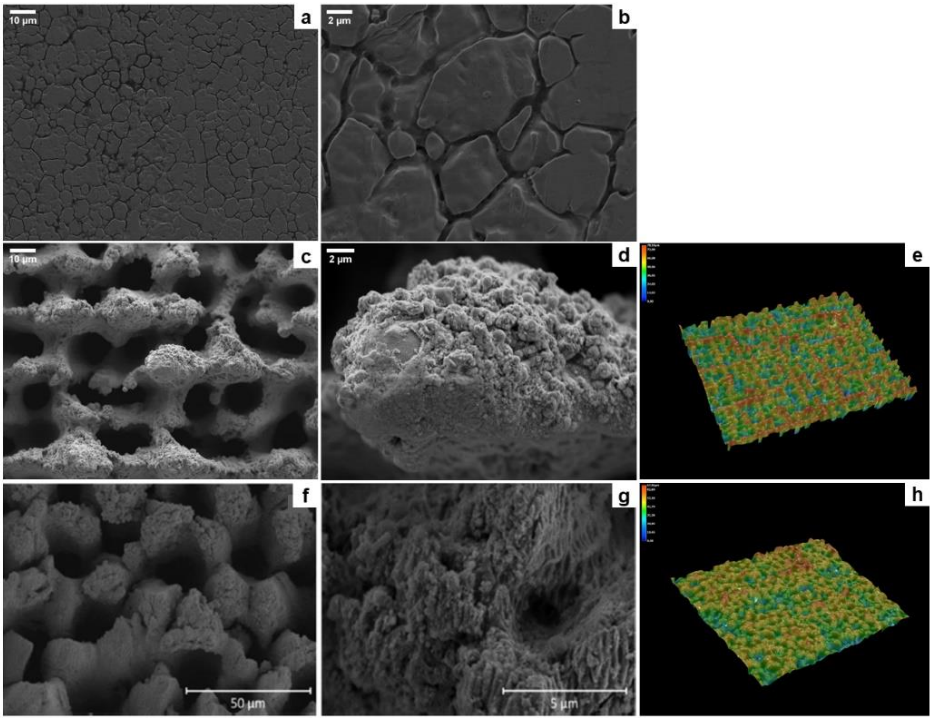

Figure 85. SEM images of bare stainless steel (a, b) and laser-structured (Yb laser: c, d and Ti:Sapphire laser: f, g) stainless steel highlighting micro and nano-roughness and 3D images of laser-structured SS (Yb laser: e and Ti:Sapphire laser: h).

Surface roughness (R_a) and depth (R_v) of the profile were characterized. Nevertheless, as observed by SEM, structured surfaces are not periodic thus, the assessment of the roughness of the entire surface could be more relevant. Surface roughness (S_a) and depth (S_v) areas were evaluated using digital microscopy, which allows also to obtain 3D images (Figure 85 e).

Roughness parameters are gathered in Table 40. Laser ablation allowed to increase surface roughness (R_a) from 40 nm to 6.6 µm as well as to make the surface significantly deeper (R_v), from 330 nm to 19.6 µm. It can be noticed that values obtained by digital microscopy (S_a and S_v) are higher than R_a and R_v values. However, comparing profile roughness parameters to area roughness parameters is complex as these latter are not normalized. Moreover, although the profilometer tip is quite thin (2 µm), it seems that the surface bottom was not reached.

Table 40. Roughness parameters of bare and structured stainless steel

Roughness parameters	Arithmetic mean roughness (µm) (profile: R_a and area: Sa)		Maximum valley depth (µm) (profile: R_v and area: S_v)	
	R_a	S_a	R_v	S_v
Bare stainless steel (REF)	0.04 ± 0.01	0.11 ± 0.01	0.33 ± 0.13	0.54 ± 0.07
Structured-stainless steel (Yb laser)	6.56 ± 0.77	10.09 ± 1.02	19.64 ± 2.50	44.98 ± 6.72
Structured-stainless steel (Ti:Sapphire laser)	6.95 ± 1.43	7.35 ± 2.27	21.47 ± 4.61	42.29 ± 4.27

Roughness parameters of stainless steel surfaces by Ti:Sapphire laser (Figure 85 c, d and e) do not differ from those of structured-stainless steel by Yb laser (Figure 85 f, g and h). Therefore, with two different laser sources, it is possible to obtain quite similar morphologies with equivalent physical properties. Nonetheless, Yb laser allows to structure stainless steel surfaces faster as stated by Nisoli *et al.*[295] Therefore, the industrialization of stainless steel structuration by a Ytterbium-doped fiber laser could potentially be considered.

To validate the optimization of manufacturing laser parameters, the volume of impregnated oil was assessed by weighing samples before and after the infusion. Then a pasteurization run was carried out to evaluate the oil retention of the slippery liquid-infused surfaces obtained

V. Slippery Liquid-Infused Surfaces

According to optimization of manufacturing laser parameters, a high laser fluence combined to a relatively high velocity and a short hatch distance allow to obtain a deep chaotic structuration. This type of structuration seems more suitable to increase oil retention. In order to validate this hypothesis, previous structured surfaces were chemically modified, impregnated with a fluorinated oil and submitted to a pasteurization run.

In a second part, the development of new SLIS is presented. As fluorine-based oil previously used is not approved by the FDA and REACH [289], the aim is to replace it, which was done by using coconut oil. Finally, fouling-release performances of coconut-based SLIS are compared to those of fluorine-based SLIS.

5.1. Validation of the optimization of laser parameters

SLIS were produced according to the method developed (Figure 73) by Zouaghi *et al.*, following these three steps: (i) femtosecond laser-structuring stainless steel, (ii) chemical modification (silanization) and (iii) oil impregnation.

5.1.1. Chemical modification

Prior impregnating laser structured stainless steel surfaces with oil, a chemical surface modification was performed, increasing affinity of the surface toward oil.

The structured surfaces were first treated by a UV/ozone cleaner (UV-O Cleaner, Jetlight Company Inc., 4 mW/cm² at 220 nm) for 15 min, removing any organic contaminant from the surface and generating hydroxyl groups on it. The chemical modification was then carried out

in a nitrogen purged glovebox, where the samples were immersed in a 10^{-3} M solution of trichloro(*1H,1H,2H,2H*-perfluorodecyl)silane (PFTS) (Sigma Aldrich) in n-hexane for 4 hours at room temperature. Modified surfaces were gently rinsed with hexane, dichloromethane, ethanol and dried under nitrogen flow.

5.1.2. Assessment of the impregnation method and volume of impregnated oil

Afterwards, the resulting surfaces were impregnated with a hydrophobic lubricant: Krytox GPL 103 perfluorinated oil (DuPont, Belgium) (Figure 86). It was chosen because of its chemical inertness, its good durability and its very low surface tension (around 20 mN/m). The lubricant was deposited using two methods, which were further compared by weighing the mass of impregnated oil.

$$F\text{-}(\underset{\underset{CF_3}{|}}{CF}\text{-}CF_2\text{-}O)_n\text{-}CF_2CF_3 \qquad \text{where } n = 10 – 60$$

Figure 86. Chemical structure of Krytox GPL oils

The first one (Figure 87 a) consists in pouring dropwise the lubricant on surfaces until full surface coverage and use a spin-coater (Delta 10, Suss MicroTec, Garching, Germany) to remove oil excess. Spin-coater parameters were set to 1300 rpm, 30 s with an acceleration of 2 and two cycles were done.

The second one (Figure 87 b) consists in positioning surfaces at a random angle and in pouring dropwise the lubricant on it until full coverage. Surfaces were left tilted overnight to ensure complete infusion. Oil excess was finally removed by spin-coating (v:1300 rpm, t: 30 s, a: 2 and c: 1).

In order to validate the optimization of laser parameters, samples were weighed before and after the impregnation step using a micro-balance (balance XPR36, Mettler Toledo). Samples presented in section 3.2.1. were first impregnated by spin-coating and then submitted to a pasteurization run to assess oil retention. They were cleaned in a 2 % (w./v.) NaOH solution for 60 min and rinsed with distilled water for 5 min. These two steps were performed in an ultrasonic bath. Cleaned surfaces were checked by measuring the water contact angle and by digital microscopy (Annex 4 Figure 110).

The surfaces were re-impregnated by gravimetric draining and spin-coating and submitted to pasteurization cycle as well.

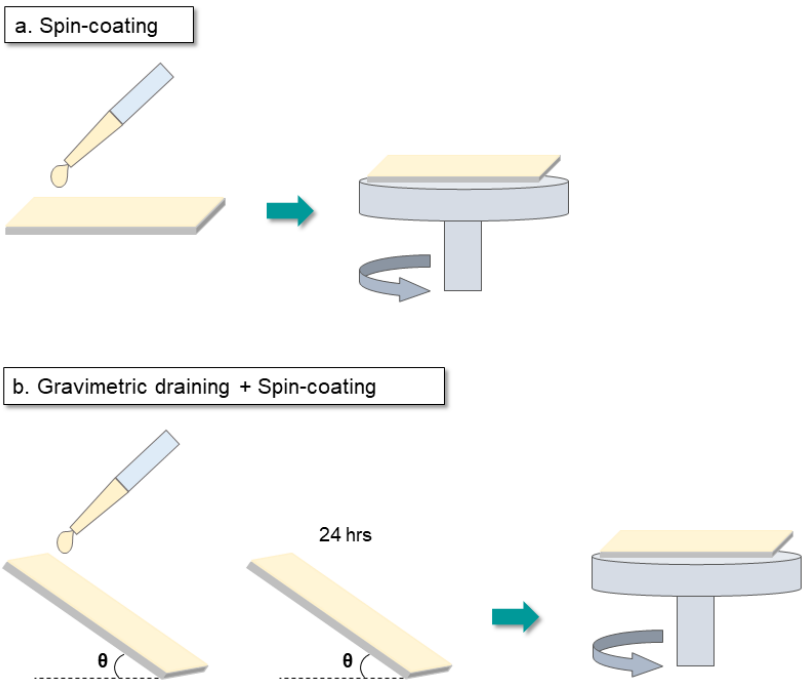

Figure 87. Schematic diagram of impregnation methods. (a) Spin-coating. (b) Gravimetric draining and spin-coating.

Figure 88 displays volume of impregnated oil as a function of the velocity, of hatch distance for both impregnation methods (A: spin-coating and B: gravimetric draining and spin-coating).

First the comparison of both methods demonstrates that for each sample, the volume of infused oil is almost equivalent. For instance, the amount of impregnated oil in the sample structured at 75 mm/s with a hatch distance of 19 µm is 5.0 µL by spin-coating and 5.3 µL by gravimetric draining and spin-coating.

Secondly, regarding the hatch distance, at 75 mm/s, the volume of oil is quite similar whatever the hatch distance (between 5.5 and 5.0 µL according to the spin-coating method). However, at 100 mm/s, the difference in term of infused oil is more important. For example, between samples structured with a hatch distance of 38 and 19 µm, the volume of oil varies from 3.4 to 4.6 µL (according to the spin-coating method).

Finally, concerning the velocity, globally, the quantity of oil is higher at 75 mm/s (~ 5.3 µL) than at 100 mm/s (~ 4.0 µL). Nonetheless, it can be observed that for a hatch distance of 19 µm, the oil variation is very low (5.0 and 4.6 µL for 75 and 100 mm/s respectively). This corroborates the results of the maximum profile valley depth.

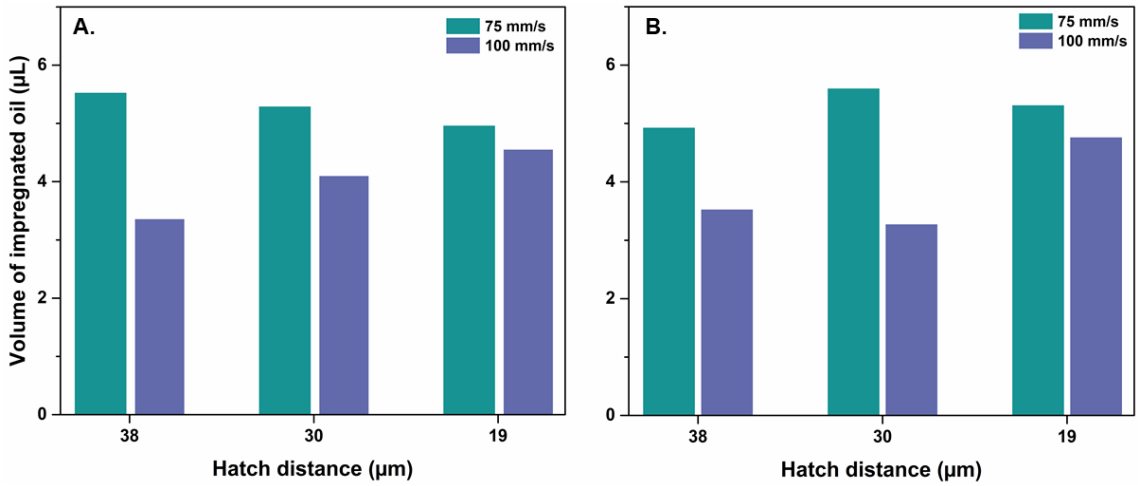

Figure 88. Volume of impregnated oil as the function of the velocity and hatch distance. (A) Using the spin-coating method. (B) Using the gravimetric draining and spin-coating method.

In this part, the influence of the impregnation method, velocity and hatch distance on the amount of infused oil has been discussed. The method used for the impregnation has no impact on the lubricant volume. However, this latter depends on both the velocity and hatch distance and to maximize the impregnation it seems suitable to structure stainless steel surface with a short hatch distance (19 µm) at a quite high velocity (75 mm/s). Assessment of oil retention of all samples were then carried out through a pasteurization run.

5.1.3. Fouling performances and assessment of oil retention rate

Anti-fouling and fouling-release performances of SLIS impregnated by gravimetric draining and spin-coating method were assessed. The fouling test was run for one hour, using WPC powder batch U20454. Samples were then removed from sample holder to be weighed and put back inside sample holder to be rinsed with hot water for 20 min. In Figure 89 both anti-fouling and fouling-release results are presented. Only one sample demonstrates good anti-fouling properties with a fouling deposit reduction of 72%, corroborating previous results observed by Zouaghi *et al.*[13] Regarding fouling-release performances, all samples structured at 75 mm/s and one at 100 mm/s showed excellent results. Nonetheless, a fouling deposit reduction higher than 100 % was obtained, owed by an oil loss, which was evaluated by weighing samples.

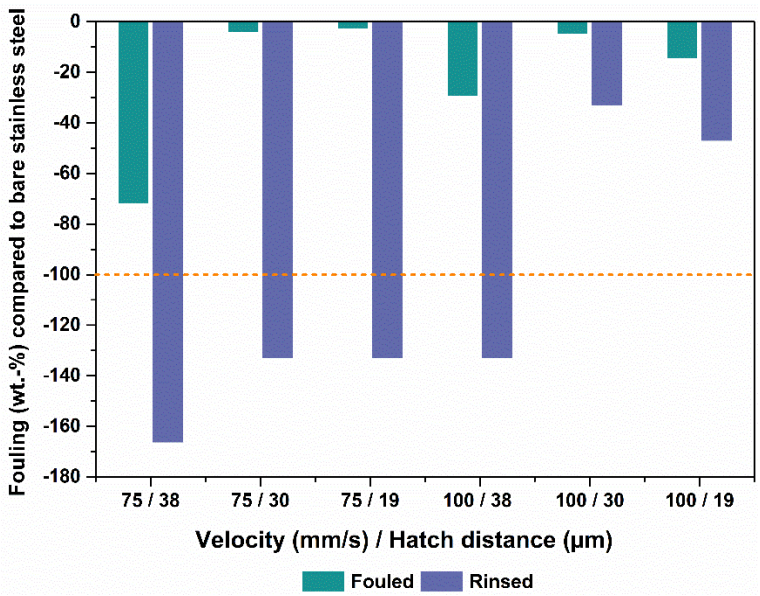

Figure 89. Anti-fouling and fouling-release (rinsed) performances compared to bare stainless steel

Samples were weighed using a micro-balance for the assessment of oil retention. Mass of lost oil and oil retention are displayed in Table 41. Samples 75/30, 75/19 and 100/38 demonstrate a lower oil loss than sample 75/38. Nonetheless, oil retention of sample 100/38 is lower than that of samples 75/30 and 75/19, due to a lower amount of impregnated oil before the pasteurization cycle. Both samples 75/30 and 75/19 allow a good oil retention but sample 75/19 was slightly deeper, thus a higher volume of oil could be infused into structured-surface. Consequently, laser process parameters corresponding to sample 75/19 were taken on for further SLIS fabrication.

Table 41. Assessment of oil retention after a pasteurization run

Sample	Fouling reduction (wt.-%)	Volume of infused oil (µL)	Volume of lost oil (µL)	Oil retention (wt.-%)
75 / 38	166	4.94	2.50	49
75 / 30	133	5.61	1.52	78
75 /19	133	5.32	1.25	76
100 / 38	133	3.54	1.25	65

In bold: selected laser parameters for next part

To obtain well-defined and deep structures, an optimization of laser manufacturing parameters was performed, leading to the combination of: (i) a high laser fluence (11 J/cm²), (ii) a high beam velocity (75 mm/s) and (iii) a short hatch distance (19 µm).

The amount of impregnated oil and oil retention were assessed. Both impregnation method and hatch distance had not influence whereas the amount of oil increased with the decrease of velocity.

Finally, surface structured at 75 mm/s with a hatch distance of 19 µm demonstrated good fouling-release performances with an oil retention of 76 %. Taking into account its depth and mass of infused oil, this surface was thus selected for SLIS fabrication.

5.2. Development of new SLIS

5.2.1. Laser structuration of stainless steel surfaces

Laser structuration was performed based on the previous optimization of laser manufacturing parameters. The selected conditions used are gathered in Table 39 and stainless steel surfaces (15 mm x 10 mm) were structured following a grid-like pattern (Figure 84).

Two types of SLIS were fabricated: fluorine-based and coconut-based SLIS. As these latter slightly differ from the one of fluorine-based SLIS, they will be presented separately.

5.2.2. Fluorine-based SLIS design

Regarding fluorine-based SLIS, after the laser structuration samples were chemically modified and then impregnated.

5.2.2.1. Chemical modifications

Silanization

Surfaces were chemically modified as described in section 4.1.1. This type of modification will be further named PFTS. The silanization was verified by measuring water contact angle. For all samples, the deposition of droplets was impossible due to their superhydrophobocity, proving the silanization effectiveness.

Plasma coating

In Chapter 3, superhydrophobic fluorine-based bilayers were deposited by atmospheric pressure plasma torch. Thus in order to replace the silanization step carried out in glovebox, chemical modification of structured stainless steel was performed by APP torch. As described in Chapter 3, HMDSO (Hexamethyldisiloxane) and pFOTES (*1H,1H,2H,2H-*

perfluorooctyltriethoxysilane) were alternatively nebulized into the N_2 plasma post-discharge and deposited using the Lab-Scan system. Plasma parameters are reported in Table 42.

Table 42. Plasma parameters used for the fluorine-based bilayer deposition.

	N_2 plasma (L/min)	Frequency (kHz)	Distance (mm)	Speed (mm/s)	Cycles	HMDSO (mL/h)	N_2 Carrier (L/min)	pFOTES (mL/h)	N_2 Carrier (L/min)
Pre-treatment	60	80	20	100	4	0	0	0	0
Coating Deposition	60	80	20	100	2	20	1.1	20	1.1

Plasma bilayers applied onto structured stainless steel surfaces were observed by SEM. Nanoparticles that were also observed when these bi-layers were applied on raw stainless steel, (in Chapter 3) modify the surface morphology (Figure 55, 113). Nonetheless, as illustrated in Figure 90 c, the deposition onto structured stainless steel surfaces drives to a heterogeneous thin film, which partly covers voids. EDX analysis confirms that the large layer covering voids corresponds to the plasma coating.

The chemical modification by APP was verified by measuring water contact angle. Measurements showed values > 150°, thus validating the effectiveness of the bilayer deposition.

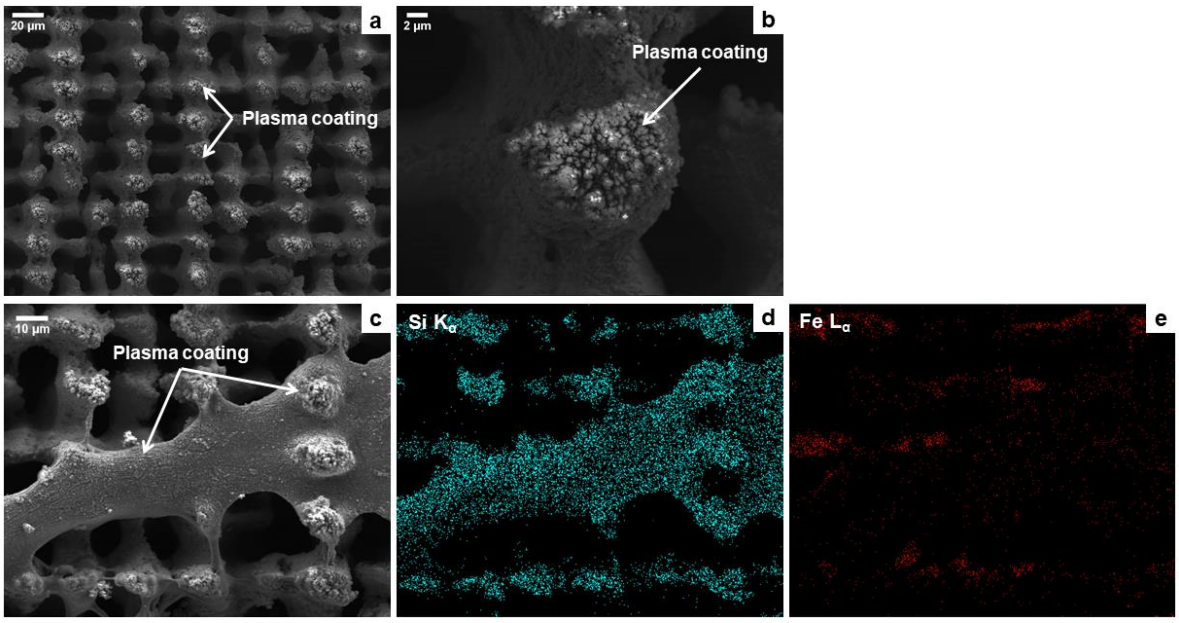

Figure 90. SEM images of the HMDSO/pFOTES bilayer onto structured stainless steel (a, b and c) and EDX analysis highlighting the heterogeneous plasma deposition (d: Silicon element and e: Iron element).

5.2.2.2. Impregnation

Once samples were chemically modified by PFTS, they were impregnated with the lubricant Krytox GPL 103 by spin-coating as illustrated in Figure 91 a. WCA measurements were then performed to control the impregnation step. Nevertheless, higher values of WCA (126 ± 3 °) were observed compared to those previously obtained (117 ± 1° for the sample structured at 75 mm/s, with a hatch distance of 19 µm).

Consequently, another method was tested, consisting in saturating stainless steel surfaces with the lubricant. They were left for 30 min to ensure the infusion. Oil excess was finally removed by spin-coating (v:1300 rpm, t: 30 s, a: 2 and c: 1). WCA decreased of about 10° to reach about 113°, corroborating also WCA values obtained by Zouaghi *et al.*[13]

Furthermore, an oil lip pulling up against the edges of the water drop can be observed in Figure 91. According to the literature, this pull-up phenomenon corresponds to the cloaking phenomenon *i.e.* encapsulation of the water droplet in a thin oil film. It was pointed out by Smith *et al.* by dying the lubricant with a fluorescent compound.[302] From this, they described several states to distinguish the possible configurations of SLIS depending on the affinity of the substrate and lubricant. On the one hand, the oil fills in the cavities and corresponds to the impregnated-emerged state. On the other hand, the oil fills in the cavities and covers completely the substrate, making an oil thin film corresponds to encapsulated state, which is desirable to eliminate pinning and favour slipping.

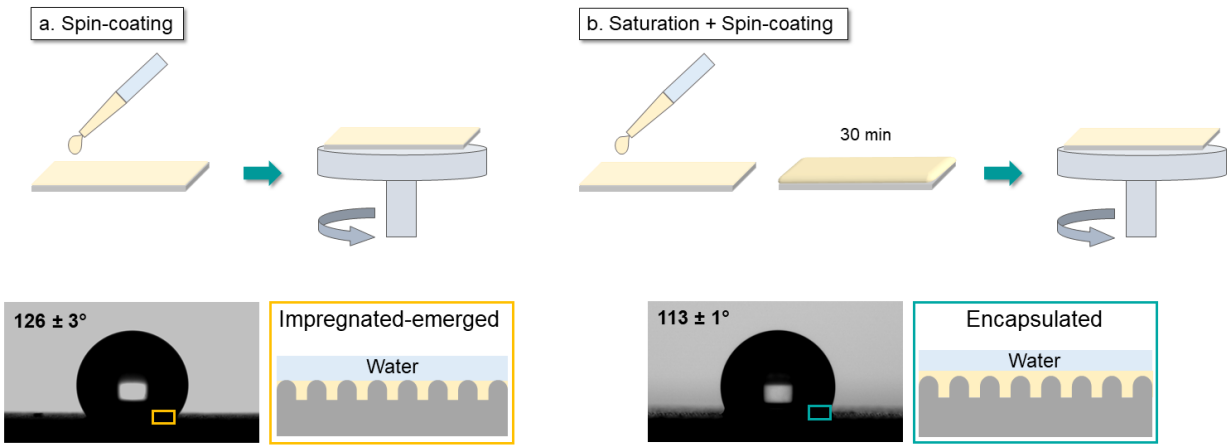

Figure 91. Schematic diagram of impregnation methods. (a) Spin-coating. (b) Lubricant saturation and spin-coating.

The second impregnation process allows SLIS to be in the encapsulated state, thus, it will be used for coconut oil impregnation. Fluorine-based SLIS will be referred as PFTS-Krytox and HMDSO/pFOTES-Krytox in the manuscript.

5.2.3. Coconut-based SLIS design

Coconut oil was chosen in order to replace fluorine-based oil (Krytox GPL 103). Although this latter presents numerous advantages (chemical inertness, low surface tension and low vapour pressure, it is not food-compatible. Coconut oil is a vegetal, edible and not part of allergen foods.

5.2.3.1. Chemical modifications

Silanization

As coconut oil is composed of fatty acids (mainly dodecanoic acid 46 % according to Table 43), modifying stainless steel surfaces with a perfluorosilane like PFTS seemed not relevant. To confirm this hypothesis, two stainless steel surfaces were modified by PFTS and OTS (octadecyltrichlorosilane, Sigma Aldrich) using the same protocol as that described in section 4.1.1 and one surface was not modified.

Table 43. Fraction of fatty acids in coconut oil[303]

Fatty acid	Systematic name	Composition (%)	Chemical structure
Lauric acid	Dodecanoic acid	46.10	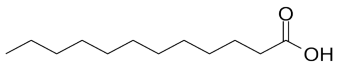
Myristic acid	Tetradecanoic acid	21.56	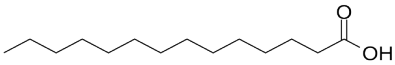
Palmitic acid	Hexadecanoic acid	8.52	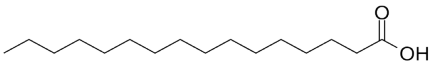
Caprylic acid	Octanoic acid	6.87	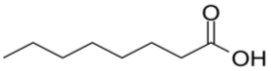
Capric acid	Decanoic acid	6.12	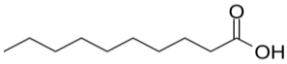

The spreading of a coconut oil droplet on modified surfaces was analyzed. Coconut oil was beforehand heated to 50°C (it is solid at room temperature) and deposited using the DSA 100 (Krüss, Germany). Figure 92 shows the spreading of a coconut oil droplet onto stainless steel depending on the surface chemistry. The contact angle on the PFTS-modified surface is higher than that on the OTS-modified and unmodified surfaces (45° against 27° and 20° respectively). Furthermore, as the spreading of coconut oil seemed better onto the unmodified sample than onto the OTS-modified sample, some of laser structured samples were silanized with OTS and some other remained unmodified.

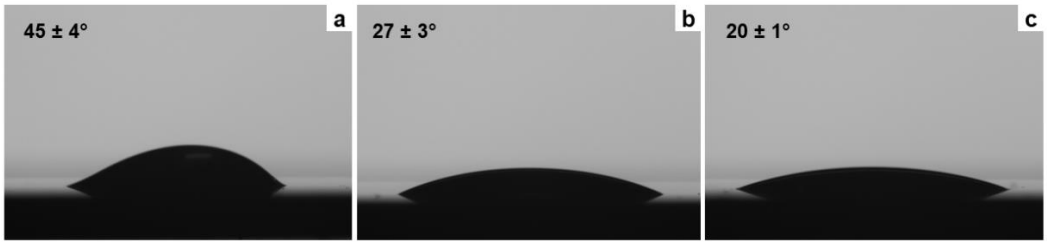

Figure 92. Spreading analysis of coconut oil onto stainless steel surfaces with different surface chemistries. (a) PFTS-modified. (b) OTS-modified. (c) unmodified.

It has to be noticed that silanization with OTS was checked by WCA measurements showing values >150° and thus validating the chemical modification.

Carnauba wax

In order to replace the silanization step performed in glovebox, another chemical modification was done from carnauba wax (Aromazone) based on two works [176], [284]. The composition of carnauba wax is reported in Table 44.[304]

Table 44. Composition of carnauba wax according to Vandenburg et al.[304]

Compound	Amount (wt.-%)
Aliphatic esters	38-40
Diesters of 4-hydroxycinnamic acid	20-23
Diesters of 4-methoxycinnamic acid	5-7
Esters of ω-hydroxycarboxylic acids	12-14
Free alcohols	10-12
Free acids	5-7
Hydrocabons[12] (paraffins)	0.3-1
Triterpene diols	0.4

A 1 % (w./v.) carnauba wax-ethanol emulsion was prepared by first heating the mixture at 80°C for 45 min to dissolve carnauba wax. The carnauba wax-ethanol emulsion was cooled down for 30 min until precipitation. Then, the solution was placed into an ultrasonic bath for 2 h to form smaller particles. The emulsion was finally sprayed onto structured-samples by loading it into a spray gun (LG60, Tricolor Industries) using an air pressure of 200 kPa. The resulting coating was annealed in an oven at 40°C for 5 min in order to enhance its mechanical stability.

Carnauba coated stainless steel surfaces were observed by SEM. Carnauba wax makes surface morphology more complex, bringing a desert rose-like structure (Figure 93). WCA was also measured and coated surfaces revealed to be superhydrophobic as water drops did not stick to the surface.

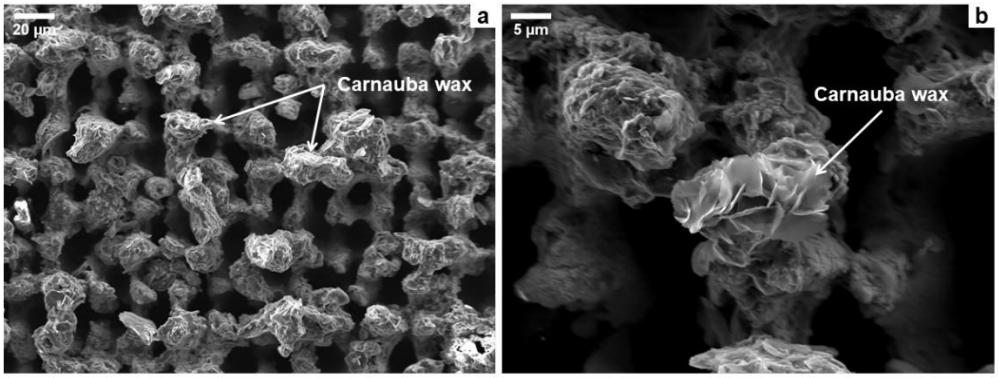

Figure 93. SEM images of carnauba-coated SS surfaces

Plasma coating

HMDSO thin film was deposited by APP torch to chemically modify structured stainless steel samples. The Lab-Scan system presented in Chapter 3 was for the deposition of HMDSO. Table 45 reports manufacturing plasma parameters used.

Table 45. Plasma parameters used for the silane-based layer deposition.

	N_2 plasma (L/min)	Frequency (kHz)	Distance (mm)	Speed (mm/s)	Cycles	HMDSO (mL/h)	N_2 Carrier (L/min)
Pre-treatment	60	80	20	100	4	0	0
Coating Deposition	60	80	20	100	1	20	1.1

HMDSO plasma coatings deposited onto structured samples were observed by SEM (Figure 94). As for HMDSO/pFOTES plasma bilayer, HMDSO thin film is formed of nanoparticles and spreading layer, which also covers voids (Figure 94 c). To control the chemical modification effectiveness, WCA was measured, showing values > 150°.

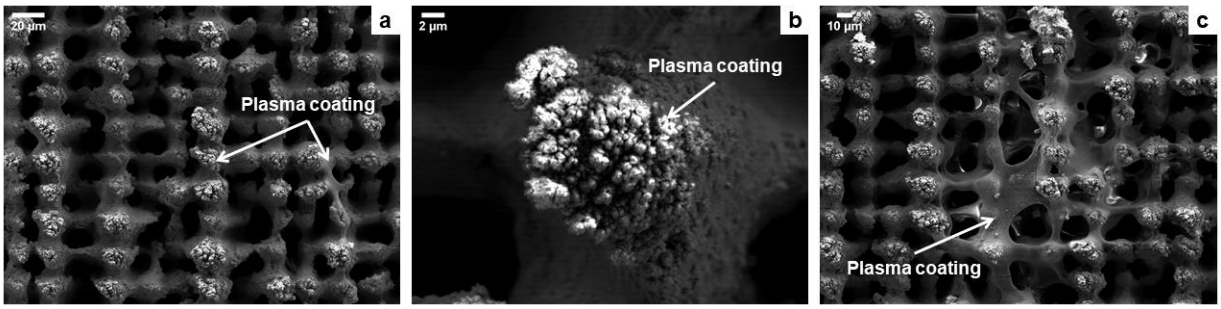

Figure 94. SEM images of the HMDSO layer onto structured stainless steel (a, b and c)

5.2.3.2. Impregnation

Modified (by OTS, carnauba wax and HMDSO) and unmodified samples were impregnated with coconut oil (Aromazone). Coconut oil was heated at 50°C to make it completely liquid. The same method previously used for fluorine-based SLIS was chosen, oil saturation followed by a spin-coating cycle to remove the excess of oil (Figure 91 b). To avoid the oil solidification during the oil saturation step, samples were placed onto a heat-plate at 50°C. Impregnated modified surfaces will be referred as OTS-Coconut, HMDSO-Coconut and Carnauba-Coconut and impregnated unmodified surfaces as Coconut in the manuscript.

5.2.4. Characterizations

Prior to assess the fouling-release performances of fluorine-based and coconut-based SLIS, the mass of impregnated Krytox and coconut oil was also evaluated, in order to characterize oil retention. Moreover, CA with water and model fluid in static and dynamic modes were measured. The model fluid corresponds to the solution prepared for fouling trials.

5.2.4.1. Volume of impregnated oil

The mass of impregnated oil (Krytox and coconut) was assessed by weighing samples before and after the impregnation using the micro-balance. Figure 95 gathers the resulting volumes using Krytox and coconut oil densities (1.92 at 0°C and 0.91 at 25°C).

A higher amount of Krytox has infused by saturation and spin-coating (~ 8.2 µL) than by spin-coating only (~ 5.4 µL). Therefore, the impregnation by saturation and spin-coating allows to impregnate a higher volume of oil.

By comparing SLIS impregnated with Krytox, the volume infused into PFTS-Krytox surfaces is almost equivalent to the one infused into HMDSO/pFOTES-Krytox samples (8.2 ± 0.9 µL against 7.7 ± 0.9 µL respectively).

Regarding Coconut-based SLIS, all surfaces submitted to a chemical modification show an infused volume around 9 µL whereas unmodified surfaces show an infused volume lower were (7.0 ± 0.5 µL). This emphasizes that the chemical modification is an important step as it allows to increase the volume of infused oil.

No strong difference is observed between the impregnated volume of Krytox and coconut oil as all volumes are in the same order of magnitude.

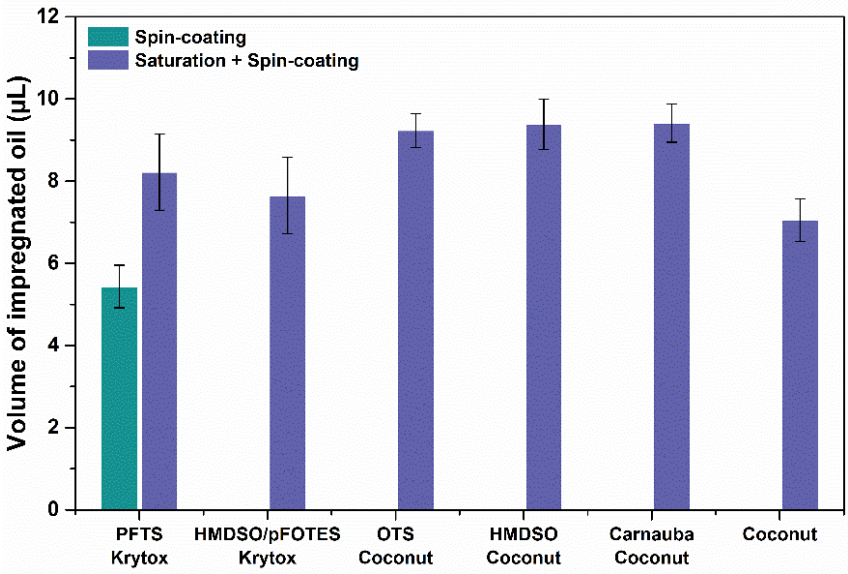

Figure 95. Volume of impregnated coconut oil compared to fluorine-based oil.

5.2.4.2. Wettability and contact angle hysteresis

Contact angle measurements were performed using (1) water to assess wettability and (2) the model fluid (fouling solution) beforehand heated to 85°C. Contact angle hysteresis (CAH) measurements were carried out as well by the tilting method with both water and model fluid. Before CA and CAH measurements, coconut-based SLIS were heated at 25°C for 2 min to obtain an oily interface.

Fluorine-based SLIS are hydrophobic (Figure 96 A) which is in agreement with previous studies.[13], [266] This was expected as the surface tension of Krytox is quite low, around 20 mN/m. Regarding coconut oil, the four types of SLIS (OTS-Coconut, HMDSO-Coconut, Carnauba-Coconut and Coconut) have a lower WCA (around 80°) very close to that of bare stainless steel (83°). A decrease of around 10° was observed onto bare SS using model fluid, leading to a CA of 72° which is consistent with the work of Ozden [240] who measured a CA of 72° onto stainless steel with whole milk.

For all SLIS, the same trend is obtained, a CA reduction of about 10° was noticed. This can be explained by the lower surface tension of the model fluid (53.2 ± 1.1 mN/m), which was measured by the pendant drop method. This value can be explained by the temperature (the model fluid was beforehand heated before) and by the presence of proteins. [241], [242]

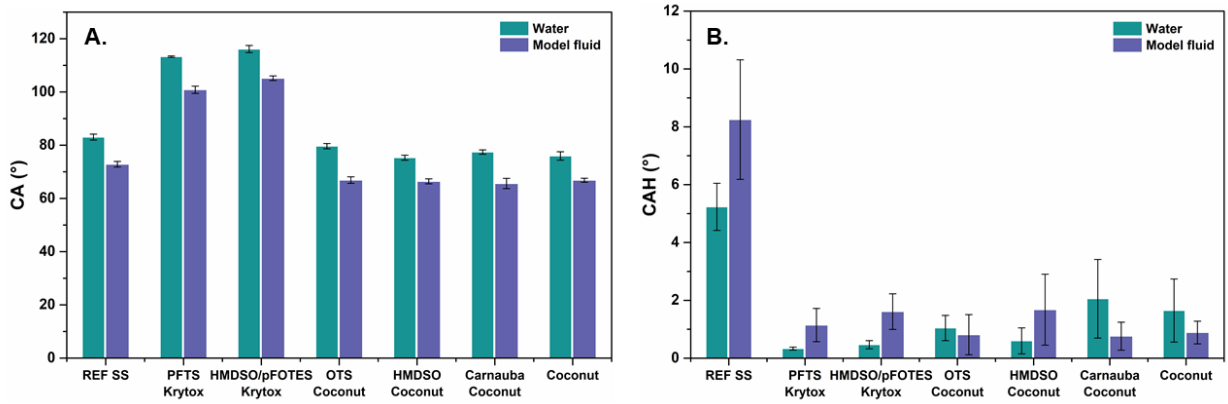

Figure 96. (A) Contact angle measurements using water and model fluid. (B) Contact angle hysteresis measurements using water and model fluid

Figure 96 B displays CAH measurements with both water and model fluid. Low CAH values (< 4°) were obtained for both types of surfaces, confirming their slippery behaviour. Contrary to SLIS, bare SS demonstrates a CAH value higher than 10° with model fluid. According to the literature [13], [111], low CAH could ease fouling removal with a water-rinse only. SLIS were then submitted to fouling runs with rinsing step to characterize their fouling-release performances.

5.2.5. Fouling-release performances

As observed in part 4.1.3. slippery surfaces showed excellent fouling-release performances. Therefore, in this part fouling-release properties were only assessed. The fouling test was run for one hour, using WPC powder batch U20454 followed by a hot water-rinsing for 20 min.

Figure 97 displays the fouling-release performances of both fluorine-based and coconut-based SLIS compare to bare stainless steel. PFTS-Krytox SLIS demonstrate excellent fouling-release properties (deposit weight reduction of 123 ± 16 wt.-%), which confirms the observation of Zouaghi *et al.*[13] HMDSO/pFOTES Krytox SLIS do not allow to totally remove fouling after the rinsing as they show a fouling deposit weight reduction of 75 ± 16 wt.- %. This could be explained by the heterogeneous chemical modification carried out by APP. As voids of structured stainless steel surfaces were covered, oil was potentially less well-retained.

Regarding coconut-based SLIS, unmodified surfaces, referred to as Coconut, show promising fouling-release performances (deposit weight reduction of 114 ± 19 wt.-%), while OTS-Coconut, HMDSO-Coconut, Carnauba-Coconut allow to reduce partially fouling deposit (deposit weight reduction of 79 ± 32 wt.-%, of 54 ± 7 wt.-% and of 69 ± 50 wt.-% respectively). High standard deviations can be noted for both OTS-Coconut and Carnauba-Coconut SLIS. It

could be possible that coconut oil layer was less homogeneous onto these SLIS, generating irregularities which favour protein adhesion and thus fouling growth. Moreover, regarding HMDSO-Coconut, which is the less efficient SLIS, the same explanation as for HDMSO/pFOTES SLIS can be given. Images of SLIS before and after pasteurization test are displayed in Annex 5.

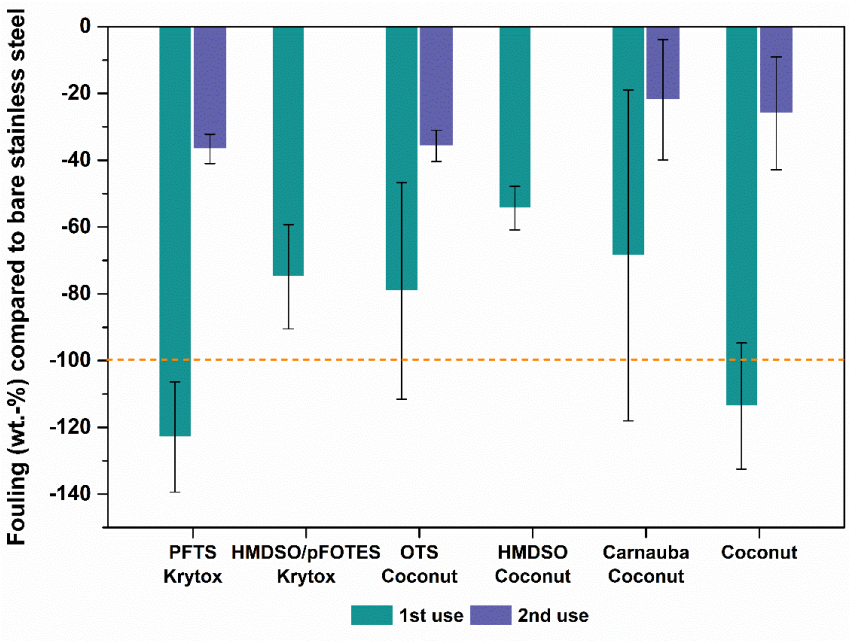

Figure 97. Fouling-release performances of fluorine-based and coconut-based SLIS.

Furthermore, a fouling deposit reduction higher than 100 % is observed, which is likely related to the oil loss during the fouling test as previously noted in section 3.2.3. Samples without fouling trace were thus analyzed to quantify oil retention and to determine their configuration: (i) impregnated-emerged or (ii) encapsulated. Five samples over six were analyzed for PFTS-Krytox and Coconut SLIS while only two over six for OTS-Coconut and Carnauba-Coconut SLIS. Table 46 shows oil retention of SLIS after the pasteurization test. All SLIS exhibit an oil retention around 60-65 wt.-%. To know if this retention rate is sufficient and to assess their durability, a second pasteurization run was performed.

Table 46. Assessment of oil retention after one pasteurization run

Sample	Fouling reduction (wt.-%)	Volume of infused oil (µL)	Volume of lost oil (µL)	Oil retention (wt.-%)
PFTS-Krytox	123 ± 16	8.22 ± 0.93	2.83 ± 0.52	67 ± 5
OTS-Coconut	79 ± 32	9.23 ± 0.41	3.32 ± 0.18	64 + 4
Carnauba-Coconut	69 ± 50	9.42 ± 0.47	3.36 ± 0.38	65 ± 1
Coconut	114 ± 19	7.05 ± 0.52	2.89 ± 0.28	59 ± 5

Regarding the wettability, WCA (Figure 98 A) increased of about 5° only, for all SLIS. Nonetheless, WCA images point out that the cloacking effect (white arrow) is no longer observed following the rinsing step (Figure 99 b and d). According to Zouaghi *et al.*, this could correspond to the impregnated-emerged state.[13] CAH was also assessed and the Figure 98 B shows higher CAH value for all SLIS, thus some structured parts are likely no longer encapsulated.

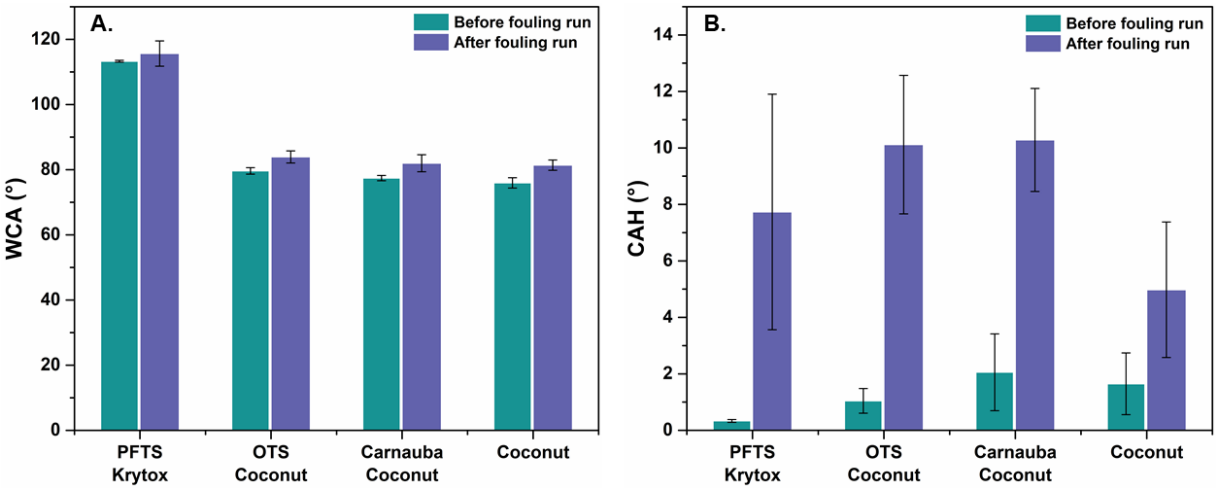

Figure 98. (A). WCA measurements before and after one pasteurization run and (B). CAH measurements before and after one pasteurization run.

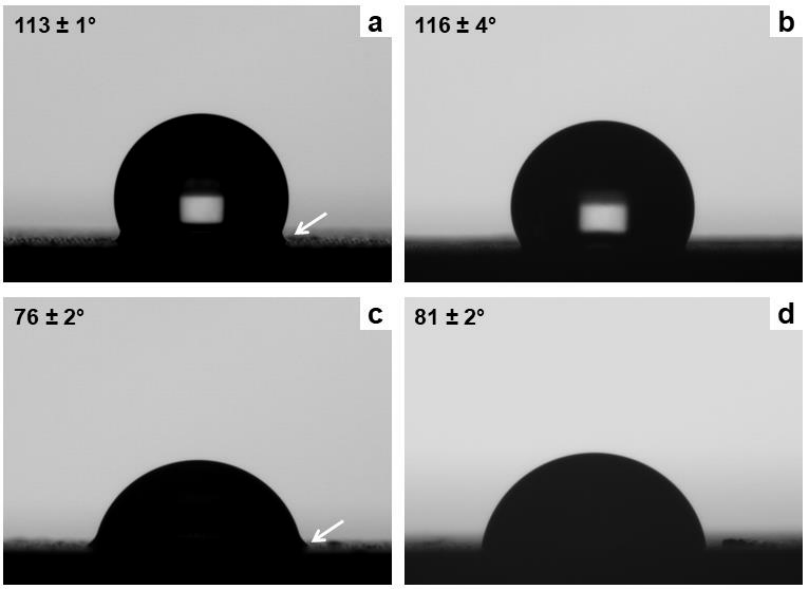

Figure 99. WCA images after impregnation (a: PFTS-Krytox and c: Coconut) and after the pasteurization run (b: PFTS-Krytox and d: Coconut).

Fouling-release performances obtained after the second run are presented in Figure 97. As previously pointed out by Zouaghi *et al.*[13] SLIS were less efficient to remove fouling after the rinsing step, due to the loss of oil. Therefore, an oil retention of about one third is not enough to guarantee the durability of SLIS for at least two pasteurization runs.

Oil retention is a key parameter for the SLIS durability. Other types of structures could be considered such as re-entrant structures or herringbones with modified and unmodified parts, which could also influence a flow modification.

VI. Conclusion

Former SLIS used to mitigate dairy fouling adhesion demonstrated excellent fouling-release performances, but had a limited lifetime and were not food-compatible. In order to improve SLIS durability and make them food-compatible, all steps of SLIS fabrication were studied and optimized, respectively: (i) structuration of stainless steel surface, (ii) chemical modification of structured-surface and (iii) infusion of the surface with a lubricant.

The structuration was performed by a femtosecond laser source, with the aim of obtaining deep microstructures to maximize oil retention. The optimization of laser parameters was performed by studying (i) laser fluence, (ii) beam velocity and (iii) hatch distance. Several observations were made. First, structuration scale increased with laser fluence, and to obtain microstructures, the maximum fluence of 11 J/cm² was required. Secondly, well-defined structures were observed at high velocity (75-100 mm/s), with a maximum of infused oil reached at 75 m/s. Finally, deeper structures were obtained with the decrease of hatch distance, with an optimum reached with 19 µm. Following a grid-like laser pattern, these optimized parameters drove to the formation of deep, well-defined micro-structures, which allowed the retention of 76% of the infused oil after a pasteurization run.

To replace fluorine-based lubricant, greener and food-compatible SLIS were developed using coconut oil. Three types of coconut-based SLIS were produced: one by infusing coconut oil into unmodified structured-surfaces, two by infusing it on modified structured-surfaces, either by silanization or by a carnauba wax layer. These surface modifications improved the volume of infused oil on coconut-based SLIS, but the unmodified coconut-based SLIS demonstrated better fouling-release performances, similar to those of fluorine-based SLIS, with comparable oil retention. Nonetheless, the durability was not improved as SLIS were efficient

for one pasteurization run only. Other types of structures could be considered such as re-entrant structures or herringbones with modified and unmodified parts, which could also influence a flow modification. Preliminary results on patterned surfaces will be presented in outlooks.

GENERAL CONCLUSION

This work aims at designing durable and food-compatible surfaces to mitigate fouling deposit onto stainless steel surface. Innovative techniques and concepts for surface modification were used. The understanding of modified surfaces demonstrating promising fouling-release performances was carried out by assessing surface properties (wettability, surface free energy and roughness) as well as complementary surface analyses.

The state of the art reviewed in the first chapter emphasized that although fouling tests were performed in both batch and continuous flow, similar conclusions regarding the influence of surface properties could have been emitted. It seemed that the reduction of fouling deposit could be managed either by acting on surface free energy or by combining both SFE and roughness. **Nonetheless, correlating fouling behaviour and surface properties remains complex as fouling and cleaning tests are not standardized.**

In this study, pasteurization tests were performed in continuous flow using whey protein concentrate powder to achieve reproducible fouling behaviours. However, the use of four WPC powder batches led to a high variability in surface density of fouling deposit. Potential causes were identified: (i) WPC powder composition, (ii) water content in $CaCl_2$ added to the model fluid and (iii) mechanical stress on fouling layer while targeting both anti-fouling and fouling-release properties. Consequently, to minimize the variability in surface density of fouling deposit onto bare and modified stainless steel surfaces, **$CaCl_2$ was stored in oven at 105°C** to limit its ageing. Moreover, **anti-fouling and fouling-release performances were preferentially assessed separately,** avoiding delamination of fouling layer owed by a mechanical stress.

To mitigate fouling deposition, innovative techniques and concepts were used to modify surface of stainless steel substrates.

Plasma polymer thin films were quickly deposited using an atmospheric pressure plasma torch. Nonetheless, as the plasma process was moved in three laboratories, this study revealed the influence of air extraction speed on coatings adhesion, which is a primordial requirement. As plasma thin coatings demonstrated a good adhesion (adhesion grade 5B) at an air extraction speed of 13 m/s, experiments were then carried out at this speed.

First, hydrophobic coatings were deposited from HMDSO precursor. The potential influence of 6 parameters to minimize fouling deposit was screened using an experimental design (Plackett-Burman). The most important parameters to reduce fouling deposit were the gas flow rate and the nozzle-to-substrate distance. The optimization of plasma parameters was coherent with experimental results as it led to the condition 3 which demonstrated excellent fouling-release performances for at least two uses. Surface properties, chemistry and morphology show that a **low polar part**, likely due to a certain carbon content in the thin film and a **roughness lower than 60 nm,** lead to a **fouling deposit reduction of 86% after two uses**.

In a second time, superhydrophobic bilayer thin coatings were deposited from two precursors: HMDSO and pFOTES. ToF-SIMS depth profile analyses highlighted the position of the two layers. The bilayer was less efficient (48 ± 24%) to ease fouling removal than the fluorine-based monolayer (62 ± 17%), likely due to its complex morphology (nanoparticles and large aggregates). Nevertheless, as the bilayer revealed more stable than the fluorine-based monolayer, HMDSO flow rate and power were optimized to improve fouling-release performances of the bilayer. Decreasing HMDSO flow rate did not lead to better fouling-release properties, while the **decrease of power allowed to reach a fouling deposit reduction of 72 ± 20%.** At low power the resulting bilayer showed a low polar part and a smooth surface (*i.e.* without nanoparticles or aggregates). **To enhance the effectiveness of superhydrophobic bilayer plasma coatings, an equilibrium could be found between the deposition of very small particles and the deposition of thin film with a low polar part**. Moreover, the replacement of fluorosilane precursor by a silane with a long alkyl chain could make the plasma bilayer food-compatible.

Former slippery liquid-infused surfaces (SLIS) have already demonstrated excellent fouling-release performances, but had a limited lifetime and were not food-compatible. In order to improve SLIS durability and make them food-compatible, all steps of SLIS fabrication were studied and optimized, respectively: (i) structuration of stainless steel surface, (ii) chemical modification of structured-surface and (iii) infusion of the surface with a lubricant.

In this work, an Yb-doped fiber femtosecond laser was used to structure stainless steel surfaces. Therefore, laser parameters were optimized to obtain similar structures to those resulting from Sapphire:Titanium laser structuration. Comparable deep microstructures were obtained for a high laser fluence (11 J/cm^2), a high velocity (75 mm/s) and a short hatch distance (19 µm). **The velocity of the Yb laser being hundred times higher than the Sapphire:Titanium, the structuration of a 150 mm^2 surface area is three times faster.**

Optimized laser parameters were validated by exhibiting an oil retention of 76% after a pasteurization run.

To replace fluorine-based lubricant, greener and food-compatible SLIS were developed using coconut oil. Four types of coconut-based SLIS were produced: one by infusing coconut oil into unmodified structured-surfaces, three by infusing it on modified structured-surfaces, by silanization, by a plasma coating or by a carnauba wax layer. Although the durability was not improved as SLIS were efficient for one pasteurization run only, the **unmodified coconut-based SLIS demonstrated promising fouling-release performances: fouling deposit reduction of 114 ± 19%, similar to those of fluorine-based SLIS: fouling deposit reduction of 123 ± 16%**, with comparable oil retention (59 ± 5% against 67 ± 5% respectively).

To summarize, surface modifications of stainless steel allowed to reduce fouling deposit through innovative techniques (atmospheric pressure plasma torch) and concepts (SLIS) (Table 47). Although deposition by atmospheric pressure plasma is quick, further optimization of parameters have to be performed to improve fouling-release performances of the bilayer. Moreover, the food compatibility of the precursors used has to be evaluated. Regarding SLIS, although the durability was not enhanced, the structuration by femtosecond laser was faster and the infusion by coconut oil made resulting SLIS food-compatible. Furthermore, promising fouling-release performances were obtained. SLIS durability could be enhanced by either circulating hot coconut oil to refill structured surfaces or by designing specific patterns (such as herringbones with modified and unmodified parts) to generate a flow modification.

Table 47. Comparison between plasma bilayer coating and slippery coconut-infused surface

	Plasma bilayer coating	Slippery coconut-infused surfaces
Fabrication method	Bottom-up	Top-down and bottom-up
Industrialisable technique	✓ (Easily implantable in line production)	~ (oil infusion method)
Stability	✓	N/D
Fouling-release performances	~ (Improvable: -72 wt.%)	✓ (-114 wt.%)
Food-compatibility	✗	✓
Durability	✗	✗
Surface regeneration	✗	✓

OUTLOOKS

In this section, preliminary results on two other pathways modifying stainless steel surface are presented. The first one consists in designing patterned surfaces (SLIS or hydrophilic-hydrophobic surface) and the second one consists in combining two concepts (amphiphilic and self-stratifying coatings)

Patterned surfaces

As mentioned previously, another way to reduce fouling adhesion could be the design of patterned surfaces. Indeed, patterned surfaces can limit the growth of fouling organisms by preventing strong binding and enhancing fouling release. The development of non-toxic fouling-release coatings using microtopography/micropatterning has been widely explored in marine field.[305]–[307] Therefore, a preliminary study was led to design patterned surfaces for the mitigation of dairy fouling. Being extensively used in microfluidic systems[308]–[310] to modifying the flow and increasing the mixing of solutions, herringbone pattern was chosen to design new surfaces.

Herringbone design was performed by Santino Jesulín Zapiain Merino (Master 2 student from Erasmus Mondus program). The patterning was then carried out by laser structuration used the femtosecond laser source previously presented in Chapter 4. The resulting sample is displayed in Figure 100 a. The dimensions of the pattern are pitch = 350 µm, width = 100 µm, and angle = 90°, which were confirmed by SEM analyses (Figure 100 b). The depth of laser-structured parts was assesed by digital microscopy (Figure 100 c), leading to a depth of 35 ± 5 µm which is consistent with values previously obtained in Chapter 4.

The resulting patterned stainless steel surface was then chemically modified by PFTS as described in section 4.1.1. Following the silanization, Krytox GPL 103 oil (DuPont, Belgium) was infused by spin coating (v:1300 rpm, t: 30 s, a: 2 and c: 1).

Prior assessment of fouling-release performances of the herringbone-structured SLIS, contact angle measurements were performed using water to assess wettability and using the model fluid (fouling solution) beforehand heated to 85°C to facilitate its spreading onto the sample. Contact angle hysteresis (CAH) measurements were carried out as well by the tilting method with both water and model fluid.

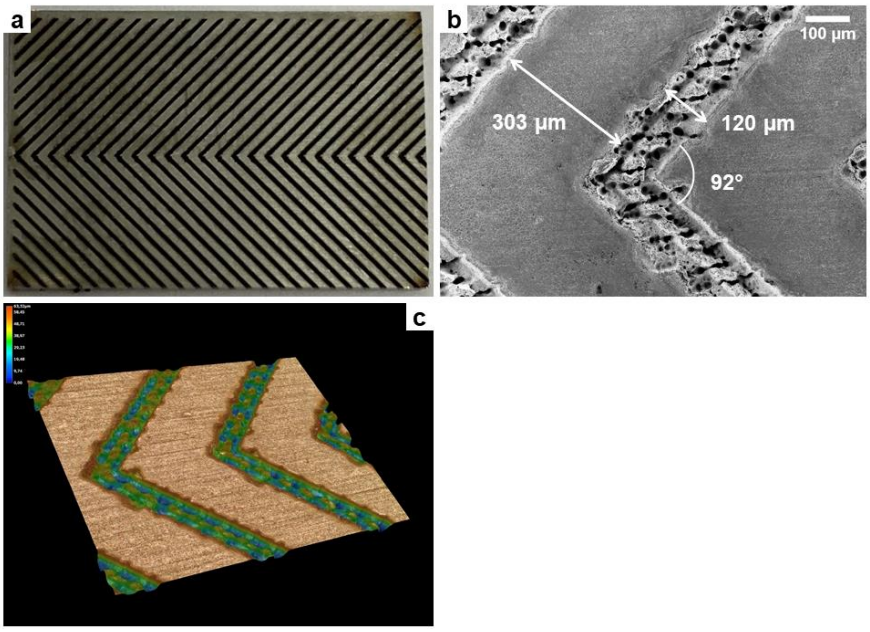

Figure 100. (a) Herringbone-structured stainless steel sample, (b) SEM image of herringbone pattern and (c) 3D image of herringbone-structured stainless steel

Regarding CA measurements, equivalent values to PFTS-Krytox SLIS are obtained with both water and model fluid. Nonetheless, resulting CAH values are much higher than those obtained for PFTS-Krytox SLIS (water: 16.0 ± 9.6° against 0.3 ± 0.1° respectively). Contary to PFTS-Krytox SLIS, no slippery movement was noticed for the herringbone-structured SLIS, which could be due to the unmodified parts which act as a pinning site for the droplets (Figure 101).

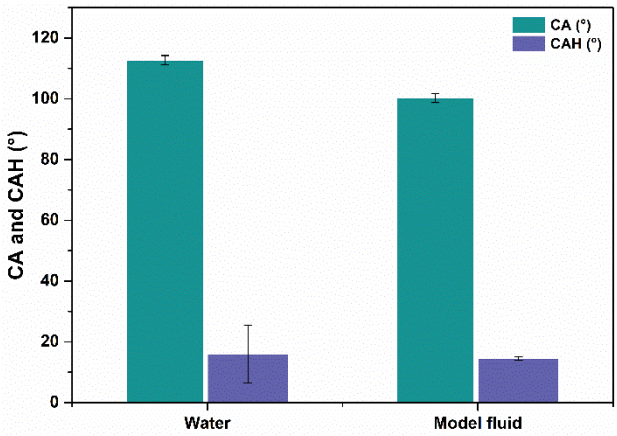

Figure 101. Contact angle and contact angle hysteresis measurements using water and model fluid.

Fouling-release performances of herringbone-structured SLIS were assessed. The fouling test was run for one hour, using WPC powder batch U20454, followed by a hot water-rinsing for 20 min.

Excellent fouling-release properties were obtained (fouling deposit reduction of 113 %) as observed for PFTS-Krytox SLIS in Chapter 4. The durability was also evaluated by submitting the herringbone sample to a second fouling run. As displayed in

Table 48, although the oil retention is twice lower than that of PFTS-Krytox SLIS, the herringbone-structure SLIS shows a better durability. Indeed, it allows to reduce fouling by 71% after the second use without being re-infused between the two pasteurization runs. These promising results could be due to the presence of both structured and unstructured parts. Indeed, theoretically, unmodified parts of the herringbone sample are expected to contain no oil, leading to a heterogeneous interface, which could potentially destabilize whey proteins adhesion.

Table 48. Fouling-release performances and oil retention of the herringbone-structured SLIS.

Sample	Fouling reduction (wt.-%)	Volume of infused oil (µL)	Volume of lost oil (µL)	Oil retention (wt.-%)
Herringbone (1st use)	113	4.22	2.94	30
Herringbone (2nd use)	71	1.28[a]	0.25	24[b]

a: corresponds to the remaining oil volume after the first pasteurization run, b: oil retention after two pasteurization tests.

Consequently, heterogeneous hydrophilic-hydrophobic surfaces could be designed to confirm this hypothesis. Preliminary herringbone designs were performed by Santino Jesulín Zapiain Merino. To do so, silicon wafers were first patterned using photolithography process as illustrated in Figure 102. TEOS was then deposited using the APP torch to create hydrophilic parts and hydrophobic parts were then revealed by removing the photoresist. Several herringbone patterns were studied, by varying (i) pitch, (ii) width and (iii) angle.

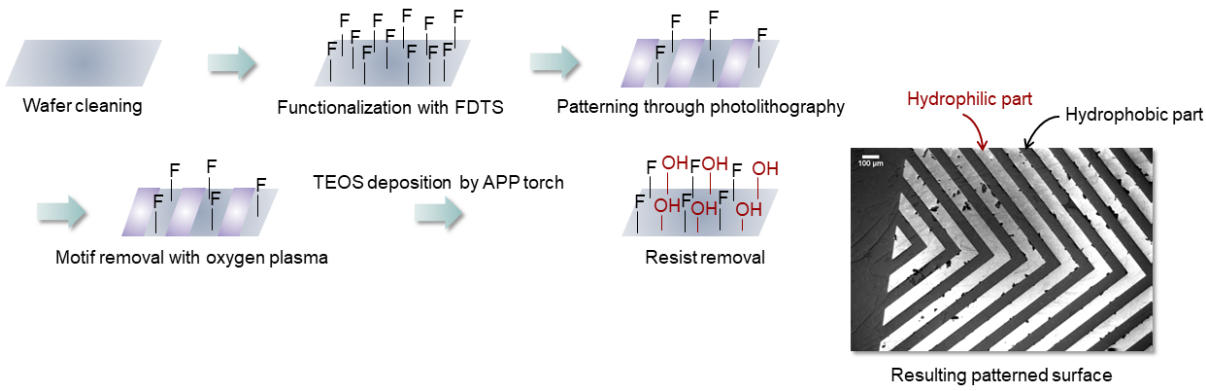

Figure 102. Schematic workflow for the development of patterned surfaces and SEM image of the herringbone hydrophilic-hydrophobic surface.

Based on this approach, the combination of both femtosecond laser ablation and atmospheric pressure plasma process could be considered for the development of heterogeneous hydrophilic-hydrophobic surfaces.

Self-stratifying amphiphilic coating

A previous study highlighted excellent anti-fouling properties of amphiphilic coatings (Figure 103 B) for five pasteurization cycles.[108] The amphiphilic coating consists in a PEO-siloxane with cross-linkable triethoxy end groups, which was incorporated in an elastomeric matrix enhancing PEO resistance and stability. Nonetheless after five pasteurization runs, the erosion of the amphiphilic coating was noticed and the primer used for its adhesion to stainless steel is classified as carcinogenic mutagenic reprotoxic, which could cause health issues. Therefore, in order to replace this primer, an epoxy resin was tested through another concept: self-stratification.

This approach allows reducing the number of steps of the process.[311] Once applied on a substrate in one step, two distinct layers with excellent interfacial adhesion are formed: an underlayer and the top layer (Figure 103 A). Self-stratifying coatings were already developed for marine[312], [313] or antimicrobial[314], [315] applications.

Consequently, the idea is to combine both self-stratification and amphiphilic coating to replace the primer and obtain a one-step process as illustrated in Figure 103 C.

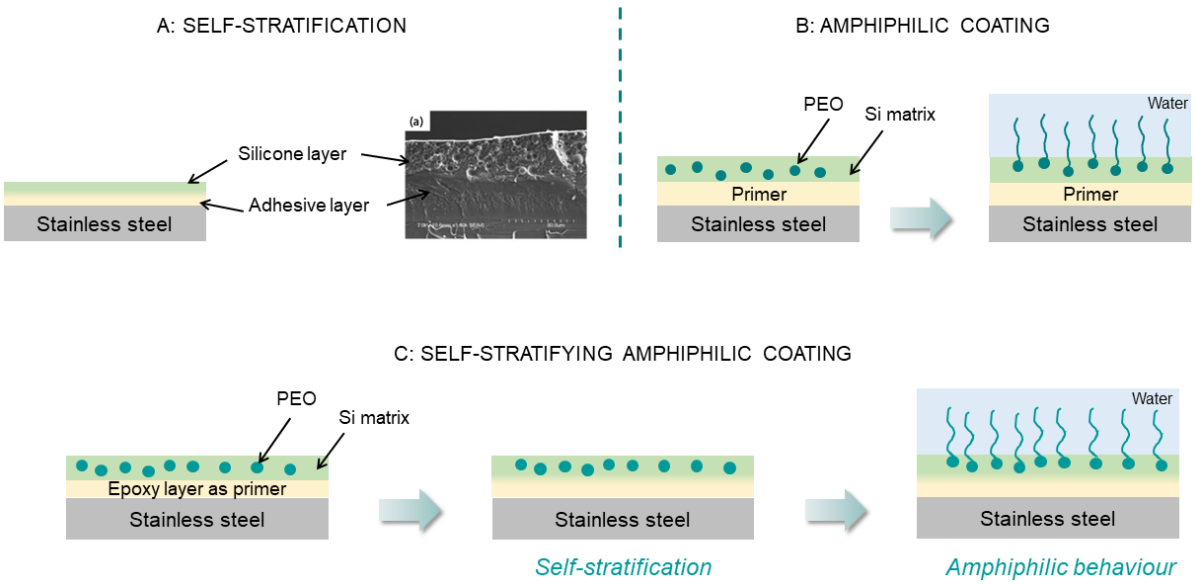

Figure 103. Diagram of (A) self-stratification approach, (B) amphiphilic coating and (C) the combination of both concepts.

Self-stratifying amphiphilic coating was prepared as detailed in Annex 6 - Figure 112. Its amphilic behaviour was assessed by WCA measurements for 150 s. In fact, a quick increase of the wettability is typically observed when water droplets are deposited. This behaviour was well observed as displayed in Figure 104 A. Indeed, when the water droplet is deposited, a WCA of 114° is measured and after 20 s only, the WCA reached 50°. The self-stratification was controlled by EDS mapping analyses. As observed in Figure 104 B, two distincts layers can be noticed, corresponding to a Type I self-stratification.[316] The first one, onto stainless steel substrate, corresponds to the epoxy resin and the second one corresponds to the amphiphilic coating (Si-PEO).

Consequently, these analyses allowed to validate the combination of both self-stratification and amphiphilic coating. However, the resulting self-stratifying amphiphilic coating revealed non-adhesive properties to stainless steel substrate. Moreover, a reproducibility issue was noticed. As shown in Figure 104 A, in September, the resulting coating was less hydrophilic than the one deposited in June. This could be due to external parameters such as the temperature or relative humidity and/or to the high volatity of hexane. Due to a supply issue of elastomeric matrix, it was impossible to perform further experiments. Nevertheless, this type of coaing remains promising as it could be deposited onto stainless steel in one step and could reduce the toxicity of the adhesive layer by choosing food-compatible resin.

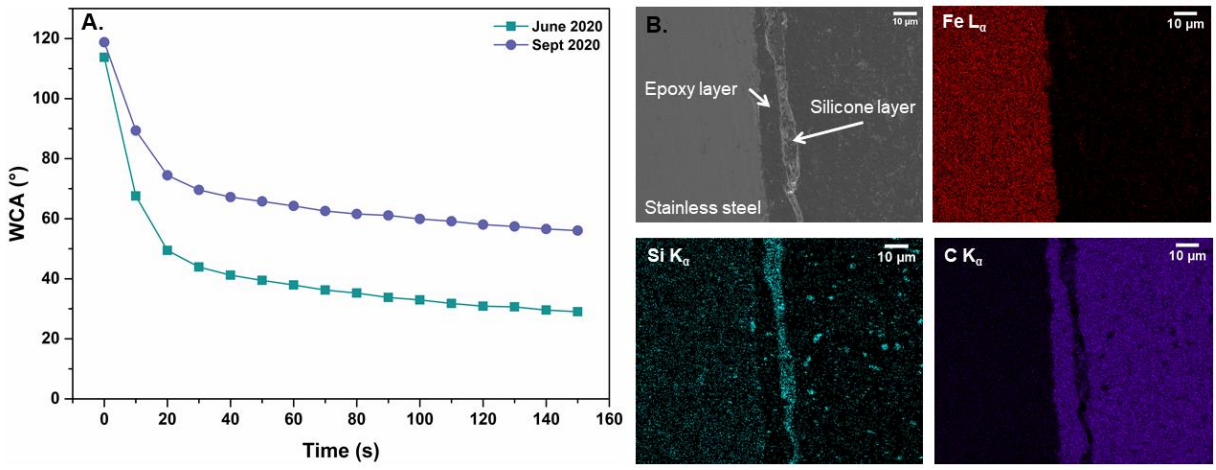

Figure 104. (A) Evaluation of the amphiphilic behaviour and (B) observation of the self-stratification by EDS mapping analyses.

To sum-up, promising fouling-release performances were obtained using herringbone-structured SLIS. This surface showed a fouling deposit reduction of 71% after two pasteurization runs without being re-infused in between. Further experiments could be done to assess fouling-release performances of this type of patterned SLIS using coconut oil.

The combination of both amphiphilic and self-stratifying coatings seems encouraging as the amphiphilic behaviour and type I self-stratification were obtained. However, adhesion issue has to be resolved in order to evaluate anti-fouling performances of this type of coating.

Overall, surface modification techniques used in this project allowed to design new types of coatings, demonstrating good fouling-release performances. The development of coatings for food applications has to deal with durability and food-compatibility. **This was partly improved using coconut-SLIS, but the key could finally be the design of a heterogeneous hydrophilic-hydrophobic surface.**

MATERIALS AND METHODS

This section is meant to present the substrates used in this study, their preparation before any surface modifications and the analytical techniques used to characterize them. Numerous techniques were used in order to obtain physico-chemical, chemical, structural and adhesion information at different scales (Figure 105).

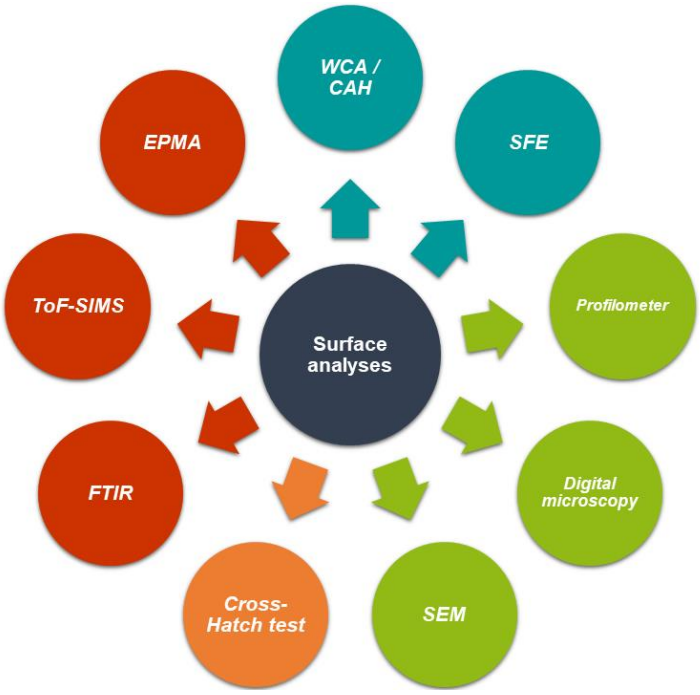

Figure 105. Characterization techniques. Blue: Physico-chemistry, Green: Roughness and Morphology, Orange: Adhesion and Red: Chemistry

I. Samples preparation

1.1. Substrates

As 316L stainless steel is widely used in food processing industries, surface modifications were thus carried out onto this type of stainless steel. 316L stainless steel with a 2B finish was purchased from GoodFellow (United-Kingdoms). Following the ASTM A480 standard 2B finish corresponds to a smooth, moderately reflective cold-rolled annealed and pickled. Its chemical composition was analyzed by WDS (Wavelength Dispersive Spectroscopy) using the Electron Probe MicroAnalysis and is reported in Table 49. Stainless steel substrate was almost

used for all surface characterizations and fouling tests. Regarding ToF-SIMS analyses, p-type doped (100) oriented silicon wafers were used.

Table 49. Chemical composition of 316L-2B stainless steel

Fe (%)	Cr (%)	Ni (%)	Mn (%)	Si (%)
70.28 ± 0.33	17.30 ± 0.05	10.12 ± 0.33	1.78 ± 0.03	0.52 ± 0.03

1.2. Laser cutting

Targeted dimensions of stainless steel samples were obtained by laser cutting (Chronolaser, France). The large substrates: 45 x 15 x 1 mm^3 were used for surface characterizations and fouling tests, the smaller ones: 10 x 15 x 1 mm^3 were used for surface characterizations under vacuum (SEM and AFM).

1.3. Surface cleaning

Prior to any surface modification, samples were degreased in ethanol and acetone (50/50 (v/v)) for 10 min, then washed in a 2 % solution of a commercial detergent (RBS T 105, Sigma Aldrich) at 65 °C for 10 min. Samples were finally rinsed with deionized water at 65 °C and at room temperature for 5 min and dried in air. These four steps were performed in ultrasonic bath (Bransonic) at 135 W and 42 kHz.

II. Surface characterizations

2.1. Wettability (static and dynamic) and surface free energy

2.1.1. Wettability

Static water contact angle was measured using a DSA100 drop shape analyzer (Krüss, Germany) by applying the Young equation (Eq. 24). At least three droplets of 2 µL of deionised water were deposited on each surface.

$$\gamma_S = \gamma_{SL} + \gamma_L \cos\theta \quad (24)$$

where θ is the contact angle between the liquid and the solid phase,γ_S is the solid–vapour interfacial energy, γ_{SL} the solid–liquid interfacial energy, and γ_L the liquid–vapor interfacial energy.

2.1.2. Contact angle hysteresis

Dynamic water contact angle or contact angle hysteresis (CAH), which is the difference between the advancing and receding contact angles, was measured through the tilting method (Figure 106) on the DSA100. At least three droplets of 5 µL of deionised water were deposited on each surface.

Figure 106. Diagram of the assessment of CAH by the tilting method.

2.1.3. Static and dynamic contact angles with model fluid

Static and dynamic contact angles were also measured using the model fluid prepared for pasteurization run. Thus, model fluid was prepared prior measurements and heated at 85 °C. At least three droplets of 2 µL were deposited on each surface for static measurements and three droplets of 5 µL for dynamic measurements.

2.1.4. Surface free energy

Surface free energy calculations were performed by depositing three droplets of 2µL of water, diiodomethane and formamide. Their surface free energies are reported in Table 50.

Table 50. Surface free energies of probing fluids for SFE calculation

Fluid	γ^{TOT} (mN/m)	γ^{D} (mN/m)	γ^{P} (mN/m)
Water	72.8	21.8	51.0
Diiodomethane	50.8	50.8	0.0
Formamide	58.2	18.7	39.5

The Owens, Wendt, Rabel and Kaelble (OWRK) approach was used to calculate the SFE (γ^{TOT}) and to decompose it into a dispersive (γ^{D}) and polar (γ^{P}) component (Eq. 25):

$$\gamma_{SL} = \gamma_S + \gamma_L - 2\left(\sqrt{\gamma_L^D \gamma_S^D} + \sqrt{\gamma_L^P \gamma_S^P}\right) \quad (25)$$

where γ_L, γ_L^D and γ_L^P represent surface free energy, dispersive and polar components of the probing fluid, respectively, and γ_S^D and γ_S^P are the dispersive and polar components of the solid surface to calculate to obtain the total surface free energy.

SFE results were then obtained with Advance 3.0 (Krüss, Germany) which uses the geometrical mean method. It consists in combining equations 24 and 25 and linearizing equation 26, leading to equation 27 as:

$$\gamma_L(1 + cos\,\theta) = 2\sqrt{\gamma_L^D \gamma_S^D} + 2\sqrt{\gamma_L^P \gamma_S^P} \quad (26)$$

$$\frac{0.5 \times \gamma_L \times (1+\cos\theta)}{\sqrt{\gamma_L^D}} = \sqrt{\gamma_S^P} \times \left(\frac{\gamma_L^P}{\gamma_L^D}\right)^{1/2} + \sqrt{\gamma_S^D} \quad (27)$$

where $\sqrt{\gamma_S^P}$ and $\sqrt{\gamma_S^D}$ are the slope and the ordinate to the origin in a linear plot, respectively, and the variables $0.5\gamma_L(1 + \cos\theta)/\sqrt{\gamma_L^D}$ and $\sqrt{\gamma_L^D}$ represent the ordinate and abscissa respectively. Using three probing fluids, three points are obtained and fitted by linear fitting method.

2.2. Profilometer

Sample profile was acquired with the Dektak XT stylus profilometer (Brüker). The scanning speed was set at 200 µm/s, the tip (2 µm) scanned the surface on 2000 µm-long segment and the stylus force applied on the surface was set at 15 mg. At least three measurements were carried out on each surface.

Arithmetic mean roughness (R_a) and maximum profile valley depth (R_v) (Figure 107) were extracted from primary profile with Vision64 software.

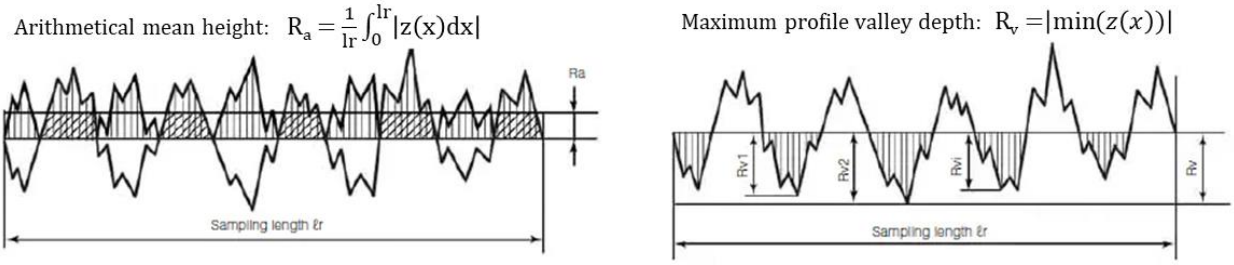

Figure 107. Roughness parameters (R_a and R_v)

2.3. Digital microscopy

A digital microscope VHZ-7000 from Keyence was used to measure S_v area roughness parameter. S_v corresponds to the absolute value of the height of the largest pit within the defined area, thus S_v is an areal extension of R_v parameter.

3D images of laser-structured surfaces were obtained with the digital microscope, at a magnification of 400.

2.4. Scanning Electron Microscopy (SEM)

2.4.1. Surface morphology

Surface morphology of plasma-treated and laser-structured stainless steel samples was observed with a JEOL JSM-7500F LV scanning electron microscope (Japan). Images were acquired at 5 and 10kV and at a working distance of 10 mm. Prior to observation, plasma-treated samples were carbon coated using a BAL-TEC SDC 005 Sputter coater.

2.4.2. X-Ray mappings

Energy Dispersive X-Ray mappings (SEM-EDX) were performed to validate the presence of plasma coatings onto structured stainless steel surfaces. Observations were performed with a JEOL JSM-7500F LV scanning electron microscope (Japan) at 10 kV and at a working distance of 10 mm. Mappings of silicon and iron enable to identify and localise each element.

2.5. Fourier Transform Infrared spectroscopy (FTIR)

Attenuated Total Reflectance (ATR) FTIR spectra of plasma-treated stainless steel samples were acquired on a IS50 spectrometer (Thermofischer, United States of America), in the spectral range 350 to 4000 cm^{-1} with a resolution of 4 cm^{-1}. The number of scans was set at 40. At least three measurements were performed on three samples.

Spectra post-treatment was done with Omnic 9 software and deconvolution of spectra was performed with OriginPro 2016. Multiple peak fit tool (baseline mode: share and fixe y_0; fitting function: Gaussian) was used on all the spectra with adj. R-square > 0.999.

2.6. Electron Probe Micro-Analysis (EPMA)

X-ray mappings were performed at 15 kV, 40 nA using a Camera SX100 electron probe microanalyzer (Electron Probe Mirco-Analysis: EPMA) (Cameca, Gennevilliers, France). A TAP crystal is used to detect the Si K_α X-ray and a LiF crystal is used to detect the Fe K_α. On

the mapping, a color-coded legend characterizes the elemental concentration (black color: absence of the targeted element to red color: highest concentration).

X-ray mappings were performed using at 15 kV, 20 nA using a Camera SX100 electron probe microanalyzer (Electron Probe Mirco-Analysis: EPMA) (Cameca, Gennevilliers, France). On the mapping, a color-coded legend characterizes the elemental concentration (black color: absence of the targeted element to red color: highest concentration).

2.7. Time-of-Flight Secondary Ion Mass Spectrometry (ToF-SIMS)

ToF-SIMS analyses were performed on both bare and modified silicon wafers in order to confirm the presence of two layers after plasma deposition. ToF-SIMS spectra and depth profiles were recorded using a ToF-SIMS V instrument (ION-TOF GmbH Germany) (Figure 108) equipped with a bismuth liquid metal ion gun (LMIG). Charge effects were compensated by means of a 20 eV pulsed electron flood gun. A 300 × 300 μm^2 surface area was sputtered with the Cs^+ ion beam (1 kV, 70nA) before analysis with the Bi_3^+ primary ion beam (25 kV, 0.3 pA) rastered over a 100 × 100 μm^2 surface area.

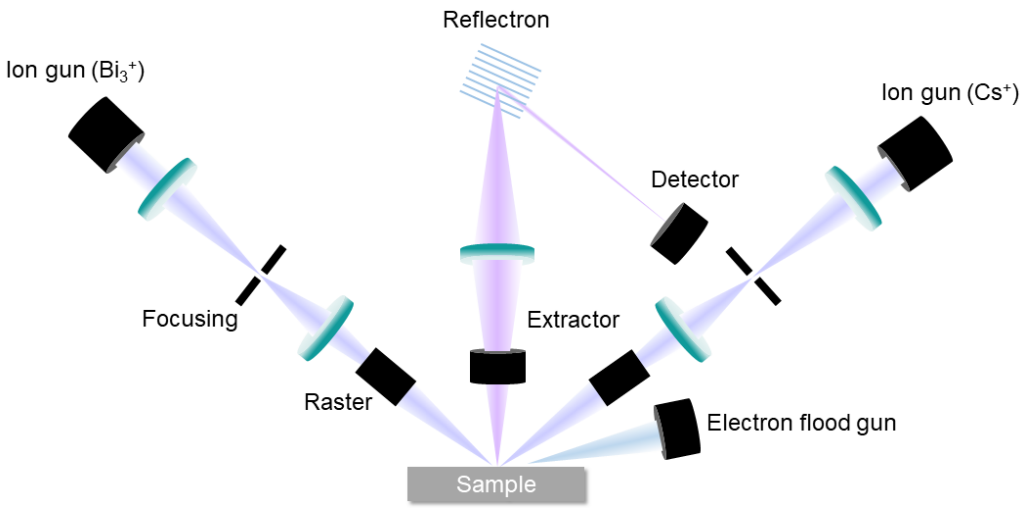

Figure 108. Diagram of key ToF-SIMS components

2.8. Cross-Hatch Adhesion Tests

Plasma coating adhesion on stainless steel substrates was evaluated following the ASTM D3359-B standard with an Elcometer 107 cross-hatch cutter of 1 mm with 11 teeth. It allows to classify coatings adhesion from 5B (very good adhesion) to 0B (poor adhesion) ranges (Table 51).

Table 51. ASTM standard corresponding to cross-hatch test results

Classification	5B	4B	3B	2B	1B	0B
Appearance of cross-cut area after tape removal	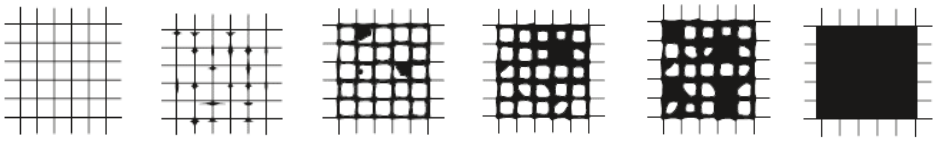					

References

[1] C. Françolle De Almeida, M. Saget, G. Delaplace, M. Jimenez, V. Fierro, and A. Celzard, "Innovative fouling-resistant materials for industrial heat exchangers: A review," *Rev. Chem. Eng.*, 2021.

[2] I. Banerjee, R. C. Pangule, and R. S. Kane, "Antifouling coatings: Recent developments in the design of surfaces that prevent fouling by proteins, bacteria, and marine organisms," *Adv. Mater.*, vol. 23, no. 6, pp. 690–718, 2011.

[3] J. Visser and T. J. M. Jeurnink, "Fouling of heat exchangers in the dairy industry," *Exp. Therm. Fluid Sci.*, vol. 14, no. 4, pp. 407–424, 1997.

[4] "Food and Agriculture Organization of United Nations." [Online]. Available: https://www.fao.org/dairy-production-products/production/en/. [Accessed: 25-Feb-2022].

[5] A. Sharma and S. Macchietto, "Fouling and cleaning of plate heat exchangers: Dairy application," *Food Bioprod. Process.*, vol. 126, pp. 32–41, 2021.

[6] P. Van Asselt, A. J.; Vissers, M. M.; Smit, F.; De Jong, "In-Line Control of Fouling," in *Proceedings of Heat Exchanger Fouling and Cleaning: Challenges and Opportunities*, 2005.

[7] M. Khaldi, "Etude du lien entre la physico-chimie de dérivés laitiers et leur aptitude à l'encrassement lors du traitement thermomécanique en échangeur de chaleur," Université de Lille, 2016.

[8] H. Burton, "Seasonal variation in deposit formation from whole milk on a heated surface," *J. Dairy Res.*, vol. 34, no. 2, pp. 137–143, 1967.

[9] M. Förster, W. Augustin, and M. Bohnet, "Influence of the adhesion force crystal/heat exchanger surface on fouling mitigation," *Chem. Eng. Process. Process Intensif.*, vol. 38, no. 4–6, pp. 449–461, 1999.

[10] C. Boxler, "Fouling by Milk Constituents and Cleaning of Modified Surfaces," Technischen Universität Carolo-Whilhelmina zu Braunschweig, 2014.

[11] S. Zouaghi, "Dairy Fouling on Stainless Steel and Design of Antifouling Surfaces," Université de Lille, 2018.

[12] O. M. Magens, "Mitigating fouling of heat exchangers with fluoropolymer coatings," University of Cambridge, 2019.

[13] S. Zouaghi *et al.*, "Antifouling Biomimetic Liquid-Infused Stainless Steel: Application to Dairy Industrial Processing," *ACS Appl. Mater. Interfaces*, vol. 9, no. 31, pp. 26565–26573, 2017.

[14] V. H. HOLSINGER, K. T. RAJKOWSKI, and J. R. STABEL, "Milk pasteurisation and safety: a brief history and update," *Rev. Sci. Tech. l'OIE*, vol. 16, no. 2, pp. 441–451, 1997.

[15] G. Bylund, "Cleaning of dairy equipment," in *Dairy processing handbook*, Teknotext AB, Ed. Lund, Sweden: Tetra Pak Processing Systems AB, 1995, pp. 403–414.

[16] C. Hagsten, "Cleaning of ultra-high temperature milk fouling Structural and compositional changes," Lund University, 2016.

[17] A. R. Hinton, K. T. Trinh, J. D. Brooks, and G. J. Manderson, "Thermophile survival in milk fouling and on stainless steel during cleaning," *Food Bioprod. Process. Trans. Inst. Chem. Eng. Part C*, vol. 80, no. 4, pp. 299–304, 2002.

[18] T. R. Bott, *Industrial biofouling*. Oxford, 2011.

[19] S. Marchand, J. De Block, V. De Jonghe, A. Coorevits, M. Heyndrickx, and L. Herman, "Biofilm Formation in Milk Production and Processing Environments; Influence on Milk Quality and Safety," *Compr. Rev. Food Sci. Food Saf.*, vol. 11, no. 2, pp. 133–147, 2012.

[20] J. Verran and J. Redfern, *Testing Surface Cleanability in Food Processing*. Elsevier Ltd, 2016.

[21] C. C. Hall, "The Use of Stainless Steel in the Food Industry," *R.S.I*, pp. 741–753, 1939.

[22] R. H. Schmidt, D. J. Erickson, S. Sims, and P. Wolff, "Characteristics of food contact surface materials: Stainless steel," *Food Prot. Trends*, vol. 32, no. 10, pp. 574–584, 2012.

[23] M. Lalande, F. Rene, and J. P. Tissier, "Fouling and its control in heat exchangers in the dairy industry," *Biofouling*, vol. 1, no. 3, pp. 233–250, 1989.

[24] S. D. Changani, M. T. Belmar-Beiny, and P. J. Fryer, "Engineering and chemical factors associated with fouling and cleaning in milk processing," *Exp. Therm. Fluid Sci.*, vol. 14, no. 4, pp. 392–406, 1997.

[25] L. Schnöing, W. Augustin, and S. Scholl, "Fouling mitigation in food processes by modification of heat transfer surfaces: A review," *Food Bioprod. Process.*, vol. 121, pp. 1–19, 2020.

[26] P. Blanpain-Avet *et al.*, "Effect of the phosphate/calcium molar ratio on fouling deposits generated by the processing of a whey protein isolate in a plate heat exchanger," *Food Bioprod. Process.*, vol. 121, pp. 154–165, 2020.

[27] W. Liu, X. D. Chen, R. Jeantet, C. André, S. Bellayer, and G. Delaplace, "Effect of casein/whey ratio on the thermal denaturation of whey proteins and subsequent fouling in a plate heat exchanger," *J. Food Eng.*, vol. 289, no. December 2019, 2020.

[28] R. L. J. Lyster, "The composition of milk deposits in an U.H.T. plant.," *J. Dairy Res.*, vol. 32, no. 1, pp.

203–208, 1965.
[29] M. Lalande and F. Rene, "Fouling by Milk and Dairy Product and Cleaning of Heat Exchange Surfaces," *Fouling Sci. Technol.*, pp. 557–573, 1988.
[30] T. JEURNINK, P. WALSTRA, and C. DE KRUIF, "Mechanisms of fouling in dairy processing," *Mech. fouling dairy Process.*, vol. 50, no. 3, pp. 407–426, 1996.
[31] M. Lalande, J. Tissier, and G. Corrieu, "Fouling of Heat Transfer Surfaces Related to β-Lactoglobulin Denaturation During Heat Processing of Milk," *Biotechnol. Prog.*, vol. 1, no. 2, pp. 131–139, 1985.
[32] J. P. Tissier and M. Lalande, "Experimental Device and Methods for Studying Milk Deposit Formation on Heat Exchange Surfaces," *Biotechnol. Prog.*, vol. 2, no. 4, pp. 218–229, 1986.
[33] H. Burton, "Section G. Deposits from whole milk in heat treatment plant—a review and discussion," *J. Dairy Res.*, vol. 35, no. 2, pp. 317–330, 1968.
[34] C. Hagsten *et al.*, "Composition and structure of high temperature dairy fouling," *Food Struct.*, vol. 7, pp. 13–20, 2016.
[35] F. Delplace, J. C. Leuliet, and D. Levieux, "A reaction engineering approach to the analysis of fouling by whey proteins of a six-channels-per-pass plate heat exchanger," *J. Food Eng.*, vol. 34, no. 1, pp. 91–108, 1997.
[36] G. W. Smithers *et al.*, "New Opportunities from the Isolation and Utilization of Whey Proteins," *J. Dairy Sci.*, vol. 79, no. 8, pp. 1454–1459, 1996.
[37] B. G. Carter, N. Cheng, R. Kapoor, G. H. Meletharayil, and M. A. Drake, "Invited review: Microfiltration-derived casein and whey proteins from milk," *J. Dairy Sci.*, vol. 104, no. 3, pp. 2465–2479, 2021.
[38] P. T. Robbins, B. L. Elliott, P. J. Fryer, M. T. Belmar, and A. P. M. Hasting, "A comparison of milk and whey fouling in a pilot scale plate heat exchanger: Implications for Modelling and Mechanistic Studies," *Food Bioprod. Process. Trans. Inst. Chem. Eng. Part C*, vol. 77, no. 2, pp. 97–106, 1999.
[39] A. Fickak, A. Al-Raisi, and X. D. Chen, "Effect of whey protein concentration on the fouling and cleaning of a heat transfer surface," *J. Food Eng.*, vol. 104, no. 3, pp. 323–331, 2011.
[40] Z. Polat, "Integrated Approach To Whey Utilization Through Natural Zeolite Adsorption / Desorption and Fermentation," Institute of Technology of Izmir, 2009.
[41] J. N. De Wit, "Thermal Stability and Functionality of Whey Proteins," *J. Dairy Sci.*, vol. 73, no. 12, pp. 3602–3612, 1990.
[42] M. A. M. Hoffmann and P. J. J. M. Van Mil, "Heat-Induced Aggregation of β-Lactoglobulin: Role of the Free Thiol Group and Disulfide Bonds," *J. Agric. Food Chem.*, vol. 45, no. 8, pp. 2942–2948, 1997.
[43] M. T. Belmar-Beiny, S. M. Gotham, W. R. Paterson, P. J. Fryer, and A. M. Pritchard, "The effect of Reynolds number and fluid temperature in whey protein fouling," *J. Food Eng.*, vol. 19, no. 2, pp. 119–139, 1993.
[44] R. Guérin, G. Ronse, L. Bouvier, P. Debreyne, and G. Delaplace, "Structure and rate of growth of whey protein deposit from in situ electrical conductivity during fouling in a plate heat exchanger," *Chem. Eng. Sci.*, vol. 62, no. 7, pp. 1948–1957, 2007.
[45] J. Petit, A. L. Herbig, A. Moreau, and G. Delaplace, "Influence of calcium on β-lactoglobulin denaturation kinetics: Implications in unfolding and aggregation mechanisms," *J. Dairy Sci.*, vol. 94, no. 12, pp. 5794–5810, 2011.
[46] B. M. A. Delsing and J. Hiddink, "Fouling of Heat Tranfer Surfaces by Dairy Liquids," *Netherlands Milk Dairy J.*, vol. 37, pp. 139–148, 1983.
[47] M. Jimenez *et al.*, "Toward the understanding of the interfacial dairy fouling deposition and growth mechanisms at a stainless steel surface: A multiscale approach," *J. Colloid Interface Sci.*, vol. 404, pp. 192–200, 2013.
[48] B. Bansal and X. D. Chen, "A Critical Review of Milk Fouling in Heat Exchangers," *Compr. Rev. Food Sci. Food Saf.*, vol. 5, pp. 27–33, 2006.
[49] E. Sadeghinezhad, S. N. Kazi, A. Badarudin, M. N. M. Zubair, B. L. Dehkordi, and C. S. Oon, "A review of milk fouling on heat exchanger surfaces," *Rev. Chem. Eng.*, vol. 29, no. 3, pp. 169–188, 2013.
[50] E. Sadeghinezhad, S. N. Kazi, M. Dahari, M. R. Safaei, R. Sadri, and A. Badarudin, "A Comprehensive Review of Milk Fouling on Heated Surfaces," *Crit. Rev. Food Sci. Nutr.*, vol. 55, no. 12, pp. 1724–1743, 2015.
[51] P. J. Fryer and G. K. Christian, "Improving the cleaning of heat exchanger," in *Handbook of hygiene control in the food industry*, M. A. M. and J. H. H. L. M. Lelieveld, Ed. 2005, pp. 468–496.
[52] P. J. Fryer and M. T. Belmar-Beiny, "Fouling of heat exchangers in the food industry: a chemical engineering prespective," *Trends Food Sci. Technol.*, vol. 2, no. C, pp. 33–37, 1991.
[53] P. De Jong, "Impact and control of fouling in milk processing," *Trends Food Sci. Technol.*, vol. 8, no. 12, pp. 401–405, 1997.
[54] C. L. Foster and M. L. Green, "A model heat-exchange apparatus for the investigation of fouling of stainless steel surfaces by milk I. deposit formation at 100 °C," *J. Dairy Res.*, vol. 56, no. 2, pp. 201–209,

1989.
[55] M. T. Belmar-Beiny and P. J. Fryer, "Preliminary Stages of Fouling from Whey Protein Solutions," *J. Dairy Res.*, vol. 60, no. 4, pp. 467–483, 1993.
[56] N. Epstein, "Thinking about heat transfer fouling: A 5 × 5 matrix," *Heat Transf. Eng.*, vol. 4, no. 1, pp. 43–56, 1983.
[57] M. Bohnet, "Fouling of Heat Transfer Surfaces," *Chem. Eng. Technol*, vol. 10, pp. 113–125, 1987.
[58] Y. Mahdi, A. Mouheb, and L. Oufer, "A dynamic model for milk fouling in a plate heat exchanger," *Appl. Math. Model.*, vol. 33, no. 2, pp. 648–662, 2009.
[59] F. Albert, W. Augustin, and S. Scholl, "Roughness and constriction effects on heat transfer in crystallization fouling," *Chem. Eng. Sci.*, vol. 66, no. 3, pp. 499–509, 2011.
[60] S. Zouaghi *et al.*, "Influence of stainless steel surface properties on whey protein fouling under industrial processing conditions," *J. Food Eng.*, vol. 228, pp. 38–49, 2018.
[61] E. S. Gadelmawla, M. M. Koura, T. M. A. Maksoud, I. M. Elewa, and H. H. Soliman, "Roughness parameters," *J. Mater. Process. Technol.*, vol. 123, no. 1, pp. 133–145, 2002.
[62] B. Derjaguin and L. Landau, "Theory of the stability of strongly charged lyophobic sols and of the adhesion of strongly charged particles in solutions of electrolytes," *Acta Phys. Chem. URSS*, vol. 14, pp. 633–662, 1941.
[63] E. J. W. Verwey and J. T. G. Overbeek, *Theory of the stability of lyophobic colloids*. Amsterdam, 1948.
[64] A. Al-Janabi, M. R. Malayeri, and H. Müller-Steinhagen, "Experimental fouling investigation with electroless Ni-P coatings," *Int. J. Therm. Sci.*, vol. 49, no. 6, pp. 1063–1071, 2010.
[65] C. J. van Oss, "Hydrophobicity of biosurfaces - Origin, quantitative determination and interaction energies," *Colloids Surfaces B Biointerfaces*, vol. 5, no. 3–4, pp. 91–110, 1995.
[66] F. M. Fowkes, "Attractive forces at interfaces," *Ind. Eng. Chem.*, vol. 56, no. 12, pp. 40–52, 1964.
[67] C. J. Van Oss, R. J. Good, and M. K. Chaudhury, "Determination of the Hydrophobic Interaction Energy-Application to Separation Processes," *Sep. Sci. Technol.*, vol. 22, no. 1, pp. 1–24, 1987.
[68] D. Grasso, K. Subramaniam, M. Butkus, K. Strevett, and J. Bergendahl, "A review of non-DLVO interactions in environmental colloidal systems," *Rev. Environ. Sci. Biotechnol.*, vol. 1, no. 1, pp. 17–38, 2002.
[69] C. J. Van Oss, "Long-range and short-range mechanisms of hydrophobic attraction and hydrophilic repulsion in specific and aspecific interactions," *J. Mol. Recognit.*, vol. 16, no. 4, pp. 177–190, 2003.
[70] T. J. Walstra, P., Wouters, J. T. M., & Geurts, *Dairy Science and Technology (Vol. 2)*. Boca Raton, FL, US, 2005.
[71] T. Young, "An essay to the cohesion of fluids," *Philoshopical Trans. R. Soc. London*, pp. 65–87, 1804.
[72] W. A. ZISMAN, "Relation of the Equilibrium Contact Angle to Liquid and Solid Constitution," pp. 1–51, 1964.
[73] D. K. Owens and R. C. Wendt, "Estimation of the surface free energy of polymers," *J. Appl. Polym. Sci.*, vol. 13, no. 8, pp. 1741–1747, 1969.
[74] D. H. Kaelble, "Dispersion-Polar Surface Tension Properties of Organic Solids," *J. Adhes.*, vol. 2, no. 2, pp. 66–81, 1970.
[75] S. Wu, "Polar and nonpolar interactions in adhesion," *J. Adhes.*, vol. 5, no. 1, pp. 39–55, 1973.
[76] C. J. van Oss, M. K. Chaudhury, and R. J. Good, "Interfacial Lifshitz—van der Waals and Polar Interactions in Macroscopic Systems," *Chem. Rev.*, vol. 88, no. 6, pp. 927–941, 1988.
[77] C. J. van Oss, *Interfacial Forces in Aqueous Media*, Second edi. CRC Press, 2006.
[78] J. Jeevahan, M. Chandrasekaran, G. Britto Joseph, R. B. Durairaj, and G. Mageshwaran, "Superhydrophobic surfaces: a review on fundamentals, applications, and challenges," *J. Coatings Technol. Res.*, vol. 15, no. 2, pp. 231–250, 2018.
[79] R. N. Wenzel, "Resistance of solid surfaces to wetting by water," *Ind. Eng. Chem.*, vol. 28, no. 8, pp. 988–994, 1936.
[80] E. Bormashenko, "Young, Boruvka-Neumann, Wenzel and Cassie-Baxter equations as the transversality conditions for the variational problem of wetting," *Colloids Surfaces A Physicochem. Eng. Asp.*, vol. 345, no. 1–3, pp. 163–165, 2009.
[81] A. B. D. Cassie and S. Baxter, "Of porous surfaces," *Trans. Faraday Soc.*, vol. 40, no. 5, pp. 546–551, 1944.
[82] Y. Y. Yan, N. Gao, and W. Barthlott, "Mimicking natural superhydrophobic surfaces and grasping the wetting process: A review on recent progress in preparing superhydrophobic surfaces," *Adv. Colloid Interface Sci.*, vol. 169, no. 2, pp. 80–105, 2011.
[83] H. B. Eral, D. J. C. M. 'T Mannetje, and J. M. Oh, "Contact angle hysteresis: A review of fundamentals and applications," *Colloid Polym. Sci.*, vol. 291, no. 2, pp. 247–260, 2013.
[84] G. McHale, N. J. Shirtcliffe, and M. I. Newton, "Contact-angle hysteresis on super-hydrophobic surfaces," *Langmuir*, vol. 20, no. 23, pp. 10146–10149, 2004.

[85] L. Gomes Da Cruz, E. M. Ishiyama, C. Boxler, W. Augustin, S. Scholl, and D. I. Wilson, "Value pricing of surface coatings for mitigating heat exchanger fouling," *Food Bioprod. Process.*, vol. 93, no. May, pp. 343–363, 2015.

[86] M. Britten, M. L. Green, M. Boulet, and P. Paquin, "Deposit formation on heated surfaces: Effect of interface energetics," *J. Dairy Res.*, vol. 55, no. 4, pp. 551–562, 1988.

[87] R. Rosmaninho and L. F. Melo, "Calcium phosphate deposition from simulated milk ultrafiltrate on different stainless steel-based surfaces," *Int. Dairy J.*, vol. 16, no. 1, pp. 81–87, 2006.

[88] M. Mauermann, U. Eschenhagen, T. Bley, and J. P. Majschak, "Surface modifications - Application potential for the reduction of cleaning costs in the food processing industry," *Trends Food Sci. Technol.*, vol. 20, no. SUPPL. 1, 2009.

[89] C. Boxler, W. Augustin, and S. Scholl, "Fouling of milk components on DLC coated surfaces at pasteurization and UHT temperatures," *Food Bioprod. Process.*, vol. 91, no. 4, pp. 336–347, 2013.

[90] H. Itoh *et al.*, "Adsorption of β-Lactoglobulin onto the Surface of Stainless Steel Particles," *Biosci. Biotechnol. Biochem.*, vol. 59, no. 9, pp. 1648–1651, 1995.

[91] S. A. Kirtley and J. McGuire, "On Differences in Surface Constitution of Dairy Product Contact Materials," *J. Dairy Sci.*, vol. 72, no. 7, pp. 1748–1753, 1989.

[92] W. Augustin, T. Geddert, and S. Scholl, "Surface treatment for the mitigation of whey protein fouling," *Heat Exch. Fouling Clean. VII*, 2007.

[93] R. Rosmaninho and L. F. Melo, "Protein-calcium phosphate interactions in fouling of modified stainless-steel surfaces by simulated milk," *Int. Dairy J.*, vol. 18, no. 1, pp. 72–80, 2008.

[94] J. Piepiórka Stepuk, K. Tandecka, and M. Jakubowski, "An analysis of milk fouling formed during heat treatment on a stainless steel surface with different degrees of roughness," *Czech J. Food Sci.*, vol. 34, no. 3, pp. 271–279, 2016.

[95] J. S. Patel, B. Bansal, M. I. Jones, and M. Hyland, "Fouling behaviour of milk and whey protein isolate solution on doped diamond-like carbon modified surfaces," *J. Food Eng.*, vol. 116, no. 2, pp. 413–421, 2013.

[96] O. Santos, T. Nylander, K. Schillén, M. Paulsson, and C. Trägårdh, "Effect of surface and bulk solution properties on the adsorption of whey protein onto steel surfaces at high temperature," *J. Food Eng.*, vol. 73, no. 2, pp. 174–189, 2006.

[97] N. Rungraeng, Y. C. Cho, S. H. Yoon, and S. Jun, "Carbon nanotube-polytetrafluoroethylene nanocomposite coating for milk fouling reduction in plate heat exchanger," *J. Food Eng.*, vol. 111, no. 2, pp. 218–224, 2012.

[98] D. Z. Liu, S. Jindal, J. Amamcharla, S. Anand, and L. Metzger, "Short communication: Evaluation of a sol-gel–based stainless steel surface modification to reduce fouling and biofilm formation during pasteurization of milk," *J. Dairy Sci.*, vol. 100, no. 4, pp. 2577–2581, 2017.

[99] J. McGUIRE and K. R. SWARTZEL, "THE INFLUENCE of SOLID SURFACE ENERGETICS ON MACROMOLECULAR ADSORPTION FROM MILK," *J. Food Process. Preserv.*, vol. 13, no. 2, pp. 145–160, 1989.

[100] A. B. Kananeh, E. Scharnbeck, U. D. Kück, and N. Räbiger, "Reduction of milk fouling inside gasketed plate heat exchanger using nano-coatings," *Food Bioprod. Process.*, vol. 88, no. 4, pp. 349–356, 2010.

[101] J. Huo, J. Xiao, T. V. Kirk, and X. D. Chen, "Effects of Fluorolink® S10 surface coating on WPC fouling of stainless steel surfaces and subsequent cleaning," *Food Bioprod. Process.*, vol. 118, pp. 130–138, 2019.

[102] R. Rosmaninho and L. F. Melo, "Effect of proteins on calcium phosphate deposition in turbulent flow as a function of surface properties," *Exp. Therm. Fluid Sci.*, vol. 32, no. 2, pp. 375–386, 2007.

[103] R. Rosmaninho, G. Rizzo, H. Müller-Steinhagen, and L. F. Melo, "Deposition from a milk mineral solution on novel heat transfer surfaces under turbulent flow conditions," *J. Food Eng.*, vol. 85, no. 1, pp. 29–41, 2008.

[104] C. Boxler *et al.*, "On-Line Monitoring of Deposition and Removal of Milk Salts on Coated Surfaces," in *Heat Exchanger Fouling and Cleaning*, 2011, pp. 429–432.

[105] C. Boxler, W. Augustin, and S. Scholl, "Influence of surface modification on the composition of a calcium phosphate-rich whey protein deposit in a plate heat exchanger," *Dairy Sci. Technol.*, vol. 94, no. 1, pp. 17–31, 2013.

[106] M. Beuf *et al.*, "Heat Exchanger Fouling and Cleaning : Fundamentals and Applications Fouling and Cleaning of Modified Stainless Steel Plate Heat Exchangers Processing Milk Products," *Heat Exch. Fouling Clean. Fundam. Appl.*, no. January, pp. 1–8, 2003.

[107] S. Zouaghi *et al.*, "Graphite-based composites for whey protein fouling and bacterial adhesion management," *Int. Dairy J.*, vol. 86, pp. 69–75, 2018.

[108] S. Zouaghi *et al.*, "Antifouling amphiphilic silicone coatings for dairy fouling mitigation on stainless steel," *Biofouling*, vol. 34, no. 7, pp. 769–783, 2018.

[109] K. P. Gordon, D. J. Hankinson, and C. E. Carver, "Deposition of Milk Solids on Heated Surfaces," *J.*

Dairy Sci., vol. 51, no. 4, pp. 520–526, 1968.
[110] J. YOON and D. B. LUND, "Magnetic Treatment of Milk and Surface Treatment of Plate Heat Exchangers: Effects on Milk Fouling," *J. Food Sci.*, vol. 59, no. 5, pp. 964–969, 1994.
[111] J. A. Barish and J. M. Goddard, "Anti-fouling surface modified stainless steel for food processing," *Food Bioprod. Process.*, vol. 91, no. 4, pp. 352–361, 2013.
[112] M. Jimenez, H. Hamze, A. Allion, G. Ronse, G. Delaplace, and M. Traisnel, "Antifouling stainless steel surface: Competition between roughness and surface energy," *Mater. Sci. Forum*, vol. 706–709, pp. 2523–2528, 2012.
[113] S. Zouaghi *et al.*, "Atmospheric pressure plasma spraying of silane-based coatings targeting whey protein fouling and bacterial adhesion management," *Appl. Surf. Sci.*, vol. 455, no. February, pp. 392–402, 2018.
[114] R. E. Baier, "Surface behaviour of biomaterials: The theta surface for biocompatibility," *J. Mater. Sci. Mater. Med.*, vol. 17, no. 11, pp. 1057–1062, 2006.
[115] Q. Zhao, S. Wang, and H. Müller-Steinhagen, "Tailored surface free energy of membrane diffusers to minimize microbial adhesion," *Appl. Surf. Sci.*, vol. 230, no. 1–4, pp. 371–378, 2004.
[116] Q. Zhao, Y. Liu, C. Wang, S. Wang, and H. Müller-Steinhagen, "Effect of surface free energy on the adhesion of biofouling and crystalline fouling," *Chem. Eng. Sci.*, vol. 60, no. 17, pp. 4858–4865, 2005.
[117] Q. Zhao, C. Liu, and Y. Liu, "Bacterial and protein adhesion on NI-P-PTFE coated surfaces," *ECI Symp. Ser. Heat Exch. Fouling Clean. VI*, p. 237, 2007.
[118] Q. Zhao and H. Müller-Steinhagen, "Intermolecular and adhesion forces of deposits on modified heat transfer surfaces," in *Proceedings of heat exchanger fouling, fundamental approaches and technical solutions*, 2001.
[119] A. K. Leonardi and C. K. Ober, "Polymer-Based Marine Antifouling and Fouling Release Surfaces: Strategies for Synthesis and Modification," *Annu. Rev. Chem. Biomol. Eng.*, vol. 10, no. 1, pp. 241–264, 2019.
[120] R. Rosmaninho *et al.*, "Modified stainless steel surfaces targeted to reduce fouling - Evaluation of fouling by milk components," *J. Food Eng.*, vol. 80, no. 4, pp. 1176–1187, 2007.
[121] M. DUPEYRAT, J.-P. LABBÉ, F. MICHEL, F. BILLOUDET, and G. DAUFIN, "Mouillabilité et interactions solide-liquide dans l'encrassement de divers matériaux par du lactosérum et du lait," *Lait*, vol. 67, no. 4, pp. 465–486, 1987.
[122] S. Balasubramanian and V. M. Puri, "FOULING MITIGATION DURING PRODUCT PROCESSING USING A MODIFIED PLATE HEAT EXCHANGER SURFACE," *Am. Soc. Agric. Biol. Eng.*, vol. 51, no. 2, pp. 629–639, 2008.
[123] S. Balasubramanian and V. M. Puri, "REDUCTION OF MILK FOULING IN A PLATE HEAT EXCHANGER," *Am. Soc. Agric. Biol. Eng.*, vol. 52, no. 5, pp. 1603–1610, 2009.
[124] K. Huang and J. M. Goddard, "Influence of fluid milk product composition on fouling and cleaning of Ni-PTFE modified stainless steel heat exchanger surfaces," *J. Food Eng.*, vol. 158, pp. 22–29, 2015.
[125] C. A. C. Karlsson, M. C. Wahlgren, and A. C. Trägårdh, "β-lactoglobulin fouling and its removal upon rinsing and by SDS as influenced by surface characteristics, temperature and adsorption time," *J. Food Eng.*, vol. 30, no. 1–2, pp. 43–60, 1996.
[126] Y. Liu, Y. Zou, L. Zhao, W. Liu, and L. Cheng, "Investigation of adhesion of CaCO3 crystalline fouling on stainless steel surfaces with different roughness," *Int. Commun. Heat Mass Transf.*, vol. 38, no. 6, pp. 730–733, 2011.
[127] J. Petit, T. Six, A. Moreau, G. Ronse, and G. Delaplace, "β-lactoglobulin denaturation, aggregation, and fouling in a plate heat exchanger: Pilot-scale experiments and dimensional analysis," *Chem. Eng. Sci.*, vol. 101, pp. 432–450, 2013.
[128] F. T. Ndoye, N. Erabit, D. Flick, and G. Alvarez, "In-line characterization of a whey protein aggregation process: Aggregates size and rheological measurements," *J. Food Eng.*, vol. 115, no. 1, pp. 73–82, 2013.
[129] R. N. Zúñiga, A. Tolkach, U. Kulozik, and J. M. Aguilera, "Kinetics of formation and physicochemical characterization of thermally-induced β-Lactoglobulin aggregates," *J. Food Sci.*, vol. 75, no. 5, 2010.
[130] R. Rosmaninho, G. Rizzo, H. Müller-Steinhagen, and L. F. Melo, "Study of The Influence of Bulk Properties and Surface Tension on the Deposition Process of Calcium Phosphate on Modi ed Stainless Steel," in *Heat Exchanger Fouling and Cleaning: Fundamentals and Applications*, 2003, no. January.
[131] A. Dey *et al.*, "The role of prenucleation clusters in surface-induced calcium phosphate crystallization," *Nat. Mater.*, vol. 9, no. 12, pp. 1010–1014, 2010.
[132] J. G. Detry, M. Sindic, and C. Deroanne, "Hygiene and cleanability: A focus on surfaces," *Crit. Rev. Food Sci. Nutr.*, vol. 50, no. 7, pp. 583–604, 2010.
[133] H. S. Ahn *et al.*, "International Journal of Heat and Mass Transfer Anti-fouling performance of chevron plate heat exchanger by the surface modification," *Int. J. Heat Mass Transf.*, vol. 144, p. 118634, 2019.
[134] A. Grill, "Review of the tribology of diamond-like carbon," *Wear*, vol. 168, no. 1–2, pp. 143–153, 1993.
[135] J. Robertson, "Diamond-like amorphous carbon," *Mater. Sci. Eng. R Reports*, vol. 37, no. 4–6, pp. 129–

281, 2002.
[136] K. Trojan, M. Grischke, and H. Dimigen, "Network Modification of DLC Coatings to Adjust a Defined Surface Energy," *Phys. Status Solidi*, vol. 145, no. 2, pp. 575–585, 1994.
[137] C. Donnet, "Recent progress on the tribology of doped diamond-like and carbon alloy coatings: A review," *Surf. Coatings Technol.*, vol. 100–101, no. 1–3, pp. 180–186, 1998.
[138] P. Hu, Q. Xie, C. Ma, and G. Zhang, "Silicone-Based Fouling-Release Coatings for Marine Antifouling," *Langmuir*, vol. 36, no. 9, pp. 2170–2183, 2020.
[139] O. Santos *et al.*, "Modified stainless steel surfaces targeted to reduce fouling - Surface characterization," *J. Food Eng.*, vol. 64, no. 1, pp. 63–79, 2004.
[140] P. Dimitrakellis and E. Gogolides, "Hydrophobic and superhydrophobic surfaces fabricated using atmospheric pressure cold plasma technology: A review," *Adv. Colloid Interface Sci.*, vol. 254, pp. 1–21, 2018.
[141] J. W. Mayer, L. Eriksson, and J. A. Davies, *Ion implantation in semiconductors: silicon and germanium*, Academic p. New-York, 1970.
[142] Q. Zhao and B. M. Burnside, "DROPWISE CONDENSATION OF STEAM ON ION IMPLANTED CONDENSER SURFACES," *Heat Recover. Syst. CHP*, vol. 14, no. 5, pp. 525–534, 1994.
[143] H. Müller-Steinhagen and Q. Zhao, "Investigation of low fouling surface alloys made by ion implantation technology," *Chem. Eng. Sci.*, vol. 52, no. 19, pp. 3321–3332, 1997.
[144] M. Dhillon, "The effect of silver ion-implantation of stainless steel on bacterial adhesion and biofilm formation," Massey University, Palmerston North, 2012.
[145] C. Howell, A. Grinthal, S. Sunny, M. Aizenberg, and J. Aizenberg, "Designing Liquid-Infused Surfaces for Medical Applications: A Review," *Adv. Mater.*, vol. 1802724, pp. 1–26, 2018.
[146] J. Wei, D. B. Ravn, L. Gram, and P. Kingshott, "Stainless steel modified with poly(ethylene glycol) can prevent protein adsorption but not bacterial adhesion," *Colloids Surfaces B Biointerfaces*, vol. 32, no. 4, pp. 275–291, 2003.
[147] H. Ma, J. Hyun, P. Stiller, and A. Chilkoti, "'Non-Fouling' Oligo(ethylene glycol)-Functionalized Polymer Brushes Synthesized by Surface-Initiated Atom Transfer Radical Polymerization," *Adv. Mater.*, vol. 16, no. 4, pp. 338–341, 2004.
[148] A. Hucknall, S. Rangarajan, and A. Chilkoti, "In pursuit of zero: Polymer brushes that resist the adsorption of proteins," *Adv. Mater.*, vol. 21, no. 23, pp. 2441–2446, 2009.
[149] André Laschewsky, "Structures and Synthesis of Zwitterionic Polymers," *Polymers (Basel).*, vol. 6, pp. 1544–1601, 2014.
[150] Y. D. Kim, J. S. Dordick, and D. S. Clark, "Siloxane-based biocatalytic films and paints for use as reactive coatings," *Biotechnol. Bioeng.*, vol. 72, no. 4, pp. 475–482, 2001.
[151] P. Asuri, S. S. Karajanagi, R. S. Kane, and J. S. Dordick, "Polymer-nanotube-enzyme composites as active antifouling films," *Small*, vol. 3, no. 1, pp. 50–53, 2007.
[152] B. Jovanović, "Critical review of public health regulations of titanium dioxide, a human food additive," *Integr. Environ. Assess. Manag.*, vol. 11, no. 1, pp. 10–20, 2015.
[153] D. A. TIMPERLEY and C. N. M. SMEULDERS, "Cleaning of dairy HTST plate heat exchangers: comparison of single- and two-stage procedures," *Int. J. Dairy Technol.*, vol. 40, no. 1, pp. 4–7, 1987.
[154] O. M. Magens, E. M. Ishiyama, and D. I. Wilson, "Quantifying the 'implementation gap' for antifouling coatings," *Appl. Therm. Eng.*, vol. 99, pp. 683–689, 2016.
[155] S. Zouaghi *et al.*, "Investigating the Effect of an Antifouling Surface Modification on the Environmental Impact of a Pasteurization Process: An LCA Study," *ACS Sustain. Chem. Eng.*, vol. 7, no. 10, pp. 9133–9142, 2019.
[156] S. Premathilaka, M. Hyland, X. Chen, and B. Bansal, "A study of the effects of surface chemistry on the initial deposition mechanisms of dairy fouling," *Food Bioprod. Process.*, vol. 84, no. 4 C, pp. 265–273, 2006.
[157] S. S. Premathilaka, M. M. Hyland, X. D. Chen, L. R. Watkins, and B. Bansal, "Interaction of Whey Protein With Modified Stainless Steel Surfaces," in *Heat Exchanger Fouling and Cleaning - Challenges and Opportunities*, 2007.
[158] C. S. Gudipati, J. A. Finlay, J. A. Callow, M. E. Callow, and K. L. Wooley, "The antifouling and fouling-release perfomance of hyperbranched fluoropolymer (HBFP)-poly(ethylene glycol) (PEG) composite coatings evaluated by adsorption of biomacromolecules and the green fouling alga ulva," *Langmuir*, vol. 21, no. 7, pp. 3044–3053, 2005.
[159] V. Kumar, J. Pulpytel, G. Giudetti, H. Rauscher, F. Rossi, and F. Arefi-Khonsari, "Amphiphilic copolymer coatings via plasma polymerisation process: Switching and anti-biofouling characteristics," *Plasma Process. Polym.*, vol. 8, no. 5, pp. 373–385, 2011.
[160] G. Galli and E. Martinelli, "Amphiphilic Polymer Platforms: Surface Engineering of Films for Marine Antibiofouling," *Macromol. Rapid Commun.*, vol. 38, no. 8, pp. 8–12, 2017.

[161] T. Mérian and J. M. Goddard, "Advances in nonfouling materials: Perspectives for the food industry," *J. Agric. Food Chem.*, vol. 60, no. 12, pp. 2943–2957, 2012.
[162] Y. Chen and S. Thayumanavan, "Amphiphilicity in homopolymer surfaces reduces nonspecific protein adsorption," *Langmuir*, vol. 25, no. 24, pp. 13795–13799, 2009.
[163] Y. Cho *et al.*, "Triblock copolymers with grafted fluorine-free, amphiphilic, non-ionic side chains for antifouling and fouling-release applications," *Macromolecules*, vol. 44, no. 12, pp. 4783–4792, 2011.
[164] Z. Zhou *et al.*, "Amphiphilic triblock copolymers with PEGylated hydrocarbon structures as environmentally friendly marine antifouling and fouling-release coatings," *Biofouling*, vol. 30, no. 5, pp. 589–604, 2014.
[165] H. S. Sundaram *et al.*, "Fluorine-free mixed amphiphilic polymers based on PDMS and PEG side chains for fouling release applications," *Biofouling*, vol. 27, no. 6, pp. 589–602, 2011.
[166] M. L. Hawkins, F. Faÿ, K. Réhel, I. Linossier, and M. A. Grunlan, "Bacteria and diatom resistance of silicones modified with PEO-silane amphiphiles," *Biofouling*, vol. 30, no. 2, pp. 247–258, 2014.
[167] M. L. Hawkins *et al.*, "Anti-protein and anti-bacterial behavior of amphiphilic silicones," *Polym. Chem.*, vol. 8, no. 34, pp. 5239–5251, 2017.
[168] M. A. Rufin *et al.*, "Enhancing the protein resistance of silicone via surface-restructuring PEO-silane amphiphiles with variable PEO length," *J. Mater. Chem. B*, vol. 3, no. 14, pp. 2816–2825, 2015.
[169] M. A. Rufin, M. E. Barry, P. A. Adair, M. L. Hawkins, J. E. Raymond, and M. A. Grunlan, "Protein resistance efficacy of PEO-silane amphiphiles: Dependence on PEO-segment length and concentration," *Acta Biomater.*, vol. 41, pp. 247–252, 2016.
[170] F. Faÿ, M. L. Hawkins, K. Réhel, M. A. Grunlan, and I. Linossier, "Non-toxic, anti-fouling silicones with variable PEO – silane amphiphile content," *Green Mater.*, vol. 4, no. 2, pp. 53–62, 2016.
[171] T. S. Wong *et al.*, "Bioinspired self-repairing slippery surfaces with pressure-stable omniphobicity," *Nature*, vol. 477, no. 7365, pp. 443–447, 2011.
[172] A. K. Epstein, T. S. Wong, R. A. Belisle, E. M. Boggs, and J. Aizenberg, "Liquid-infused structured surfaces with exceptional anti-biofouling performance," *Proc. Natl. Acad. Sci. U. S. A.*, vol. 109, no. 33, pp. 13182–13187, 2012.
[173] H. F. Bohn and W. Federle, "Insect aquaplaning: Nepenthes pitcher plants capture prey with the peristome, a fully wettable water-lubricated anisotropic surface," *Proc. Natl. Acad. Sci.*, vol. 101, no. 39, pp. 14138–14143, 2004.
[174] C. Howell *et al.*, "Self-replenishing vascularized fouling-release surfaces," *ACS Appl. Mater. Interfaces*, vol. 6, no. 15, pp. 13299–13307, 2014.
[175] C. Zhang, Y. Xia, H. Zhang, and N. S. Zacharia, "Surface Functionalization for a Nontextured Liquid-Infused Surface with Enhanced Lifetime," *ACS Appl. Mater. Interfaces*, vol. 10, no. 6, pp. 5892–5901, 2018.
[176] G. Zhang, B. Liang, Z. Zhong, Y. Huang, and Z. Su, "One-Step Solvent-Free Strategy for Covalently Attached, Substrate-Independent Transparent Slippery Coating," *Adv. Mater. Interfaces*, vol. 5, no. 20, pp. 1–7, 2018.
[177] X. Jing and Z. Guo, "Fabrication of biocompatible super stable lubricant-immobilized slippery surfaces by grafting a polydimethylsiloxane brush: Excellent boiling water resistance, hot liquid repellency and long-term slippery stability," *Nanoscale*, vol. 11, no. 18, pp. 8870–8881, 2019.
[178] U. Manna and D. M. Lynn, "Fabrication of liquid-infused surfaces using reactive polymer multilayers: Principles for manipulating the behaviors and mobilities of aqueous fluids on slippery liquid interfaces," *Adv. Mater.*, vol. 27, no. 19, pp. 3007–3012, 2015.
[179] K. Manabe, K. H. Kyung, and S. Shiratori, "Biocompatible slippery fluid-infused films composed of chitosan and alginate via layer-by-layer self-assembly and their antithrombogenicity," *ACS Appl. Mater. Interfaces*, vol. 7, no. 8, pp. 4763–4771, 2015.
[180] S. Nishioka *et al.*, "Facile design of plant-oil-infused fine surface asperity for transparent blood-repelling endoscope lens," *RSC Adv.*, vol. 6, no. 53, pp. 47579–47587, 2016.
[181] R. Togasawa, M. Tenjimbayashi, T. Matsubayashi, T. Moriya, K. Manabe, and S. Shiratori, "A Fluorine-free Slippery Surface with Hot Water Repellency and Improved Stability against Boiling," *ACS Appl. Mater. Interfaces*, vol. 10, no. 4, pp. 4198–4205, 2018.
[182] L. A. Scudeller *et al.*, "Calcium Chelation by Phosphate Ions and its Influence on Fouling Mechanisms of Whey protein solutions in a Plate Heat Exchanger," *J. Ind. Eng. Chem.*, 2021.
[183] M. Khaldi *et al.*, "Effect of the calcium/protein molar ratio on β-lactoglobulin denaturation kinetics and fouling phenomena," *Int. Dairy J.*, vol. 78, pp. 1–10, 2018.
[184] D. de Guibert *et al.*, "Flow process and heating conditions modulate the characteristics of whey protein aggregates.," *J. Food Eng.*, vol. 264, no. March 2019, 2020.
[185] M. J. H. Simmons, P. Jayaraman, and P. J. Fryer, "The effect of temperature and shear rate upon the aggregation of whey protein and its implications for milk fouling," *J. Food Eng.*, vol. 79, no. 2, pp. 517–

528, 2007.
[186] M. Wolz, E. Mersch, and U. Kulozik, "Thermal aggregation of whey proteins under shear stress," *Food Hydrocoll.*, vol. 56, pp. 396–404, 2016.
[187] F. Hejda, P. Solaˇ, and J. Kousal, "Surface Free Energy Determination by Contact Angle Measurements – A Comparison of Various Approaches," *WDS'10 Proc. Contrib. Pap.*, no. 3, pp. 25–30, 2010.
[188] D. J. Hankinson and C. E. Carver, "Fluid Dynamic Relationships Involved in Circulation Cleaning," *J. Dairy Sci.*, vol. 51, no. 11, pp. 1761–1767, 1968.
[189] D. A. TIMPERLEY and C. N. M. SMEULDERS, "Cleaning of dairy HTST plate heat exchangers: optimization of the single-stage procedure," *Int. J. Dairy Technol.*, vol. 41, no. 1, pp. 4–7, 1988.
[190] K. R. Goode, K. Asteriadou, P. T. Robbins, and P. J. Fryer, "Fouling and cleaning studies in the food and beverage industry classified by cleaning type," *Compr. Rev. Food Sci. Food Saf.*, vol. 12, no. 2, pp. 121–143, 2013.
[191] M. Khaldi *et al.*, "Effect of calcium content and flow regime on whey protein fouling and cleaning in a plate heat exchanger," *J. Food Eng.*, vol. 147, no. C, pp. 68–78, 2015.
[192] C. Cunault *et al.*, "A novel set-up and a CFD approach to study the biofilm dynamics as a function of local flow conditions encountered in fresh-cut food processing equipments," *Food Bioprod. Process.*, vol. 93, no. July, pp. 217–223, 2015.
[193] F. Gaucheron, "The minerals of milk," *Reprod. Nutr. Dev.*, vol. 45, no. 4, pp. 473–483, 2005.
[194] C. Holt, D. G. Dalgleish, and R. Jenness, "Calculation of the ion equilibria in milk diffusate and comparison with experiment," *Anal. Biochem.*, vol. 113, no. 1, pp. 154–163, 1981.
[195] C. Holt, "An equilibrium thermodynamic model of the sequestration of calcium phosphate by casein micelles and its application to the calculation of the partition of salts in milk," *Eur. Biophys. J.*, vol. 33, no. 5, pp. 421–434, 2004.
[196] G. Tanguy, F. Siddique, E. Beaucher, A. C. Santellani, P. Schuck, and F. Gaucheron, "Calcium phosphate precipitation during concentration by vacuum evaporation of milk ultrafiltrate and microfiltrate," *LWT - Food Sci. Technol.*, vol. 69, pp. 554–562, 2016.
[197] S. Karunadasa, "Dehydration of Calcium Chloride as Examined by High-temperature X-ray Powder Diffraction," *Int. Multidiscip. Res. J.*, no. 07-2019, pp. 37–43, 2019.
[198] H. Bidmus, J. Chau, and K. Dechant, "Absolute roughness of pipes from different manufacturing and treatment methods and impact on pipeline design," in *PSIG*, 2019, pp. 1–11.
[199] B. Bansal and X. D. Chen, "A Critical Review of Milk Fouling in Heat Exchangers," *Food Sci. Food Saf.*, vol. 6, pp. 27–33, 2006.
[200] S. Bhatt, J. Pulpytel, and F. Aref-Khonsari, "Low and atmospheric plasma polymerisation of nanocoatings for bio-applications," *Surf. Innov.*, vol. 3, no. 2, pp. 63–83, 2015.
[201] F. Massines, C. Sarra-Bournet, F. Fanelli, N. Naudé, and N. Gherardi, "Atmospheric pressure low temperature direct plasma technology: Status and challenges for thin film deposition," *Plasma Process. Polym.*, vol. 9, no. 11–12, pp. 1041–1073, 2012.
[202] C. Tendero, C. Tixier, P. Tristant, J. Desmaison, and P. Leprince, "Atmospheric pressure plasmas: A review," *Spectrochim. Acta - Part B At. Spectrosc.*, vol. 61, no. 1, pp. 2–30, 2006.
[203] C. Tendero, "Torche plasma micro-onde à la pression atmosphérique : application au traitement de surfaces métalliques," Université de Limoges, 2005.
[204] A. Schütze, J. Y. Jeong, S. E. Babayan, J. Park, G. S. Selwyn, and R. F. Hicks, "The atmospheric-pressure plasma jet: A review and comparison to other plasma sources," *IEEE Trans. Plasma Sci.*, vol. 26, no. 6, pp. 1685–1694, 1998.
[205] G. S. Selwyn, H. W. Herrmann, J. Park, and I. Henins, "Materials processing using an atmospheric pressure, RF-generated plasma source," *Contrib. to Plasma Phys.*, vol. 41, no. 6, pp. 610–619, 2001.
[206] T. Belmonte, G. Henrion, and T. Gries, "Nonequilibrium atmospheric plasma deposition," *J. Therm. Spray Technol.*, vol. 20, no. 4, pp. 744–759, 2011.
[207] L. Bres, "Interaction entre un plasma froid à la pression atmosphérique et des surfaces thermoplastiques industrielles : application à l'activation de surface ?????," Université Toulouse 3 Paul Sabatier, 2017.
[208] S. E. Babayan, J. Y. Jeong, V. J. Tu, J. Park, G. S. Selwyn, and R. F. Hicks, "Deposition of silicon dioxide films with an atmospheric-pressure plasmajet," *Plasma Sources Sci. Technol.*, vol. 7, no. 3, pp. 286–288, 1998.
[209] F. Fanelli and F. Fracassi, "Atmospheric pressure non-equilibrium plasma jet technology: general features, specificities and applications in surface processing of materials," *Surf. Coatings Technol.*, vol. 322, pp. 174–201, 2017.
[210] J. H. Yim, V. Rodriguez-Santiago, A. A. Williams, T. Gougousi, D. D. Pappas, and J. K. Hirvonen, "Atmospheric pressure plasma enhanced chemical vapor deposition of hydrophobic coatings using fluorine-based liquid precursors," *Surf. Coatings Technol.*, vol. 234, pp. 21–32, 2013.
[211] R. Múgica-Vidal, F. Alba-Elías, E. Sainz-García, and J. Ordieres-Meré, "Atmospheric plasma-

polymerization of hydrophobic and wear-resistant coatings on glass substrates," *Surf. Coatings Technol.*, vol. 259, no. PC, pp. 374–385, 2014.

[212] D. P. Dowling, C. E. Nwankire, M. Riihimäki, R. Keiski, and U. Nylén, "Evaluation of the anti-fouling properties of nm thick atmospheric plasma deposited coatings," *Surf. Coatings Technol.*, vol. 205, no. 5, pp. 1544–1551, 2010.

[213] W. C. Ma, C. H. Lin, and C. Huang, "Deposition of fluorine-containing thin film by atmospheric pressure plasma jet and film surface structural transition," *Plasma Process. Polym.*, vol. 12, no. 4, pp. 362–371, 2015.

[214] C. Huang, J. H. Lin, C. H. Li, I. C. Yu, and T. L. Chen, "Atmospheric-pressure-plasma-enhanced fabrication of nonfouling nanocoatings for 316 stainless steel biomaterial interfaces," *Jpn. J. Appl. Phys.*, vol. 57, no. 3, pp. 1–7, 2018.

[215] C. W. Kan, C. H. Kwong, and S. P. Ng, "Surface modification of polyester synthetic leather with tetramethylsilane by atmospheric pressure plasma," *Appl. Surf. Sci.*, vol. 346, pp. 270–277, 2015.

[216] Z. Fang, Z. Ding, T. Shao, and C. Zhang, "Hydrophobic surface modification of epoxy resin using an atmospheric pressure plasma jet array," *IEEE Trans. Dielectr. Electr. Insul.*, vol. 23, no. 4, pp. 2288–2293, 2016.

[217] C. E. Nwankire, G. Favaro, Q. H. Duong, and D. P. Dowling, "Enhancing the mechanical properties of superhydrophobic atmospheric pressure plasma deposited siloxane coatings," *Plasma Process. Polym.*, vol. 8, no. 4, pp. 305–315, 2011.

[218] J. Yang, Y. Pu, D. Miao, and X. Ning, "Fabrication of durably superhydrophobic cotton fabrics by atmospheric pressure plasma treatment with a siloxane precursor," *Polymers (Basel).*, vol. 10, no. 4, 2018.

[219] C. Huang, H. H. Lin, and C. Li, "Atmospheric Pressure Plasma Polymerization of Super-Hydrophobic Nano-films Using Hexamethyldisilazane Monomer," *Plasma Chem. Plasma Process.*, vol. 35, no. 6, pp. 1015–1028, 2015.

[220] Y. Y. Ji, S. S. Kim, O. P. Kwon, and S. H. Lee, "Easy fabrication of large-size superhydrophobic surfaces by atmospheric pressure plasma polymerization with non-polar aromatic hydrocarbon in an in-line process," *Appl. Surf. Sci.*, vol. 255, no. 8, pp. 4575–4578, 2009.

[221] D. J. Marchand *et al.*, "Atmospheric rf plasma deposition of superhydrophobic coatings using tetramethylsilane precursor," *Surf. Coatings Technol.*, vol. 234, pp. 14–20, 2013.

[222] A. J. Beck, R. D. Short, and A. Matthews, "Deposition of functional coatings from acrylic acid and octamethylcyclotetrasiloxane onto steel using an atmospheric pressure dielectric barrier discharge," *Surf. Coatings Technol.*, vol. 203, no. 5–7, pp. 822–825, 2008.

[223] J. Pulpytel, V. Kumar, P. Peng, V. Micheli, N. Laidani, and F. Arefi-Khonsari, "Deposition of organosilicon coatings by a non-equilibrium atmospheric pressure plasma jet: Design, analysis and macroscopic scaling law of the process," *Plasma Process. Polym.*, vol. 8, no. 7, pp. 664–675, 2011.

[224] S. Asadollahi, J. Profili, M. Farzaneh, and L. Stafford, "Development of Organosilicon-based superhydrophobic coatings through atmospheric pressure plasma polymerization of HMDSO in nitrogen plasma," *Materials (Basel).*, vol. 12, no. 2, 2019.

[225] U. Lommatzsch and J. Ihde, "Plasma polymerization of HMDSO with an atmospheric pressure plasma jet for corrosion protection of aluminum and low-adhesion surfaces," *Plasma Process. Polym.*, vol. 6, no. 10, pp. 642–648, 2009.

[226] Y. A. Ussenov, L. Hansen, T. Krüger, T. S. Ramazanov, and H. Kersten, "Particle formation during deposition of SiO x nanostructured thin films by atmospheric pressure plasma jet," *Jpn. J. Appl. Phys.*, vol. 59, no. SH, 2020.

[227] M. C. Kim *et al.*, "Surface modification for hydrophilic property of stainless steel treated by atmospheric-pressure plasma jet," *Surf. Coatings Technol.*, vol. 171, no. 1–3, pp. 312–316, 2003.

[228] D. F. Williams, E. J. C. Kellar, D. A. Jesson, and J. F. Watts, "Surface analysis of 316 stainless steel treated with cold atmospheric plasma," *Appl. Surf. Sci.*, vol. 403, pp. 240–247, 2017.

[229] J. Žigon *et al.*, "Enhancement of strength of adhesive bond between wood and metal using atmospheric plasma treatment," *Cellulose*, vol. 27, no. 11, pp. 6411–6424, 2020.

[230] M. Bashir and S. Bashir, "Hydrophobic–Hydrophilic Character of Hexamethyldisiloxane Films Polymerized by Atmospheric Pressure Plasma Jet," *Plasma Chem. Plasma Process.*, vol. 35, no. 4, pp. 739–755, 2015.

[231] Y. C. Lin and M. J. Wang, "Fabrication of hydrophobic/hydrophilic HMDSO films by atmospheric pressure plasma jet deposition," *Jpn. J. Appl. Phys.*, vol. 58, no. SA, pp. 1–6, 2019.

[232] Plinio Innocenzi, "Infrared spectroscopy of sol–gel derived silica-based films: a spectra-microstructure overview," *J. Non. Cryst. Solids*, vol. 316, pp. 309–319, 2003.

[233] A. Grill and D. A. Neumayer, "Structure of low dielectric constant to extreme low dielectric constant SiCOH films: Fourier transform infrared spectroscopy characterization," *J. Appl. Phys.*, vol. 94, no. 10, pp. 6697–6707, 2003.

[234] W. Bensch and W. Bergholz, “An FT-IR study of silicon dioxides for VLSI microelectronics,” *Semicond. Sci. Technol.*, vol. 5, no. 5, pp. 421–428, 1990.
[235] R. Múgica-Vidal, F. Alba-Elías, E. Sainz-García, and M. Pantoja-Ruiz, “Hydrophobicity attainment and wear resistance enhancement on glass substrates by atmospheric plasma-polymerization of mixtures of an aminosilane and a fluorocarbon,” *Appl. Surf. Sci.*, vol. 347, pp. 325–335, 2015.
[236] G. Mertz *et al.*, “Atmospheric pressure plasma co-polymerization of two acrylate precursors: Toward the control of wetting properties,” *Plasma Process. Polym.*, vol. 15, no. 10, pp. 1–11, 2018.
[237] M. M. Hossain, Q. H. Trinh, D. B. Nguyen, M. S. P. Sudhakaran, and Y. S. Mok, “Robust hydrophobic coating on glass surface by an atmospheric-pressure plasma jet for plasma-polymerisation of hexamethyldisiloxane conjugated with (3-aminopropyl) triethoxysilane,” *Surf. Eng.*, vol. 35, no. 5, pp. 466–475, 2019.
[238] M. Mokter Hossain, Q. H. Trinh, M. S. P. Sudhakaran, L. Sultana, and Y. S. Mok, “Improvement of mechanical strength of hydrophobic coating on glass surfaces by an atmospheric pressure plasma jet,” *Surf. Coatings Technol.*, vol. 357, no. July 2018, pp. 12–22, 2019.
[239] G. Wulf, B. Mayer, and U. Lommatzsch, “Plasma Co-Polymerization of HMDSO and Limonene with an Atmospheric Pressure Plasma Jet,” *Plasma*, vol. 5, no. 1, pp. 44–59, 2022.
[240] H. O. Ozden, “EXPERIMENTAL AND COMPUTATIONAL ANALYSIS OF REDUCTION IN FOULING BY LOW ENERGY SURFACES,” 2009.
[241] T. Nylander, A. Hamraoui, and M. Paulsson, “Interfacial properties of whey proteins at air / water and oil / water interfaces studied by dynamic drop tensiometry , ellipsometry and spreading kinetics,” pp. 573–585, 1999.
[242] E. K. Marta TOMCZYŃSKA-MLEKO *et al.*, “Changes of Secondary Structure and Surface Tension of Whey Protein Isolate Dispersions upon pH and Temperature,” vol. 32, no. 1, pp. 82–89, 2014.
[243] R. d’Agostino, P. Flavia, and F. Fracassi, *Plasma processing and polymers*. Dordrecht: Kluwer Academic, 1997.
[244] T. H. Tran, D. Debarnot, J. Ortiz, and F. Poncin-Epaillard, “Role of the surface chemistry of plasma polymer layers on their long-term antifogging behavior,” *Plasma Process. Polym.*, vol. 17, no. 4, 2020.
[245] G. Giannuzzi *et al.*, “Short and long term surface chemistry and wetting behaviour of stainless steel with 1D and 2D periodic structures induced by bursts of femtosecond laser pulses,” *Appl. Surf. Sci.*, vol. 494, no. July, pp. 1055–1065, 2019.
[246] L. O. Neill, P. A. F. Herbert, C. Stallard, and D. P. Dowling, “Investigation of the Effects of Gas versus Liquid Deposition in an Aerosol-Assisted Corona Deposition Process,” pp. 43–50.
[247] J. Carpentier and G. Grundmeier, “Chemical structure and morphology of thin bilayer and composite organosilicon and fluorocarbon microwave plasma polymer films,” *Surf. Coatings Technol.*, vol. 192, no. 2–3, pp. 189–198, 2005.
[248] C. Roth, G. Oberbossel, E. Buitrago, R. Heuberger, and P. Rudolf Von Rohr, “Nanoparticle synthesis and growth in a continuous plasma reactor from organosilicon precursors,” *Plasma Process. Polym.*, vol. 9, no. 2, pp. 119–134, 2012.
[249] J. F. V Vincent, “Proceedings of the Institution of Mechanical Engineers , Part H : Journal of Engineering in Medicine,” 2009.
[250] “CEEBIOS.” .
[251] K. Liu, J. Du, J. Wu, and L. Jiang, “Superhydrophobic gecko feet with high adhesive forces towards water and their bio-inspired materials,” *Nanoscale*, vol. 4, no. 3, pp. 768–772, 2012.
[252] W. Barthlott *et al.*, “The salvmia paradox: superhydrophobic surfaces with hydrophilic pins for air retention under water,” *Adv. Mater.*, vol. 22, no. 21, pp. 2325–2328, 2010.
[253] G. Sun, Y. Fang, Q. Cong, and L. quan Ren, “Anisotropism of the Non-Smooth Surface of Butterfly Wing,” *J. Bionic Eng.*, vol. 6, no. 1, pp. 71–76, 2009.
[254] B. Bormashenko, E.; Nosonovsky, M.; Whyman, G.; Bhushan, “Chapter 6: Towards Undersanding Wetting Transitions on Biomimetic Surfaces: Scaling Arguments and Physical Mechanisms.,” in *Green Tribology: Biomimetic, Energy Conservation and Sustainability*, Springer, Ed. Berlin, 2012, p. 127–147.
[255] E. Fadeeva and B. Chichkov, “Biomimetic Liquid-Repellent Surfaces by Ultrafast Laser Processing,” 2018.
[256] C. H. Whitnah, “The Surface Tension of Milk. A Review,” *J. Dairy Sci.*, vol. 42, no. 9, pp. 1437–1449, 1959.
[257] A. Tuteja, W. Choi, J. M. Mabry, G. H. McKinley, and R. E. Cohen, “Robust omniphobic surfaces,” *Proc. Natl. Acad. Sci. U. S. A.*, vol. 105, no. 47, pp. 18200–18205, 2008.
[258] A. K. Kota, G. Kwon, and A. Tuteja, “The design and applications of superomniphobic surfaces,” *NPG Asia Mater.*, vol. 6, no. 6, pp. 1–16, 2014.
[259] E. Salimi, “Omniphobic surfaces: state-of-the-art and future perspectives,” *J. Adhes. Sci. Technol.*, vol. 33, no. 12, pp. 1369–1379, 2019.

[260] M. Villegas, Y. Zhang, N. Abu Jarad, L. Soleymani, and T. F. Didar, "Liquid-Infused Surfaces: A Review of Theory, Design, and Applications," *ACS Nano*, vol. 13, no. 8, pp. 8517–8536, 2019.
[261] S. Sunny, N. Vogel, C. Howell, T. L. Vu, and J. Aizenberg, "Lubricant-Infused Nanoparticulate Coatings Assembled by Layer-by-Layer Deposition," *Adv. Funct. Mater.*, vol. 24, no. 42, pp. 6658–6667, 2014.
[262] Z. Lian, J. Xu, Z. Wang, and H. Yu, "Biomimetic Superlyophobic Metallic Surfaces: Focusing on Their Fabrication and Applications," *J. Bionic Eng.*, vol. 17, no. 1, pp. 1–33, 2020.
[263] S. B. Subramanyam, G. Azimi, and K. K. Varanasi, "Designing Lubricant-Impregnated Textured Surfaces to Resist Scale Formation," *Adv. Mater. Interfaces*, vol. 1, no. 2, pp. 1–6, 2014.
[264] C. Lee, A. Kim, and J. Kim, "Electrochemically etched porous stainless steel for enhanced oil retention," *Surf. Coatings Technol.*, vol. 264, pp. 127–131, 2015.
[265] A. B. Tesler, P. Kim, S. Kolle, C. Howell, O. Ahanotu, and J. Aizenberg, "Extremely durable biofouling-resistant metallic surfaces based on electrodeposited nanoporous tungstite films on steel," *Nat. Commun.*, vol. 6, 2015.
[266] K. Doll *et al.*, "Development of Laser-Structured Liquid-Infused Titanium with Strong Biofilm-Repellent Properties," *ACS Appl. Mater. Interfaces*, vol. 9, no. 11, pp. 9359–9368, 2017.
[267] Y. Cheng *et al.*, "A femtosecond Bessel laser for preparing a nontoxic slippery liquid-infused porous surface (SLIPS) for improving the hemocompatibility of NiTi alloys," *Biomater. Sci.*, vol. 8, no. 23, pp. 6505–6514, 2020.
[268] Q. Ma, W. Wang, and G. Dong, "Facile fabrication of biomimetic liquid-infused slippery surface on carbon steel and its self-cleaning, anti-corrosion, anti-frosting and tribological properties," *Colloids Surfaces A Physicochem. Eng. Asp.*, vol. 577, no. March, pp. 17–26, 2019.
[269] P. Kim, T. S. Wong, J. Alvarenga, M. J. Kreder, W. E. Adorno-Martinez, and J. Aizenberg, "Liquid-infused nanostructured surfaces with extreme anti-ice and anti-frost performance," *ACS Nano*, vol. 6, no. 8, pp. 6569–6577, 2012.
[270] R. Qiu *et al.*, "Fabrication of slippery liquid-infused porous surface based on carbon fiber with enhanced corrosion inhibition property," *Colloids Surfaces A Physicochem. Eng. Asp.*, vol. 453, no. 1, pp. 132–141, 2014.
[271] X. Gao and Z. Guo, "Mechanical stability, corrosion resistance of superhydrophobic steel and repairable durability of its slippery surface," *J. Colloid Interface Sci.*, vol. 512, pp. 239–248, 2018.
[272] H. Luo, S. Yin, S. Huang, F. Chen, Q. Tang, and X. Li, "Fabrication of slippery Zn surface with improved water-impellent, condensation and anti-icing properties," *Appl. Surf. Sci.*, vol. 470, no. October 2018, pp. 1139–1147, 2019.
[273] Z. Qiu, R. Qiu, Y. Xiao, J. Zheng, and C. Lin, "Slippery liquid-infused porous surface fabricated on CuZn: A barrier to abiotic seawater corrosion and microbiologically induced corrosion," *Appl. Surf. Sci.*, vol. 457, pp. 468–476, 2018.
[274] S. Yang, R. Qiu, H. Song, P. Wang, Z. Shi, and Y. Wang, "Slippery liquid-infused porous surface based on perfluorinated lubricant/iron tetradecanoate: Preparation and corrosion protection application," *Appl. Surf. Sci.*, vol. 328, pp. 491–500, 2015.
[275] H. Luo *et al.*, "Robust platform for water harvesting and directional transport," *J. Mater. Chem. A*, vol. 6, no. 14, pp. 5635–5643, 2018.
[276] P. Wang, D. Zhang, Z. Lu, and S. Sun, "Fabrication of Slippery Lubricant-Infused Porous Surface for Inhibition of Microbially Influenced Corrosion," *ACS Appl. Mater. Interfaces*, vol. 8, no. 2, pp. 1120–1127, 2016.
[277] P. Wang, Z. Lu, and D. Zhang, "Slippery liquid-infused porous surfaces fabricated on aluminum as a barrier to corrosion induced by sulfate reducing bacteria," *Corros. Sci.*, vol. 93, pp. 159–166, 2015.
[278] Z. Shi, Y. Xiao, R. Qiu, S. Niu, and P. Wang, "A facile and mild route for fabricating slippery liquid-infused porous surface (SLIPS) on CuZn with corrosion resistance and self-healing properties," *Surf. Coatings Technol.*, vol. 330, pp. 102–112, 2017.
[279] P. Yu, Z. Lian, J. Xu, and H. Yu, "Slippery liquid infused porous surfaces with corrosion resistance potential on aluminum alloy," *RSC Adv.*, vol. 11, no. 2, pp. 847–855, 2020.
[280] S. Peppou-Chapman, J. K. Hong, A. Waterhouse, and C. Neto, "Life and death of liquid-infused surfaces: A review on the choice, analysis and fate of the infused liquid layer," *Chem. Soc. Rev.*, vol. 49, no. 11, pp. 3688–3715, 2020.
[281] D. C. Leslie *et al.*, "A bioinspired omniphobic surface coating on medical devices prevents thrombosis and biofouling," *Nat. Biotechnol.*, vol. 32, no. 11, pp. 1134–1140, 2014.
[282] J. Chen *et al.*, "An immobilized liquid interface prevents device associated bacterial infection in vivo," *Biomaterials*, vol. 113, pp. 80–92, 2017.
[283] A. Waterhouse *et al.*, "Rapid Coating Process Generates Omniphobic Dentures in Minutes to Reduce C. albicans Biofouling," *ACS Biomater. Sci. Eng.*, vol. 5, no. 2, pp. 420–424, 2019.
[284] D. Wang, Z. Guo, and W. Liu, "Bioinspired Edible Lubricant-Infused Surface with Liquid Residue

Reduction Properties," *Research*, vol. 2019, pp. 1–12, 2019.
[285] D. F. Miranda, C. Urata, B. Masheder, G. J. Dunderdale, M. Yagihashi, and A. Hozumi, "Physically and chemically stable ionic liquid-infused textured surfaces showing excellent dynamic omniphobicity," *APL Mater.*, vol. 2, no. 5, 2014.
[286] R. W. Bittner, K. Bica, and H. Hoffmann, "Fluorine-free, liquid-repellent surfaces made from ionic liquid-infused nanostructured silicon," *Monatshefte fur Chemie*, vol. 148, no. 1, pp. 167–177, 2017.
[287] Y. Galvan, K. R. Phillips, M. Haumann, P. Wasserscheid, R. Zarraga, and N. Vogel, "Ionic-Liquid-Infused Nanostructures as Repellent Surfaces," *Langmuir*, vol. 34, no. 23, pp. 6894–6902, 2018.
[288] X. Q. Wang, C. D. Gu, L. Y. Wang, J. L. Zhang, and J. P. Tu, "Ionic liquids-infused slippery surfaces for condensation and hot water repellency," *Chem. Eng. J.*, vol. 343, no. February, pp. 561–571, 2018.
[289] "ECHA - European Chemicals Agency." [Online]. Available: https://echa.europa.eu/hot-topics/perfluoroalkyl-chemicals-pfas. [Accessed: 05-Feb-2022].
[290] "LEAF EquipEX." [Online]. Available: https://leaf-equipex.iemn.univ-lille1.fr/. [Accessed: 05-Feb-2022].
[291] C. Hairaye, "Fonctionnalisation de surfaces par microstructuration laser," Université de Srasbourg, 2017.
[292] R. Le Harzic, N. Huot, E. Audouard, P. Jonin, and P. Laporte, "Comparison of heat-affected zones due to nanosecond and femtosecond laser pulses using transmission electronic microscopy," *Appl. Phys. Lett.*, vol. 3886, no. 21, pp. 1–4, 2012.
[293] E. Audouard, "Lasers à impulsions ultrabrèves : applications Lasers à impulsions ultrabrèves :," *Tech. l'ingénieur*, vol. 33, no. 0, 2019.
[294] S. Landon, "Micro- et nano-usinage par laser à impulsions ultracourtes : amélioration de procédés par des méthodes tout optique To cite this version : Amélioration de procédés par des méthodes tout optique," 2012.
[295] M. Nisoli, S. De Silvestri, O. Svelto, and R. Szip, "Compression of high-energy laser pulses below 5 fs," vol. 22, no. 8, pp. 522–524, 1997.
[296] A. Y. Vorobyev and C. Guo, "Femtosecond laser nanostructuring of metals," vol. 14, no. 6, pp. 2164–2169, 2006.
[297] M. Martinez-Calderon, A. Rodriguez, A. Dias, M. C. Morant-Minana, M. Gomez-Aranzadi, and S. M. Olaizola, "Femtosecond laser fabrication of highly hydrophobic stainless steel surface with hierarchical structures fabricated by combining ordered microstructures and LIPSS," *Appl. Surf. Sci.*, no. 374, pp. 81–89, 2015.
[298] K. M. T. Ahmmed and A. Kietzig, "Soft Matter superhydrophobic surfaces †," *Soft Matter*, no. 2007, 2016.
[299] A. Y. Vorobyev and C. Guo, "Multifunctional surfaces produced by femtosecond laser pulses Multifunctional surfaces produced by femtosecond laser pulses," vol. 033103, 2015.
[300] P. T. Mannion, J. Magee, E. Coyne, G. M. O. Connor, and T. J. Glynn, "The effect of damage accumulation behaviour on ablation thresholds and damage morphology in ultrafast laser micro-machining of common metals in air," vol. 233, pp. 275–287, 2004.
[301] S. Moradi, S. Kamal, and S. G. Hatzikiriakos, "Superhydrophobic laser-ablated stainless steel substrates exhibiting cassie-baxter stable state," *Surf. Innov.*, vol. 3, no. 3, pp. 151–163, 2015.
[302] J. D. Smith *et al.*, "Droplet mobility on lubricant-impregnated surfaces," vol. 9, no. 6, 2013.
[303] "Aroma Zone." [Online]. Available: https://www.aroma-zone.com/info/fiche-technique/huile-vegetale-coco-bio-aroma-zone. [Accessed: 02-Mar-2022].
[304] L. E. Vandenburg and E. A. Wilder, "The structural constituents of carnauba wax," *J. Am. Oil Chem. Soc.*, vol. 47, no. 12, pp. 514–518, 1970.
[305] C. M. Magin, S. P. Cooper, and A. B. Brennan, "Non-toxic antifouling strategies," *Mater. Today*, vol. 13, no. 4, pp. 36–44, 2010.
[306] P. Shivapooja, Q. Wang, B. Orihuela, D. Rittschof, G. P. Lõpez, and X. Zhao, "Bioinspired surfaces with dynamic topography for active control of biofouling," *Adv. Mater.*, vol. 25, no. 10, pp. 1430–1434, 2013.
[307] A. M. Brzozowska *et al.*, "Biomimicking micropatterned surfaces and their effect on marine biofouling," *Langmuir*, vol. 30, no. 30, pp. 9165–9175, 2014.
[308] S. L. Stott *et al.*, "Isolation of circulating tumor cells using a microvortex-generating herringbone-chip," *Proc. Natl. Acad. Sci. U. S. A.*, vol. 107, no. 43, pp. 18392–18397, 2010.
[309] S. Wang, Y. Cho, X. Cheng, S. Yang, Y. Liu, and Y. Liu, "Integration of hierarchical Micro-/Nanostructures in a microfluidic chip for efficient and selective isolation of rare tumor cells," *Micromachines*, vol. 10, no. 10, pp. 1–10, 2019.
[310] S. Wang, A. Thomas, E. Lee, S. Yang, X. Cheng, and Y. Liu, "Highly efficient and selective isolation of rare tumor cells using a microfluidic chip with wavy-herringbone micro-patterned surfaces," *Analyst*, vol. 141, no. 7, pp. 2228–2237, 2016.
[311] A. Beaugendre *et al.*, "Self-stratifying coatings: A review," *Prog. Org. Coatings*, vol. 110, pp. 210–241,

2017.
[312] R. B. Bodkhe *et al.*, “The effect of formulation variables on fouling-release performance of stratified siloxane-polyurethane coatings,” *J. Coatings Technol. Res.*, vol. 9, no. 3, pp. 235–249, 2012.
[313] C. Liu, C. Ma, Q. Xie, and G. Zhang, “Self-repairing silicone coatings for marine anti-biofouling,” *J. Mater. Chem. A*, vol. 5, no. 30, pp. 15855–15861, 2017.
[314] M. B. Yagci, S. Bolca, J. P. A. Heuts, W. Ming, and G. De With, “Self-stratifying antimicrobial polyurethane coatings,” *Prog. Org. Coatings*, vol. 72, no. 3, pp. 305–314, 2011.
[315] J. Zhao, W. Millians, S. Tang, T. Wu, L. Zhu, and W. Ming, “Self-Stratified Antimicrobial Acrylic Coatings via One-Step UV Curing,” *ACS Appl. Mater. Interfaces*, vol. 7, no. 33, pp. 18467–18472, 2015.
[316] A. Toussaint, “Self-stratifying coatings for plastic substrates (brite euram project RI 1B 0246 C(H)),” *Prog. Org. Coatings*, vol. 28, no. 3 SPEC. ISS., pp. 183–195, 1996.

PhD Communications

Written communications

M. Saget, C. Françolle de Almeida, V. Fierro, A. Celzard, G. Delaplace, V. Thomy, Y. Coffinier, M. Jimenez, A critical review on surface modifications mitigating dairy fouling, *Compr Rev Food Sci Food Saf.* 2021; 20: 4324 – 4366

C. Françolle de Almeida, M. Saget, G. Delaplace, M. Jimenez, V. Fierro, A. Celzard, Innovative fouling-resistant materials for industrial heat exchangers: a review, *Rev Chem Eng*. 2021

Oral communications

M. Saget, V. Thomy, G. Delaplace, Y. Coffinier, M. Jimenez, *Atmospheric pressure plasma hydrophobic silane-based coating to limit dairy fouling adhesion*, GDR B2I & Happybio, Paris, France, Oct 2019

M. Saget, F. Braud, S. J. Zapiain Merino, S. Zouaghi, L. Azevedo-Scudeller, G. Delaplace, V. Thomy, Y. Coffinier, M. Jimenez, *Optimization of laser manufacturing conditions to improve lubricant retention of slippery liquid-infused surface*, GDR B2I, Toulouse, France, Sept 2021

M. Saget, F. Braud, S. J. Zapiain Merino, L. Azevedo-Scudeller, G. Delaplace, V. Thomy, Y. Coffinier, M. Jimenez, *Surface engineering of stainless steel to limit dairy fouling adhesion,* IFHN (Food Science & Human Nutrition), Osaka, Japan, Oct 2021 (Online)

M. Saget, F. Braud, S. J. Zapiain Merino, L. Azevedo-Scudeller, G. Delaplace, V. Thomy, Y. Coffinier, M. Jimenez, *Surface engineering of stainless steel to limit dairy fouling adhesion,* GDR 288 Biomim, Nov 2021 (Online)

M. Saget, F. Braud, S. J. Zapiain Merino, S. Zouaghi, L. Azevedo-Scudeller, G. Delaplace, V. Thomy, Y. Coffinier, M. Jimenez, *Optimization of laser manufacturing conditions to improve lubricant retention of slippery liquid-infused surface*, Réseau OPAL, Lens, France, Nov 2021

M. Saget, F. Braud, S. J. Zapiain Merino, L. Azevedo-Scudeller, G. Delaplace, V. Thomy, Y. Coffinier, M. Jimenez, *Surface engineering of stainless steel to limit dairy fouling adhesion,* FCFP (Fouling and Cleaning in Food Processing), Lille France, March 2022

M. Saget, N. Nuns, L. Azevedo-Scudeller, G. Delaplace, V. Thomy, Y. Coffinier, M. Jimenez, *Atmospheric pressure plasma superhydrophobic bilayer coatings to limit dairy fouling adhesion,* PlasmaTech, Barcelona, Spain, April 2022 (online)

Poster

M. Saget, S. Zouaghi, V. Thomy, Y. Coffinier, G. Delaplace, M. Jimenez, *Design of biomimetic surfaces for food antifouling*, JJC UGePE 2018, Villeneuve d'Ascq, France, Nov 2018

M. Saget, S. Zouaghi, F. Braud, G. Delaplace, V. Thomy, Y. Coffinier, M. Jimenez, *Optimization of laser manufacturing conditions to improve lubricant retention of slippery liquid-infused surface*, JJC GEPROC 2019, Mons, Belgique, Nov 2019 (Best price)

ANNEXES

Annex 1

Table 52. Impact of surface properties on fouling behaviour in batch conditions, adapted from [10], [11]

Investigated parameter	Observations	Coating / Surface	[a]SFE, [b]γ^p, [c]γ^- (mN/m)	WCA (°)	R_a (µm)	Tested fluid	Tested parameters	Rinsing/Cleaning parameters	Reference
Surface free energy (SFE)	An optimal SFE value allows to reduce protein adsorption	standard 304 SS	78.4[a] / 38.3[b]	-	-	β-Lactoglobulin in phosphate buffer solution (PBS)	Batch (360 min) T_{bulk} = 30 °C		[91]
		Glass	159[a] / 127[b]	-	-				
		Nylon	87.6[a] / 47.5[b]	-	-				
		PE HD	60.4[a] / 22[b]	-	-				
		PE	47.9[a] / 12[b]	-	-				
		PP	68.5[a] / 29.7[b]	-	-				
		PTFE	22.6[a] / 0[b]	-	-				
	Low SFE improves the cleanability	304 AISI SS	38.3[a] / 6.6[b]	-	0.15	WPI in water	Batch T_{bulk} = 60 to 80 °C	2 % NaOH solution spray Water spray	[88]
		Nanocomposite I	23.6[a] / 2.4[b]	-	0.07				
		Nanocomposite V	29.8[a] / 7.1[b]	-	0.6				
		FEP	19.8[a] / 1.5[b]	-	0.3				
		PEEK + fluoropolymer	13.4[a] / 0.1[b]	-	2				
		Si-O-DLC (PACVD)	29.9[a] / 2[b]	-	0.2				
		Ti-DLC (PVD)	41.8[a] / 0.4[b]	-	0.2				
Polar component	Low polar component decreases adhesion strength of protein and calcium phosphate	polished 316 SS	-	-	0.05	Raw whole milk	Batch (60 min) T_{bulk} = 60 °C	Distilled water at 25 °C (90 s)	[86]
		standard 316 SS	-	-	0.8				
		PMMA	49.9[a] / 19.3[b]	-	0.2				
		PS	43.1[a] / 17.1[b]	-	0.1				
		Nylon	67.7[a]/ 19.3[b]	-	2				
		Cellulose acetate	52.6-49.3[a] / 29.5-25.1[b]	-	0.2-0.6				
		Agarose coating	72.1[a] / 50.5[b]	-	0.3				
	Low polar component reduces fouling amount and calcium phosphate adhesion	2R 316 SS	51.9[a] / 39[c]	35.6	-	Simulated Milk Ultrafiltrate (SMUF)	Batch (5 and 120 min) T_{bulk} = 44 °C		[87]
		MoS_2	45.7[a] / 20.4[c]	57.8	-				
		SiF^+	49.4[a] / 36.8[c]	40.3	-				
		SiO_x	55.5[a] / 50.6[c]	18.6	-				
		Ni-P-PTFE	15.5[a] / 0.2[c]	118.4	-				

	An optimal polar component leads to decreased fouling resistance and amount	SS	42[a] / 8.3[c]	-	0.18	WPI and SMUF SMUF WPI	Batch T_{bulk} = 50 °C and 40 °C for SMUF $T_{surface}$ = 80, 105, 120 °C		[89]
		DLC	45[a] / 11.1[c]	-	0.13				
		SICON	46[a] / 13.4[c]	-	0.12				
		SICAN	46[a] / 19[c]	-	0.12				
		SS	42[a] / 8.4[c]	-	0.18	WPI and SMUF SMUF WPI	Batch T_{bulk} = 50 °C and 40 °C for SMUF $T_{surface}$ = 80, 105, 120 °C	0.25 % NaOH solution at 30 °C 0.5 % NaOH solution at 30 °C	[10]
		Electropolished SS	46[a] / 15.1[c]	-	0.1				
		DLC coating	45.2[a] / 13[c]	-	0.13				
		DLC on electropolished SS	47.6[a] / 11[c]	-	0.1				
		SICAN	45.2[a] / 15.5[c]	-	0.12				
		SICAN on electropolished SS	52.3[a] / 14[c]	-	0.11				
		SICON	47.9[a] / 22[c]	-	0.12				
		SICON on electropolished SS	55.1[a] / 24[c]	-	0.11				
	High polar component decreases fouling amount	2R 316 SS	24.3-39[c]	-	-	SMUF WPI in SMUF	Batch (10 and 120 min) T_{bulk} = 44 and 70°C for SMUF and 50 and 85 °C for WPI in SMUF		[93]
		MoS_2	50.6-53.8[c]	-	-				
		DLC-Si-O (plasma CVD)	12.4-15.3[c]	-	-				
		SiO_x (plasma CVD)	15-15.6[c]	-	-				
		Ni-P-PTFE	20.4[c]	-	-				
		Silica sol-gel	0.2-10[c]	-	-				
Roughness	Smooth surface leads to lower milk deposit	SS	-	-	0.028	Whole milk	Batch (30 min) T_{bulk} = 90 °C		[94]
			-	-	0.174				
			-	-	0.445				
Polar component and roughness	High polar component and smooth surface reduce fouling resistance	SS	34[a] / 4[b]			WPC in water	Batch (25h) T_{bulk} = 50 °C $T_{surface}$ = 70-80 °C	-	[92]
		Electropolished SS	44[a] / 13[b]						
		Aluminium	40[a] / 10.5[b]						
		Copper	35[a] / 3[b]						
		DLC (PECVD)	45[a] / 12[b]						
		SICAN	43.5[a] / 6.5[b]						
		SICON	40[a] / 19[b]						
		SICAN on electropolished SS	32[a] / 3[b]						

SS: stainless steel, **PE HD:** polyethylene high density, **PP:** polypropylene, **PTFE:** polytetrafluoroethylene, **FEP:** Fluorinated ethylene propylene, **PEEK:** polyetheretherketone, **DLC:** diamond-like carbon, **PMMA:** poly(methyl methacrylate), **PS:** polystyrene, **SICAN:** Si-doped DLC, **SICON:** Si- and O-doped DLC, **PVD:** physical vapour deposition, **CVD:** chemical vapour deposition, **PACVD:** plasma assisted CVD, **PECVD**: plasma-enhanced CVD

Annex 2

Table 53. Impact of surface properties on fouling behaviour in continuous conditions, adapted from [10], [11]

Investigated parameter	Observations	Coating / Surface	[a]SFE, [b]γ^p, [c]γ^- (mN/m)	WCA (°)	Ra (µm)	Tested fluid	Tested parameters	Rinsing/Cleaning parameters	Reference
Surface free energy	Low surface free energy resulted in lower absorbed amounts of protein/ in lower mass of fouling	2R 316 SS	-	69	30 nm	Whey protein isolate (WPI) in PBS	Continuous flow, T_{bulk} = 25 and 85 °C	-	[96]
		SiF_3^+	-	61	24 nm				
		MoS_2	-	49	25 nm				
		TiC	-	-	20 nm				
		Silica sol-gel	-	-	35 nm				
		DLC (sputtering)	-	84	30 nm				
		DLC (plasma CVD)	-	65	28 nm				
		DLC-Si-O (plasma CVD)	-	-	27 nm				
	An optimal surface free energy decreases the fouling deposition rate	316 stainless steel	32[a]	72.1	-	Pasteurized milk	Continuous flow with recirculation in single channel PHE (1h, 3h 5h) T_{bulk} = 60 °C	-	[97]
		PTFE	5[a]	119.6	-				
		CNT-PTFE	1[a]	141.1	-				
		2B 316L SS	41.4[a]	82.9	0.149	Raw milk	Continuous flow in a benchtop PHE (7,5h) T_{bulk} = 85 °C		[98]
		Thermolon sol-gel coating	32.4[a]	105.5	0.199				
		Teflon	22.1[a]	-	76	Whole milk	Continuous flow, no recirculation, Milk heated from room temperature to 100, 130 and 154 °C		[99]
		polished 304 SS	46.4[a]	-	1.5				
		standard 304 SS	51.4[a]	-	16				
		aluminosilicate coating onto 303 SS	38.6[a]	-	91				
	Low SFE/hydrophobic coating improves the cleanability	SS	-	83.8	0.15	WPC in water	Continuous flow with recirculation (17 min) T_{bulk} = 45 °C $T_{substrate}$ = 96,5 °C Continuous flow no recirculation in PHE (4 h) T_{bulk} = 85 °C	0.1 molar NaOH solution	[100]
		Electrically polished SS	-	61.7 / 60.3	0.17 / 2.69				
		Epoxy resin-based coating	-	97.6 / 91 / 95.8	0.92 / 0.95 / 1.14				
		Polyurethane-based coating	-	93.4	0.06				
		PTFE	-	92.2	0.23				
		304 SS	46.4[a]	-	62.4	WPC in water	Continuous flow (3500 s)		[101]

		Fluorolink S10 coating	19[a]	-	106.7		T_{bulk} = 60 °C	0.5 % NaOH solution at 60 °C (600 s)	
Polar component	Polar component affects fouling resistance and amount	2R 316 SS	39[c]	-	-	WPI in SMUF	Continuous flow, no recirculation (1080 - 1800 min) T_{bulk} = 48 °C	-	[102]
		TiN 1	55.3[c]	-	-				
		TiN 25	23[c]	-	-				
		TiN 3	46.2[c]	-	-				
	An optimal polar component reduces fouling resistance and amount	SS	43.5[a] / 4.6[c]	-	0.17	WPI in SMUF	Continuous flow in PHE T_{bulk} = 62-85 °C	-	[105]
		DLC	47.5[a] / 9.2[c]	-	0.21				
		SICON	46.8[a] / 13.2[c]	-	0.17				
		SICAN	47.2[a] / 8.7[c]	-	0.23				
	Low polar component leads to decreased deposition rate and final amount	2R 316 SS	39[c]	-	-	SMUF	Continuous flow (60 h) T_{bulk} = 48 °C	Water at 48 °C (48h)	[103]
		TiN 1	55.3[c]	-	-				
		TiN 2	23[c]	-	-				
		TiN 3	46.2[c]	-	-				
		TiN 4	18.4[c]	-	-				
		TiN 5	26[c]	-	-				
		304 SS	40.5[a] / 8.4[c]	-	0.2	SMUF	Continuous flow with recirculation (900 min) T_{bulk} = 52 °C $T_{surface}$ = 50 °C	0.5 % HNO_3 solution at 52 °C	[104]
		DLC (PECVD)	44.7[a] / 13.1[c]	-	0.13				
		Si-DLC (PECVD)	39.4[a] / 6.4[c]	-	0.125				
		Si-O-DLC (PECVD)	34.5[a] / 7.2[c]	-	0.125				
	Low polar parts tend to reduce mass deposit	2R 304 SS	32.6[c]	57.1	40 nm	Raw milk and WP solution	Continuous flow in microfluidic heat exchanger device (120 min) T_{bulk} = 60-70 °C $T_{surface}$ = 105°C Continuous flow with recirculation in bench-scale heat exchanger rig (150 min) T_{bulk} = 60-70 °C $T_{surface}$ = 89 °C	-	[12]
		PP film	0.26[c]	103.5	190 nm				
		PFA-2, PFA-4 (dry powder)	0.53-1.0[c]	110.3 / 108	617 / 574 nm				
		PFA-3 (water-based suspension)	0.93[c]	108.2	698 nm				
		FEP-2, FEP-3 (water-based suspension)	0.76-1.1[c]	108.4 / 108.1	482 / 269 nm				
		PTFE-2 (water-based suspension)	1.4[c]	106.9	2814 nm				
		PTFE-1 (dispersed in epoxy resin)	11.5[c]	81.1	956 nm				
		V2 SS	41[a] / 14.5[b]	-	0.04			Water at 60 °C (10 min)	[106]

	Low polar component improves the cleanability	DLC	36[a] / 9[b]	-	0.1	Whole milk with whey protein, sugar, xanthan gum	Continuous flow in PHE, no recirculation, $T_{bulk\ oulet}$ = 102 °C	0.5 NaOH solution at 60 °C (15 min) Water at 60 °C (10 min)	[107]
		Silica	-	-	-				
		SiO_x	40[a] / 13.5[b]	-	0.15				
		Ni-P-PTFE	20.2[a] / 5.5[b]	-	0.25				
		Excalibur	21.7[a] / 0.9[b]	-	1.77				
		Xylan	21.5[a] / 0.95[b]	-	1.81				
		Ion implantation (SiF^+, MoS_2)	45[a] / 8[b] / 40[a] / 12[b]	-	0.2 / 0.15				
	High polar component could prevent protein adhesion	2B 316L SS	39[a] / 3.1[b]	84	0.05	WPI and $CaCl_2$ in water	Continuous flow (1.5 h) T_{bulk} = 85 °C	Half of samples rinsed with water at 85 °C (20 min)	[108]
		Carbonised garaphite	48.8[a] / 0.6[b]	124.7	0.54				
		PTFE impregnated graphite	49.1[a] / 0[b]	116.8	0.27				
		2B 316L SS	41.9[a] / 3.7[b]	84.2	0.068	WPI and $CaCl_2$ in water	Continuous flow (1.5 h) T_{bulk} = 85 °C	2 % NaOH solution at 85 °C (20 min) Water at 85 °C (20 min) 2 % HNO_3 solution at 85 °C (20 min) Water at 85 °C (5 min)	
		Si-PEO coating without adhesive layer	51.8[a] / 16.7[b]	33.6	0.04				
		Si-PEO coating on plasma activated SS	39.1[a] / 9.23[b]	61.6	0.03				
		Si-PEO coating on polydopamine coated SS	50.0[a] / 14.1[b]	30.7	0.04				
		Si-PEO coating on NuSil SP120 coated SS	68.8[a] / 30.1[b]	28.8	0.02				
Roughness	Micrometric roughness does not reduce fouling or cleanability	standard 304 SS	-	26	0.13	Raw whole milk	Continuous flow, milk heated in a PHE (72-82 min) T_{bulk} = 86-90 °C	Water at 65 °C (7 min) 1 % NaOH solution at 65 °C (14 min) (Only for Teflon)	[110]
		electropolished SS	-	45	0.08				
		titanium	-	29	0.19				
		polysiloxane	-	76	0.1				
		Teflon	-	90	0.6				
	Smooth surface leads to decreased fouling amount	SS	-	-	pickle finish	Raw milk	Continuous flow with recirculation T_{heat}= 100 °C T_{bulk} = 82 °C	-	[109]
			-	-	120 grit finish				
			-	-	180 grit finish				
					320 grit finish				

Low surface free energy and smooth surface	Tend to reduce fouling amount	316 SS	41.4[a]	78.8	0.32	Raw milk	Continuous flow in PHE (8h) T_{bulk} = 85 °C	No rinse / low flow water rinse / high flow water rinse / high flow 1 M NaOH rinse	[111]
		Ni-P-PTFE	24.7[a]	115	0.17				
		2B 316L SS	40.5[a] / 3.5[c]	92.9	0.068	WPI and $CaCl_2$ in water	Continuous flow (1.5 h) T_{bulk} = 85 °C	Water rinse Half of samples rinsed with water at 85 °C (20 min)	[13]
		Laser texturized SS	-	0	1243				
		Fluorosilanized laser texturized SS	-	132.9	1364				
		Slippery surface (fluorine oil Krytox GPL 103)	17.4[a] / 3.7[c]	111.6	-				
		2B 316L SS	40.5[a] / 3.5[b]	92.9	0.07	WPI and $CaCl_2$ in water	Continuous flow (1.5 h) T_{bulk} = 85 °C	-	[60]
		Mirror-like polished SS	42.5[a] / 17.0[b]	63.9	0.003				
		Textured SS	-	0	36				
		Fluorosilanized SS	27.6[a] / 1.1[b]	111.9	0.98				
		Fluorosilanized mirror-like polished SS	18.8[a] / 1.8[b]	105.9	0.004				
		Fluorosilanized textured SS	-	132.9	36				
Polar component and nanostructured surface	Low polar component and nanoroughness lead to reduce fouling amount	2B 316L SS	-	-	105 nm	β-Lg and calcium solution in water	Continuous flow T_{bulk} = 93 °C	-	[112]
		2B 316L SS (grade 240)	-	-	111 nm				
		2B 316L SS (grade 400)	-	-	68 nm				
		2R 304 SS	-	-	16 nm				
		2B 304 SS	-	-	114 nm				
		TMDSO	0 / 0.5 / 0.7[c]	113 / 112.7 / 112.8	240 / 256 / 280 nm				
		PTFE-PPS	0.8[c]	116.5	1070 nm				
		Commercial PTFE based coating	5 / 6.4 / 0.3 / 3.5[c]	87.7 / 84.3 / 98.9 / 88.3	430 / 451/ 1055 / 1064 nm				
	High polar component and nanoroughness decrease final fouling amount	2B 316L SS	41.9[a] / 3.7[b]	84.2	0.068	WPI and $CaCl_2$ in water	Continuous flow(1.5 h) T_{bulk} = 85 °C	Water at 85 °C (20 min)	[113]
		Plasma activated SS	64.7[a] / 29.0[b]	23.5	0.07				

		HMDSO coating (APP) PL 1	37.7[a] / 3.9[b]	95.7	0.045				
		PL 2	38.4[a] / 2.8[b]	79.3	0.051				
		PL 3	44[a] / 15.8[b]	101.2	0.043				
		PL 4	46.5[a] / 14.5[b]	101.5	0.041				
		PL 5	43.3[a] / 7.1[b]	97.1	0.064				
		PL 6	41.5[a] / 7.1[b]	94.3	0.049				
		PL 7	48.5[a] / 12.7[b]	95	0.04				
		PL 8	42.3[a] / 10.2[b]	95.4	0.051				
Surface properties	Do not affect fouling amount eiher the cleanability	2B 316L SS	50.8[a] / 30.2[c]	58.6	0.17	Whole and skim milk and WPI	Batch (120 min) T_{bulk} = 80 °C Continuous flow in PHE (240 min) T_{bulk} = 84 °C	0.25 % NaOH solution at 75 °C (10 min) 0.5% HNO_3 solution at 65 °C (10 min)	[95]
		doped DLC 1 (PACVD)	48[a] / 21.8[c]	56.6	0.12				
		doped DLC 2 (PACVD)	43.5[a] / 21.2[c]	60.7	0.15				
		doped DLC 3 (PACVD)	41.3[a] / 35.2[c]	50.7	0.13				

SS: stainless steel, **DLC:** diamond-like carbon, **SICAN:** Si-doped DLC, **SICON:** Si- and O-doped DLC, **PTFE:** polytetrafluoroethylene, **CNT**: carbon nanotubes, **FEP:** Fluorinated ethylene propylene, **PFA:** perfluoroalkoxy, **PP:** polypropylene **PEO:** polyethylene oxide, **PPS:** polyphenylene sulfide, **TMDSO:** tetramethyldisiloxane, **HMDSO:** hexamethyldisiloxane, **PVD:** physical vapour deposition, **CVD:** chemical vapour deposition, **PACVD:** plasma-assisted CVD, **PECVD**: plasma-enhanced CVD, **APP:** Atmospheric pressure plasma

Annex 3

Evolution of plasma power generated by the APP torch (AcXys Technologies). The Figure 109 shows that power variation depends on both N_2 flow rate and frequency.

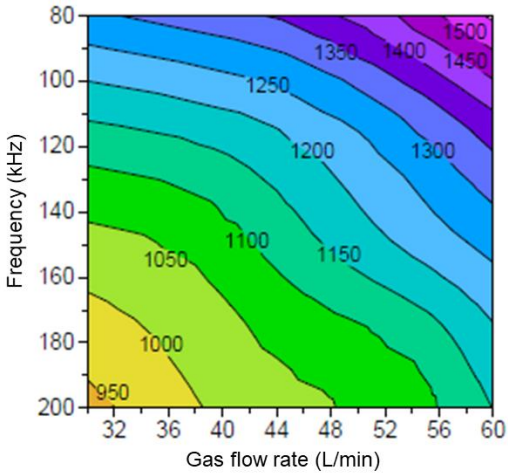

Figure 109. Power curves in N_2 plasma at atmospheric pressure[207]

Annex 4

Fouled SLIS were cleaned in a 2% NaOH in ultrasonic bath. After 60 min, WCA measurements performed and structured surfaces were observed using digital microscopy. As illustrated in Figure 110 b and c, this cleaning allows to remove remaining fouling deposit. This was confirmed by WCA measurements, since for almost all samples former WCA was recovered. Consequently, it was not needed to modify structured samples and all surfaces were re-infused after the NaOH cleaning.

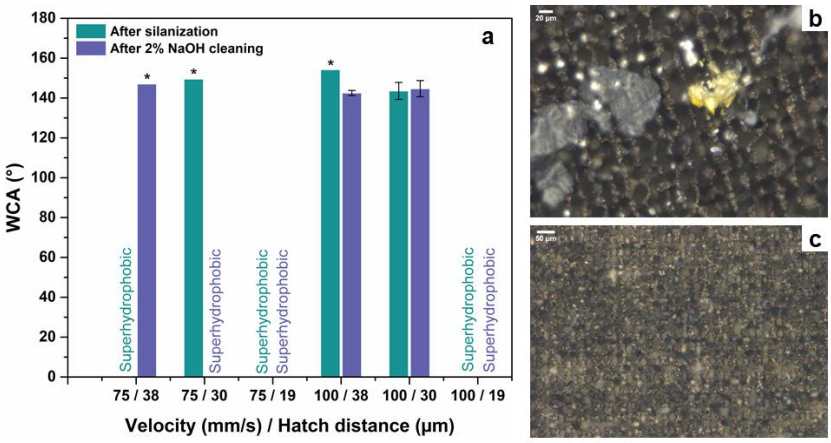

Figure 110. Effectivness of 2 % NaOH cleaning assessed by WCA mesurements (a) and microscopy (b) before cleaning and (c) after cleaning. (*) Only one measurement was carried out.

Annex 5

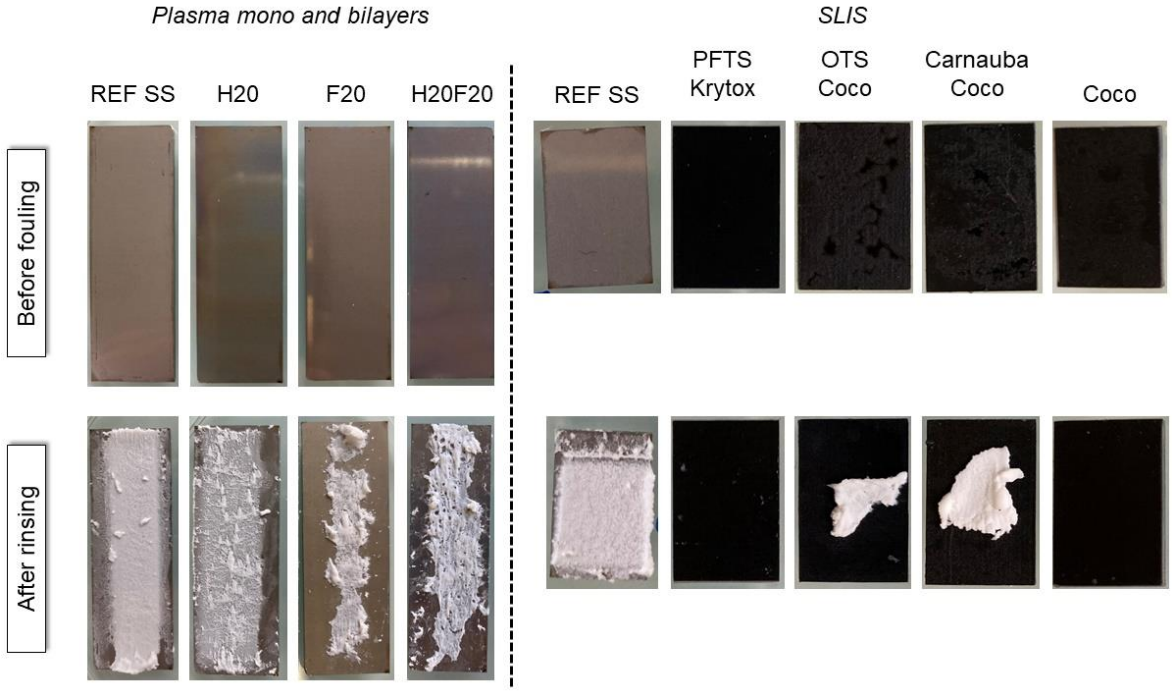

Figure 111. Samples before and after a pasteurization test. (Left) Plasma mono and bilayers and (Right) Fluorine-Based and coconut-based SLIS.

Annex 6

The self-stratifying amphiphilic coating (Figure 112) was prepared by the separate dissolution of the elastomeric matrix with the amphiphilic molecule (Si-PEO) and the epoxy resin, at 30 wt% in a common solvent blend. Then, both solutions were then mixed at a 1:1 ratio with the same mechanical stirrer. The curing agent was added in the mixture with respect to the epoxy number (1:1). The resulting solution was then further mixed for 5 min before application. The coating was sprayed onto stainless steel at RT with an air pressure of 200 kPa in a spray booth (Labo 600 from Tricolor Industries, Décines-Charpieu, France), using a regular spray gun (LG60 from Tricolor Industries). Finally, the obtained coating was left for 15 min at room temperature, 1h at 110°C (allowing phases separation) and 1 week at room temperature.

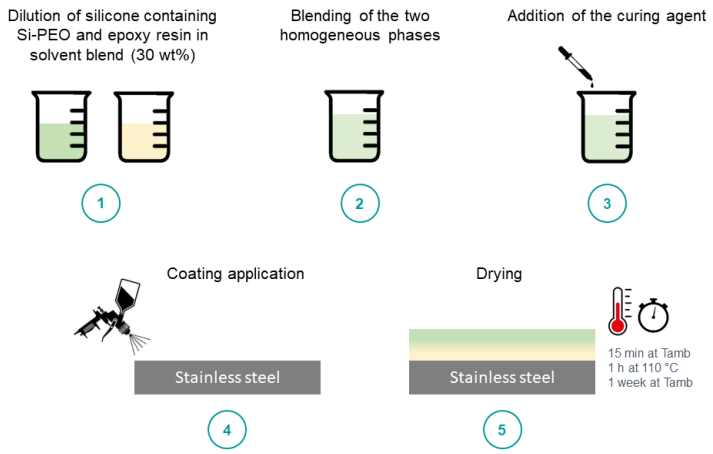

Figure 112. Processing steps for the elaboration of self-stratifying amphiphilic coating.

Surface engineering of stainless steel for dairy fouling management

Abstract: In dairy industries, production costs are highly impacted by the deposition of fouling onto equipment. Promising coatings to prevent fouling adhesion (i.e. anti-fouling) or to ease fouling removal (i.e. fouling-release) were previously developed. Nonetheless, their durability and food-compatibility were limited. Consequently, to overcome these limitations, this work aims at designing coatings based on innovative surface modification techniques and concepts: (i) polymer deposition by atmospheric pressure plasma torch and (ii) bioinspired slippery surfaces by femtosecond laser ablation and oil infusion. The first technique allowed the deposition of hexamethyldisiloxane (HMDSO) which demonstrated good fouling-release performances but did not allow the durability improvement. The alternative deposition of two precursors (HMDSO and *1H,1H,2H,2H* perfluorooctyltriethoxysilane) was studied. Superhydrophobic and very stable bilayers were deposited onto stainless steel, showing good but still improvable fouling-release properties (fouling reduction of 72%). The second research axis consisted in designing slippery liquid-infused surfaces (SLIS) following three steps: (i) laser structuration of stainless steel, (ii) chemical modification of structured surface and (iii) lubricant impregnation. An optimization of laser parameters allowed to reach quickly various types of deep microstructures. Food-compatible SLIS were developed by replacing fluorine-based lubricant by coconut oil. Although a poor durability due to a loss of oil, coconut-SLIS exhibited promising fouling-release performances with a fouling deposit reduction of 114%.

Keywords: Surface modification, plasma bilayer, coconut-SLIS, antifouling, pasteurization process

Résumé : Les industries laitières sont extrêmement impactées par l'encrassement des équipements de pasteurisation et de stérilisation. Une des solutions envisagées pour limiter l'adhésion de l'encrassement consiste à modifier la surface de l'acier inoxydable des échangeurs thermiques. Différents types de revêtements, limitant l'adhésion ou facilitant le nettoyage, ont précédemment démontré des résultats prometteurs. Cependant ces revêtements doivent être durables et compatibles avec les aliments. Cette thèse vise donc à développer des surfaces stables, non toxique et durables à haute température et en régime turbulent. Des techniques de modification de surface innovantes ont été utilisées pour concevoir ces revêtements : (i) dépôt de couches minces par plasma à pression atmosphérique et (ii) surfaces glissantes bio-inspirées obtenues par ablation laser et infusion/imprégnation d'un lubrifiant. La première technique a permis de déposer des couches minces d'hexaméthyldisiloxane (HMDSO) facilitant le nettoyage de l'encrassement mais présentant une faible durabilité. Le dépôt en alternance de deux précurseurs (HMDSO et *1H,1H,2H,2H* perfluorooctyltriethoxysilane) a également été étudié. Cela a permis de déposer des bicouches originales, stables et superhydrophobes. Les paramètres de dépôt pourront encore être optimisés pour améliorer leur nettoyabilité (réduction de l'encrassement après rinçage : 72%). Les surfaces glissantes bio-inspirées (SLIS) ont été fabriquées suivant trois étapes : (i) structuration de l'acier inoxydable par ablation laser, (ii) modification chimique de la surface structurée et (iii) imprégnation avec un lubrifiant d'huile. Une optimisation des paramètres laser a permis d'atteindre rapidement divers types de microstructures de différentes profondeurs. L'huile fluorée habituellement infusée a été remplacée par de l'huile de coco, rendant la surface compatible au contact alimentaire. Malgré une faible durabilité dûe à la perte d'huile, les surfaces glissantes infusées à l'huile de coco ont permis de faciliter le nettoyage (réduction de l'encrassement après rinçage : 114%).

Mots clés : Traitement de surface, bicouche plasma, surface glissante, huile de coco, anti-encrassant, procédé de pasteurisation